Nicolaus Copernicus University in Toruń
Doctoral School of Exact and Natural Sciences

Deriving the nature of the methanol masers in high-mass star-forming regions via multi-wavelength and polarimetric observations

Agnieszka Kobak

Supervisor: **Dr. Hab. Anna Bartkiewicz, Prof. NCU**
Institute of Astronomy
Nicolaus Copernicus University in Torun

Co-supervisor: **Dr. Katharina Immer**
European Southern Observatory

Toruń 2025

Contents

Abstract

This work presents research on high-mass star formation via maser emission, particularly the 6.7 GHz methanol maser transition. The observations were made via high-resolution interferometric networks, for radio wavelengths via Very Long Baseline Array (VLBA), the European VLBI Network (EVN), and Multi-Element Remotely Linked Interferometer Network (MERLIN), and for millimeter wavelengths via Atacama Large Millimeter/submillimeter Array (ALMA). The publication summarizes the maser flare for the three maser transitions (6.7, 12.2, and 22.2 GHz) in young high-mass stellar objects. The detailed analysis of the distribution and morphology of maser cloudlets, as well as infrared and submillimeter counterparts, during the flare indicates a lack of episodic-accretion burst events and indicates the less energetic phenomena. The publication II focuses on the coincidence between 6.7 GHz methanol transition and 6.035 GHz exited OH transition in ten high-mass star formation regions to put constraints on physical conditions around young stars. We analyze the mutual alignment of these two masers, their infrared, radio continuum, and submillimeter counterparts, and then we discuss the age of the sources. The results show that coincidence of two maser transitions is associated mostly with the local changes of physical properties on the small scales, a few hundred au. We also estimated the strength and the orientation of the magnetic field using the 6.035 GHz exited OH transition. The results show that the typical values of magnetic field strength are a few milligauss, and no relation between magnetic field orientation and the outflows. The publication III focuses on the magnetic field for two maser transitions (6.7 GHz methanol and 6.035 GHz OH). We attempted to determine which of the theoretical values of the splitting coefficient is dominant at the 6.7 GHz transition. As a result, we narrowed the choice of possible coefficients to three among eight. In the last chapter, we present the relation between thermal disc/shocks tracers and 6.7 GHz methanol maser emission in five high-mass star-forming regions where the ring-line morphology was derived at the 6.7 GHz line before. The ALMA data for the first time allow us to look directly into the environment of a forming high-mass star at a similar angular resolution as the VLBI observations of masers. Preliminary results indicate that the methanol

masers do not relate to disks in all cases; more complicated/sophisticated scenarios must be considered.

Chapter 1

Introduction

1.1 Formation of high-mass stellar objects - general view

The stars with masses above eight Solar masses are called high-mass stars. They constitute a tiny percentage of all stars in our Galaxy, but show brightness a thousand times larger than the Solar luminosity, and their impact on the surrounding environment is significant. They release an enormous amount of energy via molecular outflows/jets, ultraviolet (UV) radiation, and supernova (SN) explosions. Their high luminosities heat and/or ionize the interstellar medium (ISM), and their strong stellar winds concentrate or disperse the surrounding matter. During SN explosions, heavy particles that are essential for life are produced (Arcones and Thielemann, 2023).

High-mass stars are born in giant molecular clouds (GMCs). The complex of these clouds can be extended at or over 100 pc, whereas a single cloud has sizes of a few parsecs (Motte et al., 2018). The amount of gas and dust comprising GMCs (the mass of GMC is of an order of 10^5-10^6 $M_\odot$) does not allow direct observations in the optical wavelength range because of high opacity. Moreover, when a young high-mass star ignites hydrogen, it is still deeply embedded in the dense molecular cloud. These factors all make the high-mass star formation process still not well-known.

So far, two main theoretical scenarios have been discussed in the literature. The first one is the turbulent core (TC) model (also called core accretion; McKee and Tan, 2003), which is an extension of the low-mass star formation model (Shu et al., 1987) where the single or multiple low-mass stars are formed by the gravitational collapse of an isolated, dense prestellar core or cores via the accretion disk (Larson, 1981; Shu et al., 1987). The cores arise during the fragmentation of the GMC. First inside the cloud arise the smaller *clumps* with sizes 0.1-1 pc and densities order 10^4-10^6 cm^{-3}, which can be seen as infrared dark clumps (IRDCs; Motte

et al., 2018). Inside the clumps rise the massive, dense cores (MDCs) with sizes ∼0.1 pc and masses 75-1000 $M_\odot$ and densities from 10^5-10^7 cm^{-3} (Motte et al., 2018; Tigé et al., 2017). During the last phase, the MDC contracts to the prestellar core of size ∼0.03 pc. In the TC model, most of the mass of a future star is already in the gravitationally bound, prestellar core. After contraction to the star, only a slight fraction of mass can be accreted via the disc. The second competitive accretion (CA) model (Bonnell and Bate, 2002; Bonnell et al., 2004; Bonnell and Bate, 2006) does not predict the existence of a gravitationally bound, prestellar core. In this model, gas is gathered via chaotic accretion from a wide region of the clump/MDC. The total mass of the forming massive star is a small fraction of the total mass of the clump, and consequently, the future high-mass star is surrounded by a lot of low-mass stars. The CA model also allows for numerous stellar collisions, especially in the center of the clump, where the number of forming stars is the highest. These stellar mergers can contribute to the origin of the most massive stars, in particular stars above 140 $M_\odot$, which cannot be created only due to CA.

Regardless of the original mechanism of birth, when a protostar reaches 8 $M_\odot$, its luminosity rapidly grows and the star becomes bright in infrared (IR) radiation. In this phase, the radiation pressure is so big that the star can accrete matter only via a disk. The accretion disks can have sizes of 100-1000 au (e.g., Chen et al. 2016; Guzmán et al. 2020). With the accretion disk, bipolar outflows also appear, which can extend from hundreds of astronomical units to even a few parsecs (e.g., Greenhill et al. 2013; Fedriani et al. 2018). A very high luminosity of the protostar causes ionization of the ambient gas. The regions of ionized hydrogen (HII) are tightly correlated with the HMYSOs, and can spread up to 10 pc (Motte et al., 2018). Ultra-compact HII regions (UCHII) can be created close to young stars with sizes less than 0.1 pc or hyper-compact HII regions (HCHII) with sizes 0.05 pc (Murphy et al., 2010).

1.2 Maser emission

Astrophysical masers are ubiquitous in cosmic space; they are observed around young and old stars, in the surroundings of comets, supernova remnants, and the atmospheres of planets (e.g., Jupiter); they are also detected beyond the Galaxy or even the Local Group and are referred to as kilo- and megamasers. Nowadays, masers, especially those associated with selected transitions in OH, H_2O, and CH_3OH molecules, are widely used to study the HMYSOs. The centimeter radio waves can easily escape the GMC, where these massive stars are born, and reach medium-sized radio telescopes on Earth.

1.2.1 Stimulated emission

Maser action stands for Microwave Amplification by Stimulated Emission of Radiation. This phenomenon can arise when gas is in a state known as population inversion, which means the number of excited atoms or molecules has to be higher than the number of atoms or molecules in the ground state. When this condition is achieved, the stimulated emission can occur. The Figure 1.1 shows the schematic diagram of stimulated emission for an atom.

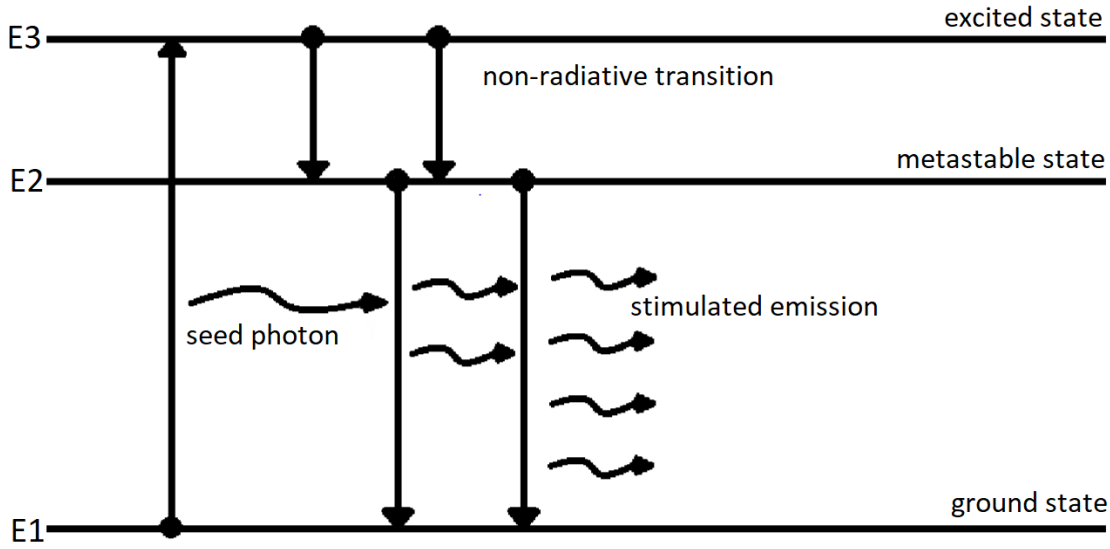

Figure 1.1: The schematic diagram of stimulated emission.

First, the atom has to be excited to the upper level. First, the atom must be excited to a higher energy level. In the case of a single atom, the valence electron gains energy and moves to a higher energy level. In the case of a molecule, the excitation process can occur through the excitation of an electron or a change in the vibrational or rotational state of the molecule. For example, the 6.7 GHz CH_3OH maser transition is a rotational transition of the molecule. The excitation process is called pumping, and there are three ways this process can occur: radiative, collisional, and via chemical reaction. A particle can be pumped in multiple ways depending on the surrounding environment and frequency of the transition. Right after excitation, the atom is in an unstable state; therefore, it immediately undergoes a spontaneous, usually non-radiative, transition to a lower, metastable level, where the atom can persist long enough to encounter a photon that forces the stimulated emission. That photon is referred to as a seed photon. The energy of the seed photon has to be equal to the difference between the atom's energy in the metastable state and in the ground state. When the seed photon encounters the atom, it triggers stimulated emission, which means that the atom moves to the ground level, emitting exactly the same photon (with the same properties, e.g., direction, phase, or energy)

as the seed photon. The seed photon is not absorbed by the atom, so that both photons, seeded as well as emitted, may cause further stimulated emission. That provides an exponential gain of emission along the way of amplification, resulting in very bright, concentrated emission. Worth noting that maser is a directional effect; if the direction of amplification is different from the line-of-sight, maser emission is not visible to the observer. All of the above yield that only a part of the gas in HMYSO is visible via maser emission, regions with proper physical conditions for amplification, and lying in a suitable direction for observation.

1.2.2 Masers in HMYSOs

In HMYSOs, a few species of masers can be observed. The most popular and very ubiquitous are methanol (CH_3OH), the hydroxyl group at ground (OH) and excited (ex-OH) levels, and the water (H_2O) masers ((e.g., Menten, 1991; Breen et al., 2010a; Fujisawa et al., 2014; Szymczak et al., 2020)). Rarely, formaldehyde (H_2CO; Liu et al., 2023), semi-heavy water (HDO), and isocyanic acid (HNCO; Chen et al., 2020), carbon monosulfide (CS; Ginsburg and Goddi, 2019), or ammonia (NH_3; Wu et al., 2023b) masers can be found.

Among all these species, the methanol maser has been the most widely observed since its discovery, because the 6.7 GHz transition is exclusively related to high-mass stellar regions, so it is an undisputed sign that a high-mass star is forming nearby (Breen et al., 2013). In general, there are two classes of methanol masers (Batrla et al., 1987; Menten, 1987): (1) Class I – masers are pumped by collisions with molecular hydrogen and are associated with bipolar outflows, e.g., transitions at 25, 36, 44, 95 GHz, and (2) Class II – masers are pumped radiative by dust infrared radiation, e.g. 6.7 and 12.2 GHz. This class is related to HII regions, infrared (IR) emission, and OH, as well as ex-OH masers. As I stated above, the most common transition of methanol masers in HMYSOs is the 6.7 GHz line. Since its first detection in 1991 (Menten, 1991), numerous sources have been discovered during large sky surveys (e.g., Szymczak et al., 2000, 2002; Green et al., 2009; Breen et al., 2015; Yang et al., 2018; Rickert et al., 2019; Aberfelds et al., 2023b). The models show that 6.7 and 12.2 GHz transitions occur in the gas density range of 10^5-$10^{8.3}$ cm^{-3} about temperature ∼30-150 K, whereby the brightness is bigger for 6.7 GHz maser (Cragg et al., 2002). The dust temperature needed for effective pumping should be above 100 K and always bigger than the gas temperature (Cragg et al., 2002). Breen et al. (2010b) found that 12.2 GHz transition is associated with 6.7 GHz in ∼60% of sources and confirmed that 6.7 GHz is almost always brighter; in a few cases, the 12.2 GHz maser was marginally stronger, which is not predicted by theory. The life time of 6.7 GHz was first time

estimated by van der Walt (2005) at $2.5 - 4.5 \times 10^4$ yr, later Billington et al. (2019) specify this at 3.3×10^4 yr, and Breen et al. (2010b) estimated the life time of 12.2 GHz maser at 2.1×10^4 yr, that numbers explain why 6.7 GHz maser can be observe without counterparts of 12.2 GHz. It is worth noting that 6.7 GHz maser exists over the longest period of time among all maser species (Jones et al., 2020).

The second maser molecule observed in HMYSOs, often correlated with methanol, is the ground-state transition of OH (1.665 GHz and 1.667 GHz) and excited OH (6.035 GHz). Those masers are also pumped by dust infrared radiation, hence can arise in the vicinity of 6.7 GHz transition. The OH and ex-OH masers prefer the lower gas temperatures (Cragg et al., 2002), i.e., the brightness of 1.665 GHz transition in gas temperature 30 K is independent of density for gas density at 10^8 cm^{-3} and of dust temperature, but when gas temperature achieves 150 K maser is existing only at low gas density below 10^7 cm^{-3} and also need a high dust temperature above 200 K. The ex-OH masers are present only when gas temperature is below 70 K and they require a high gas density in the range $10^{6.5} - 10^{8.5}$ cm^{-3}. All OH masers occur as the latest with the time evolution of HMYSOs (Jones et al., 2020). They have short lifetimes estimated between $3.3 - 8.3 \times 10^3$ yr for ex-OH (Avison et al., 2016) and up to 10^4 yr for ground-state OH (Jones et al., 2020).

The third popular maser molecule is H_2O maser with the most common transition at 22.2 GHz. This maser is pumped via collisions with H_2 molecules and thereupon is associated with outflows/shocks/jets. The 22.2 GHz transition needs the gas densities $\sim 10^7$ cm^{-3} and high gas temperatures in order $\sim$400 K to arise (Beuther et al., 2002). The lifetime was estimated as $0.6 - 2.3 \times 10^4$ yr (Jones et al., 2020). Depending on the physical conditions in the HMYSO region, different kinds of masers are observed. There is a given short timespan (around the relative age of $22 - 25 \times 10^3$ yr; Jones et al., 2020) when all these maser species could exist in the same time, but this state requires proper dust and gas temperatures, and gas density, which makes it usually, in one YSO, is observed masers from one or two different molecules.

To study the morphology of masers, interferometric observations are utilized, as sub-arcsecond or even milliarcsecond angular resolution is required. A radio interferometer is a network of radio telescopes (e.g., The European VLBI Network (EVN), The Karl G. Jansky Very Large Array (VLA), Multi Element Remotely Linked Interferometer Network (MERLIN)), which, during simultaneous observation, can build a map of the observed region of sky. Owing to very good angular resolution and sensitivity of such instruments, we can study the distribution of single maser clouds. So far, observations have revealed a few maser morphologies (structures)

in HMYSOs: single/compact, linear, elongated/filamentary, arched/curved, ring-like/elliptical, and complex (e.g., for methanol masers Bartkiewicz et al. 2009, 2011, 2014, 2016; Sugiyama et al. 2008; Sanna et al. 2010a,b; Pandian et al. 2011; Hu et al. 2016; for OH and ex-OH masers Hutawarakorn et al. 2002; Fish et al. 2005; Nammahachak et al. 2006; Green et al. 2007; for water masers Nagayama et al. 2008; Surcis et al. 2023).

The maser's morphology can be variable in time. The changes can be small, like the slow expansion of the ring structure (Bartkiewicz et al., 2020) or the slow outflow of linear structure (Aberfelds et al., 2023a). In order to track these displacements, the proper motions of the maser spots and cloudlets are determined For this, more than one observational epoch by interferometers is needed, preferably at intervals of several months to years, or even more than a dozen years. Such studies require careful data calibration and a few assumptions: the maser spot should have stable brightness (however, none significant changes in the spectrum do not guarantee there are no rapid changes in the maser morphology/distribution (see next paragraph)), and the single spot should not change its local-standard-of-rest velocity ($V_{\rm LSR}$) over all epochs, if a spot has the same $V_{\rm LSR}$ in every observational epoch, we can track its path on the sky. Having the path and the time, we simply calculate the speed of this spot in the sky, and this is the proper motion. The results are typically averaged for groups of spots located within a half-beam at consecutive spectral channels, creating so-called cloudlets to minimize the possibility of a false assumption that all spots achieve their $V_{\rm LSR}$. The proper motions are a useful tool to track the kinematics of gas on the smallest scales, like expansion, rotation, contraction, outflow, or inflow (e.g., Fish and Reid, 2007; Sanna et al., 2010b; Moscadelli et al., 2011; Bartkiewicz et al., 2020, 2024; Wu et al., 2023a).

The variations in masers' morphology can also occur more rapidly, often correlated with variability in their brightness, and are characterized by the appearance and disappearance of maser spots and/or entire clouds. Sometimes the variability can be periodic, with alternate spans of stability and flares of luminosity, lasting from several dozen to several hundred days (e.g., Szymczak et al., 2015; Olech et al., 2020; Durjasz et al., 2022). In other cases, a very strong, sudden brightness increase is observed, which is called a maser burst (e.g., Bayandina et al., 2019; Burns et al., 2020b).

There are two causes for maser brightness variability. The first one stems from a geometric effect, because maser emission strongly depends on direction (the observer sees only emission directly towards, along the line-of-sight, as I mentioned above). If two maser-emitting regions overlap, the amplification path is longer, and it can be seen as an increase in brightness. That kind of variability would be rather random and caused, for example, by turbulence in the gas

(e.g., Durjasz et al., 2019; Bayandina et al., 2019; Burns et al., 2020a).

The second cause is related to physical changes in the source, which impact the pumping process, like changes in protostar luminosity, i.e., bigger luminosity provides stronger dust heating and an increase in IR radiation, which pumps the methanol and OH masers. One of the reasons for luminosity changes is episodic accretion, which occurs when massive protostars gather most of their mass during short, sudden surges in the accretion rate (Kenyon and Hartmann, 1995; Meyer et al., 2017, 2019). This model was born as an answer to the *luminosity problem*, where newborn stars have much smaller luminosity than was predicted by standard models of star formation. These models imply a stable accretion with persistent, high velocity via disc, which should let out the bulk of energy and lead to very high luminosity of a newborn star, but observations did not confirm that. Adding the episodic accretion caused that for most of the time the star has a small luminosity, and only in a short period of time, a violent increase of luminosity could be observed, which could also be observed as sudden maser bursts. The observational evidence on the existence of episodic accretion appeared for the first time in the source S255IR-NIRS3 for methanol maser; many observations confirmed that the central object accumulated huge mass ($\sim 3.4 \times 10^{-3}\,\mathrm{M}_{\odot}$) in a short period of time (around 9 months) (Caratti o Garatti et al., 2017; Moscadelli et al., 2017; Szymczak et al., 2018b). The other reason for luminosity changes is stellar pulsation of outer layers (Inayoshi et al., 2013). In this model, the variability of masers is triggered by changes in UV radiation emitted by stars and absorbed by dust, which changes the re-emission of IR. In this case, the periodic maser variability is expected. Different models for periodic masers involve a binary system. The first one is called a Colliding Wind Binary (CWB; van der Walt, 2011; van den Heever et al., 2019), where interaction between stellar winds causes extra free-free emission; these added photons become the seed photons for maser emission. The second one describes the impact of the interaction between spiral shocks generated in the central gap of the disk and denser matter in the disc, which yields warming up of the dust and increasing IR radiation (Parfenov and Sobolev, 2014). Not always can the pattern of the variations be explained by only one model; some sources show a more complicated structure, which could be a mix of all or some different processes (Szymczak et al., 2015; Olech et al., 2019).

1.2.3 The observed maser counterparts in HMYSO

Masers related to high-mass star-forming regions are associated with other observable tracers of star formation, like IR emission, radio continuum emission, and millimeter emission. It has

only been recently that we can reach close sub-arcsecond resolution to properly compare the strength and mutual alignment of masers and their counterparts. For example, to locate the masers in the disk or outflow, we can verify their coincidence with the millimeter emission, which is a tracer of warm dust and gas. The thermal millimeter lines, such as SiO, SO, and ^{13}CO, are associated with outflows/jets as tracers of shocks (e.g., Hirano et al., 2006; Guzmán et al., 2018; Bjerkeli et al., 2019). The other molecules like CH_3CN, HC_3N, and H_2CO are warm, dense gas tracers associated with the stellar disk or envelopes (e.g., Johnston et al., 2015; Cesaroni et al., 2017; Sanna et al., 2019). The continuum millimeter emission as a tracer of warm dust allows for the location of a cluster/clump/stiffening of dense dust, which is interpreted as the embedded dusty core harboring one or more young stellar objects (YSO; e.g., Maud et al., 2018; Williams et al., 2022).

The radio continuum emission can be a sign of radio jets or HII/UCHII regions. The major distinction between them is morphology. The HII/UCHII regions have an extended, often symmetrical shape, which is a product of the interaction between the ionizing radiation of the star and the surrounding dense gas (Kurtz et al., 1994; Motte et al., 2018). Whereas jets have an elongated, collimated shape, sometimes with bipolar morphology as a sign of stellar outflows (Anglada et al., 2018; Purser et al., 2021). The HII/UCHII are often associated with OH masers, which can be found around expanding UCHII regions (e.g, Argon et al., 2000; Fish and Reid, 2006; Fish and Sjouwerman, 2010). On the other hand, the radio jets are often associated with water masers, which trace the shocked gas in bipolar outflows (e.g, Nagayama et al., 2008; Bayandina et al., 2019).

Class II methanol masers and OH masers are directly associated with IR emission because of their radiative pumping mechanism. Additionally, the IR emission can provide insights into the evolutionary stages or activity of HMYSOs. Typically, three ranges of IR emission are differentiated: Near-Infrared (NIR), Mid-Infrared (MIR), and Far-Infrared (FIR), and they trace different regions and components of the HMYSOs. NIR emission (0.65-2.4 μm) comes from a protostar, the hottest, inner part of the disc, or warm shock gas in outflows. The more evolved stars are brighter in NIR and fainter in the longer IR wavelength, because their vicinity contains fewer dust grains that could absorb short-wavelengths. The MIR (3-25 μm) comes from dust grains with temperatures above 100 K and traces cooler regions of HMYSOs; it is responsible for maser pumping. The correlation between maser bursts/flares and sudden increase of the MIR flux was confirmed (e.g., Durjasz et al., 2019; Olech et al., 2020, 2022; Stecklum et al., 2021; Chen et al., 2021). The FIR (wavelengths above 28 μm) probes the coolest and the most distinct environment of HMYSO. The significant surge in this radiation

can be a sign of a maser burst (Stecklum et al., 2021). The good indicator of evolutionary stage is ratio of 70 μm emission and 24 μm (or 22 μm) emission (S_{70}/S_{24}). Both these values increase during evolution when the protostar becomes bigger and brighter, but S_{24} surges faster. The HMYSO with low (S_{70}/S_{24}), below ∼100 are considered as evolved YSO, whereas the higher ratio, the earlier the evolutionary stage (Purser et al., 2021).

1.3 Magnetic field

1.3.1 Role of the magnetic field in high-mass star formation

The role of the magnetic field in the high-mass star formation process is widely discussed. Theoretical models, as well as observational data, show that the magnetic field has a strong influence on every stage of high-mass star formation (comprehensive reviews, e.g., Hennebelle and Inutsuka, 2019; Krumholz and Federrath, 2019; Tsukamoto et al., 2023; Pattle et al., 2023). Firstly, it reduces the fragmentation of gas in the molecular cloud due to magnetic pressure and tension, which support the radiative pressure forces and act against gravity, generating the large filament structures and reducing the number of clumps and cores. That provides that the clumps and cores that are created are bigger, and owing to that, a young proto-star has more surrounding gas to accrete. The magnetic pressure, acting against the gravitational force, also increases the minimum mass required for gravitational collapse (the effective Jeans mass), resulting in more massive cores being formed.

Second, an important influence is that the magnetic field removes the angular momentum away from collapsing cores, which allows, during the beginning phase, for spherical accretion; only the matter with low momentum can freely fall to the star. Later, as the protostar becomes larger and dominates accretion through the disk (radiation pressure stops attracting material from the surroundings), the removal of momentum by the magnetic field slows down the material in the disk enough that frictional and viscous forces allow material to be transported into the star, instead of spreading the material around. The angular momentum is carried by the outflow, which is perpendicular to the disk. Due to the magnetic field, the outflow can arise in the very early phase of formation. There exists some evidence on the dependence between the orientation of the magnetic field and gas kinematics in the outflows/jets. The submillimeter dust continuum polarization observations show that in many cores in high-mass star formation regions, an hourglass shape of the magnetic field was observed, which is created when the collapsing core drags the magnetic field lines (Li et al., 2015; Beltrán et al., 2019). Later, the

rotating protostar and disk drag the magnetic field, twisting it, leading to magneto-centrifugal winds and toroidal forces which collimate the matter in outflows/jets (Moscadelli et al., 2022).

1.3.2 Magnetic field from masers

Maser emission from paramagnetic molecules plays a crucial role in direct measurements of the magnetic field via the Zeeman effect, which splits a spectral line into several components. The number of components is related to the magnetic field strength and to the quantum property of the specific molecule. In the astronomical observations, the Zeeman triplet is observed, consisting of one, non-shifted π component and two, shifted σ components. In the spectral observations, the triplet is visible as linear and circular polarizations. The π component is always polarized linearly, but the σ components can be polarized both circularly and also linearly (Figure 1 in Crutcher and Kemball, 2019). Polarimetric observations are based on four Stokes parameters: I and V are related to circular polarization, and Q and U to linear polarization. Stokes I (the total intensity) is equal to 0.5×(RHCP+LHCP), and Stokes V is equal to 0.5×(RHCP−LHCP), where LHCP is the left-handed circular polarization and RHCP is right-handed circular polarization. The LHCP and RHCP respond to circularly polarized σ components. The strength ($P_{\rm l}$) and the orientation on the sky-plane ($\chi_{\rm l}$) of linear polarization is calculated by $(Q^2+U^2)^{0.5}$ and $0.5\times\arctan(U/Q)$, respectively. To find out which component (σ or π) is responsible for linear polarization, we check the position of the peak of $P_{\rm l}$ on the spectra toward the position of peaks of LHCP and RHCP. The linear polarization comes from π component, as a non-shifted emission, should appear between LHCP and RHCP emissions.

In HMYSOs, the best molecule to measure the magnetic field is OH, because as a paramagnetic molecule, it is very sensitive to a magnetic field due to its unpaired electron, and Zeeman splitting is relatively easily observed. Moreover, the OH (and in consequence exited OH) has a simple hyperfine transition and the Landé g-factor and following splitting coefficient ($\alpha_{\rm Z}$) is well determined for decades (Davies, 1974). The splitting coefficient allows for determining the magnetic field strength along the line-of-sight ($B_{||}$) by the formula $B_{||} = \Delta V_{\rm Z}/\alpha_{\rm Z}$, where $\Delta V_{\rm Z}$ is the velocity difference between the LHCP and RHCP (the Zeeman splitting). For OH and ex-OH masers, the $\Delta V_{\rm Z}$ has a typical value of a few hundred meters per second, which means that at a typical spectral resolution of several dozen meters per second, it is easily measurable at the centimeter wavelength range using radio spectrometers. The magnetic field in HMYSOs using OH and ex-OH masers has been measured many times, with an average strength of a few milligauss (mG) (e.g., Baudry et al., 1997; Hutawarakorn et al., 2002; Etoka et al., 2005; Fish

and Reid, 2007; Asanok et al., 2010; Green et al., 2015; Edris et al., 2017; Darwish et al., 2020; Ashimbaeva et al., 2023).

Note, this method allows only to measure $B_{||}$, which is one component of the total magnetic field ($B_{\rm TOT}$), and that is $B_{||} = B_{\rm TOT} \times cos\theta$, where θ angle, which describes the angle between the total magnetic field orientation and the line-of-sight. There is no method to measure the other component $B_{\perp} = B_{\rm TOT} \times sin\theta$, because we do not know the value of θ. Indeed, for OH and ex-OH masers in many cases the linear polarization is only a small percentage, and it was proven that most of the polarization comes from σ components, indicating that $B_{\perp}$ is negligible and we can roughly assume that $B_{\rm TOT} \approx B_{||}$ (Fish et al., 2005; Nammahachak et al., 2006; Green et al., 2015).

Over the last few years, a method for measuring the magnetic field using the CH_3OH molecule has also been developed. The particle is non-paramagnetic, indicating that the molecule is not susceptible to a magnetic field, and the Zeeman splitting is very small and difficult to measure. The splitting between RHCP and LHCP components is an order of a few meters per second (e.g., Surcis et al., 2012, 2013). This value is smaller than the radio spectral resolution, which means that the standard measuring procedure, as in the case of the OH maser, is not possible. One of the methods for estimating that small splitting is the cross-correlation method, which allows for direct measurement using RHCP and LHCP spectra (for a detailed description, see Appendix B of Modjaz et al., 2005). This method works best for simple spectra, as it assumes persistent Zemann splitting across the entire spectrum. For a more complicated spectral profile with multiple Gaussian features, the full radiative transfer method (FRTM) code is employed, which comes down to fitting the theoretical profile to the individual spectral features (more details in Vlemmings et al., 2010; Surcis et al., 2019). This method enables us to find not only the desirable splitting but also some physical parameters, such as the emerging brightness temperature, intrinsic line, and the most important θ angle, which facilitate us to estimate $B_{\rm TOT}$.

Another problem appearing in the estimation of magnetic field strength by methanol masers is a complicated hyperfine structure of the 6.7 GHz transition. The theoretical calculations show that 8 possible sub-transitions, which can contribute to the 6.7 GHz transition (Lankhaar et al., 2018), each of them with its own Landé g-factor and consequently with its own splitting coefficient. Nonetheless, some transitions, F=3→4, F=6→7A, and F=7→8 are considered as preferred (Lankhaar et al., 2018; Surcis et al., 2022; Dall'Olio et al., 2020). The estimated values of $B_{||}$ based on methanol maser observations and the most probable splitting coefficients are often larger than those computed from the OH masers, and reach values from a few to

even several hundred milligauss (Vlemmings, 2008; Surcis et al., 2011, 2019, 2022). These differentials point to the necessity of further studies in this regard.

The P_l and χ_l can be calculated in the same way for OH and methanol masers (see the first paragraph of the Chapter 1.3.2). These two parameters allow tracking the magnetic field orientations on the sky plane. The masers trace the magnetic field on the smallest scales in the direct vicinity of a high-mass protostar. So far, the observations do not give uniform results for the dependence between the magnetic field and the outflow direction. In some sources, they align, and in other cases, the magnetic field is perpendicular to the outflows (Hutawarakorn et al., 2002; Nammahachak et al., 2006; Fish and Sjouwerman, 2010; Surcis et al., 2012, 2013, 2015, 2019, 2022). Hence, an open question remains about the magnetic field orientation as of up to date.

1.4 Project goal

The primary objective of this project is to investigate the environment of HMYSOs, placing constraints on physical conditions, including magnetic fields, in these dense and distant regions of the Galaxy. Using multi-species masers and multi-wavelength data of maser emission, an approach has been developed to understand the kinematics at the scales of accretion discs around high-mass proto- and young stars, and to connect them to the larger-scale kinematics of the system. In the following three publications, was analyzed multi-wavelength maser behavior during the 6.7 GHz methanol maser flare in HMYSO G24.33+0.14, derived physical conditions in a sample of HMYSOs via methanol (6.7 GHz) and ex-OH (6.03 GHz) maser observations, and attempted to estimate the splitting coefficient for the 6.7 GHz methanol transition.

- "Multi-frequency VLBI observations of maser lines during the 6.7 GHz maser flare in the high-mass young stellar object G24.33+0.14", Kobak A., Bartkiewicz A., Szymczak M., Olech M., Durjasz M., Wolak P., Chibueze J.O., Hirota T., Eislöffel J., Stecklum B., Sobolev A., Bayandina O., Orosz G., Burns R.A., Kim K.-T., van den Heever S.P., Astronomy & Astrophysics, 2023, 671, A135, 1-26.

- "Physical conditions around high-mass young star-forming objects via simultaneous observations of excited OH and methanol masers", Kobak A., Bartkiewicz A., Rygl K.L.J., Richards A.M.S., Szymczak M., Wolak P., Astronomy & Astrophysics, 2025, 695, A149, 1-14.

- "A search for the favored hyperfine transition of a 6.7 GHz methanol maser line", Kobak

A., Surcis G., Bartkiewicz A., Vlemmings W.H.T., Szymczak M., Astronomy & Astrophysics, 2025, 701, A101, 1-13.

Moreover, we have studied the thermal millimeter emission of counterparts of a unique sample of methanol maser sources in which the maser spots form ring-like structures. The primary results are presented in the Chapter 5.

Chapter 2

Multi-frequency VLBI observations of maser lines during the 6.7 GHz maser flare in the high-mass young stellar object G24.33+0.14 - Publication I

The aim of this publication was to derive the kinematics and physical conditions in the close environment of a HMYSO G24.33+0.14 during a burst that was detected at the 6.7 GHz methanol maser line in September 2019 (Wolak et al., 2019) via multi-epoch and multi-frequency studies of masers. We analyzed data at three frequencies: two methanol maser transitions (6.7 GHz and 12.2 GHz) and a water maser transition (22.2 GHz). These observations were carried out using the VLBA interferometer at all three transitions over three epochs: 27 September 2019 (DOY:270), 27 October 2019 (DOY:300), and 2 December 2019 (DOY:336). Furthermore, we used three more epochs for the 6.7 GHz transition from the EVN interferometer on 1 June 2009 and 7 October 2019 (DOY:152/2009 and DOY:280, respectively) and the LBA interferometer on 28 September 2019 (DOY:271). For clarity, I state that the preliminary results of the project, specifically related to: imaging of observations, searching for a maser coincidence, and millisecond analysis for all maser cloudlets, were presented in the MSc thesis "Analysis of the methanol maser outburst in the source G24.33+0.14" (Archive of Diploma Theses).

Under this PhD thesis, the following subjects were studied:

- Analysis of the evolution of 6.7 GHz methanol maser cloudlets during three epochs. We found that cloudlets in epoch DOY:300 are 60% and 40% brighter than in epochs DOY:270 and DOY:336, respectively. Among 14 cloudlets, 9 do not change size, 1 cloudlet shrinks, and 4 cloudlets expand. The expanding cloudlets do not change their brightness and lie

further from the central source. The velocity gradient and position angle remain constant during the burst. The overall morphologies of masers did not show significant variability throughout the flare.

- Analysis of long-term variability using data from the single-dish RT4 in Toruń. We estimated that the burst lasted 280±3 days and was preceded by small-amplitude variations with a period of approximately 6 months.

- Comparison maser burst with IR emission using data from WISE AND NEOWISE database. We showed the increase of the 3.4 μm and 4.6 μm emission during maser flare; it confirmed the infrared pumping mechanism of the 6.7 GHz methanol maser transition.

- Comparison of the water masers distribution to the ALMA 229.758 GHz class I methanol maser line (reported by Hirota et al. (2022)) and to the 43 GHz radio continuum (presented by Purser et al. (2021)). The Q-band ionized jet and both maser emissions are aligned along the same direction. This supports the scenario that 22.2 GHz water masers trace the outflow.

- Fitting the Keplerian rotation model using the 6.7 GHz methanol maser and the central mass of 8.8$M_{\odot}$ estimated by Hirota et al. (2022). We obtained the inclination angle of $85° \pm 3°$. The results indicate that 6.7 GHz methanol maser traces the inner part of the disc.

- Estimation of the time lags of selected 6.7 GHz maser cloudlets during the bursts. The outcome shows a trend of increasing brightness with the distance from the central star. The maximum time lag was 59.5 days, indicating that the maser flare propagated at around 0.33 of the speed of light.

In summary, the above results suggest that the maser flare was triggered by an episode of enhanced production of infrared photons and could be caused by an accretion event. Although the brightening of the 6.7 GHz methanol maser line was registered, the multi-band and multi-epoch imaging of masers and investigations of IR data indicate a lack of episodic accretion burst as it was detected, e.g., in G358 (Burns et al., 2020b). The remaining morphology throughout the flare and its similarity to that of the quiescent state, the less-energetic accretion event than in G358.

Chapter 3

Physical conditions around high-mass young star-forming objects via simultaneous observations of excited OH and methanol masers - Publication II

In this publication, we analyzed 10 HMYSOs with emission of 6.7 GHz methanol masers and 6.035 GHz excited OH masers. Observations were carried out using the e-Merlin[1] interferometer, nearly simultaneously in full-polarization mode, under the project CY10206 in the periods of July–October 2020 and August 2022. The project aims were: 1) to derive the physical conditions in a sample of HMYSOs via combined observations of ex-OH and methanol masers, the spatial coincidence or avoidance of these two masers can depend on the parameters like gas or dust temperature, gas density (Cragg et al., 2002), and 2) to derive the strength and orientation of magnetic field via ex-OH maser polarimetric observations.

In this publication, we presented:

- The spectra and distributions of both maser transitions for ten HMYSOs. We note that eight ex-OH masers were imaged for the first time. The methanol maser was always brighter than the ex-OH maser. We estimated the whole masing areas in these targets, and noted that in three cases, the ex-OH maser exhibited a more complex distribution. We fitted the linear function to the masers' distribution to estimate directions of their elongations.

- Identification of the Zeeman splittings. We detected 37 Zeeman pairs at the ex-OH

[1] https://www.e-merlin.ac.uk/

transition and estimated the magnetic field strength in eight sources with values from −10.6 mG to +8.5 mG (negative values imply the direction of the magnetic field toward the observer, positive values directed away from the observer). Moreover, we identified the eight Zeeman triplet candidates in four sources.

- For nine sources, we detected components with linear polarization and determined the magnetic field orientation on the plane sky.

- Analysis of the counterparts of our targets using the archival data:

  – Using the archival ALMA data, we studied the mutual alignment between the millimeter dust continuum emission and both kinds of maser emission.

  – We also compared masers with VLA radio continuum emissions (we found them for 8 sources) and identified 4 of them as UC HII regions. Two sources do not show any radio emission (Hu et al., 2016).

  – Using above radio continuum data and the spectral ALMA data, employing disk tracers (H_2CO, CH_3CN, HC_3N), shock tracers (SO, SiO), or outflow tracers (^{12}CO, ^{13}CO, $C^{18}O$), we determined the outflow directions in HMYSOs from our sample.

  – To constrain the clump properties, we analyzed the mid-IR emission (3.5, 4.5, 6, 8, and 24 μm) from *Spitzer*, and the far-IR 70 μm *Herschel*.

  – From the Hi-Gal catalog, we took the clump properties like mass, dust temperature, luminosity, and the luminosity-to-mass ratio.

- Description of the evolutionary stage of HMYSOs. Using parameters such as the luminosity-to-mass ratio, continuum radii, and UCHII emission, as well as the ratio of 70 μm to 24 μm (Purser et al., 2021), we aligned sources according to their evolutionary stage.

- Comparison of the orientation of the magnetic field with the direction of masers' distribution. We used the Kolmogorov-Smirnov test to compare the derived directions of outflows, the orientations of the magnetic fields, and the elongations of the masers' distribution.

- Deriving the physical conditions by identification of co-propagating maser lines. In six targets, we found the coincidences of both transitions in both: positions and the LSR velocity domains. Among them, we encountered two cases: one where some regions in the source coincide and some show only methanol emission, and two where some regions

in the source coincide and some show only ex-OH emission. We analyzed the relationship between coincidence and masers' brightness, dust and gas temperatures, densities, kinematic structures, morphology, YSO evolution, and magnetic field strength.

In summary, we state that coincidence or avoidance occurs due to local changes in gas or dust temperature and/or gas density at the scale of a few hundreds of au, which are related only to the distance from the YSO. The rest of the indicators do not impact on coincidence. We confirmed that the more evolved sources have more complex ex-OH emission, which is in agreement with theory (Jones et al., 2020). The Kolmogorov-Smirnov test reveals a nonrandom relationship between the distributions of both kinds of masers, indicating that they can be excited in the same kinematic region. We found a random relationship between outflows and magnetic field orientation, as well as between maser distribution and magnetic field orientation, which is consistent with the literature (Surcis et al., 2022). We detected only eight possible Zeeman triplets among 37 Zeeman pairs, confirming that for the OH molecule, most of the linear polarization originates from σ components (Green et al., 2015).

Chapter 4

A search for favored hyperfine transition of 6.7 GHz methanol maser line - Publication III

This publication aimed to determine which hyperfine transition among the eight ones contributes to the 6.7 GHz CH_3OH transition. Each of the hyperfine transitions has its own Landé g-factor and follows the Zeeman-splitting coefficient (α_Z). The theoretical values were calculated by Lankhaar et al. (2018).

Using the European VLBI Network (EVN), we followed up on the results obtained in Paper II. We selected two HMYSOs, where a clear coincidence of strong emission of 6.7 GHz methanol and 6.035 GHz ex-OH masers was detected using eMERLIN. The aim was to measure the magnetic field using the well-studied ex-OH molecule and to estimate the Landé g-factor of the 6.7 GHz methanol maser transition, assuming that both lines trace the same gas volume. The observations were made simultaneously in full-polarization mode, under the project EK052 on 29 May – 1 June 2023.

The method was as follows: first, we measured the Zeeman splitting (ΔV_Z) for both sources, W75N and ON1, for both maser transitions (the methods were described in Chapter 1.3.2). For ex-OH, by identifying LHCP and RHCP spectral features coming from the same position on the sky, we calculated $B_{||}^{\mathrm{ex-OH}}$. Second, under the assumption that overlapping maser clouds of methanol and ex-OH have the same $B_{||}$, we calculated the Zeeman splitting for the 6.7 GHz transition using formula $\alpha_Z^{\mathrm{CH_3OH}} = \Delta V_Z^{CH_3OH} / B_{||}^{\mathrm{ex-OH}}$. However, this straightforward method was not fully successful; we obtained the Zeeman-splitting coefficients at least one order higher than the theoretical ones.

In the second approach, we used theoretical $\alpha_Z^{\mathrm{CH_3OH}}$ for the three most probable transitions,

and using them, we calculated $B_{||}^{\mathrm{CH_3OH}}$. In that case, the obtained values were one or two orders higher than $B_{||}^{\mathrm{ex-OH}}$. In the next step, we estimated the gas density using the relation $B \sim n_{H_2}^{0.5}$ (Crutcher and Kemball, 2019) and compared it with the theoretical ranges of gas densities where masers can arise, as proposed by Cragg et al. (2002, 2005). In this way, we checked if the obtained values of magnetic field strength for methanol emission are reliable. Our calculation confirmed that newly obtained values of $B_{||}^{\mathrm{CH_3OH}}$ are in agreement with theoretical ones. Additionally, we compiled the available literature values of $B_{||}$ over the past 20 years and found that the magnetic field orientation on the sky-plane is stable for both transitions and both sources. Whereas the magnetic field strength is stable only for the ex-OH transition, and variable for the methanol transition. It is challenging to determine whether these changes are genuine or are the result of the variations in the dominating hyperfine transition. In conclusion, we were unable to identify the dominant hyperfine transition, but were able to narrow down the choice to three possibilities.

Chapter 5

The puzzle of the methanol maser ring - observations at high-angular resolution using ALMA

5.1 Introduction

The morphology of the 6.7 GHz methanol maser emission can take many forms (see Chapter 1.2.2). The most interesting are these regular ones, such as circular/ellipsoidal, also known as ring-like ones, because they give hope of directly relating them to structures around HMYSOs. That kind of morphology strongly suggests it arises in a circumstellar disk and/or in an outflow cone directed towards the observer. To find out where the maser arises, we need to link it with other gas tracers like CH_3CN or SiO, strongly related to disks or shocks, respectively (e.g., Sanna et al., 2019; Maud et al., 2018; Zinchenko et al., 2024). For this purpose, we chose five methanol maser sources that exhibited ring-like morphologies, and for some of them, proper motions were derived via multi-epoch VLBI measurements (Bartkiewicz et al., 2009, 2020, 2024). The long-term monitoring of these sources via the Torun 32-m radio telescope showed none or little variations in brightness over at least four years (Szymczak et al., 2018a). The names of the sources, distances, major- and minor-axes of maser rings, motions of rings examined by proper motions, the maximum intensities ($S_{\rm peak}$) of the 6.7 GHz methanol masers and the velocities for the maximum intensities ($V_{\rm peak}$) are listed in the Table 5.1. To estimate the evolutionary stage, we listed the infrared flux ratio $S_{70\mu m}/S_{22\mu m}$, which was taken from the NASA/IPAC Infrared Science Archive[1] using band 4 (22 μm) data from the *WISE* catalogue and 70 μm data from *Spitzer* catalogue.

[1] https://irsa.ipac.caltech.edu/frontpage/

The primary objective of the project is to investigate the spatial and kinematic co-location of the ring with the thermal tracers. We expect the co-location with the dust continuum emission and with thermal CH_3CN line emission, if the masers arise in the circumstellar disk. However, if masers originate in the outflow, we expect them to be co-located with shock tracers, such as SiO, SO, or outflow tracers, like $C^{18}O$ or ^{13}CO.

Table 5.1: Details of the methanol maser rings that were followed up using ALMA.

Name	Distance	Semi-axes	Semi-axes	Proper motions	[5] $S_{\rm peak}$	[5] $V_{\rm peak}$	$\frac{S_{70\mu m}}{S_{22\mu m}}$
		of methanol rings		kind, mean vleocity			
	(kpc)	(mas×mas)	(au×au)	- , ($\mathrm{km\,s^{-1}}$)	($\mathrm{Jy\,beam^{-1}}$)	($\mathrm{km\,s^{-1}}$)	
G23.389+00.185	[1] $4.8^{+0.7}_{-0.5}$	[3] 105×51	504×245	[3] expansion, 3.4	21.55	75.4	3.4
G23.657−00.127	[1] $3.2^{+0.5}_{-0.4}$	[4] 136×125	435×400	[4] expansion, 3.2	3.62	82.6	2.7
G24.634−00.324	[1] $4.1^{+1.0}_{-0.7}$	[5] 36.5×10.5	150×43	-	3.03	35.4	6.4
G25.411+00.105	[2] $5.8^{+0.6}_{-0.6}$	[5] 112.5×81	652×470	-	3.43	97.3	15.2
G31.581+00.077	[1] $5.5^{+1.2}_{-0.9}$	[3] 108×74	594×407	[3] rotation, 1.8	2.72	95.6	29.2

[1] Reid et al. (2019), [2] Reid et al. (2016), [3] Bartkiewicz et al. (2024), [4] Bartkiewicz et al. (2020), [5] Bartkiewicz et al. (2009).

5.2 Observation

All five targets were previously observed by the ALMA interferometer on band 6 in the large survey ALMAGAL (2019.1.000195.L), so we could verify the existence of above mentioned lines. Since the ALMAGAL project has an insufficient angular resolution ($0.15''-0.27''$) to allow for connecting thermal and maser emission, we proposed observations with almost ten times better angular resolution ($0.03''$). The observations were made under the project 2022.1.01735.S using C-9 configuration in August 2023[2]. The spectral setup comprises four spectral windows (spws), 25, 27, 29, and 31, with the central frequencies of 217.25 GHz, 219.40 GHz, 218.32 GHz, 220.40 GHz, respectively. Each spw has a bandwidth of 937.5 MHz and a resolution of 488 kHz, yielding a velocity resolution (channel spacing) of $0.674\,\mathrm{km\,s^{-1}}$. The data were calibrated using the standard ALMA pipeline, and the continuum was subtracted from the four spectral windows (spws) with the CASA task *uvcontsub*. The images were produced with CASA version 6.7.0 with the *tclean* command. For continuum cubes, we used a standard robust parameter of +0.5, and for continuum-free line cubes, we used a robust parameter of +1 to increase sensitivity

[2]This paper makes use of the following ALMA data 2019.1.000195.L. ALMA is a partnership of ESO (representing its member states), NSF (USA), and NINS (Japan), together with NRC (Canada), MoST and ASIAA (Taiwan), and KASI (Republic of Korea), in cooperation with the Republic of Chile. The Joint ALMA Observatory is operated by ESO, AUI/NRAO, and NAOJ.

and enhance the brightness of line emission. The root mean square (rms) noise (1σ) for all continuum images and spectral cubes, the beam sizes and position angles, are reported in Table 5.2.

Table 5.2: The details of ALMA observations for continuum images and spectral cubes.

Name	$\sigma_{\rm cont}$	$\sigma_{\rm line}^{\rm spw25}$	$\sigma_{\rm line}^{\rm spw27}$	$\sigma_{\rm line}^{\rm spw29}$	$\sigma_{\rm line}^{\rm spw31}$
	(mJy beam^{-1})	(mJy beam^{-1})	(mJy beam^{-1})	(mJy beam^{-1})	(mJy beam^{-1})
	beam$_{\rm cont}$	beam$_{\rm cont}^{\rm spw25}$	beam$_{\rm cont}^{\rm spw31}$	beam$_{\rm line}^{\rm spw29}$	beam$_{\rm line}^{\rm spw31}$
	(mas×mas, °)	(mas×mas, °)	(mas×mas, °)	(mas×mas, °)	(mas×mas, °)
G23.389+00.185	0.027	1.0	0.95	0.91	1.0
	30.1×22.2, 85	34.3×26.9, 85	34.0×26.7, 86	33.9×26.7, 83	34.0×27.0, 80
G23.657−00.127	0.039	1.0	1.0	0.9	1.1
	29.4×22.1, 85	34.3×26.9, 85	34.0×26.8, 85	33.9×26.7, 83	34.0×27.0, 80
G24.634−00.324	0.017	0.84	0.80	0.76	0.95
	27.5×22.0, 82	33.4×27.3, 74	33.3×27.2, 73	33.1×27.0, 71	33.8×27.3, 69
G25.411+00.105	0.024	0.81	0.8	0.74	1.0
	27.6×22.1, 83	33.4×27.4, 75	33.4×27.4, 74	33.2×27.2, 71	33.8×27.5, 70
G31.581+00.077	0.032	0.96	0.9	0.86	1.1
	26.5×20.9, −76	31.9×23.9, −68	31.8×23.8, −69	30.2×24.1, −70	29.7×24.4, −70

5.3 Results

5.3.1 Continuum

The 1.3 mm dust continuum emission for all sources with 6.7 GHz methanol maser spots is presented in Figure 5.1. Source G23.657−00.127, which exhibits the most circular maser emission, reveals a remarkable ring structure with a point-like object at its inside. Source G24.634−00.324, characterized by the smallest size of maser ring, features at least twice the smaller continuum brightness of the rest of the sample. We notice the coincidence of the dust and the methanol masers for only two sources, G23.389+00.185 and G23.657−00.127; based on $S_{70\mu m}/S_{22\mu m}$, these are the oldest sources in our sample. For the remaining three sources, G24.634−00.324, G25.411+00.105, and G31.581+00.077, the maser emission is significantly shifted northwest by ca. 50–200 mas. For the 6.7 GHz methanol maser spots, we used the observations taken in 2007 because of their best astrometric accuracy apart from all observation epochs (Bartkiewicz et al., 2009, 2020, 2024). Our ALMA observations were made 16 years later. Considering that the average value of maser proper motions is 0.5 mas per year, the uncertainty between both observations is no more than 8 mas. That means that the displacement visible on Figure 5.1 is real. The youngest source G31.581+00.077 has a bigger displacement than the second youngest G25.411+00.105. The coincidence 6.7 GHz methanol masers with the center

of millimeter dust emission seems to be correlated with the age of the source.

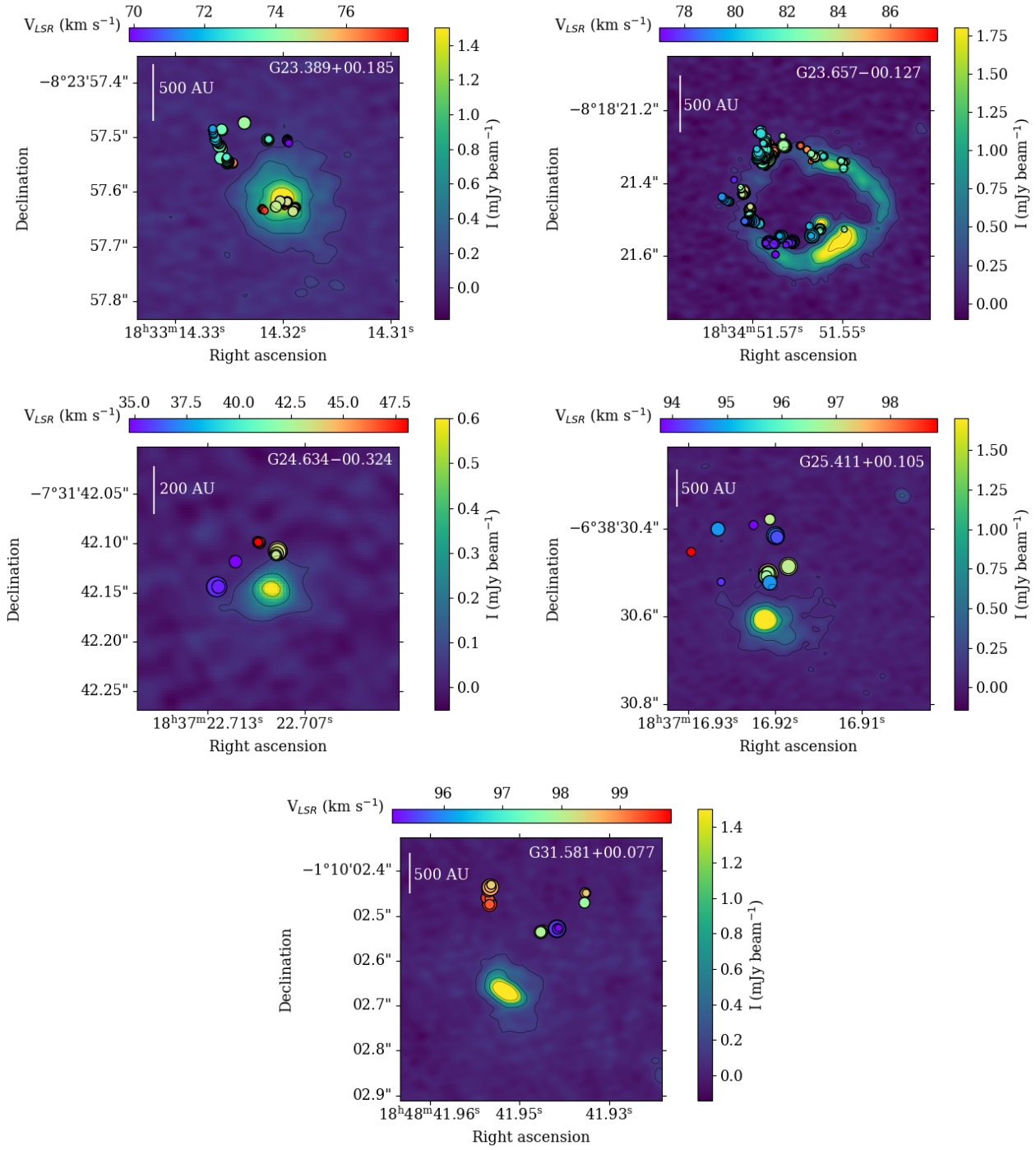

Figure 5.1: The ALMA band 6 continuum images for all five targets overlaid with the 6.7 GHz methanol maser spots. The top colorbar indicates the maser spots $V_{\rm LSR}$. The right colorbar indicates the strength of continuum emission. The contours mark 4σ, 15σ, 30σ, and 50σ levels of continuum emission for each source.

5.3.2 Spectral lines

Spectra for all targets are presented on Figures 5.2–5.5. The richest profile is shown by the source G23.657−00.127, which reveals the ring structure at the continuum source and at the

methanol maser line. Sources G23.389+00.185, G25.411+00.105, and G31.581+00.077 show very similar profiles in all spws, whereby G23.389+00.185 is the brightest, and G31.581+00.077 exhibits the strongest absorption features (i.e., for line ^{13}CO). The source G24.634−00.324, with the weakest continuum emission, shows a very line-poor spectral profile with weak emission lines.

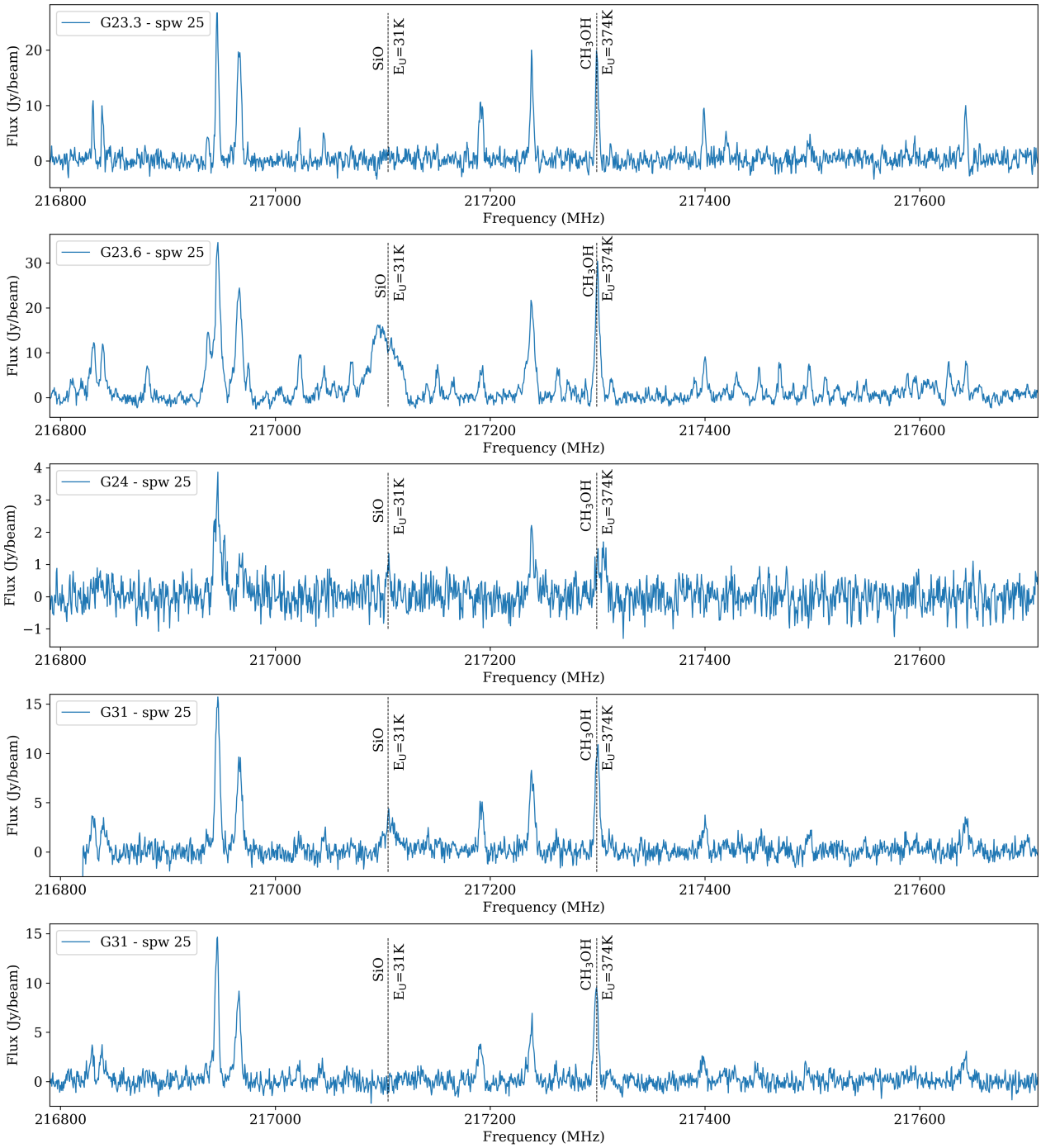

Figure 5.2: Spectra for all sources for spw 25.

Among plenty of spectral lines, we chose six to compare their morphologies and kinematics with 6.7 GHz maser emission. Three lines are related to warm gas, i.e., CH_3OH (E_U =374 K),

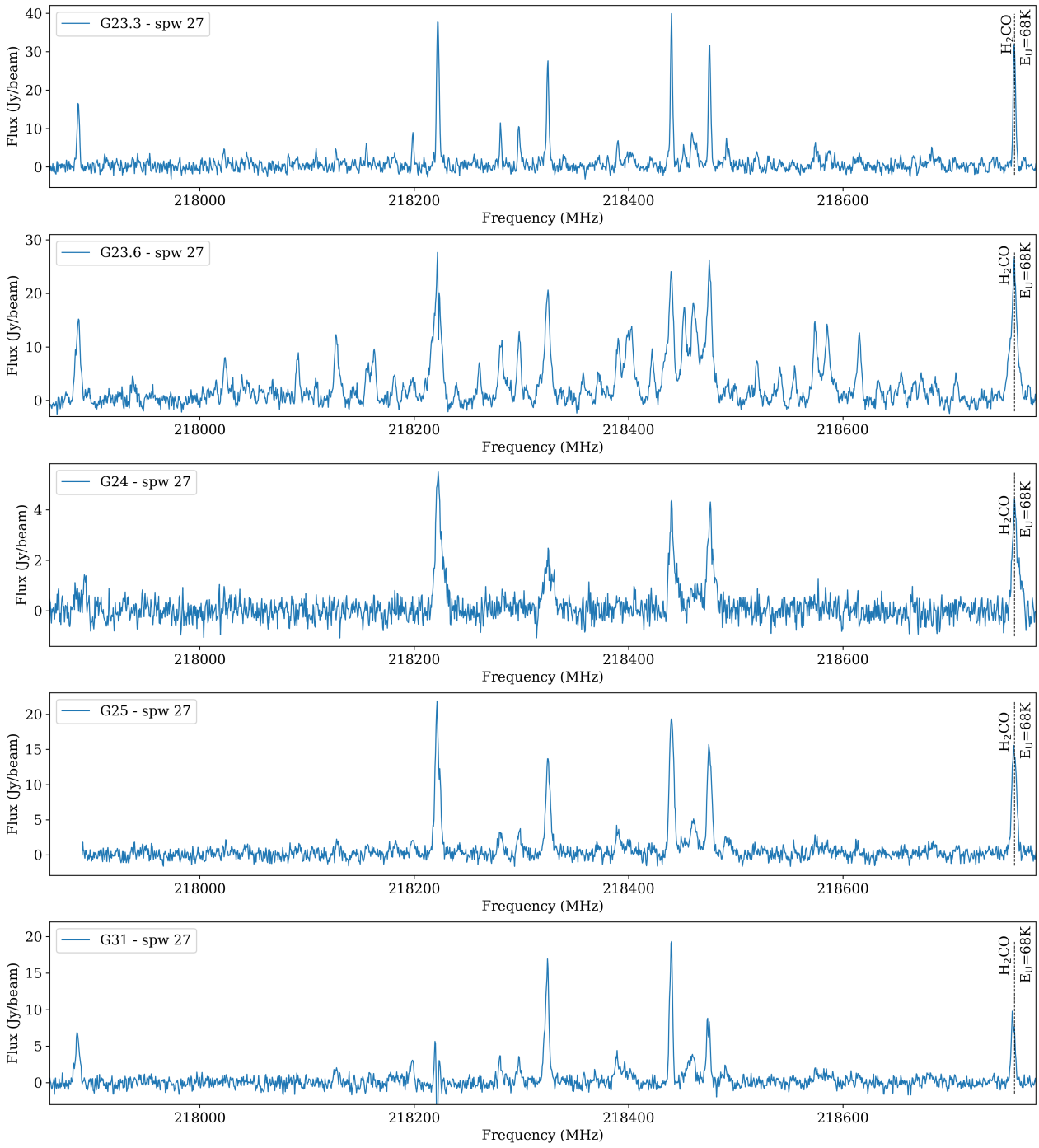

Figure 5.3: Spectra for all sources for spw 27.

CH_3CN (E_U =183 K), and H_2CO (E_U =68 K), often associated with disk (Chen et al., 2016; Maud et al., 2018). The other three lines, SO (E_U =35 K), SO_2 (E_U =353 K), and SiO (E_U =31 K) are related with shock gas in jets or envelops (Bjerkeli et al., 2019; Dewangan et al., 2022). All lines are marked on the spectra in Figures 5.2–5.5. We present the low-, middle-, and high-energy level lines to illustrate the different regions of high-mass star formation regions. The low-energy level lines trace the outer, most extensive, and coolest regions, such as envelopes our outflows, while the high-energy level lines trace the inner, hottest regions,

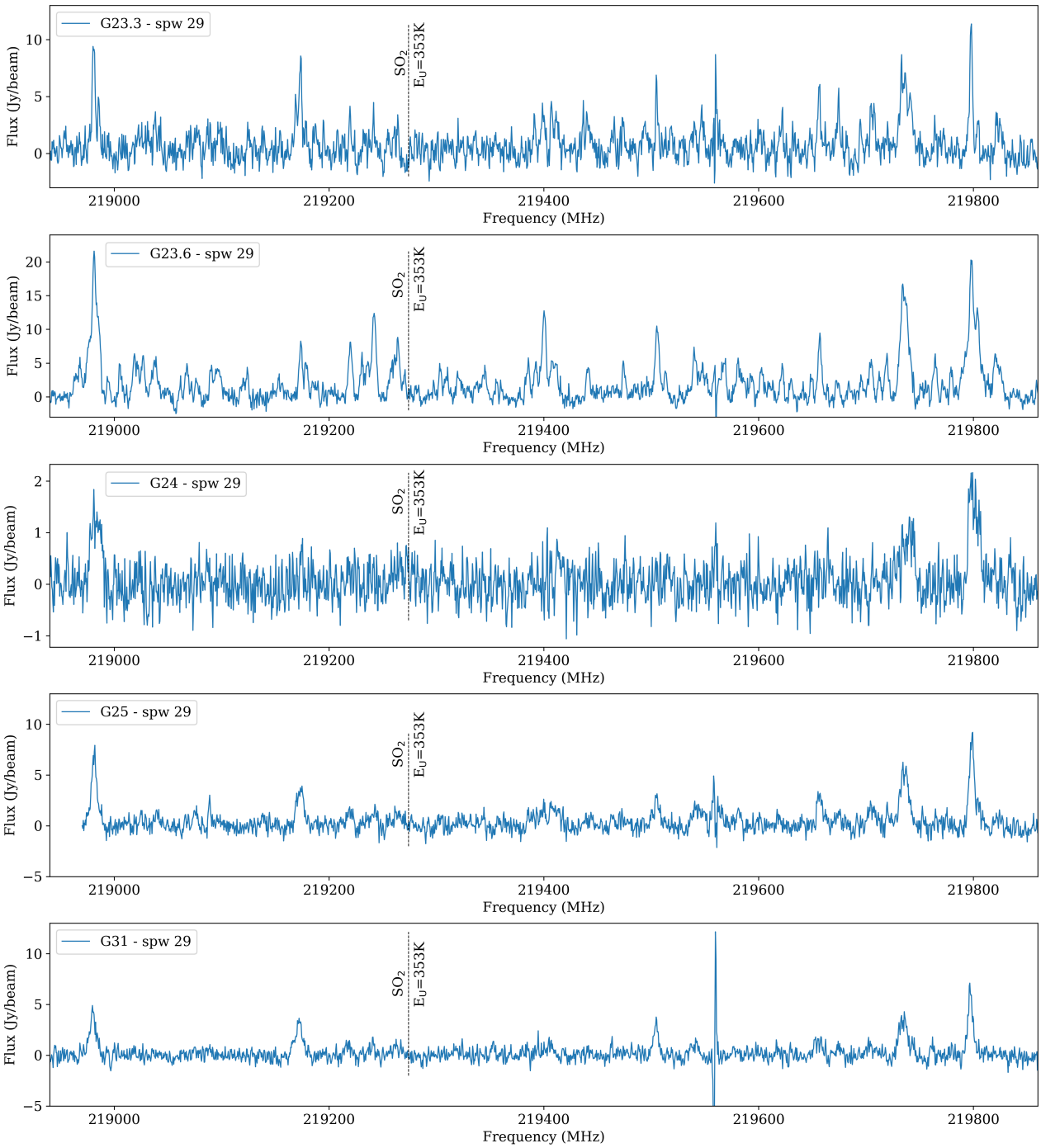

Figure 5.4: Spectra for all sources for spw 29.

like inner parts of discs or shocks.

Unfortunately, the high angular resolution of data, which allows us to study the gas and dust structures almost on the same scale as that observed via masers and radio interferometry, does not allow us to see more extended and diffuse emission like outflows traced by $C^{18}O$ and ^{13}CO. Line $C^{18}O$, which is a tracer of very diffuse gas, is not visible, and line ^{13}CO, which traces a thicker gas, can be visible only very close to the continuum emission in the densest vicinity. In Figure 5.6 we show the examples of imaged ^{13}CO emission in two sources. Blue-

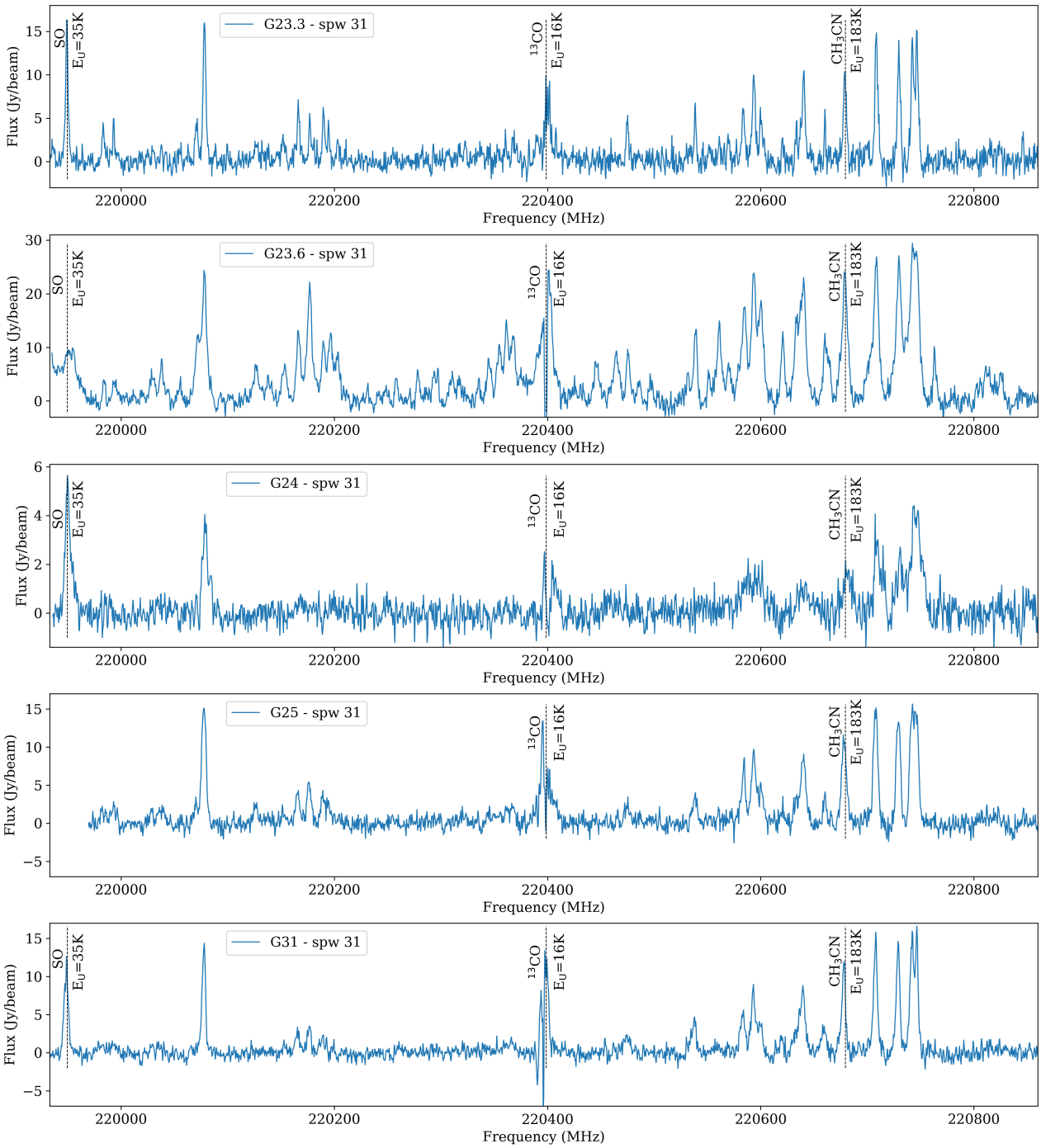

Figure 5.5: Spectra for all sources for spw 31.

and red-shifted wings are visible, but only parts/fragments that are very close to the continuum sources. Because of ^{13}CO, as an outflow tracer, it is very wide on the spectrum, and is blended with other lines like CH_3CN and CH_3OH, which are disk tracers. That means the emission seen in the Figure 5.6 can come from all these lines. Therefore, these images do not help in determining the outflow directions. Combining our data with low-resolution ALMAGAL data may allow us to see more extended emission on a large scale, farther from the continuum source and disk tracers, without losing high resolution.

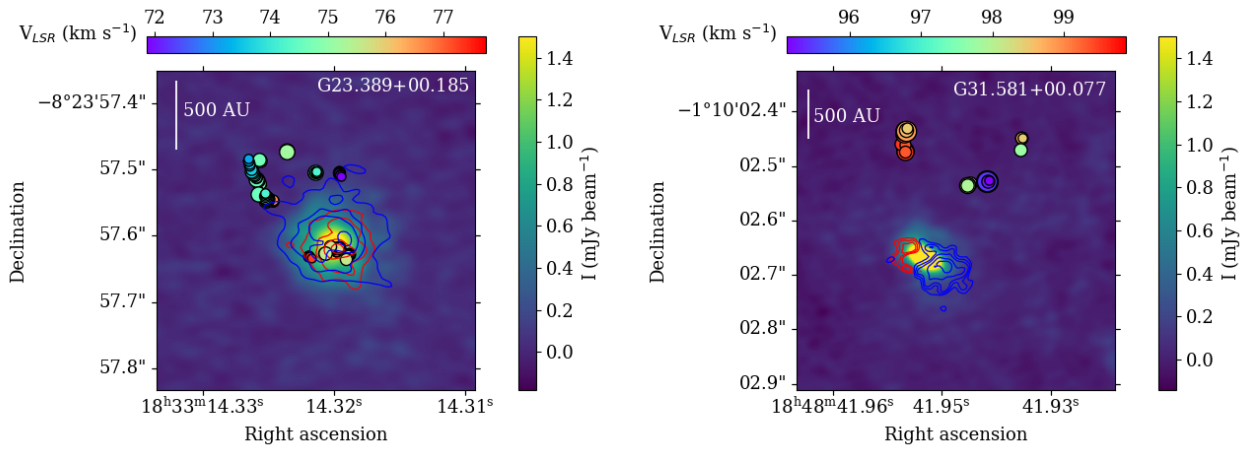

Figure 5.6: The continuum emission with methanol maser emission and ^{13}CO emission for sources G23.389+00.185 and G31.581+00.077. The top colorbar indicates the maser spots $V_{\rm LSR}$. The right colorbar indicates the strength of continuum emission. The blue and red contours indicate the zeroth moment for blue- and red-shifted wings of ^{13}CO lines.

Figures 5.7-5.16 show the zeroth moment and first moment maps for selected spectral lines. To create the zeroth moment map, we integrated the intensity of the line at $\pm$10 channels around their peaks. In the case of a first moment map, we have masked all emission below 3σ to better present the extended emission and the velocity dispersion.

Maser emission in G23.389+000.185 exhibits good spatial and kinematic coincidence with thermal CH_3OH and H_2CO lines. The third disk tracer CH_3CN in the center of dust emission is more red-shifted than the maser spots. The same effect is for shock tracer SO. Then SO_2 shows blue-shifted emission. The weak SiO emission exhibits a mix of red- and blue-shifted emission on the very small scale.

Source G23.657−00.127, which revealed the ring-structure for continuum emission, also shows the same structure for all three disk tracers, which coincide well spatially and kinematically with maser spots. The mostly red-shifted SiO emission fills the middle of the ring structure. The SO line shows blue-shifted emission, which coincides with a point-like continuum object. The weak, mostly red-shifted emission of SO_2 is observed in the southern part of the ring structure, where the disk tracers are located, which is unexpected and requires further detailed analysis.

In source G24.634−00.324 6.7 GHz methanol spots show good spatial and kinematic coincidence with thermal methanol emission, and a little worse with H_2CO. Like in the G23.389+000.185, the emission of CH_3CN and SO does not fit well kinematically. We did not detect the SiO and SO_2 lines.

Spots in G25.411+00.105 do not overlay with continuum emission, but thermal lines are

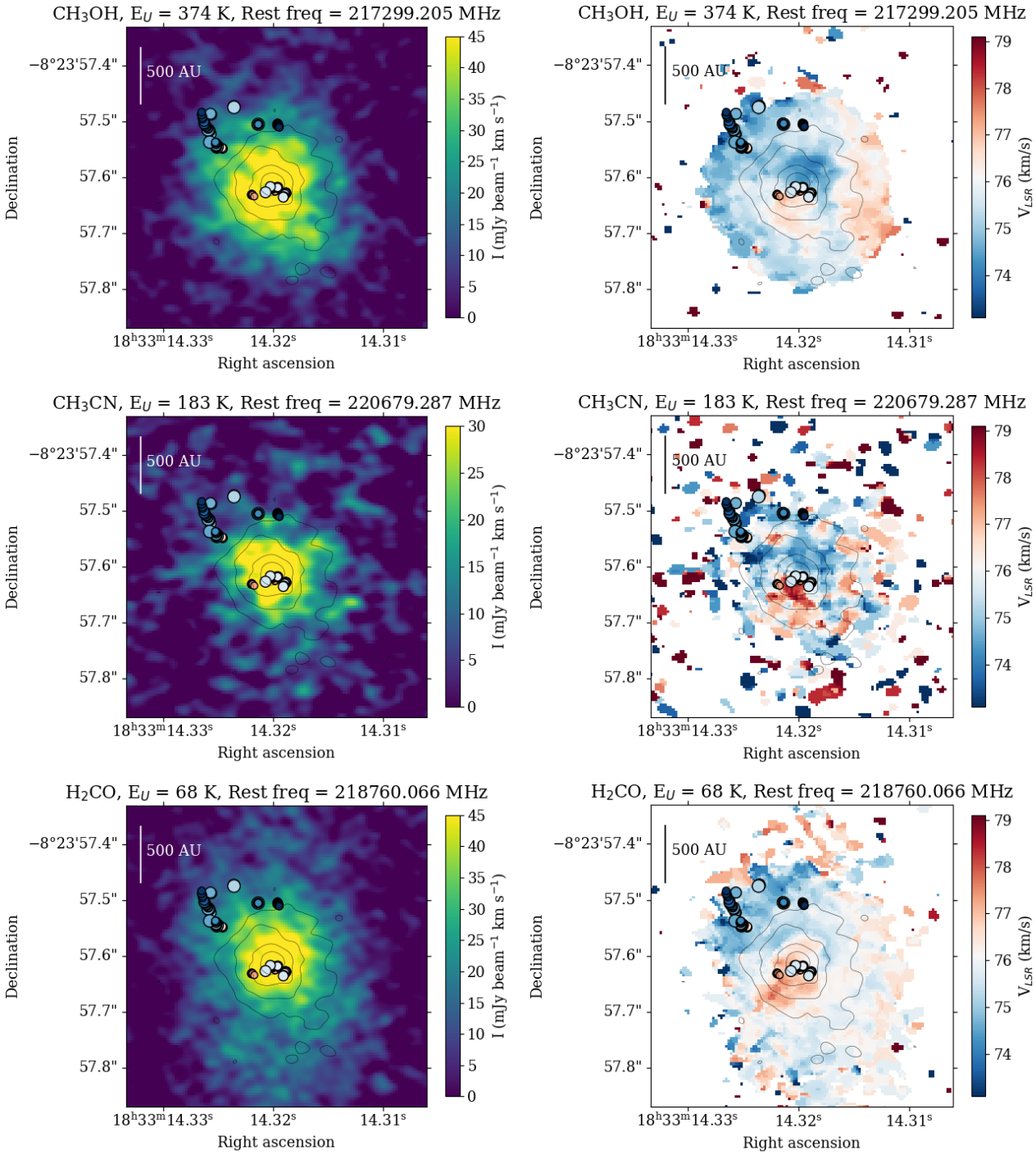

Figure 5.7: The thermal disk tracers and methanol maser emission for G23.389+00.185. *Left:* Zeroth moment maps integrated at ±10 channels around the peak of each line. The colorbar indicates the intensity of the emission. *Right:* First moment maps with 3σ masking. The colorbar indicates the $V_{\rm LSR}$ velocity for thermal millimeter line as well as for maser emission.

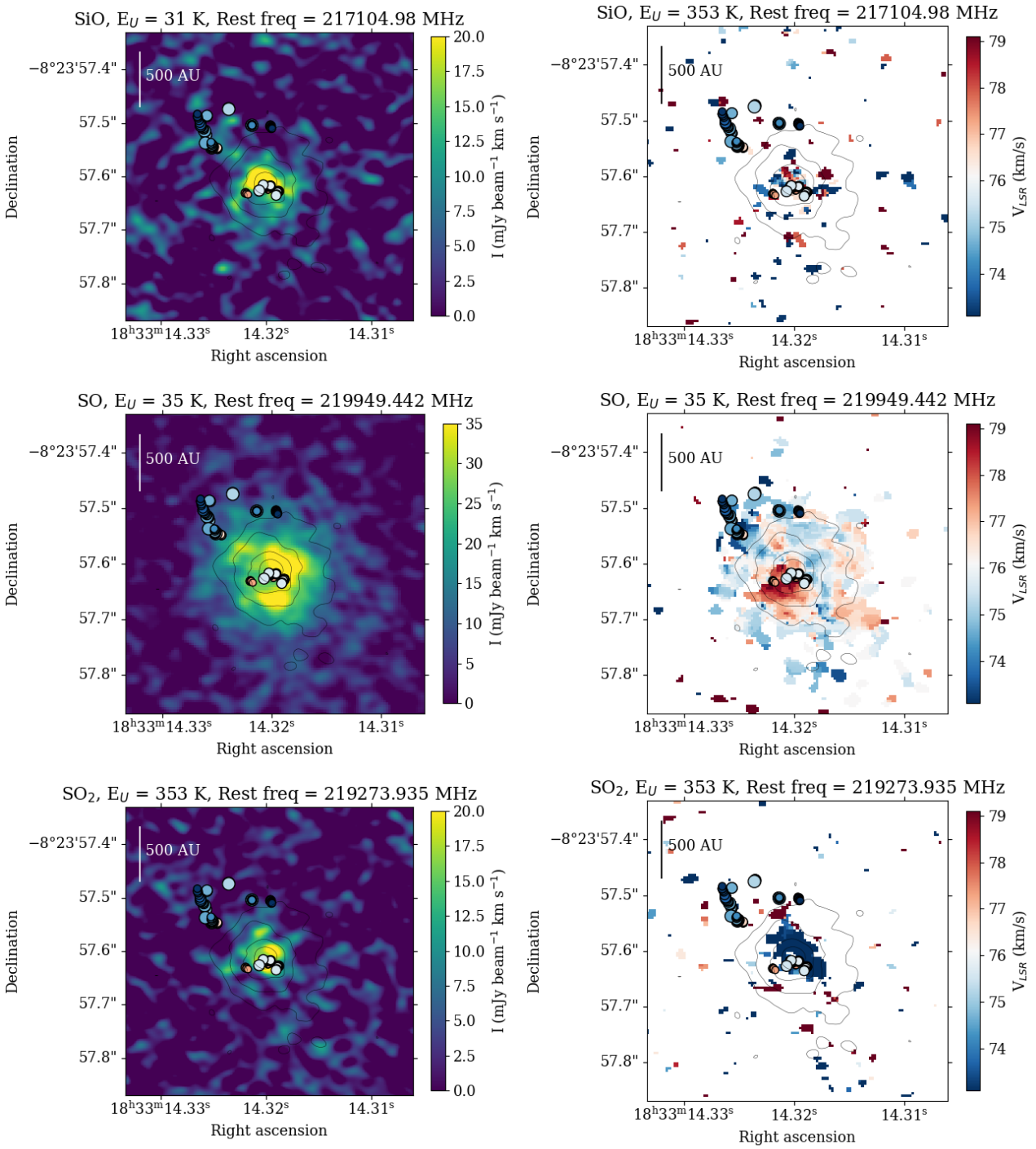

Figure 5.8: The thermal shock tracers and methanol maser emission for G23.389+00.185. *Left:* Zeroth moment maps integrated at ±10 channels around the peak of each line. The colorbar indicates the intensity of the emission. *Right:* First moment maps with 3σ masking. The colorbar indicates the $V_{\rm LSR}$ velocity for thermal millimeter line as well as for maser emission.

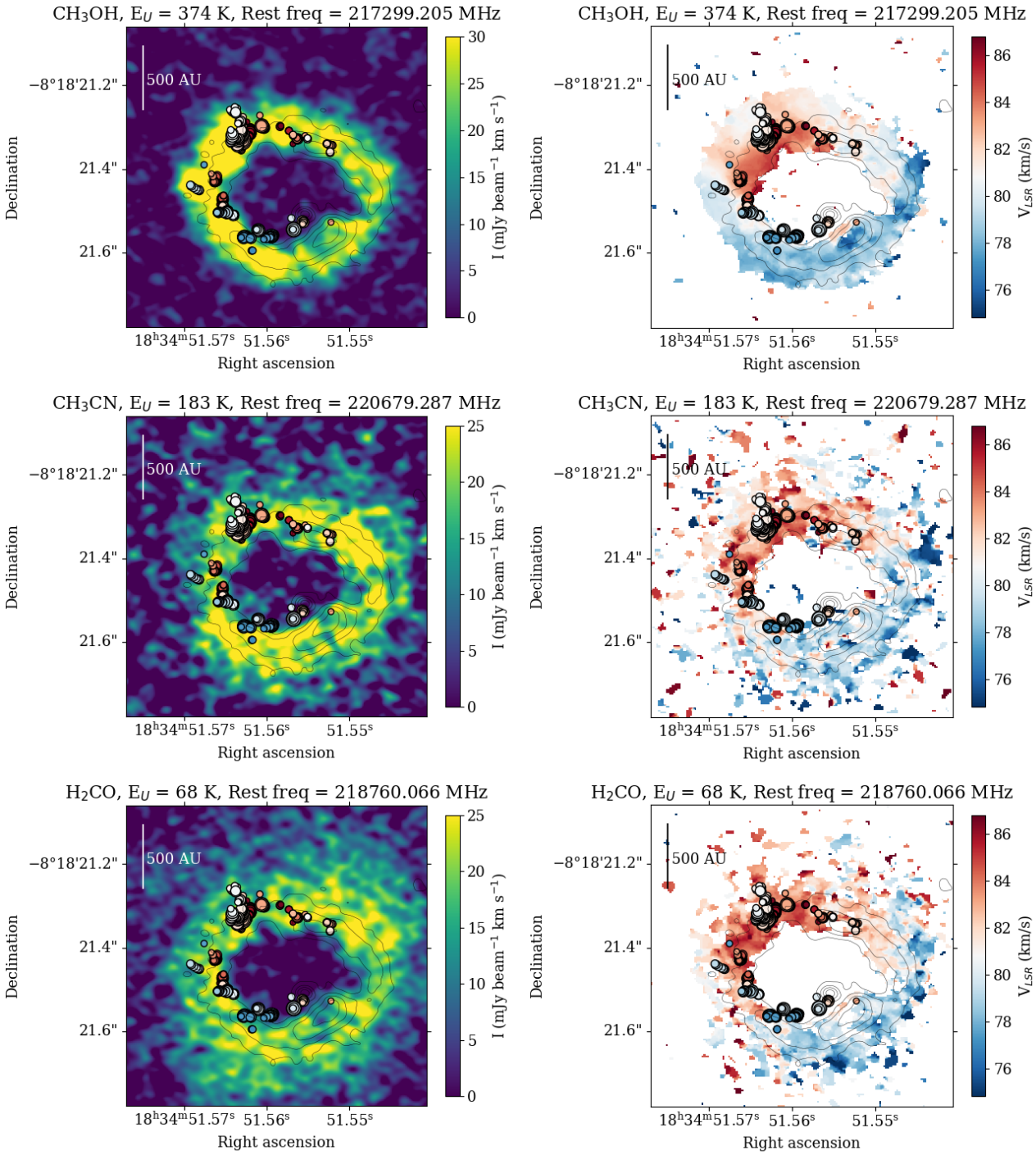

Figure 5.9: The thermal disk tracers and methanol maser emission for G23.657−00.127. *Left:* Zeroth moment maps integrated at ±10 channels around the peak of each line. The colorbar indicates the intensity of the emission. *Right:* First moment maps with 3σ masking. The colorbar indicates the $V_{\rm LSR}$ velocity for thermal millimeter line as well as for maser emission.

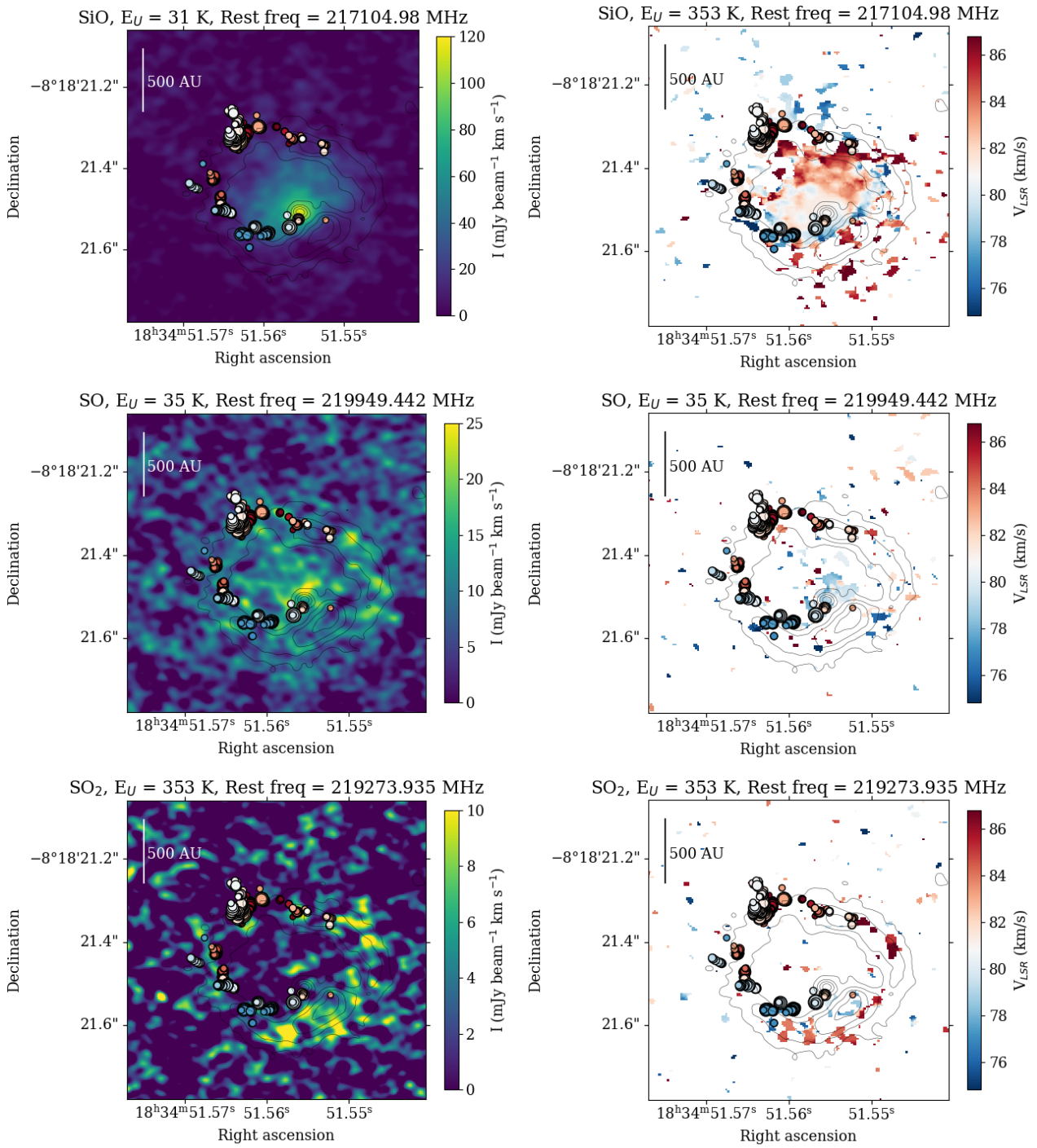

Figure 5.10: The thermal shock tracers and methanol maser emission for G23.657−00.127. *Left:* Zeroth moment maps integrated at ±10 channels around the peak of each line. The colorbar indicates the intensity of the emission. *Right:* First moment maps with 3σ masking. The colorbar indicates the $V_{\rm LSR}$ velocity for thermal millimeter line as well as for maser emission.

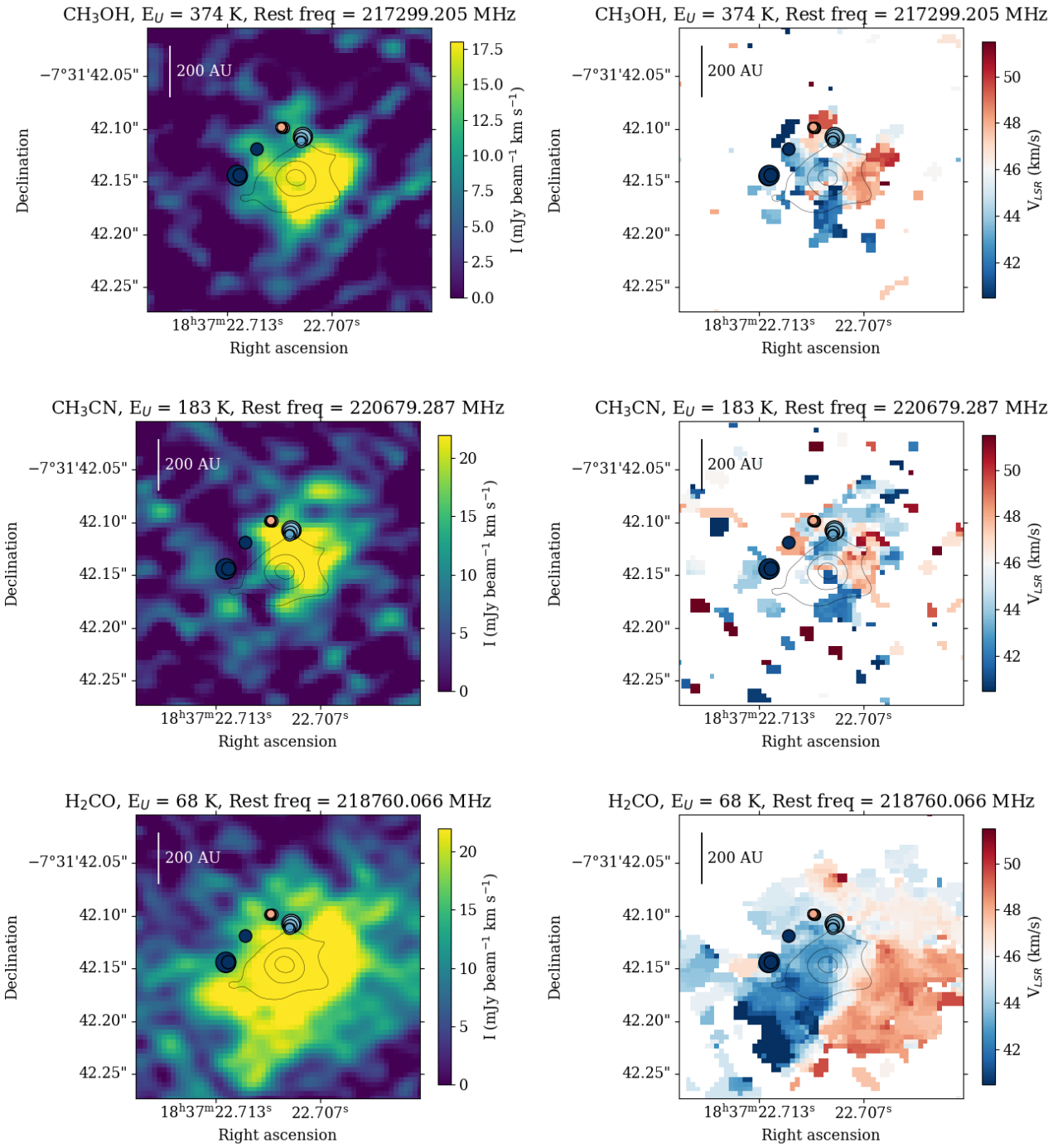

Figure 5.11: The thermal disk tracers and methanol maser emission for G24.634−00.324. *Left:* Zeroth moment maps integrated at ±10 channels around the peak of each line. The colorbar indicates the intensity of the emission. *Right:* First moment maps with 3σ masking. The colorbar indicates the $V_{\rm LSR}$ velocity for thermal millimeter line as well as for maser emission.

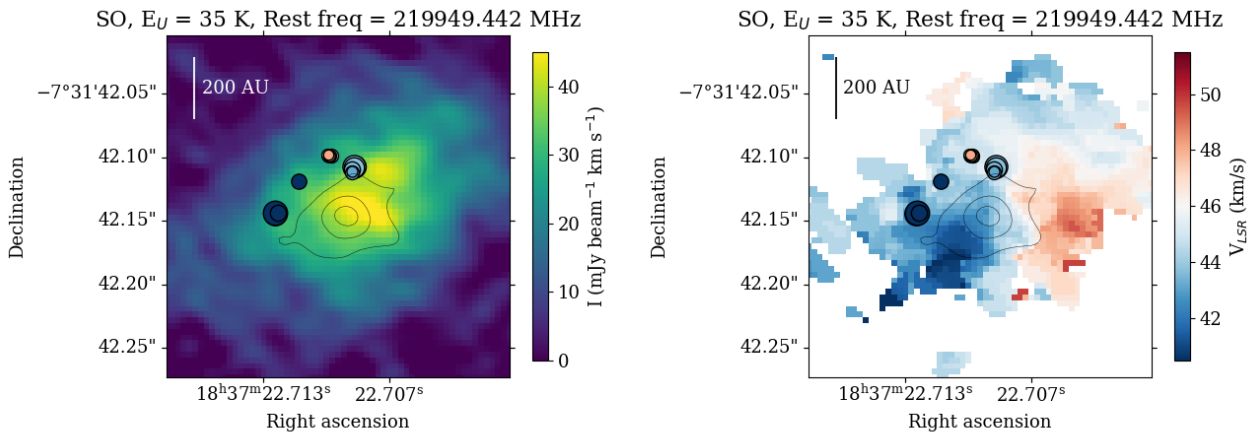

Figure 5.12: The thermal shock tracer and methanol maser emission for G24.634−00.324. *Left:* Zeroth moment maps integrated at ±10 channels around the peak of each line. The colorbar indicates the intensity of the emission. *Right:* First moment maps with 3σ masking. The colorbar indicates the $V_{\rm LSR}$ velocity for thermal millimeter line as well as for maser emission.

more extended, and a partway coincidence for disk tracers is visible. The SO line is beyond the detected frequency range. Similar to G23.389+000.185, the very weak mix of red- and blue-shifted SiO and the blue-shifted SO_2 emissions covers the central part of the continuum emission.

Since source G31.581+00.077 exhibits displacement of maser spots with both continuum emission and thermal line emission, the interpretation is not possible. We did not detect the SiO and SO_2 lines.

5.4 Discussion and Conclusion

At that stage, we are not able to indicate clearly the structures/regions that the 6.7 GHz masers are associated with. Sources G23.389+000.185, G23.657−00.127, and G24.634−00.324 indicate spatial overlaying with the warm gas tracers. Their kinematics (first moment maps) suggest a stronger connection with thermal CH_3OH and H_2CO lines, and a weaker relation with CH_3CN. The CH_3CN line traces a dense, warm gas and is usually related to the disc, whereas CH_3OH and H_2CO, especially the low-energy lines, trace the thinner, warm gas, and often is related to the most outer part of the disk or even surroundings gas/envelop (e.g., Immer et al., 2014; Law et al., 2025). The proper motions of 6.7 GHz methanol masers in G23.389+000.185 and G23.657−00.127 indicate expansions of the maser rings; that was interpreted as structures arising in sphere-like outflows or in expanding envelopes by wide-angle winds (Bartkiewicz et al., 2020). Stronger coincidence of masers with thermal CH_3OH and H_2CO lines would be

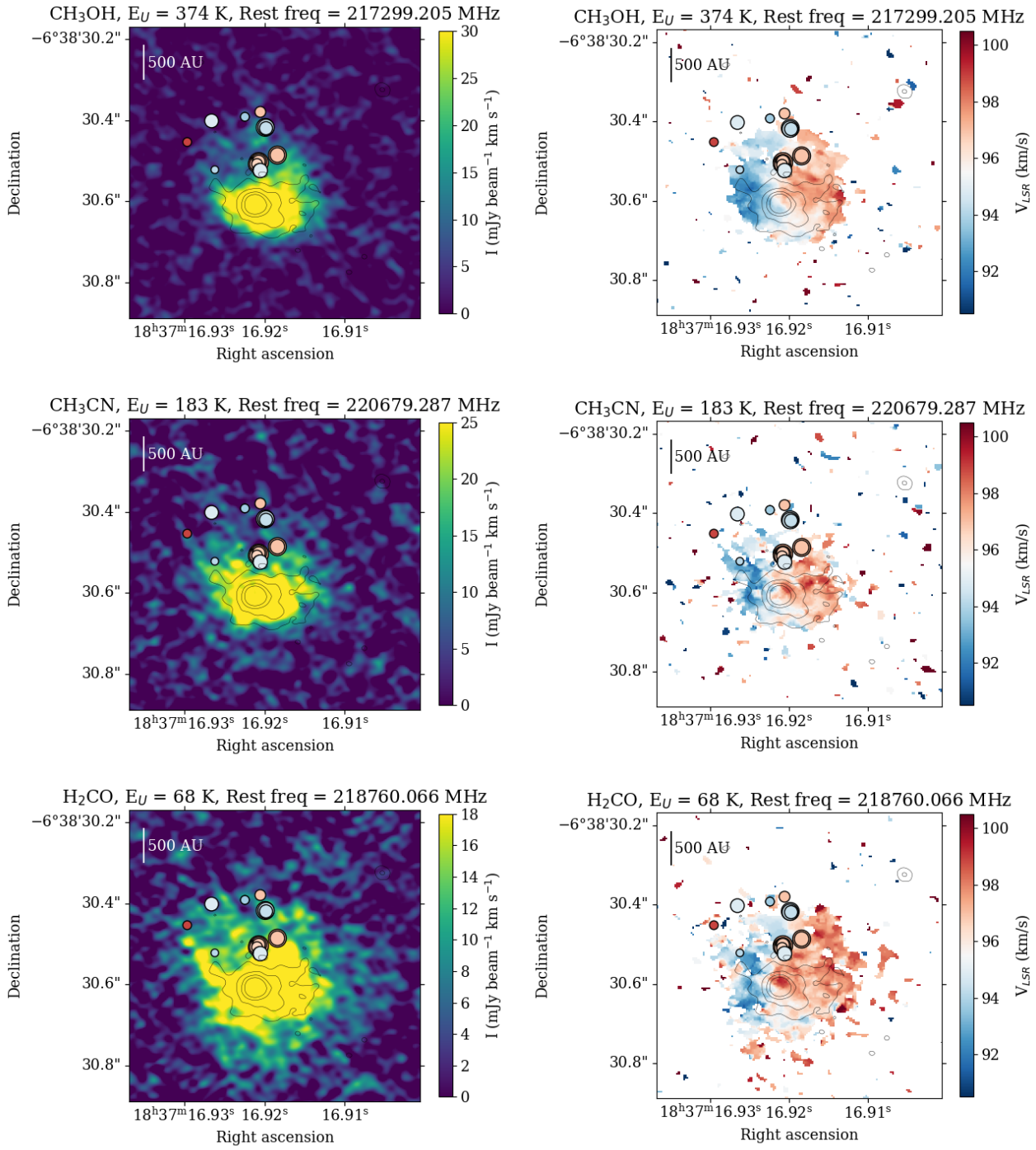

Figure 5.13: The thermal disk tracers and methanol maser emission for G25.411+00.105. *Left:* Zeroth moment maps integrated at ±10 channels around the peak of each line. The colorbar indicates the intensity of the emission. *Right:* First moment maps with 3σ masking. The colorbar indicates the $V_{\rm LSR}$ velocity for thermal millimeter line as well as for maser emission.

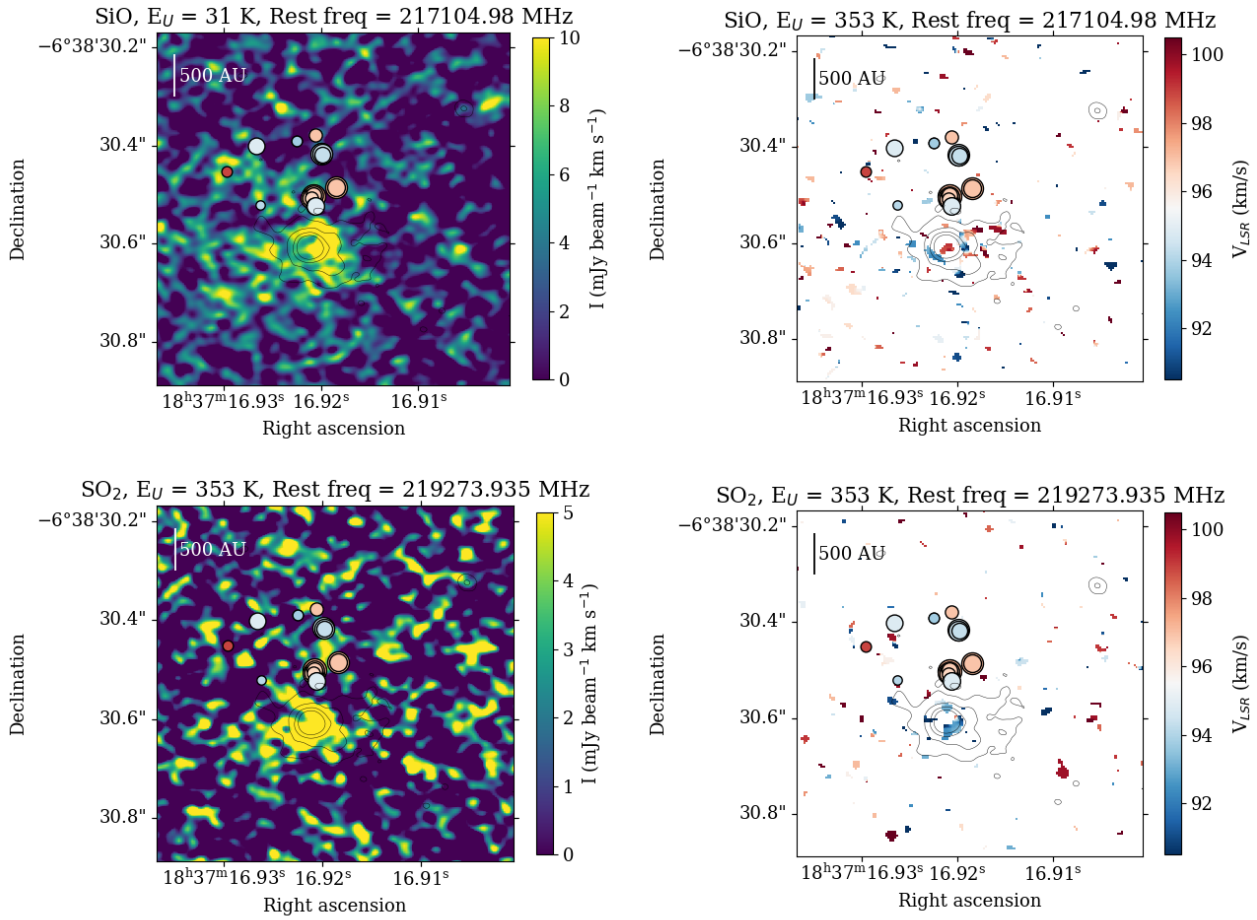

Figure 5.14: The thermal shock tracers and methanol maser emission for G25.411+00.105. *Left:* Zeroth moment maps integrated at ±10 channels around the peak of each line. The colorbar indicates the intensity of the emission. *Right:* First moment maps with 3σ masking. The colorbar indicates the $V_{\rm LSR}$ velocity for thermal millimeter line as well as for maser emission.

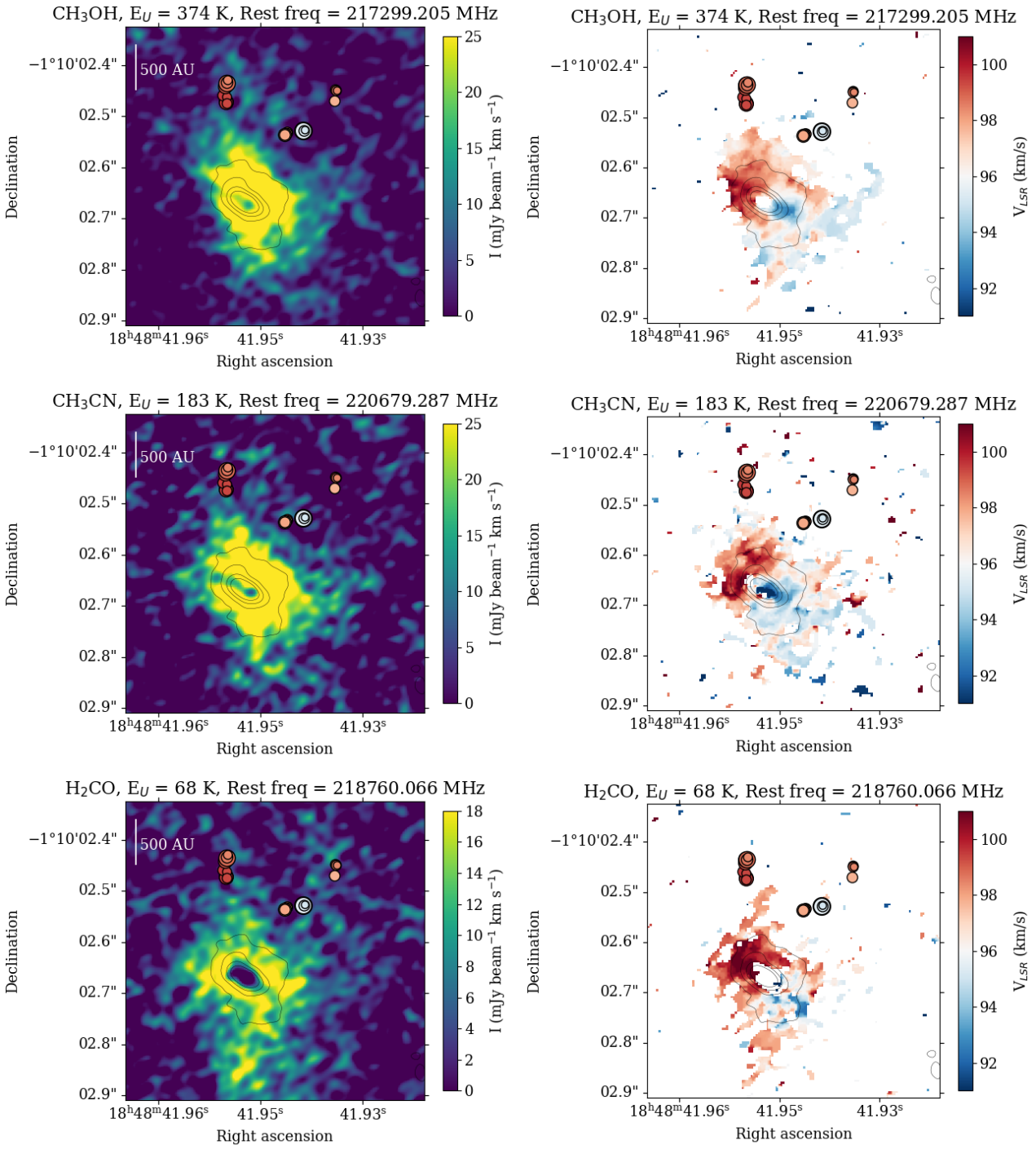

Figure 5.15: The thermal disk tracers and methanol maser emission for G31.581+00.077. *Left:* Zeroth moment maps integrated at ±10 channels around the peak of each line. The colorbar indicates the intensity of the emission. *Right:* First moment maps with 3σ masking. The colorbar indicates the $V_{\rm LSR}$ velocity for thermal millimeter line as well as for maser emission.

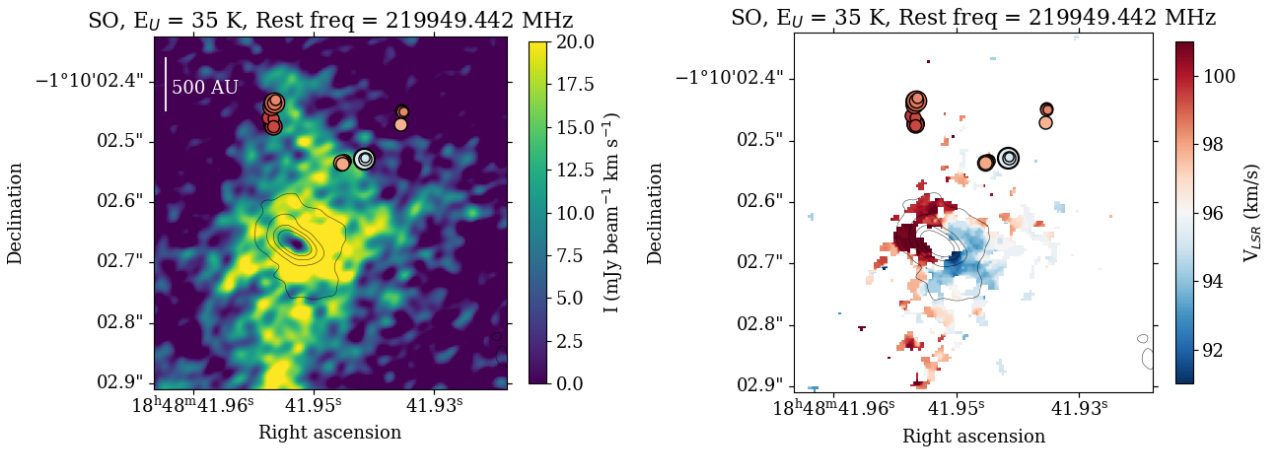

Figure 5.16: The thermal shock tracer and methanol maser emission for G31.581+00.077. *Left:* Zeroth moment maps integrated at ±10 channels around the peak of each line. The colorbar indicates the intensity of the emission. *Right:* First moment maps with 3σ masking. The colorbar indicates the $V_{\rm LSR}$ velocity for thermal millimeter line as well as for maser emission.

in good agreement with the conclusion of an expanding envelope.

The partial coincidence of masers and gas emission in G25.411+00.105 also indicates a connection with warm gas tracers, and the kinematics gave quite good agreement with CH_3CN and CH_3OH. The offset between the methanol maser and thermal emission in G31.581+00.077 may indicate a connection with an outflow or extended envelope, or even a star feeding stream of gas. The proper motions of masing cloudlets suggest the rotational movement, so that masers can be related to a rotating jet or stream. To confirm the above, the combination with low-resolution ALMAGAL data is needed. These outcomes show a more complicated scenario than it was presented by Sanna et al. (2010b, 2014, 2019, 2021) in HMYSO G023.010−00.411, where a comparison of VLBI 6.7 GHz methanol maser cloudlets with dust continuum and thermal lines images obtained using SMA and ALMA observations gave the relatively clear picture of an infalling, rotating molecular disk driving a molecular jet.

Chapter 6

Summary

This work focuses on the study of the 6.7 GHz CH_3OH maser in a broad aspect. Firstly, we discussed the multi-frequency and multi-epoch maser flare in detail. The flare at the 6.7 GHz methanol maser transition was related to a less-energetic accretion event compared to G358 (Burns et al., 2020b). The analysis of 6.7 GHz methanol maser cloudlets in comparison with 12.2 GHz methanol and 22.2 GHz water maser emission allowed us to fit a Keplerian rotation model of a disk-jet system, relate maser flare to the infrared surge, and estimate the speed of maser flare propagation as 33% speed of light. Secondly, we analyzed the coincidence of 6.7 GHz methanol and 6.035 GHz OH masers in ten HMYSOs to verify theoretical models of the physical conditions of the gas in which masers are excited. The obtained results show that only local changes on the small scales have an impact on the arising kind of masers. We also imaged the magnetic field in these targets using the OH molecule, finding that its strength is at a few milligauss and its direction shows no relationship with the direction of an outflow. Thirdly, for the first time, we attempted to prove the theoretical model of the hyperfine transition for the methanol maser proposed by Lankhaar et al. (2018). Even though this trial did not give conclusive results, this was a valuable input to the theory of maser polarization. Fourthly, the preliminary results of linking 6.7 GHz CH_3OH maser with thermal, millimeter dust and gas emission show a complex picture of high-mass star-forming regions. Based on six thermal spectral lines, we can infer that the most probable scenario is that methanol masers arise on the outer part of the disk, probably in the surrounding envelope.

Bibliography

A. Aberfelds, A. Bartkiewicz, M. Szymczak, J. Šteinbergs, G. Surcis, A. Kobak, M. Durjasz, and I. Shmeld. Milliarcsecond structure and variability of methanol maser emission in three high-mass protostars. , 524(1):599–618, Sept. 2023a. doi: 10.1093/mnras/stad1752.

A. Aberfelds, J. Šteinbergs, I. Shmeld, and R. A. Burns. Five years of 6.7-GHz methanol maser monitoring with Irbene radio telescopes. , 526(4):5699–5714, Dec. 2023b. doi: 10.1093/mnras/stad3158.

G. Anglada, L. F. Rodríguez, and C. Carrasco-González. Radio jets from young stellar objects. , 26(1):3, June 2018. doi: 10.1007/s00159-018-0107-z.

A. Arcones and F.-K. Thielemann. Origin of the elements. , 31(1):1, Dec. 2023. doi: 10.1007/s00159-022-00146-x.

A. L. Argon, M. J. Reid, and K. M. Menten. Interstellar Hydroxyl Masers in the Galaxy. I. The VLA Survey. , 129(1):159–227, July 2000. doi: 10.1086/313406.

K. Asanok, S. Etoka, M. D. Gray, P. Thomasson, A. M. S. Richards, and B. H. Kramer. OH and H_2O masers towards the star-forming region S140-IRS1. , 404(1):120–133, May 2010. doi: 10.1111/j.1365-2966.2010.16296.x.

N. T. Ashimbaeva, E. E. Lekht, V. V. Krasnov, and A. M. Tolmachev. Investigation of the Magnetic Field from Observations of the OH Maser in the G10.624-0.385 Star Formation Region. *Astronomy Reports*, 67(7):707–718, July 2023. doi: 10.1134/S1063772923070016.

A. Avison, L. J. Quinn, G. A. Fuller, J. L. Caswell, J. A. Green, S. L. Breen, S. P. Ellingsen, M. D. Gray, M. Pestalozzi, M. A. Thompson, and M. A. Voronkov. Excited-state hydroxyl maser catalogue from the methanol multibeam survey - I. Positions and variability. , 461(1):136–155, May 2016. doi: 10.1093/mnras/stw1101.

A. Bartkiewicz, M. Szymczak, H. J. van Langevelde, A. M. S. Richards, and Y. M. Pihlström. The diversity of methanol maser morphologies from VLBI observations. , 502(1):155–173, July 2009. doi: 10.1051/0004-6361/200912250.

A. Bartkiewicz, M. Szymczak, Y. M. Pihlström, H. J. van Langevelde, A. Brunthaler, and M. J. Reid. VLA observations of water masers towards 6.7 GHz methanol maser sources. , 525: A120, Jan. 2011. doi: 10.1051/0004-6361/201015235.

A. Bartkiewicz, M. Szymczak, and H. J. van Langevelde. European VLBI Network observations of 6.7 GHz methanol masers in clusters of massive young stellar objects. , 564:A110, Apr. 2014. doi: 10.1051/0004-6361/201322629.

A. Bartkiewicz, M. Szymczak, and H. J. van Langevelde. European VLBI Network imaging of 6.7 GHz methanol masers. , 587:A104, Mar. 2016. doi: 10.1051/0004-6361/201527541.

A. Bartkiewicz, A. Sanna, M. Szymczak, L. Moscadelli, H. J. van Langevelde, and P. Wolak. The nature of the methanol maser ring G23.657-00.127. II. Expansion of the maser structure. , 637:A15, May 2020. doi: 10.1051/0004-6361/202037562.

A. Bartkiewicz, A. Sanna, M. Szymczak, L. Moscadelli, H. J. van Langevelde, P. Wolak, A. Kobak, and M. Durjasz. Proper motion study of the 6.7 GHz methanol maser rings. I. A sample of sources with little variation. *arXiv e-prints*, art. arXiv:2404.07333, Apr. 2024. doi: 10.48550/arXiv.2404.07333.

W. Batrla, H. E. Matthews, K. M. Menten, and C. M. Walmsley. Detection of strong methanol masers towards galactic H II regions. , 326(6108):49–51, Mar. 1987. doi: 10.1038/326049a0.

A. Baudry, J. F. Desmurs, T. L. Wilson, and R. J. Cohen. A survey of star-forming regions in the 5 CM lines of OH. , 325:255–268, Sept. 1997.

O. S. Bayandina, R. A. Burns, S. E. Kurtz, N. N. Shakhvorostova, and I. E. Val'tts. VLA Overview of the Bursting H2O Maser Source G25.65+1.05. , 884(2):140, Oct. 2019. doi: 10.3847/1538-4357/ab3fa4.

M. T. Beltrán, M. Padovani, J. M. Girart, D. Galli, R. Cesaroni, R. Paladino, G. Anglada, R. Estalella, M. Osorio, R. Rao, Á. Sánchez-Monge, and Q. Zhang. ALMA resolves the hourglass magnetic field in G31.41+0.31. , 630:A54, Oct. 2019. doi: 10.1051/0004-6361/201935701.

H. Beuther, A. Walsh, P. Schilke, T. K. Sridharan, K. M. Menten, and F. Wyrowski. CH_3OH and H_2O masers in high-mass star-forming regions. , 390:289–298, July 2002. doi: 10.1051/0004-6361:20020710.

S. J. Billington, J. S. Urquhart, C. König, T. J. T. Moore, D. J. Eden, S. L. Breen, W. J. Kim, M. A. Thompson, S. P. Ellingsen, K. M. Menten, F. Wyrowski, and S. Leurini. ATLASGAL

- physical parameters of dust clumps associated with 6.7 GHz methanol masers. , 490(2): 2779–2798, Dec. 2019. doi: 10.1093/mnras/stz2691.

P. Bjerkeli, J. P. Ramsey, D. Harsono, H. Calcutt, L. E. Kristensen, M. H. D. van der Wiel, J. K. Jørgensen, S. Muller, and M. V. Persson. Kinematics around the B335 protostar down to au scales. , 631:A64, Nov. 2019. doi: 10.1051/0004-6361/201935948.

I. A. Bonnell and M. R. Bate. Accretion in stellar clusters and the collisional formation of massive stars. , 336(2):659–669, Oct. 2002. doi: 10.1046/j.1365-8711.2002.05794.x.

I. A. Bonnell and M. R. Bate. Star formation through gravitational collapse and competitive accretion. , 370(1):488–494, July 2006. doi: 10.1111/j.1365-2966.2006.10495.x.

I. A. Bonnell, S. G. Vine, and M. R. Bate. Massive star formation: nurture, not nature. , 349 (2):735–741, Apr. 2004. doi: 10.1111/j.1365-2966.2004.07543.x.

S. L. Breen, J. L. Caswell, S. P. Ellingsen, and C. J. Phillips. Water masers accompanying OH and methanol masers in star formation regions. , 406(3):1487–1532, Aug. 2010a. doi: 10.1111/j.1365-2966.2010.16791.x.

S. L. Breen, S. P. Ellingsen, J. L. Caswell, and B. E. Lewis. 12.2-GHz methanol masers towards 1.2-mm dust clumps: quantifying high-mass star formation evolutionary schemes. , 401(4): 2219–2244, Feb. 2010b. doi: 10.1111/j.1365-2966.2009.15831.x.

S. L. Breen, S. P. Ellingsen, Y. Contreras, J. A. Green, J. L. Caswell, J. B. Stevens, J. R. Dawson, and M. A. Voronkov. Confirmation of the exclusive association between 6.7-GHz methanol masers and high-mass star formation regions. , 435(1):524–530, Oct. 2013. doi: 10.1093/mnras/stt1315.

S. L. Breen, G. A. Fuller, J. L. Caswell, J. A. Green, A. Avison, S. P. Ellingsen, M. D. Gray, M. Pestalozzi, L. J. Quinn, A. M. S. Richards, M. A. Thompson, and M. A. Voronkov. The 6-GHz methanol multibeam maser catalogue - V. Galactic longitudes 20°-60°. , 450(4): 4109–4136, July 2015. doi: 10.1093/mnras/stv847.

R. A. Burns, G. Orosz, O. Bayandina, G. Surcis, M. Olech, G. MacLeod, A. Volvach, G. Rudnitskii, T. Hirota, K. Immer, J. Blanchard, B. Marcote, H. J. van Langevelde, J. O. Chibueze, K. Sugiyama, K.-T. Kim, I. Val'tts, N. Shakhvorostova, B. Kramer, W. A. Baan, C. Brogan, T. Hunter, S. Kurtz, A. M. Sobolev, J. Brand, and L. Volvach. VLBI observations of the G25.65+1.05 water maser superburst. , 491(3):4069–4075, Jan. 2020a. doi: 10.1093/mnras/stz3172.

R. A. Burns, K. Sugiyama, T. Hirota, K.-T. Kim, A. M. Sobolev, B. Stecklum, G. C. MacLeod, Y. Yonekura, M. Olech, G. Orosz, S. P. Ellingsen, L. Hyland, A. Caratti o Garatti, C. Brogan, T. R. Hunter, C. Phillips, S. P. van den Heever, J. Eislöffel, H. Linz, G. Surcis, J. O. Chibueze, W. Baan, and B. Kramer. A heatwave of accretion energy traced by masers in the G358-MM1 high-mass protostar. *Nature Astronomy*, 4:506–510, Jan. 2020b. doi: 10.1038/s41550-019-0989-3.

A. Caratti o Garatti, B. Stecklum, R. Garcia Lopez, J. Eislöffel, T. P. Ray, A. Sanna, R. Cesaroni, C. M. Walmsley, R. D. Oudmaijer, W. J. de Wit, L. Moscadelli, J. Greiner, A. Krabbe, C. Fischer, R. Klein, and J. M. Ibañez. Disk-mediated accretion burst in a high-mass young stellar object. *Nature Physics*, 13(3):276–279, Mar. 2017. doi: 10.1038/nphys3942.

R. Cesaroni, Á. Sánchez-Monge, M. T. Beltrán, K. G. Johnston, L. T. Maud, L. Moscadelli, J. C. Mottram, A. Ahmadi, V. Allen, H. Beuther, T. Csengeri, S. Etoka, G. A. Fuller, D. Galli, R. Galván-Madrid, C. Goddi, T. Henning, M. G. Hoare, P. D. Klaassen, R. Kuiper, M. S. N. Kumar, S. Lumsden, T. Peters, V. M. Rivilla, P. Schilke, L. Testi, F. van der Tak, S. Vig, C. M. Walmsley, and H. Zinnecker. Chasing discs around O-type (proto)stars: Evidence from ALMA observations. , 602:A59, June 2017. doi: 10.1051/0004-6361/201630184.

H.-R. V. Chen, E. Keto, Q. Zhang, T. K. Sridharan, S.-Y. Liu, and Y.-N. Su. A hot and massive accretion disk around the high-mass protostar iras 20126+4104. *The Astrophysical Journal*, 823(2):125, may 2016. doi: 10.3847/0004-637X/823/2/125. URL https://dx.doi.org/10.3847/0004-637X/823/2/125.

X. Chen, A. M. Sobolev, Z.-Y. Ren, S. Parfenov, S. L. Breen, S. P. Ellingsen, Z.-Q. Shen, B. Li, G. C. MacLeod, W. Baan, C. Brogan, T. Hirota, T. R. Hunter, H. Linz, K. Menten, K. Sugiyama, B. Stecklum, Y. Gong, and X. Zheng. New maser species tracing spiral-arm accretion flows in a high-mass young stellar object. *Nature Astronomy*, 4:1170–1176, Jan. 2020. doi: 10.1038/s41550-020-1144-x.

Z. Chen, W. Sun, R. Chini, M. Haas, Z. Jiang, and X. Chen. M17 MIR: A Massive Protostar with Multiple Accretion Outbursts. , 922(1):90, Nov. 2021. doi: 10.3847/1538-4357/ac2151.

D. M. Cragg, A. M. Sobolev, and P. D. Godfrey. Modelling methanol and hydroxyl masers in star-forming regions. , 331(2):521–536, Mar. 2002. doi: 10.1046/j.1365-8711.2002.05226.x.

D. M. Cragg, A. M. Sobolev, and P. D. Godfrey. Models of class II methanol masers based on improved molecular data. , 360(2):533–545, June 2005. doi: 10.1111/j.1365-2966.2005.09077.x.

R. M. Crutcher and A. J. Kemball. Review of Zeeman Effect Observations of Regions of Star Formation K Zeeman Effect, Magnetic Fields, Star formation, Masers, Molecular clouds. *Frontiers in Astronomy and Space Sciences*, 6:66, Oct. 2019. doi: 10.3389/fspas.2019.00066.

D. Dall'Olio, W. H. T. Vlemmings, B. Lankhaar, and G. Surcis. Polarisation properties of methanol masers. , 644:A122, Dec. 2020. doi: 10.1051/0004-6361/202039149.

M. S. Darwish, A. M. S. Richards, S. Etoka, K. A. Edris, S. M. Saad, M. M. Beheary, and G. A. Fuller. OH maser towards IRAS 06056+2131: polarization parameters and evolution status. , 499(1):1441–1449, Nov. 2020. doi: 10.1093/mnras/staa2810.

R. D. Davies. Magnetic Fields in OH Maser Clouds. In F. J. Kerr and S. C. Simonson, editors, *Galactic Radio Astronomy*, volume 60 of *IAU Symposium*, page 275, Jan. 1974.

L. K. Dewangan, I. I. Zinchenko, P. M. Zemlyanukha, S.-Y. Liu, Y.-N. Su, S. E. Kurtz, D. K. Ojha, A. G. Pazukhin, and Y. D. Mayya. The Disk-Outflow System around the Rare Young O-type Protostar W42-MME. , 925(1):41, Jan. 2022. doi: 10.3847/1538-4357/ac36dd.

M. Durjasz, M. Szymczak, and M. Olech. A highly variable methanol maser in G111.256-0.770. , 485(1):777–783, May 2019. doi: 10.1093/mnras/stz472.

M. Durjasz, M. Szymczak, M. Olech, and A. Bartkiewicz. Discovery of recurrent flares of 6.7 GHz methanol maser emission in Cepheus A HW2. , 663:A123, July 2022. doi: 10.1051/0004-6361/202243552.

K. A. Edris, G. A. Fuller, S. Etoka, and R. J. Cohen. OH masers towards IRAS 19092+0841. , 608:A80, Dec. 2017. doi: 10.1051/0004-6361/201629365.

S. Etoka, R. J. Cohen, and M. D. Gray. The association of OH and methanol masers in W3(OH). , 360(3):1162–1170, July 2005. doi: 10.1111/j.1365-2966.2005.09130.x.

R. Fedriani, A. Caratti o Garatti, D. Coffey, R. Garcia Lopez, S. Kraus, G. Weigelt, B. Stecklum, T. P. Ray, and C. M. Walmsley. Parsec-scale jets driven by high-mass young stellar objects. Connecting the au- and the parsec-scale jet in IRAS 13481-6124. , 616:A126, Aug. 2018. doi: 10.1051/0004-6361/201732180.

V. L. Fish and M. J. Reid. Full-Polarization Observations of OH Masers in Massive Star-forming Regions. II. Maser Properties and the Interpretation of Polarization. , 164(1):99–123, May 2006. doi: 10.1086/502650.

V. L. Fish and M. J. Reid. Proper Motions of OH Masers and Magnetic Fields in Massive Star-forming Regions. , 670(2):1159–1172, Dec. 2007. doi: 10.1086/522329.

V. L. Fish and L. O. Sjouwerman. Global Very Long Baseline Interferometry Observations of the 6.0 GHz Hydroxyl Masers in Onsala 1. , 716(1):106–113, June 2010. doi: 10.1088/0004-637X/716/1/106.

V. L. Fish, M. J. Reid, A. L. Argon, and X.-W. Zheng. Full-Polarization Observations of OH Masers in Massive Star-forming Regions. I. Data. , 160(1):220–271, Sept. 2005. doi: 10.1086/431669.

K. Fujisawa, K. Sugiyama, K. Motogi, K. Hachisuka, Y. Yonekura, S. Sawada-Satoh, N. Matsumoto, K. Sorai, M. Momose, Y. Saito, H. Takaba, H. Ogawa, K. Kimura, K. Niinuma, D. Hirano, T. Omodaka, H. Kobayashi, N. Kawaguchi, K. M. Shibata, M. Honma, T. Hirota, Y. Murata, A. Doi, N. Mochizuki, Z. Shen, X. Chen, B. Xia, B. Li, and K.-T. Kim. Observations of 6.7 GHz methanol masers with East-Asian VLBI Network. I. VLBI images of the first epoch of observations. , 66(2):31, Apr. 2014. doi: 10.1093/pasj/psu015.

A. Ginsburg and C. Goddi. First Detection of CS Masers around a High-mass Young Stellar Object, W51 e2e. , 158(5):208, Nov. 2019. doi: 10.3847/1538-3881/ab4790.

J. A. Green, A. M. S. Richards, W. H. T. Vlemmings, P. Diamond, and R. J. Cohen. A MERLIN Study of 6-GHz excited-state OH and 6.7-GHz methanol masers in ON1. , 382(2):770–778, Dec. 2007. doi: 10.1111/j.1365-2966.2007.12418.x.

J. A. Green, J. L. Caswell, G. A. Fuller, A. Avison, S. L. Breen, K. Brooks, M. G. Burton, A. Chrysostomou, J. Cox, P. J. Diamond, S. P. Ellingsen, M. D. Gray, M. G. Hoare, M. R. W. Masheder, N. M. McClure-Griffiths, M. Pestalozzi, C. Phillips, L. Quinn, M. A. Thompson, M. A. Voronkov, A. Walsh, D. Ward-Thompson, D. Wong-McSweeney, J. A. Yates, and R. J. Cohen. The 6-GHz multibeam maser survey - I. Techniques. , 392(2):783–794, Jan. 2009. doi: 10.1111/j.1365-2966.2008.14091.x.

J. A. Green, J. L. Caswell, and N. M. McClure-Griffiths. Excited-state hydroxyl maser polarimetry: who ate all the πs? , 451(1):74–92, July 2015. doi: 10.1093/mnras/stv936.

L. J. Greenhill, C. Goddi, C. J. Chandler, L. D. Matthews, and E. M. L. Humphreys. Dynamical evidence for a magnetocentrifugal wind from a 20m binary young stellar object. *The Astrophysical Journal Letters*, 770(2):L32, jun 2013. doi: 10.1088/2041-8205/770/2/L32. URL https://dx.doi.org/10.1088/2041-8205/770/2/L32.

A. E. Guzmán, V. V. Guzmán, G. Garay, L. Bronfman, and F. Hechenleitner. Chemistry of the High-mass Protostellar Molecular Clump IRAS 16562-3959. , 236(2):45, June 2018. doi: 10.3847/1538-4365/aac01d.

A. E. Guzmán, P. Sanhueza, L. Zapata, G. Garay, and L. F. Rodríguez. A photoionized accretion disk around a young high-mass star. *The Astrophysical Journal*, 904(1):77, nov 2020. doi: 10.3847/1538-4357/abbe09. URL https://dx.doi.org/10.3847/1538-4357/abbe09.

P. Hennebelle and S.-i. Inutsuka. The role of magnetic field in molecular cloud formation and evolution. *Frontiers in Astronomy and Space Sciences*, 6:5, Mar. 2019. doi: 10.3389/fspas.2019.00005.

N. Hirano, S.-Y. Liu, H. Shang, P. T. P. Ho, H.-C. Huang, Y.-J. Kuan, M. J. McCaughrean, and Q. Zhang. SiO J = 5-4 in the HH 211 Protostellar Jet Imaged with the Submillimeter Array. , 636(2):L141–L144, Jan. 2006. doi: 10.1086/500201.

T. Hirota, P. Wolak, T. R. Hunter, C. L. Brogan, A. Bartkiewicz, M. Durjasz, A. Kobak, M. Olech, M. Szymczak, R. A. Burns, A. Aberfelds, G. Baek, J. Brand, S. Breen, D.-Y. Byun, A. Caratti o Garatti, X. Chen, J. O. Chibueze, C. Cyganowski, J. Eislöffel, S. Ellingsen, N. Hirano, B. Hu, J.-h. Kang, J.-S. Kim, J. Kim, K.-T. Kim, M. K. Kim, B. Kramer, J.-E. Lee, H. Linz, T. Liu, G. MacLeod, T. P. McCarthy, K. Menten, K. Motogi, C.-S. Oh, G. Orosz, A. M. Sobolev, B. Stecklum, K. Sugiyama, K. Sunada, L. Uscanga, F. van den Heever, A. E. Volvach, L. N. Volvach, Y. W. Wu, and Y. Yonekura. Millimeter methanol emission in the high-mass young stellar object G24.33+0.14. , 74(5):1234–1262, Oct. 2022. doi: 10.1093/pasj/psac067.

B. Hu, K. M. Menten, Y. Wu, A. Bartkiewicz, K. Rygl, M. J. Reid, J. S. Urquhart, and X. Zheng. On the Relationship of UC HII Regions and Class II Methanol Masers. I. Source Catalogs. , 833(1):18, Dec. 2016. doi: 10.3847/0004-637X/833/1/18.

B. Hutawarakorn, R. J. Cohen, and G. C. Brebner. OH masers and magnetic fields in the bipolar outflow source W75N. , 330(2):349–364, Feb. 2002. doi: 10.1046/j.1365-8711.2002.05068.x.

K. Immer, R. Galván-Madrid, C. König, H. B. Liu, and K. M. Menten. Diversity of chemistry and excitation conditions in the high-mass star forming complex W33. , 572:A63, Dec. 2014. doi: 10.1051/0004-6361/201423780.

K. Inayoshi, K. Sugiyama, T. Hosokawa, K. Motogi, and K. E. I. Tanaka. Direct Diagnostics of Forming Massive Stars: Stellar Pulsation and Periodic Variability of Maser Sources. , 769 (2):L20, June 2013. doi: 10.1088/2041-8205/769/2/L20.

K. G. Johnston, T. P. Robitaille, H. Beuther, H. Linz, P. Boley, R. Kuiper, E. Keto, M. G. Hoare, and R. van Boekel. A Keplerian-like Disk around the Forming O-type Star AFGL 4176. , 813(1):L19, Nov. 2015. doi: 10.1088/2041-8205/813/1/L19.

B. M. Jones, G. A. Fuller, S. L. Breen, A. Avison, J. A. Green, A. Traficante, D. Elia, S. P. Ellingsen, M. A. Voronkov, M. Merello, S. Molinari, and E. Schisano. The evolutionary status of protostellar clumps hosting class II methanol masers. , 493(2):2015–2041, Apr. 2020. doi: 10.1093/mnras/staa233.

S. J. Kenyon and L. Hartmann. Pre-Main-Sequence Evolution in the Taurus-Auriga Molecular Cloud. , 101:117, Nov. 1995. doi: 10.1086/192235.

M. R. Krumholz and C. Federrath. The Role of Magnetic Fields in Setting the Star Formation Rate and the Initial Mass Function. *Frontiers in Astronomy and Space Sciences*, 6:7, Feb. 2019. doi: 10.3389/fspas.2019.00007.

S. Kurtz, E. Churchwell, and D. O. S. Wood. Ultracompact H II Regions. II. New High-Resolution Radio Images. , 91:659, Apr. 1994. doi: 10.1086/191952.

B. Lankhaar, W. Vlemmings, G. Surcis, H. J. van Langevelde, G. C. Groenenboom, and A. van der Avoird. Characterization of methanol as a magnetic field tracer in star-forming regions. *Nature Astronomy*, 2:145–150, Feb. 2018. doi: 10.1038/s41550-017-0341-8.

R. B. Larson. Turbulence and star formation in molecular clouds. , 194:809–826, Mar. 1981. doi: 10.1093/mnras/194.4.809.

C. J. Law, Q. Zhang, A. C. Frommer, K. I. Öberg, R. Galván-Madrid, E. Keto, H. B. Liu, P. T. P. Ho, A. F. Izquierdo, and L. I. Cleeves. A Wideband Chemical Survey of Massive Star-forming Regions at Subarcsecond Resolution with the Submillimeter Array. , 276(2):54, Feb. 2025. doi: 10.3847/1538-4365/ad9477.

H.-B. Li, K. H. Yuen, F. Otto, P. K. Leung, T. K. Sridharan, Q. Zhang, H. Liu, Y.-W. Tang, and K. Qiu. Self-similar fragmentation regulated by magnetic fields in a region forming massive stars. , 520(7548):518–521, Apr. 2015. doi: 10.1038/nature14291.

J.-T. Liu, X. Chen, X.-D. Chen, Z.-W. Chen, S.-M. Song, Y.-X. Wang, Y.-K. Zhang, Z. Zhao, B. Li, B. Xia, and Z.-Q. Shen. Luminosity Outburst of a High-mass Young Stellar Object Triggered by the Surrounding Radiation Field. , 951(2):L24, July 2023. doi: 10.3847/2041-8213/acdf5b.

L. T. Maud, R. Cesaroni, M. S. N. Kumar, F. F. S. van der Tak, V. Allen, M. G. Hoare, P. D. Klaassen, D. Harsono, M. R. Hogerheijde, Á. Sánchez-Monge, P. Schilke, A. Ahmadi, M. T. Beltrán, H. Beuther, T. Csengeri, S. Etoka, G. Fuller, R. Galván-Madrid, C. Goddi, T. Henning, K. G. Johnston, R. Kuiper, S. Lumsden, L. Moscadelli, J. C. Mottram, T. Peters,

V. M. Rivilla, L. Testi, S. Vig, W. J. de Wit, and H. Zinnecker. Chasing discs around O-type (proto)stars. ALMA evidence for an SiO disc and disc wind from G17.64+0.16. , 620:A31, Nov. 2018. doi: 10.1051/0004-6361/201833908.

C. F. McKee and J. C. Tan. The Formation of Massive Stars from Turbulent Cores. , 585(2): 850–871, Mar. 2003. doi: 10.1086/346149.

K. M. Menten. *Interstellar methanol towards galactic HII regions.* PhD thesis, Rheinische Friedrich Wilhelms University of Bonn, Germany, Jan. 1987.

K. M. Menten. The Discovery of a New, Very Strong, and Widespread Interstellar Methanol Maser Line. , 380:L75, Oct. 1991. doi: 10.1086/186177.

D. M. A. Meyer, E. I. Vorobyov, R. Kuiper, and W. Kley. On the existence of accretion-driven bursts in massive star formation. , 464(1):L90–L94, Jan. 2017. doi: 10.1093/mnrasl/slw187.

D. M. A. Meyer, E. I. Vorobyov, V. G. Elbakyan, B. Stecklum, J. Eislöffel, and A. M. Sobolev. Burst occurrence in young massive stellar objects. , 482(4):5459–5476, Feb. 2019. doi: 10.1093/mnras/sty2980.

M. Modjaz, J. M. Moran, P. T. Kondratko, and L. J. Greenhill. Probing the Magnetic Field at Subparsec Radii in the Accretion Disk of NGC 4258. , 626(1):104–119, June 2005. doi: 10.1086/429559.

L. Moscadelli, A. Sanna, and C. Goddi. Unveiling the gas kinematics at 10 AU scales in high-mass star-forming regions. Milliarcsecond structure of 6.7 GHz methanol masers. , 536:A38, Dec. 2011. doi: 10.1051/0004-6361/201117791.

L. Moscadelli, A. Sanna, C. Goddi, M. C. Walmsley, R. Cesaroni, A. Caratti o Garatti, B. Stecklum, K. M. Menten, and A. Kraus. Extended CH_3OH maser flare excited by a bursting massive YSO. , 600:L8, Apr. 2017. doi: 10.1051/0004-6361/201730659.

L. Moscadelli, A. Sanna, H. Beuther, A. Oliva, and R. Kuiper. Snapshot of a magnetohydrodynamic disk wind traced by water maser observations. *Nature Astronomy*, 6:1068–1076, Aug. 2022. doi: 10.1038/s41550-022-01754-4.

F. Motte, S. Bontemps, and F. Louvet. High-Mass Star and Massive Cluster Formation in the Milky Way. , 56:41–82, Sept. 2018. doi: 10.1146/annurev-astro-091916-055235.

T. Murphy, M. Cohen, R. D. Ekers, A. J. Green, R. M. Wark, and V. Moss. Ultra- and hyper-compact h ii regions at 20 ghz. *Monthly Notices of the Royal Astronomical Society*,

405(3):1560–1572, 06 2010. ISSN 0035-8711. doi: 10.1111/j.1365-2966.2010.16589.x. URL https://doi.org/10.1111/j.1365-2966.2010.16589.x.

T. Nagayama, A. Nakagawa, H. Imai, T. Omodaka, and Y. Sofue. VLBI Observations of Water Masers in Onsala1: Massive Binary Star-Forming Site? , 60:183, Apr. 2008. doi: 10.1093/pasj/60.2.183.

S. Nammahachak, K. Asanok, B. Hutawarakorn Kramer, R. J. Cohen, O. Muanwong, and N. Gasiprong. OH masers associated with bipolar outflow in ON1. , 371(2):619–625, Sept. 2006. doi: 10.1111/j.1365-2966.2006.10740.x.

M. Olech, M. Szymczak, P. Wolak, R. Sarniak, and A. Bartkiewicz. 6.7 GHz variability characteristics of new periodic methanol maser sources. , 486(1):1236–1254, June 2019. doi: 10.1093/mnras/stz926.

M. Olech, M. Szymczak, P. Wolak, E. Gérard, and A. Bartkiewicz. Long-term multi-frequency maser observations of the intermediate-mass young stellar object G107.298+5.639. , 634:A41, Feb. 2020. doi: 10.1051/0004-6361/201936943.

M. Olech, M. Durjasz, M. Szymczak, and A. Bartkiewicz. Detection of periodic flares in 6.7 GHz methanol masers G45.804−0.356 and G49.043−1.079. , 661:A114, May 2022. doi: 10.1051/0004-6361/202243108.

J. D. Pandian, E. Momjian, Y. Xu, K. M. Menten, and P. F. Goldsmith. The Arecibo Methanol Maser Galactic Plane Survey. IV. Accurate Astrometry and Source Morphologies. , 730(1): 55, Mar. 2011. doi: 10.1088/0004-637X/730/1/55.

S. Y. Parfenov and A. M. Sobolev. On the Class II methanol maser periodic variability due to the rotating spiral shocks in the gaps of discs around young binary stars. , 444(1):620–628, Oct. 2014. doi: 10.1093/mnras/stu1481.

K. Pattle, L. Fissel, M. Tahani, T. Liu, and E. Ntormousi. Magnetic Fields in Star Formation: from Clouds to Cores. In S. Inutsuka, Y. Aikawa, T. Muto, K. Tomida, and M. Tamura, editors, *Protostars and Planets VII*, volume 534 of *Astronomical Society of the Pacific Conference Series*, page 193, July 2023. doi: 10.48550/arXiv.2203.11179.

S. J. D. Purser, S. L. Lumsden, M. G. Hoare, and S. Kurtz. A Galactic survey of radio jets from massive protostars. , 504(1):338–355, June 2021. doi: 10.1093/mnras/stab747.

M. J. Reid, T. M. Dame, K. M. Menten, and A. Brunthaler. A Parallax-based Distance Estimator for Spiral Arm Sources. , 823(2):77, June 2016. doi: 10.3847/0004-637X/823/2/77.

M. J. Reid, K. M. Menten, A. Brunthaler, X. W. Zheng, T. M. Dame, Y. Xu, J. Li, N. Sakai, Y. Wu, K. Immer, B. Zhang, A. Sanna, L. Moscadelli, K. L. J. Rygl, A. Bartkiewicz, B. Hu, L. H. Quiroga-Nuñez, and H. J. van Langevelde. Trigonometric Parallaxes of High-mass Star-forming Regions: Our View of the Milky Way. , 885(2):131, Nov. 2019. doi: 10.3847/1538-4357/ab4a11.

M. Rickert, F. Yusef-Zadeh, and J. Ott. A 6.7 GHz methanol maser survey of the central molecular zone. , 482(4):5349–5361, Feb. 2019. doi: 10.1093/mnras/sty2901.

A. Sanna, L. Moscadelli, R. Cesaroni, A. Tarchi, R. S. Furuya, and C. Goddi. VLBI study of maser kinematics in high-mass star-forming regions. I. G16.59-0.05. , 517:A71, July 2010a. doi: 10.1051/0004-6361/201014233.

A. Sanna, L. Moscadelli, R. Cesaroni, A. Tarchi, R. S. Furuya, and C. Goddi. VLBI study of maser kinematics in high-mass star-forming regions. II. G23.01-0.41. , 517:A78, July 2010b. doi: 10.1051/0004-6361/201014234.

A. Sanna, R. Cesaroni, L. Moscadelli, Q. Zhang, K. M. Menten, S. Molinari, A. Caratti o Garatti, and J. M. De Buizer. A subarcsecond study of the hot molecular core in G023.01-00.41. , 565:A34, May 2014. doi: 10.1051/0004-6361/201323129.

A. Sanna, A. Kölligan, L. Moscadelli, R. Kuiper, R. Cesaroni, T. Pillai, K. M. Menten, Q. Zhang, A. Caratti o Garatti, C. Goddi, S. Leurini, and C. Carrasco-González. Discovery of a sub-Keplerian disk with jet around a 20 $M_\odot$ young star. ALMA observations of G023.01-00.41. , 623:A77, Mar. 2019. doi: 10.1051/0004-6361/201833411.

A. Sanna, A. Giannetti, M. Bonfand, L. Moscadelli, R. Kuiper, J. Brand, R. Cesaroni, A. Caratti o Garatti, T. Pillai, and K. M. Menten. Physical conditions in the warped accretion disk of a massive star. 349 GHz ALMA observations of G023.01−00.41. , 655:A72, Nov. 2021. doi: 10.1051/0004-6361/202040000.

F. H. Shu, F. C. Adams, and S. Lizano. Star formation in molecular clouds: observation and theory. , 25:23–81, Jan. 1987. doi: 10.1146/annurev.aa.25.090187.000323.

B. Stecklum, V. Wolf, H. Linz, A. Caratti o Garatti, S. Schmidl, S. Klose, J. Eislöffel, C. Fischer, C. Brogan, R. A. Burns, O. Bayandina, C. Cyganowski, M. Gurwell, T. Hunter, N. Hirano, K. T. Kim, G. MacLeod, K. M. Menten, M. Olech, G. Orosz, A. Sobolev, T. K. Sridharan, G. Surcis, K. Sugiyama, J. van der Walt, A. Volvach, and Y. Yonekura. Infrared observations of the flaring maser source G358.93-0.03. SOFIA confirms an accretion burst from a massive young stellar object. , 646:A161, Feb. 2021. doi: 10.1051/0004-6361/202039645.

K. Sugiyama, K. Fujisawa, A. Doi, M. Honma, H. Kobayashi, T. Bushimata, N. Mochizuki, and Y. Murata. Mapping Observations of 6.7 GHz Methanol Masers with the Japanese VLBI Network. , 60:23, Feb. 2008. doi: 10.1093/pasj/60.1.23.

G. Surcis, W. H. T. Vlemmings, R. M. Torres, H. J. van Langevelde, and B. Hutawarakorn Kramer. The properties and polarization of the H_2O and CH_3OH maser environment of NGC 7538-IRS 1. , 533:A47, Sept. 2011. doi: 10.1051/0004-6361/201117108.

G. Surcis, W. H. T. Vlemmings, H. J. van Langevelde, and B. Hutawarakorn Kramer. EVN observations of 6.7 GHz methanol maser polarization in massive star-forming regions. , 541: A47, May 2012. doi: 10.1051/0004-6361/201118658.

G. Surcis, W. H. T. Vlemmings, H. J. van Langevelde, B. Hutawarakorn Kramer, and L. H. Quiroga-Nuñez. EVN observations of 6.7 GHz methanol maser polarization in massive star-forming regions. II. First statistical results. , 556:A73, Aug. 2013. doi: 10.1051/0004-6361/201321501.

G. Surcis, W. H. T. Vlemmings, H. J. van Langevelde, B. Hutawarakorn Kramer, A. Bartkiewicz, and M. G. Blasi. EVN observations of 6.7 GHz methanol maser polarization in massive star-forming regions. III. The flux-limited sample. , 578:A102, June 2015. doi: 10.1051/0004-6361/201425420.

G. Surcis, W. H. T. Vlemmings, H. J. van Langevelde, B. Hutawarakorn Kramer, and A. Bartkiewicz. EVN observations of 6.7 GHz methanol maser polarization in massive star-forming regions. IV. Magnetic field strength limits and structure for seven additional sources. , 623:A130, Mar. 2019. doi: 10.1051/0004-6361/201834578.

G. Surcis, W. H. T. Vlemmings, H. J. van Langevelde, B. Hutawarakorn Kramer, and A. Bartkiewicz. EVN observations of 6.7 GHz methanol maser polarization in massive star-forming regions. V. Completion of the flux-limited sample. , 658:A78, Feb. 2022. doi: 10.1051/0004-6361/202142125.

G. Surcis, W. H. T. Vlemmings, C. Goddi, J. M. Torrelles, J. F. Gómez, A. Rodríguez-Kamenetzky, C. Carrasco-González, S. Curiel, S. W. Kim, J. S. Kim, and H. J. van Langevelde. Monitoring of the polarized H_2O maser emission around the massive protostars W75N(B)-VLA 1 and W75N(B)-VLA 2. , 673:A10, May 2023. doi: 10.1051/0004-6361/202245734.

M. Szymczak, G. Hrynek, and A. J. Kus. A survey of the 6.7 GHz methanol maser emission from IRAS sources. I. Data. , 143:269–301, Apr. 2000. doi: 10.1051/aas:2000334.

M. Szymczak, A. J. Kus, G. Hrynek, A. Kěpa, and E. Pazderski. 6.7 GHz methanol masers at sites of star formation. A blind survey of the Galactic plane between 20 degr «= 40 degr and |b| <= 052. , 392:277–286, Sept. 2002. doi: 10.1051/0004-6361:20020907.

M. Szymczak, P. Wolak, and A. Bartkiewicz. Discovery of four periodic methanol masers and updated light curve for a further one. , 448(3):2284–2293, Apr. 2015. doi: 10.1093/mnras/stv145.

M. Szymczak, M. Olech, R. Sarniak, P. Wolak, and A. Bartkiewicz. Monitoring observations of 6.7 GHz methanol masers. , 474(1):219–253, Feb. 2018a. doi: 10.1093/mnras/stx2693.

M. Szymczak, M. Olech, P. Wolak, E. Gérard, and A. Bartkiewicz. Giant burst of methanol maser in S255IR-NIRS3. , 617:A80, Sept. 2018b. doi: 10.1051/0004-6361/201833443.

M. Szymczak, P. Wolak, A. Bartkiewicz, M. Aramowicz, and M. Durjasz. A search for the OH 6035 MHz line in high-mass star-forming regions. , 642:A145, Oct. 2020. doi: 10.1051/0004-6361/202039009.

J. Tigé, F. Motte, D. Russeil, A. Zavagno, M. Hennemann, N. Schneider, T. Hill, Q. Nguyen Luong, J. Di Francesco, S. Bontemps, F. Louvet, P. Didelon, V. Könyves, P. André, G. Leuleu, J. Bardagi, L. D. Anderson, D. Arzoumanian, M. Benedettini, J. P. Bernard, D. Elia, M. Figueira, J. Kirk, P. G. Martin, V. Minier, S. Molinari, T. Nony, P. Persi, S. Pezzuto, D. Polychroni, T. Rayner, A. Rivera-Ingraham, H. Roussel, K. Rygl, L. Spinoglio, and G. J. White. The earliest phases of high-mass star formation, as seen in NGC 6334 by Herschel-HOBYS. , 602:A77, June 2017. doi: 10.1051/0004-6361/201628989.

Y. Tsukamoto, A. Maury, B. Commercon, F. O. Alves, E. G. Cox, N. Sakai, T. Ray, B. Zhao, and M. N. Machida. The Role of Magnetic Fields in the Formation of Protostars, Disks, and Outflows. In S. Inutsuka, Y. Aikawa, T. Muto, K. Tomida, and M. Tamura, editors, *Protostars and Planets VII*, volume 534 of *Astronomical Society of the Pacific Conference Series*, page 317, July 2023. doi: 10.48550/arXiv.2209.13765.

S. P. van den Heever, D. J. van der Walt, J. M. Pittard, and M. G. Hoare. Periodic methanol masers: from a colliding wind binary (CWB) perspective. , 485(2):2759–2771, May 2019. doi: 10.1093/mnras/stz576.

D. J. van der Walt. On the Methanol Masers in G9.62+0.20E and G188.95+0.89. , 141(5):152, May 2011. doi: 10.1088/0004-6256/141/5/152.

J. van der Walt. On the number and lifetime of 6.7-GHz methanol masers. , 360(1):153–158, June 2005. doi: 10.1111/j.1365-2966.2005.09026.x.

W. H. T. Vlemmings. A new probe of magnetic fields during high-mass star formation. Zeeman splitting of 6.7 GHz methanol masers. , 484(3):773–781, June 2008. doi: 10.1051/0004-6361:200809447.

W. H. T. Vlemmings, G. Surcis, K. J. E. Torstensson, and H. J. van Langevelde. Magnetic field regulated infall on the disc around the massive protostar CepheusAHW2. , 404(1):134–143, May 2010. doi: 10.1111/j.1365-2966.2010.16297.x.

G. M. Williams, C. J. Cyganowski, C. L. Brogan, T. R. Hunter, J. D. Ilee, P. Nazari, J. M. D. Kruijssen, R. J. Smith, and I. A. Bonnell. ALMA observations of the Extended Green Object G19.01-0.03 - I. A Keplerian disc in a massive protostellar system. , 509(1):748–762, Jan. 2022. doi: 10.1093/mnras/stab2973.

P. Wolak, M. Olech, M. Szymczak, A. Bartkiewicz, and M. Durjasz. Reappearance of methanol maser flare in G24.33+0.14. *The Astronomer's Telegram*, 13080:1, Sept. 2019.

G. Wu, C. Henkel, Y. Xu, A. Brunthaler, K. M. Menten, K. Qiu, J. Li, B. Zhang, and J. Esimbek. ALMA and VLBA views on the outflow associated with an O-type protostar in G26.50+0.28. , 677:A80, Sept. 2023a. doi: 10.1051/0004-6361/202345893.

J.-H. Wu, X. Chen, Y.-K. Zhang, S. P. Ellingsen, A. M. Sobolev, Z. Zhao, S.-M. Song, Z.-Q. Shen, B. Li, B. Xia, R.-B. Zhao, J.-Q. Wang, and Y.-J. Wu. Physical Environments of the Luminosity Outburst Source NGC 6334I Traced by Thermal and Maser Lines of Multiple Molecules. , 265(2):49, Apr. 2023b. doi: 10.3847/1538-4365/acbd46.

A. Y. Yang, M. A. Thompson, J. S. Urquhart, and W. W. Tian. Massive Outflows Associated with ATLASGAL Clumps. , 235(1):3, Mar. 2018. doi: 10.3847/1538-4365/aaa297.

I. I. Zinchenko, S.-Y. Liu, and Y.-N. Su. Fine structure and kinematics of the ionized and molecular gas in the jet and disk around S255IR NIRS3 from high-resolution ALMA observations. , 692:A181, Dec. 2024. doi: 10.1051/0004-6361/202452458.

A&A 671, A135 (2023)
https://doi.org/10.1051/0004-6361/202244772

Astronomy & Astrophysics

Multi-frequency VLBI observations of maser lines during the 6.7 GHz maser flare in the high-mass young stellar object G24.33+0.14

A. Kobak[1], A. Bartkiewicz[1], M. Szymczak[1], M. Olech[2], M. Durjasz[1], P. Wolak[1], J. O. Chibueze[3,4], T. Hirota[5,6], J. Eislöffel[7], B. Stecklum[7], A. Sobolev, O. Bayandina[8], G. Orosz[9], R. A. Burns[5,10,11], K.-T. Kim[11,12], and S. P. van den Heever[13]

[1] Institute of Astronomy, Faculty of Physics, Astronomy and Informatics, Nicolaus Copernicus University, Grudziadzka 5, 87-100 Torun, Poland
e-mail: akobak@astro.umk.pl
[2] Space Radio-Diagnostics Research Centre, University of Warmia and Mazury, ul. Oczapowskiego 2, 10-719 Olsztyn, Poland
[3] Centre for Space Research, North-West University, Potchefstroom 2520, South Africa
[4] Department of Physics and Astronomy, Faculty of Physical Sciences, University of Nigeria, Carver Building, 1 University Road, Nsukka, Nigeria
[5] Mizusawa VLBI Observatory, National Astronomical Observatory of Japan, Osawa 2-21-1, Mitaka-shi, Tokyo 181-8588, Japan
[6] Department of Astronomical Sciences, SOKENDAI (The Graduate University for Advanced Studies), Osawa 2-21-1, Mitaka-shi, Tokyo 181-8588, Japan
[7] Thüringer Landessternwarte Tautenburg, Sternwarte 5, 07778 Tautenburg, Germany
[8] INAF Osservatorio Astrofisico di Arcetri, Largo E. Fermi 5, 50125 Firenze, Italy
[9] Joint Institute for VLBI ERIC, Oude Hoogeveensedijk 4, 7991 PD Dwingeloo, The Netherlands
[10] Department of Science, National Astronomical Observatory of Japan, 2-21-1 Osawa, Mitaka, Tokyo 181-8588, Japan
[11] Korea Astronomy and Space Science Institute, 776 Daedeokdae-ro, Yuseong-gu, Daejeon 34055, Republic of Korea
[12] University of Science and Technology, Korea (UST), 217 Gajeong-ro, Yuseong-gu, Daejeon 34113, Republic of Korea
[13] SARAO, Hartebeesthoek Radio Astronomy Observatory, PO Box 443, Krugersdorp, 1741, South Africa

Received 19 August 2022 / Accepted 22 December 2022

ABSTRACT

Context. Recent studies have shown that 6.7 GHz methanol maser flares can be a powerful tool for verifying the mechanisms of maser production and even the specific signatures of accretion rate changes in the early stages of high-mass star formation.
Aims. We characterize the spatial structure and evolution of methanol and water masers during a flare of methanol maser emission at 6.7 GHz in the high-mass young stellar object (HMYSO) G24.33+0.14.
Methods. Very Long Baseline Array (VLBA) was used to image the 6.7 and 12.2 GHz methanol and 22.2 GHz water vapor masers at three epochs guided by monitoring the methanol line with the Torun 32m telescope. The 6.7 GHz maser maps were also obtained with the European VLBI Network (EVN) and Long Baseline Array (LBA) during the flare. The Wide-field Infrared Survey Explorer (WISE) data were used to find correlations between the 6.7 GHz maser and infrared (IR) fluxes.
Results. The 6.7 GHz methanol maser cloudlets are distributed over ~3500 au, and the morphology of most of them is stable although their brightness varies following the course of the total flux density on a timescale of two months. The 12.2 GHz methanol maser cloudlets cover an area an order of magnitude smaller than that of 6.7 GHz emission, and both transitions emerge from the same masing gas. The 22.2 GHz maser cloudlets lie in the central region and show a systematic increase in brightness and moderate changes in size and orientation, together with the velocity drift of the strongest cloudlet during two months of the Very Long Baseline Interferometry (VLBI) observing period. Time lag estimates imply the propagation of changes in the physical conditions of the masing region with a subluminal speed (~0.3c). A tight correlation of IR (4.6 μm) and 6.7 GHz flux densities is found, supporting the radiative pumping model. Proper motion analysis does not reveal any signs of expansion or inflow of the methanol cloudlets within ~6 mas over ~10 yr. Comparison with the 230 GHz Atacama Large Millimeter Array (ALMA) data indicates that the methanol masers are distributed in the inner part of the rotating disk, whereas the 22.2 GHz emission traces the compact inner component of the bipolar outflow or a jet structure.
Conclusions. The maser morphology in the target is remarkably stable over the course of the flare and is similar to the quiescent state, possibly due to less energetic accretion events that can repeat on a timescale of ~8 yr.

Key words. masers – stars: massive – stars: formation – stars: flare – radio lines: ISM

1. Introduction

Spectral line observations of high-mass young stellar object (HMYSO) are valuable probes of the kinematics and dynamics of the star formation processes. Methanol maser lines are of special interest in this context as unambiguous signposts of star formation activity (e.g., Menten 1991; Caswell 2003; Breen et al. 2015). Owing to their high brightness and compactness, they can probe neutral gas cloudlets of a few tens of au in size that reside in rotating structures, such as toroids and

disks (Beltrán & de Wit 2016 for review and references therein), or around powerful jets (e.g., Anglada et al. 2018). Moreover, brightening of the centimeter methanol maser lines is easily detectable in single-dish monitoring, and it has recently proven to be a signature of accretion events in HMYSO.

Fujisawa et al. (2015) reported the outburst of the 6.7 GHz methanol maser line in S255IR-NIRS3, the first case since the discovery of this transition by Menten (1991). This target has been presenting moderate variability on timescales of months to years over ∼23 yr (Szymczak et al. 2018b). The follow-up near-infrared imaging showed the brightening of the central source and its outflow cavities, which provided evidence of an accretion burst onto the HMYSO (Caratti o Garatti et al. 2017). A similar 6.7 GHz methanol maser flare was reported in the accretion burst source NGC 6334I−MM1 by MacLeod et al. (2018). They presented a contemporaneous flaring event of 10 maser transitions in hydroxyl, methanol, and water. The Very Large Array (VLA) imaging by Hunter et al. (2018) showed new methanol masers that appeared toward the MM1 protostellar system. Brogan et al. (2018) reported flaring of water masers with a bow-shock pattern, and proper motions studies by Chibueze et al. (2021) confirmed the radio jet influence.

Under the international collaboration M2O[1], which is focused on maser flare detections and follow-ups by radio and infrared telescopes globally (Burns et al. 2022), interesting phenomena in the HMYSO G358.93−0.03 were reported (e.g., Burns et al. 2020). Different methanol maser lines flared simultaneously, and Very Long Baseline Interferometry (VLBI) observations of methanol masers could outline the exact picture of a heat wave propagation in an accretion disk. Therefore, when the flare of the 6.7 GHz methanol maser line in the HMYSO G24.33+0.14 was reported (Wolak et al. 2019), we started following up observations of the 6.7 GHz and 12.2 GHz methanol and 22.2 GHz water maser transitions with diverse interferometric networks within the M2O collaboration. The aim of the present paper is to study the changes in the maser morphology as an effect of possible accretion burst in the source.

G24.33+0.14 (hereafter G24) is a massive young protostar, noted as an extended green object (i.e., an embedded high-mass star with molecular outflow; Cyganowski et al. 2008). The source is known to harbor methanol, water, and hydroxyl masers (Caswell & Green 2011). The 6.7 GHz maser imaged using the European VLBI Network (EVN) in June 2009 consists of three emission groups separated by 0.″2−0.″4 (Bartkiewicz et al. 2016). In mid-2011 the source experienced a strong flare of all the features at 6.7 GHz, lasting 200–400 days (Szymczak et al. 2018a). Recent observations show that the source harbors lines of ammonia at 23.9 GHz and formaldehyde at 4.8 GHz (McCarthy et al. 2022).The distance derived from H_I self-absorption is 9.5 kpc (Green & McClure-Griffiths 2011) or 7.20±0.76 kpc (with 90% probability) according to the Bayesian distance estimator based on accurate distances and proper motions of high-mass star-forming regions across the Milky Way (Reid et al. 2019). This value is adopted in the present paper. Hirota et al. (2022) compared the 230 GHz Atacama Large Millimeter Array (ALMA) data at pre- and post-flare epochs of 2016 and 2019, respectively. The 2019 dataset was obtained as a Director's Discretionary Time (DDT) project 20 days after the onset of the 6.7 GHz methanol maser flare. Three continuum sources were identified, indicating that the 6.7 GHz methanol maser coincides with the brightest one, named C1. The velocity structures of millimeter methanol lines at the C1 position show velocity gradients, implying the existence of a rotating ring-like structure of a disk–envelope system. The continuum and spectral observations suggest radiative heating in the central part of the disk, due to two flaring events involving a short-period episodicity on an 8 yr timescale traced by the methanol maser flares (Sect. 3.2), in addition to a 7000 yr timescale episodic outflow derived from multiple bow shocks traced by the 229.758 GHz methanol emission (Hirota et al. 2022). The detailed chemistry was studied by Baek et al. (2022); the results suggest that enhanced abundances of several molecules in the hot cores could be caused by the active accretion as well as different physical conditions of cores.

2. Observations

2.1. Torun 32 m monitoring

The target was observed in the 6668.519 MHz methanol line about once a week as part of the monitoring project using the Torun 32 m radio telescope. The beam full width at half maximum (FWHM) for this transition was 5.′8 with an rms pointing error of ∼25″ before mid-2016 and ∼10″ afterward. The data was taken in dual-polarization frequency-switching mode. The averaged spectra of 0.09 km s^{-1} resolution (after Hanning smoothing) had a typical rms noise level of about 0.35 Jy. The uncertainty of the flux density calibration was ∼10% (for details on the method of observation, calibration, and measurement of the flux density, see Szymczak et al. 2018a).

2.2. VLBI

The observations were conducted with diverse interferometers after detecting a flare of the 6.7 GHz methanol line. Below we briefly describe them, and in Table 1 we summarize the information on the maser transitions; dates of observations, day-of-the year (DOY) in 2019 is added for clarity; synthesized beams used in imaging; and the noise (1 $\sigma_{\rm rms}$) in the emission-free channel map.

G24.33+0.14 was observed with the Very Long Baseline Array[2] (VLBA), European VLBI Network[3] (EVN), and Long Baseline Array[4] (LBA) interferometers. The methanol 6668.519 MHz (hereafter 6.7 GHz) line was observed by all these networks. Frequency switching was used in VLBA experiments to observe both the 12 178.597 MHz methanol and 22 235.08 MHz water (hereafter 12.2 and 22.2 GHz) masers. We used a standard approach to reduce the data using the National Radio Astronomy Observatory (NRAO) Astronomical Image Processing System (AIPS) package. The quasar 3C345 was used as a delay and bandpass calibrator. The observations were conducted in phase-referencing mode with J1825−0737 as phase calibrator and J1835−1115 as the additional calibrator in LBA. The data were corrected for the effects of Earth's rotation and its

[1] https://www.masermonitoring.com/

[2] The National Radio Astronomy Observatory is a facility of the National Science Foundation operated under cooperative agreement by Associated Universities, Inc. Scientific results from data presented in this publication are derived from the following VLBA project code: BB416.

[3] The European VLBI Network is a joint facility of independent European, African, Asian, and North American radio astronomy institutes. Scientific results from data presented in this publication are derived from the following EVN Target of Opportunity project code: RB006B.

[4] The Long Baseline Array is part of the Australia Telescope National Facility, which is funded by the Australian Government for operation as a National Facility managed by CSIRO. Scientific results from data presented in this publication are derived from the following LBA project code: VX026D.

Table 1. Observing parameters.

Transition (MHz)	Date 2019 (day month)	Synthesized beam ($a \times b$; PA) (mas×mas; °)	$1\sigma_{\rm rms}$ (mJy beam^{-1})
VLBA			
6668.519	27 Sep.	2.7×1.3; +2	5.5
12 178.597	(DOY: 270)	1.9×0.7; −18	9.0
22 235.08		0.9×0.4; −9	16
6668.519	27 Oct.	6.5×2.1; −13	4.8
12 178.597	(DOY: 300)	2.1×0.6; −20	7.4
22 235.08		2.4×0.9; −14	7.1
6668.519	2 Dec.	5.2×1.3; −19	3.9
12 178.597	(DOY: 336)	2.4×0.8; −21	9.8
22 235.08		3.8×1.3; +23	7.2
LBA			
6668.519	28 Sep. (DOY: 271)	8.0×6.6; −5	12
EVN			
6668.519	7 Oct. (DOY: 280)	16.3×6.2; +7	3.4

motion within the Solar System and toward the Local standard of rest (LSR).

The VLBA observed the target in three epochs. The average on-source time per band was 1.5 h per epoch and the cycle time for phase-referencing was 1 min on phase calibrator and 2 min on the maser. We configured the baseband converter to a bandwidth of 32 MHz in dual polarization, averaged to increase the signal-to-noise ratio in the continuum data. Using the DiFX software correlator (Deller et al. 2011), channel spacings were set to 0.176 (6.7 GHz methanol), 0.096 (12.2 GHz methanol), and 0.053 km s^{-1} (22.2 GHz water). We note that for the 22.2 GHz data at the first epoch neither the phase-referencing technique nor the inverse phase-referencing was successful; therefore, we fringe-fitted the data on the brightest maser channel and estimated the absolute positions by identifying the same structures of maser spots in the second epoch.

For LBA the DiFX correlator was configured with a bandwidth of 4 MHz divided into 4092 channels and with an integration time of 2 s. The on-source time for the target was 4.48 h with a cycle time of 135 s both on the source and phase calibrators. Due to the nature of LBA observations, the initial gain amplitude calibration for the individual antennas was carried out by using the ACFIT task in AIPS, with Parkes as the reference antenna. Inspection of the autocorrelation spectra has shown that the target source flux density is ∼30% higher than for the Torun observations in the same period. Therefore, these data are considered unreliable for the recovered flux density estimation, and only the measured emission structure is analyzed in this publication as a general overview of the structure during the flare.

In EVN we used a 2 min cycle time between source and calibrator, with a total time on the source of 2.5 h. The bandwidth of 16 MHz was divided into 8192 spectral channels, yielding the velocity resolution of 0.087 km s^{-1}.

In order to analyze the parameters of milliarcsecond maser structures, we determined the position of emission peaks of maser spots that are detected in a velocity channel of an image cube and we defined a maser cloudlet as a group of maser spots that appear in at least three contiguous channels and coincide in positions within half the synthesized beam (e.g., Sanna et al. 2017).

For the amplification along the same line-of-sight path (i.e., co-propagation of 6.7 and 12.2 GHz maser transitions observed with the VLBA), we estimated the astrometric accuracy of single spot measurements on the phase-referenced images to be 0.07 ms in rectascension (RA) and 1 mas in declination (Dec) and 0.06 ms in RA and 0.8 mas in Dec for the 6.7 and 12.2 GHz data, respectively. These values were obtained considering the following factors, as recommended in Richards et al. (2022, Sect. 3.1): (1) inaccuracy of the phase-reference source position of 0.3 mas (Charlot et al. 2020); (2) the position uncertainty due to noise, given by the ratio (beam size)/(signal-to-noise), which is <0.3 mas; (3) the phase interpolation errors due to the phase calibrator–target time difference (0.03 mas); (4) the uncertainties introduced by the separation between the target and phase reference sources (2.4°), which are 0.7 and 0.6 mas at 6.7 and 12.2 GHz, respectively; and (5) the antenna position errors (with the antenna position error of 2 cm) of 0.5 and 0.3 mas at 6.7 and 12.2 GHz, respectively. Similarly, the positional accuracy of the 22 GHz water maser line observed using the VLBA is 0.08 ms in RA and 1.2 mas in Dec.

3. Results

Table 2 lists the absolute coordinates of the brightest maser spots for each transition, along with the peak velocity ($V_{\rm p}$), the peak intensity ($S_{\rm p}$), and the corresponding LSR velocity range of emission ($\Delta V_{\rm LSR}$), for all the experiments. In Fig. 1, we present a combined map resulting from the multi-frequency maser observations at epoch DOY:270.

The 6.7 and 12.2 GHz methanol lines are within the LSR velocity of 107.5 to 120.2 km s^{-1} and from 110.0 to 112.1 km s^{-1}, with the peaks at 115.3 and 110.4 km s^{-1}, respectively. The water maser emission ranges from 122.1 to 127.1 km s^{-1} with the peak at 125.1 km s^{-1}. The 6.7 GHz methanol maser spots are spread over an area of ∼0.″5×0.″5, corresponding to ∼3500 au×3500 au (Fig. 2). The 12.2 GHz methanol maser emission appears in a much smaller region of ∼0.″02×0.″06 (∼150 au×450 au), and its velocity range is a factor of 6 narrower than that of the 6.7 GHz emission. The two southern 12.2 GHz cloudlets disappeared in the third epoch (Fig. 3). The 22.2 GHz water masers are located in the central part of the 6.7 GHz maser region (Fig. 1). They form two tiny clusters of 4–12 au in length, elongated in the SE-NW direction with a clear velocity gradient (Fig. 4). The gray dashed-line ellipse represents the position of the 44 GHz radio jet reported by Purser et al. (2021). There is a ∼100 mas (∼720 au) offset between the peak position of the radio jet and the 22 GHz water masers, perhaps caused by the masers tracing the entrained gas around the jet. A small fraction of the offset could be attributed to the 7.5 mas astrometric accuracy of the VLA observations.

3.1. Emission structure during the flare and variability

3.1.1. 6.7 GHz

Figure 2 presents the 6.7 GHz methanol emission derived from all our EVN, VLBA, and LBA observations, including the archival EVN data from 2009 (Bartkiewicz et al. 2016). We note that the three masing regions seen in 2009 have persisted for more than 10 yr and that the overall distribution of all 6.7 GHz clusters was stable during the 2019 flare, at least for the 66 days of our interferometric observations. The position angle of the

Table 2. Results of the VLBA, LBA, and EVN observations.

Interferometer	Transition	Results for the brightest maser spot				
		RA (J2000)	Dec (J2000)	V_p	S_p	ΔV_{LSR}
Day-of-the-year	(GHz)	(h m s)	(° ′ ″)	(km s^{-1})	(Jy beam^{-1})	(km s^{-1})
VLBA DOY: 270	6.7 CH_3OH	18 35 08.14243±0.00007	−07 35 03.9242±0.0010	115.3	2.34	107.5–120.0
	12.2 CH_3OH	18 35 08.13433±0.00006	−07 35 04.2806±0.0008	110.3	0.97	110.1–112.1
	22.2 H_2O[(a)]	18 35 08.13231±0.00008	−07 35 04.1437±0.0012	125.1	7.72	122.1–127.1
VLBA DOY: 300	6.7 CH_3OH	18 35 08.14235±0.00007	−07 35 03.9269±0.0010	115.4	5.80	107.5–120.1
	12.2 CH_3OH	18 35 08.13428±0.00006	−07 35 04.2815±0.0008	110.3	1.03	110.0–112.1
	22.2 H_2O	18 35 08.13234±0.00008	−07 35 04.1443±0.0012	125.0	8.17	122.2–127.0
VLBA DOY: 336	6.7 CH_3OH	18 35 08.14234±0.00007	−07 35 03.9266±0.0010	115.4	2.59	109.8–120.2
	12.2 CH_3OH	18 35 08.13430±0.00006	−07 35 04.2821±0.0008	110.3	0.56	110.2–110.6
	22.2 H_2O	18 35 08.13233±0.00008	−07 35 04.1453±0.0012	124.8	9.39	122.1–127.1
LBA DOY: 271	6.7 CH_3OH	18 35 08.14238±0.00009	−07 35 03.9259±0.0014	115.3	8.97	107.6–120.1
EVN DOY: 280	6.7 CH_3OH	18 35 08.14231±0.00010	−07 35 03.9247±0.0010	115.2	7.34	108.1–120.2

Notes. [(a)]the coordinates taken from VLBA DOY: 300 (see Sect. 2.1 for details).

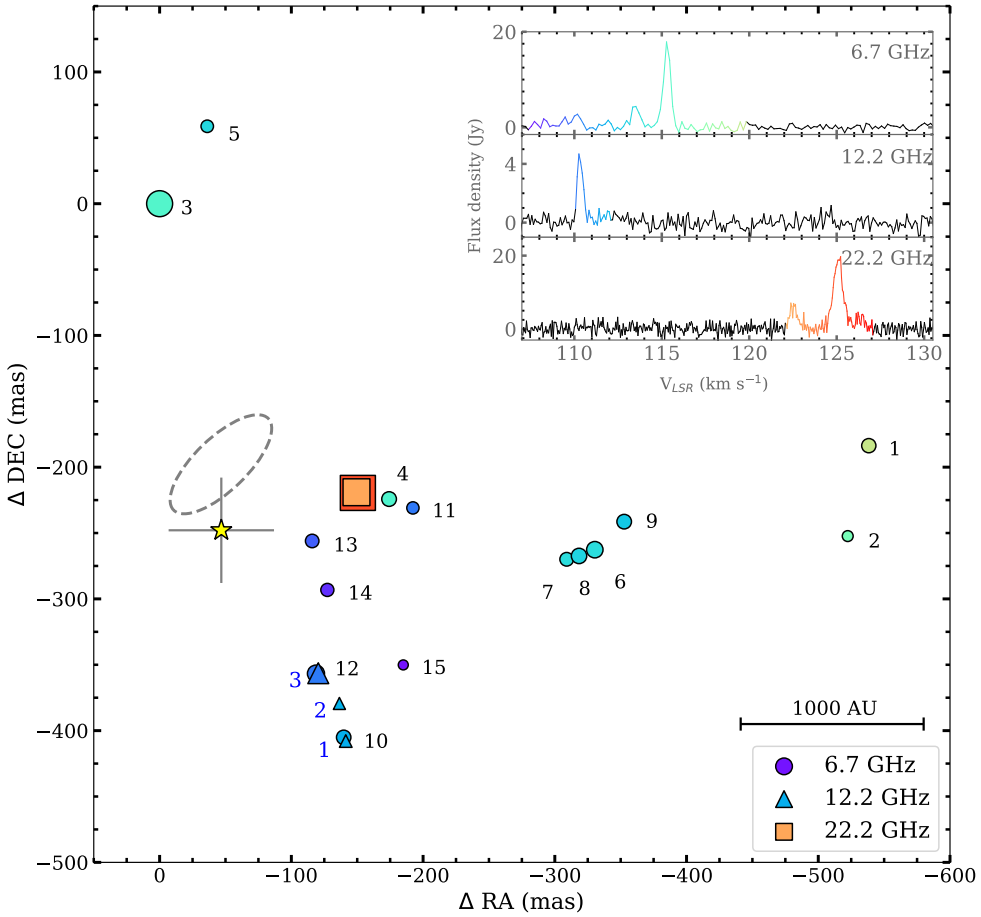

Fig. 1. Distribution of methanol and water maser cloudlets in G24 obtained with VLBA at DOY: 270. The inset shows the corresponding spectra. The circles, triangles, and squares correspond to the 6.7 GHz, 12.2 GHz methanol, and 22.2 GHz water transitions, respectively. The symbol sizes are proportional to the square root of the maser intensities. The symbol color corresponds to the LSR velocity, as indicated in the inserted spectra. The black numbers refer to groups of the 6.7 GHz methanol maser spots identified as cloudlets (Table A.1), while the blue numbers to the 12.2 GHz methanol maser cloudlets (Table A.2). The yellow star represents the brightest 230 GHz continuum source at the position of RA(J2000) = $18^h35^m08^s.13928$ and Dec(J2000) = −07°35′04″.1721, while the gray cross gives its astrometric uncertainty (Hirota et al. 2022). The (0,0) point corresponds to RA(J2000) = $18^h35^m08^s.14243$ and Dec(J2000) = −07°35′03″.9242, which is the position of the brightness maser spot at 6.7 GHz at DOY: 270. The gray dotted ellipse indicates the position of the *Q*-band jet reported in Purser et al. (2021).

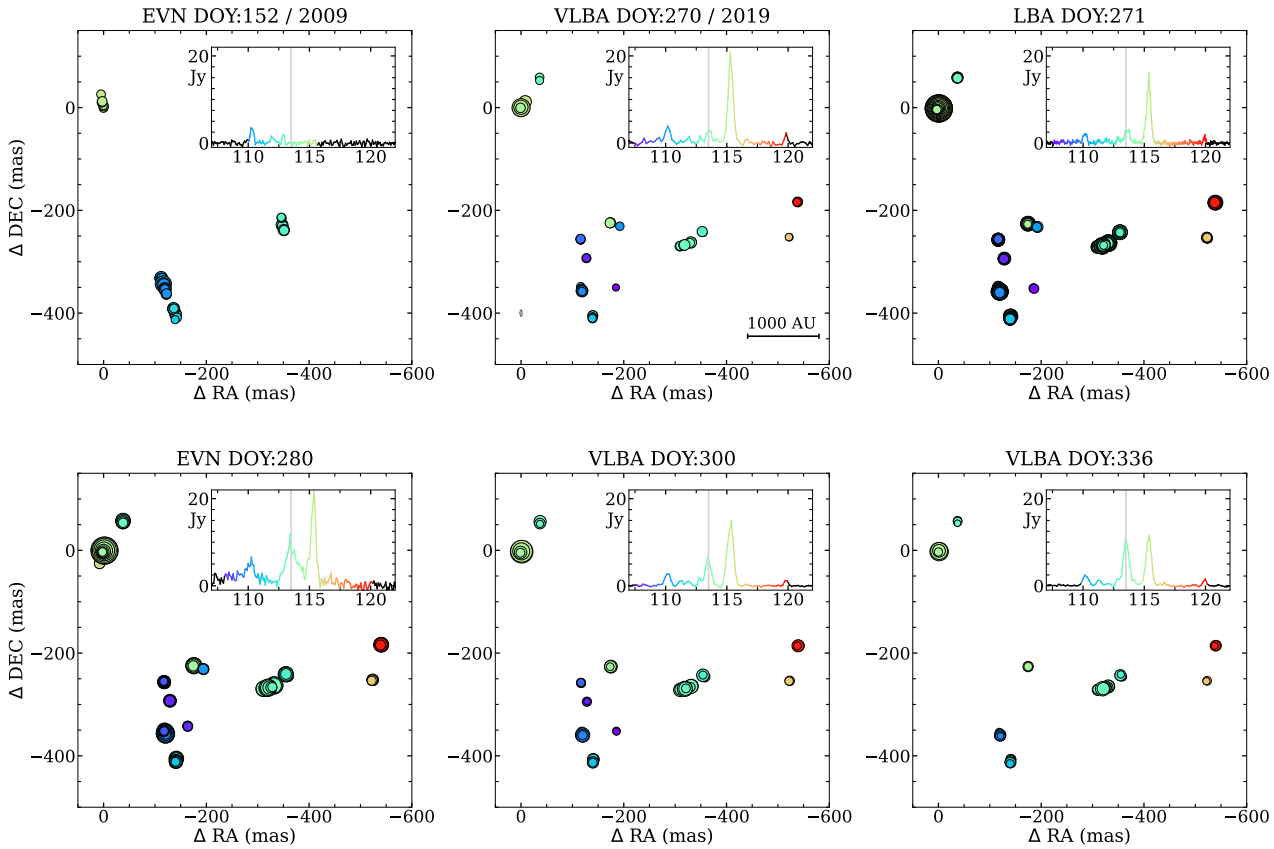

Fig. 2. Distribution of the 6.7 GHz methanol maser spots, as derived from the EVN (including archival data from Bartkiewicz et al. 2016), VLBA, and LBA observations at all epochs. The size of the circles is proportional to the square root of the intensity of a given spot. The symbol color corresponds to the LSR velocity, as indicated in the inserted spectra. The vertical gray lines at the spectra indicate the systemic velocity (Hirota et al. 2022). The (0,0) point in 2019 corresponds to the coordinates given in Fig. 1 and in 2009 to the coordinates RA(J2000) = $18^{h}35^{m}08\overset{s}{.}12683$ and Dec(J2000) = $-7°35'03\overset{''}{.}7868$ (from the BeSSeL survey, EVLA, by Hu et al. 2016).

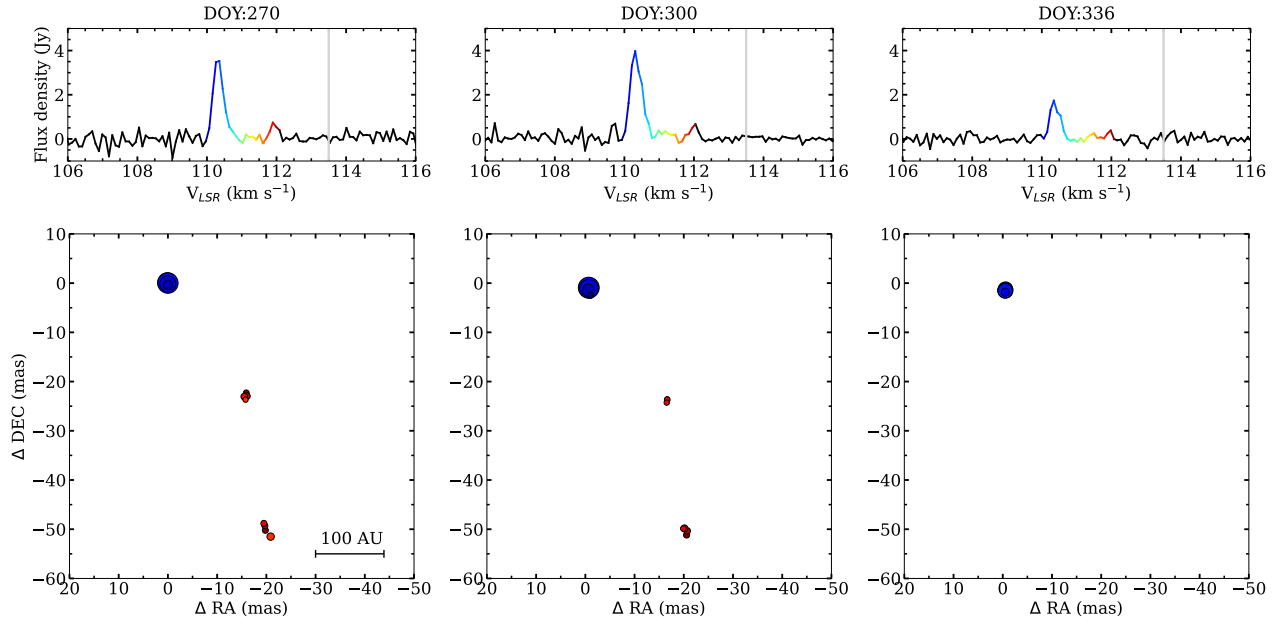

Fig. 3. VLBA maps of the 12.2 GHz methanol maser spots in G24 at three epochs. The size of the circles is proportional to the square root of the intensity of a given spot. The symbol color corresponds to the LSR velocity as indicated in the inserted spectra. The vertical gray lines at the spectra indicate systemic velocity (Hirota et al. 2022). The point (0,0) corresponds to RA(J2000) = $18^{h}35^{m}08\overset{s}{.}13433$ and Dec(J2000) = $-07°35'04\overset{''}{.}2806$, the position of the brightest spot at DOY: 270.

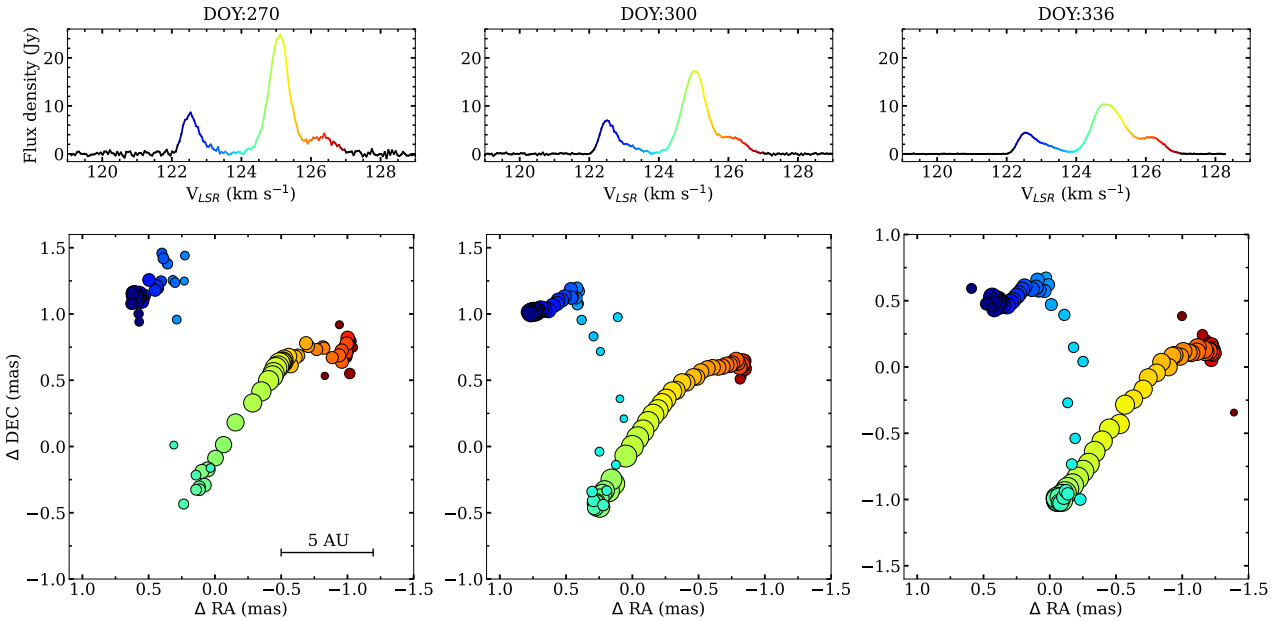

Fig. 4. Same as Fig. 3, but for 22.2 GHz water masers. The point (0,0) corresponds to RA(J2000) = $18^h35^m08^s.13231$ and Dec(J2000) = −07°35′04.″1447, the position of the brightest spot at DOY: 300. Coordinates for VLBA DOY: 270 are from VLBA DOY: 300 (see Sect. 2.2).

whole structure has also been constant over the last 10 yr with the values from 70° to 77°. The following analysis of the emission at the mas scale indicates that the brightness and size of individual cloudlets varied in phase with the flare profile.

In Table A.1, we list the following parameters of the 15 maser cloudlets detected in 2019: the LSR velocity of the brightest spot (V_p) and the projected area (i.e., the smallest rectangle that covers the whole emission, ΔRA×ΔDec); if the Gaussian fit of the emission spectrum is successful, the fitted peak velocity (V_{fit}), FWHM, and amplitude (S_{fit}). The Gaussian fits to velocity profiles of single maser cloudlets are presented in Fig. A.1. In addition, we calculated the values of the correlation coefficients of the linear fits to the spot positions on the sky plane (r_s) and to the LSR velocity change with position along the major axis of the spot distribution (r_v), as defined in Moscadelli et al. (2011). We used spots with a brightness above $15\times\sigma_{rms}$ at 6.7 GHz and $20\times\sigma_{rms}$ at 12.2 GHz and 22.2 GHz to calculate the above coefficients. In Table A.1 we present values when $r_s \geq 0.5$ and $r_v \geq 0.7$, meaning that the correlations are reliable. In such cases, we calculated the position angle (PA) of the major axis of the spot distribution using the least-squares fit and defined positive from N to E, and the velocity gradient (V_{grad}) measured as the maximum difference in velocity between spots divided by their distance. Similar to Moscadelli et al. (2011), we neglect the sign of the gradient for analysis.

We used the VLBA data to analyze the 6.7 GHz methanol cloudlet behavior during the flare, and the results are summarized in Table 3 and Fig. 5. Table 3 lists the total number of cloudlets (N_0), the number of cloudlets with single- or multiple-Gaussian velocity profiles (N), and the mean value of FWHM.

From the above analysis, we note that on DOY: 270, six cloudlets show single-Gaussian velocity profiles, and one shows a double-Gaussian velocity profile (Cloudlet 10). On DOY: 300, ten cloudlets show a single-Gaussian. Cloudlets 6, 9, and 10 show double-Gaussian profiles, while Cloudlet 11 is not detected. On DOY: 336, nine cloudlets show single and Cloudlet 10 shows double-Gaussian profiles. Cloudlets 13–15 are no longer detected (Table A.1). The FWHM values are constant

Table 3. Number of cloudlets and FWHM mean value for each epoch of VLBA observations.

DOY	N/N_0	mean FWHM (km s^{-1})
6.7 GHz		
270	7/15	0.24±0.04
300	13/14	0.18±0.02
336	10/11	0.20±0.02
12.2 GHz		
270	2/3	0.18±0.01
300	3/3	0.18±0.01
336	1/1	0.17
22.2 GHz		
270	2/2	0.35±0.01
300	2/2	0.40±0.01
336	2/2	0.43±0.01

on a timescale of ∼2 months during the flare. The VLBA data indicate that cloudlets 11, 13, and 14 are among the most variable, and they are located closest to the central object (Fig. 1), whereas the corresponding single-dish features showed a double profile during the 2011 flare (Fig. 6).

The typical projected size of an individual cloudlet (i.e., the diagonal of the area) is 3–4 mas (20–30 au; Table A.1), but there are more extended structures; for example, Cloudlet 12 is ∼10 mas (70 au) long. The cloudlets change their brightness and sometimes their size, while their velocity gradients are roughly constant (Fig. 5). In general, the cloudlets are the brightest at DOY: 300; this means that their S_{fit} were 60% and 40% greater than those at DOY: 270 and 336, respectively (Fig. 5). The sizes of the majority of the cloudlets are constant within the measurement accuracy, but Cloudlets 1, 6, 9, and 10 exhibit a gradual increase during the flare of ∼42%, ∼55%, ∼48%, and ∼78%, respectively, while Cloudlet 12 shrinks by ∼23% (Fig. 5). The

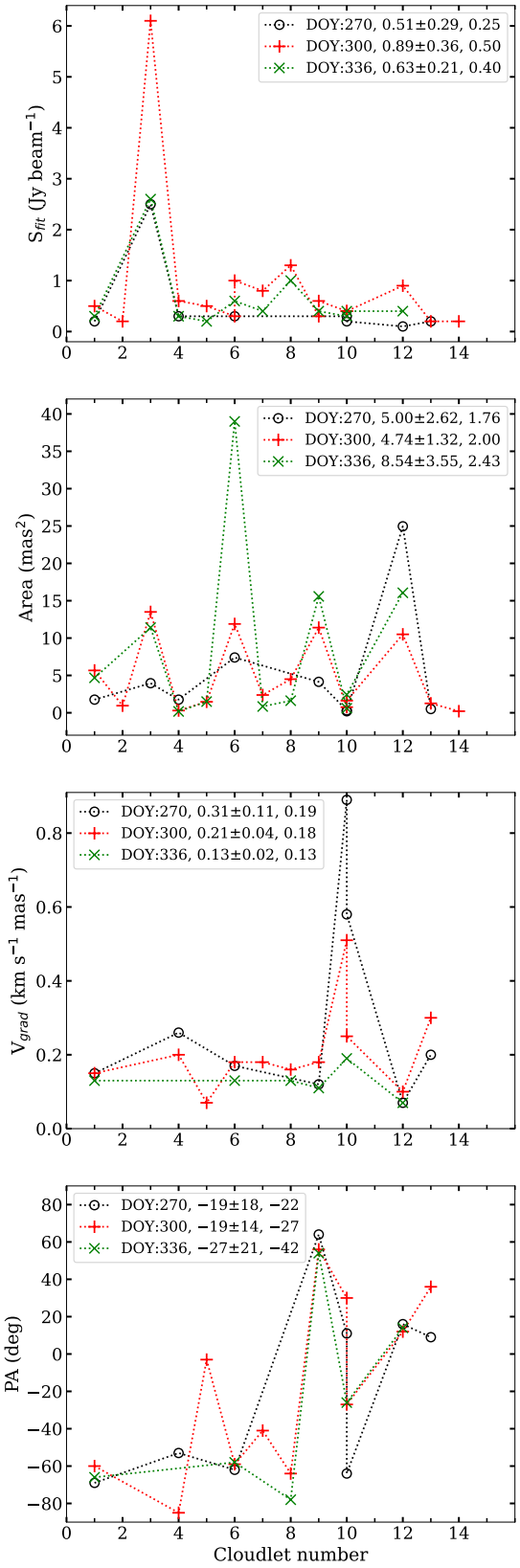

Fig. 5. Evolution of the VLBA 6.7 GHz methanol maser cloudlets listed in Table A.1. The mean of each parameter together with the standard error and the median value are given for each epoch.

swelling cloudlets do not change their brightness and tend to lie farther from the central object.

The correlation coefficients of the linear fit to the spot positions on the sky plane and to the LSR velocity variation with position (r_s, r_v) are listed in Table A.1. The cloudlets exhibit commonly linear or elongated structures with high correlation coefficients in all the maps with the three instruments and are remarkably stable over two months during the flares. The maps of sample cloudlets are shown in Fig. A.4. Cloudlet 3 represents a case of arched morphology, the best resolved with VLBA at DOY:300. Cloudlet 4 has a barely resolved structure resulting in uncertain estimates of correlation coefficients. For all the cloudlets we note the effect of probing more extending emission by the EVN and LBA compared to the VLBA. We conclude that the morphology of 6.7 GHz maser cloudlets is generally preserved on a two-month timescale during the flare.

3.1.2. 12.2 GHz

A similar analysis of cloudlet parameters was done for the 12.2 GHz methanol transition during the 6.7 GHz flare (Fig. A.2, Table A.2). We identified three 12.2 GHz cloudlets, which are numbered from south to north (Fig. 1). A Gaussian profile is successfully fitted to each cloudlet at all the epochs, except for Cloudlet 1 at DOY: 270. The mean and median FWHMs are similar to the FWHMs of the 6.7 GHz profiles (Table 3). The projected size of the cloudlet is typically 1.5 mas (10 au), which is comparable with the beam size, and a linear morphology is usually visible. The cloudlets display considerable variability; Cloudlets 1 and 2 are detected only at DOY: 270 and DOY: 300, whereas Cloudlet 3 is present at all three epochs (Table A.2, Fig. A.5). The intensity and size of Cloudlet 3 decreased at the last epoch (DOY: 336) by a factor of two compared to the values measured at the first two epochs.

3.1.3. 22.2 GHz

The parameters of the 22.2 GHz water maser cloudlets are presented in Figs. A.3 and A.6 and in Table A.3. Two cloudlets identified in the 22.2 GHz water maser line occurred at all three epochs and always showed double-Gaussian velocity profiles. The profiles are broader than the methanol line profiles (Table 3). We note a systematic increase in the brightness of all the profiles by a factor of 1.3–3.2 during the VLBA observations. The structure of Cloudlet 1 (southern) elongated at PA of about −45° is stable, and shows a clear velocity gradient of ~2 km s^{-1} mas^{-1} (~0.3 km s^{-1} au^{-1}). Furthermore, it exhibits a velocity drift of −0.17 km s^{-1} month^{-1}. Cloudlet 2 (northern) is complex, and its size increased by a factor of 2 over the 66 days (Fig. A.6).

3.2. Long-term variability

In the 6.7 GHz maser single-dish data, there are four intermittent velocity features (107.6, 108.3, 114.1, and 116.6 km s^{-1}) whose intensity was above the 3σ detection limit for specific time intervals. The light curves of these four intermittent and eight persistent spectral features of the 6.7 GHz methanol maser are presented in Fig. 6. The overall picture of variability is shown in Fig. A.7. The major flares of the strongest features at 113.5 and 115.3 km s^{-1} are preceded by small variations in amplitude (Fig. 7). The periodogram of the light curve of 115.3 km s^{-1} calculated for the time interval of MJD 57482−58620 implies a periodicity of 6 months. The pre-flare variability is synchronized for all features, but differs significantly between the 2011 and 2019 events. This may be related to pulsation of powering

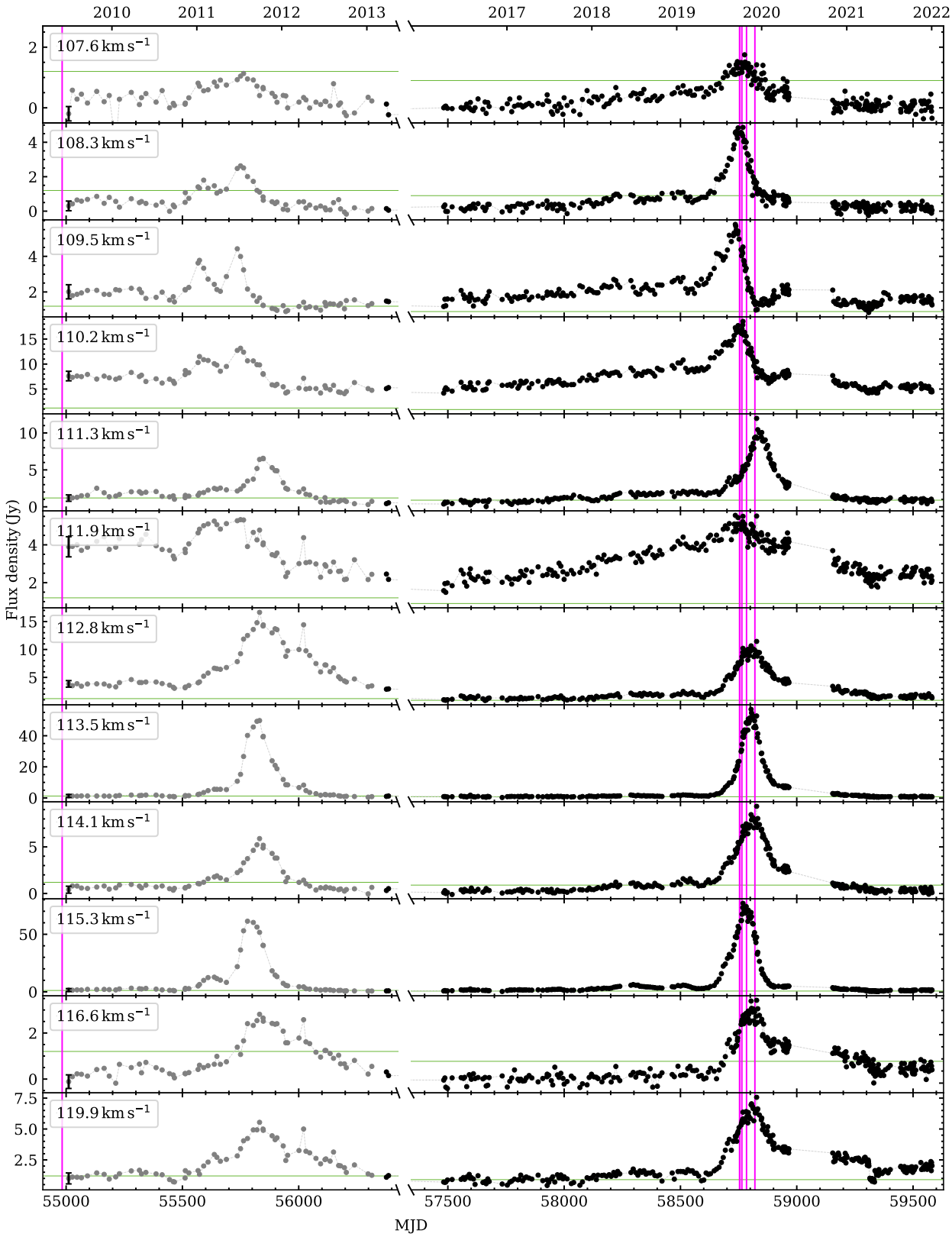

Fig. 6. Light curves of the 6.7 GHz methanol maser features. The typical 3σ noise level is shown as the green horizontal line. The observational data from before March 2013 (gray dots) were published in Szymczak et al. (2018a). The typical measurement uncertainty is shown by the bar for the first data point of each curve. No observations were made in the period of 56387<MJD<57482. The vertical magenta lines indicate the epochs of the VLBI projects presented in this paper.

HMYSO postulated by Inayoshi et al. (2013). The general flare profiles of strong features appear to be similar in the two flare events, which peaked in August 2011 and November 2019, in contrast to most of the weak features. Considering the brightest feature at the LSR velocity of 115.3 km s^{-1}, we estimate that the 2019 flare lasted 280±3 days.

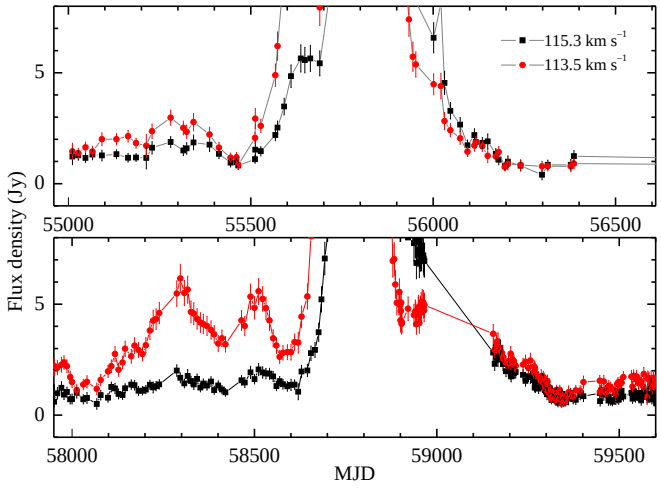

Fig. 7. Magnified images of selected parts of light curves of the two strongest features highlighting an oscillating flux variation before the flares.

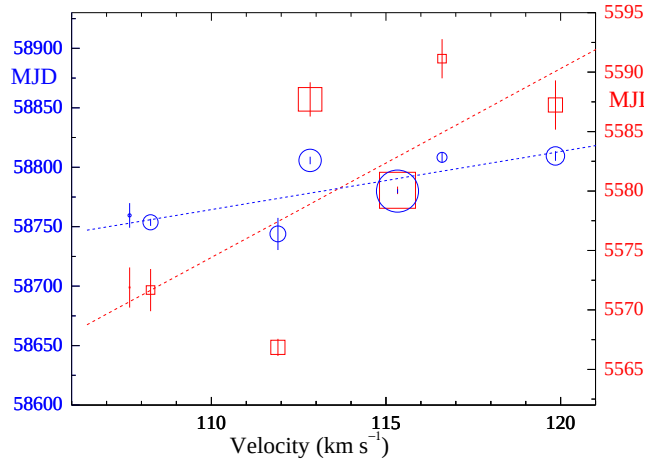

Fig. 8. Dates of the flux density maxima of the maser spectral features at 6.7 GHz at the first (red) and second (blue) flare events in 2011 and 2019, respectively. The symbol sizes are proportional to the logarithm of the flux density and the vertical bars indicate the fivefold standard error of the peak flare time maxima. The dashed lines denote the best fits to the data.

The time of the flux maximum was calculated by fitting a skewed Gaussian function using the method `CURVE_FIT` from the `SCIPY.OPTIMIZE` package (Virtanen et al. 2020), for the features shown in Fig. 6, except for those with double peaks (108.3, 109.5, and 110.2 km s^{-1}). The average flux density-weighted interval between the two flares is 2982±12 days. We checked whether each feature in the single-dish spectrum has a counterpart in the cross-correlation spectrum and a unique cloudlet in the VLBI map. It appeared that the emission of eight features (119.9, 116.6, 115.3, 112.8, 111.9, 109.5, 108.3, and 107.6 km s^{-1}) in the autocorrelation spectrum unequivocally emerge from Cloudlets 1–3, 9, 10, 13, 14, and 15 (Fig. 1). The remaining single-dish features are the effect of emission blending from spatially different cloudlets. There are two features at 111.23 and 114.1 km s^{-1} that were not detected with VLBI, indicating that their emission comes from extended structures resolved by the VLBI beam. The results of time lag estimates are summarized in Fig. 8. For the 2019 flare, the time lag of the flare peaks of the features at two extreme velocities of 107.6 and 119.9 km s^{-1} is 59.5±4.2 days. For the 2011 flare, the time lag

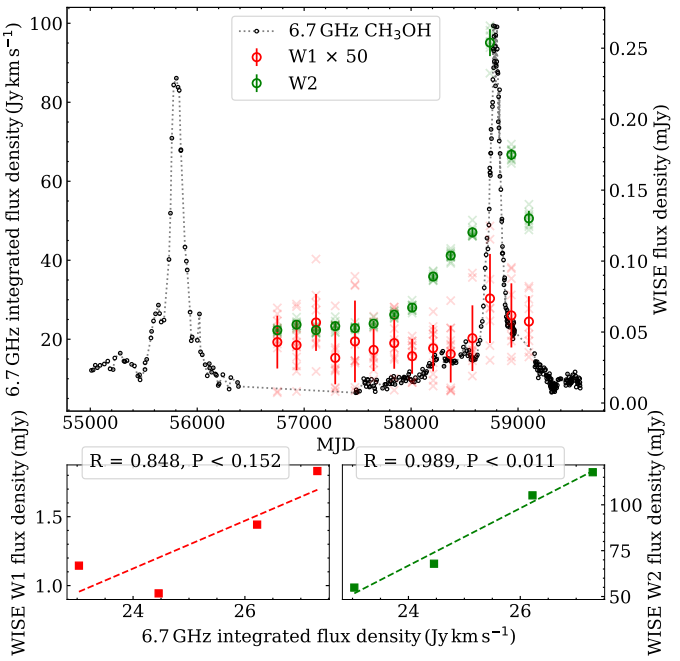

Fig. 9. WISE W1 and W2 photometric measurements superimposed with 6.7 GHz CH$_3$OH maser integrated flux density. Circles indicate the values of the WISE measurements for every epoch; transparent crosses indicate the singular WISE photometric measurements. The error bars correspond to standard deviation. Only measurements with cc_flags of 0 (unaffected by known artifacts) or h (possible contamination by scattered light from a nearby bright source), and qual_frame values no lower than 5 (high image quality) are shown. Two bottom panels show 6.7 GHz integrated flux density vs. WISE singular measurements. Here, a stricter quality criterion was also used: only ph_qual of A (source detected in this band with $S/N > 10$). Values in the boxes are Pearson correlation coefficients.

estimates are highly scattered and the average lag is almost a factor of three higher. The first flare was probed with low cadence and is discarded in further analysis because the errors of the time lags are higher than those for the 2019 epoch (Sect. 4.4).

3.3. The Wide-field Infrared Survey Explorer (WISE) observations

Photometry in the W1 (3.4 µm) and W2 (4.6 µm) bands, as well as astrometry for G24 from the WISE (Wright et al. 2010) and subsequent NEOWISE (Mainzer et al. 2014) missions, were retrieved from Infrared Science Archive[5] (IRSA) covering observations until the end of 2020. A saturation correction was applied[6] to account for a photometric bias due to the detector warm-up. The (NEO)WISE infrared (IR) fluxes rose along with the methanol flare, as pointed out by Hirota et al. (2022). NEOWISE W1 and W2 photometric measurements superimposed with 6.7 GHz CH$_3$OH maser integrated fluxes are shown in Fig. 9, accompanied by plots revealing the clear correlation between the maser and the IR flux for both bands. This is expected for the radiative excitation of this maser transition.

In Fig. 10, we present the mean centroid positions of the 4.6 µm emission from G24 and two adjacent objects for each epoch, spanning approximately 10.5 yr. The centroid distribution of G24 is clearly different from that of the comparison objects. It

[5] `https://irsa.ipac.caltech.edu`
[6] See `http://wise2.ipac.caltech.edu/docs/release/neowise/expsup/sec2_1civa.html`

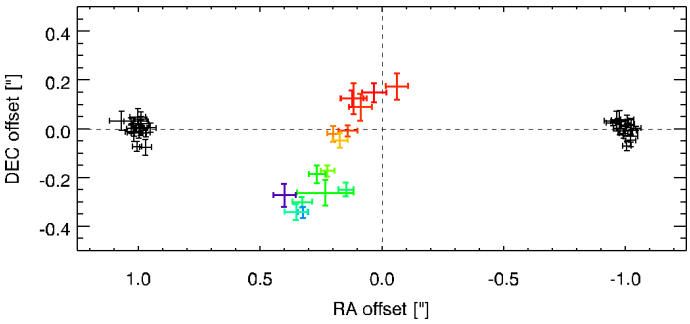

Fig. 10. Offsets from the overall mean position for each epoch for G24 (colored symbols) and two adjacent objects of similar brightness (black, shifted by ±1″ in right ascension for clarity). Colors indicate the W2 brightness (dark blue for the brightest state and red for the dimmest). The size of the symbol corresponds to the 1σ uncertainty. The intersection of the dashed lines gives the ALMA reference position of Hirota et al. (2022).

is resolved and aligned with the outflow orientation (see Fig. 11). During the dim state, the 4.6 μm centroid is closer to the ALMA reference position, while it moves by ∼0.″5 to the southeast along the outflow direction during the brightening of the source.

4. Discussion

4.1. Evidence of a disk-jet system

Linear structures in the 22.2 GHz water maser distribution around massive protostellar objects can be indicative of the presence of a bipolar outflow or jet (Chibueze et al. 2012; Burns et al. 2016). Figure 11 shows an overlay of the ALMA 229.758 GHz class I methanol maser line (gray contours) on the 1.3 mm dust continuum in grayscale (see also Hirota et al. 2022). The green filled circle represents the position of the 22.2 GHz water maser emission (to the west of the continuum source), while the red ellipse indicates the position of the Q-band ionized jet reported by Purser et al. (2021). The dashed line connects the prominent northwest and southeast knots of the 229.758 GHz class I methanol maser line through the center of the dust core cutting through the ionized jet axis and the water maser position. The northwest–southeast morphology of the ALMA 229.758 GHz CH_3OH emission is indicative of the presence of a bipolar outflow in G24 along the axis marked by the dashed line. The inset in Fig. 11 shows that the 22.2 GHz water masers are aligned along the same axis (black dashed line) of the ALMA class I methanol emission. The water maser could trace either the compact inner component of the bipolar outflow or a jet structure within G24. The PA of the axis of the jet–outflow, as indicated by the dashed lines in Fig. 11, is about −44°. The PA of the axis of the jet is similar to the PAs of water maser Cloudlets 1 (see Fig. 4 and Table A.3). This could be an indication that this cloudlet is excited by the ionized jet (Chibueze et al. 2012). We note that some of the 6.7 GHz methanol maser features used in the Keplerian disk model presented in Sect. 4.3 do not fit well, which could be attributed to the influence of the jet. Neglecting the weaker maser spots, cloudlets 1 and 2 have similar PAs, and the difference in the V_{LSR} of the two cloudlets could be attributed to jet rotation. Precession of the jet or rotation of the outflow could be responsible for the water maser excitation and the observed differences in the V_{LSR}. The Q-band jet (∼ 100 mas in size; Purser et al. 2021) has a knot at the northwest end. This knot is slightly south of the jet axis, and could be an indication of precession and/or rotation.

In agreement with the above, the ALMA 229.758 GHz CH_3OH emission is a maser line which traces the outflow cavity wall, while the 229.589 GHz CH_3OH emission is thermal emission tracing the rotation disk structures around the protostar. The eastern elongation of the 229.758 GHz CH_3OH emission could be an indication of the fragmentation of the rotating disk structure and/or spiral arm system. The position angle of the Keplerian disk is 15° ± 3°, as traced by the 229.589 GHz CH_3OH emission (see Fig. 11; Hirota et al. 2022), this is roughly perpendicular to the average of the position angles of the water masers, indicating a disk-jet–outflow system in the protostar.

4.2. Diversity of kinematics traced by the water and methanol masers

The water maser Cloudlet 1 lies on the sky within 7 mas (∼50 au) of the 6.7 GHz methanol maser Cloudlet 4, but the separation in the velocity is ∼3 km s^{-1}. This is different from the case in G31.581+00.077 presented by Bartkiewicz et al. (2012), where both masers appeared at the same LSR velocity (within 0.1 km s^{-1}), but they were separated by 133 au, (considering the distance to the source of 5.5 kpc; Reid et al. 2019). Similarly Darwish et al. (2020), toward the region IRAS 19410+2336, found methanol and water masers separated by ∼205 au and only by ∼0.17 km s^{-1} in the velocity. In G24 the velocity difference implies the physical separation of the two maser species and confirms that these masers probe different parts of the environment of HMYSO, which is strongly consistent with theoretical models showing that these two maser transitions require different physical conditions for the pumping (Cragg et al. 2005; Gray et al. 2022).

Two 12.2 GHz methanol maser cloudlets coincide with the positions of 6.7 GHz methanol masers. The 12.2 GHz Cloudlet 3 and the 6.7 GHz Cloudlet 12 with the peak at the LSR velocity of ∼110.2 km s^{-1} coincide within 1.8 mas in RA and 1 mas in Dec in the VLBA images taken simultaneously in both transitions at three epochs. That is well within the position uncertainties of a single maser spot at each transition (Sect. 2.1.1). Moreover, they both become weaker with time (Figs. 3 and 2). This indicates that the 6.7 and 12.2 GHz lines originate in the same gas volume. Similarly, the 12.2 GHz Cloudlet 1 and the 6.7 GHz Cloudlet 10 with the peak at the LSR velocity of ∼111.9 km s^{-1} coincide within 0.5 mas in RA and in Dec in the two first VLBA epochs DOY: 270 and 300. On DOY: 336 the 12.2 GHz emission in Cloudlet 1 was not visible, with an upper limit of 30 mJy (Fig. 3). The corresponding 6.7 GHz Cloudlet 10 was very weak on this date.

To compare the intensities of the two transitions in the two cloudlet sets, we created images with a similar spectral resolution by averaging two channels at the 12.2 GHz maser lines, and with the same circular synthesized beams of 6 mas×6 mas. Single-channel images for DOY: 300 are presented in Fig. 12 for both cloudlet groups. The ratios of the flux densities to the lower limits of brightness temperatures are presented in Fig. 13. The maximum uncertainties of these ratios were calculated using the total differential method, assuming 50% and 10% uncertainties in the flux densities at 12.2 and 6.7 GHz, respectively. The brightness temperature (T_b) is calculated according to Eqs. (9)–(27) in Wrobel & Walker (1999). Co-propagation of both methanol maser transitions is predicted in a broad range of physical conditions considering gas temperature and density by Cragg et al. (2002, 2005). These conditions are characterized by a relatively large difference between the temperatures of the pumping dust emission and the masering gas, which may arise

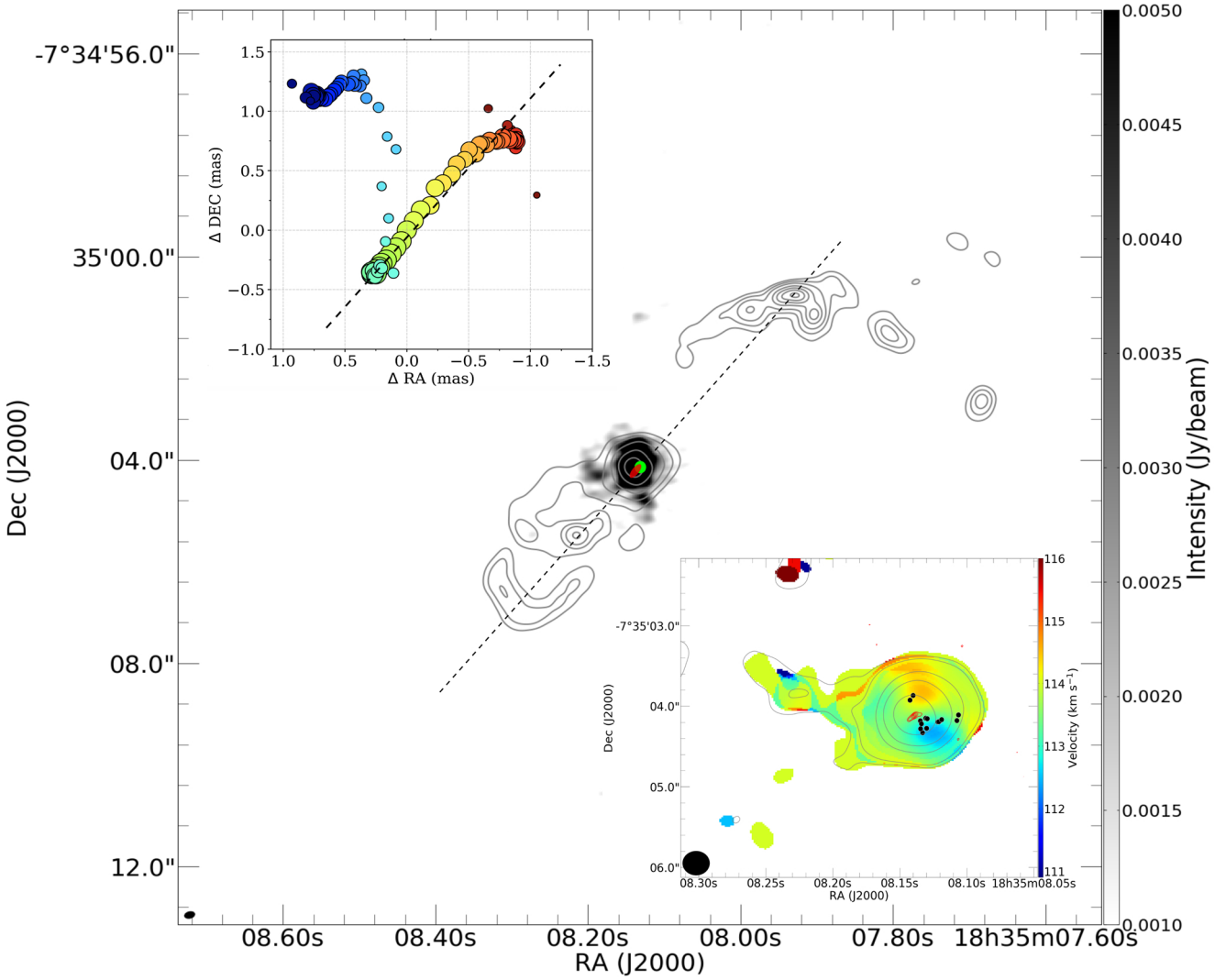

Fig. 11. Aligned large-scale and compact bipolar outflow. The grayscale background represents ALMA 1.3 mm dust continuum emission of G24, while the gray contours (levels: [0.2, 0.5, 1, 2, 3, 4, 5, 6] Jy beam^{-1} km s^{-1}) represent the moment 0 (integrated intensity) map of the 229.758 GHz class I CH_3OH maser line. The red ellipse (same as red contours in the bottom right inset) indicates the position of the 7 mm (Q-band) ionized jet reported in Purser et al. (2021) and elongated along the axis of the ALMA CH_3OH line and the VLBA 22.2 GHz water maser linear structure (top left inset). The green filled circle represents the position of the water masers in G24. The top left inset is the VLBA DOY: 336 epoch of the water maser (see Fig. 4). The dashed lines show the axes of the large-scale (in the ALMA image) and compact (in the VLBA water maser map) outflows driven by G24. The position angle derived from the ALMA millimeter data is ∼136°. The bottom right inset shows the ALMA moment 1 map of the 229.589 GHz CH_3OH line with its moment 0 maps overlaid as contours (levels: [0.04, 0.08, 0.5, 1, 2] Jy beam^{-1} km s^{-1}). The VLBI DOY: 270 positions of the 6.7 GHz methanol masers are represented by the black filled circles.

due to the flare nature of accretion onto a young star formed in G24. This difference appears because the heating of the dust occurs due to the emission of the accretion flare while the gas in this case is heated by collisions with the dust and has a considerable time lag. In our data, we do not find cases where the brightness temperature of the 12.2 GHz transition exceeds that of the 6.7 GHz, which is entirely consistent with the modeling results of Cragg et al. (2005). The variability of the two transitions is synchronized, as predicted by the model. It is interesting that the 12.2 GHz Cloudlet 2 that is visible in DOY: 270 and DOY: 300 appeared without 6.7 GHz counterpart detected within an upper limit of 210 mJy beam^{-1} (3σ). This value is higher than the flux values of the detected 12.2 GHz Cloudlet 2. So, this does not describe a contradiction with the model of Cragg et al. (2005).

4.3. Keplerian model: derivation of disk inclination

We fitted the 6.7 GHz maser positions projected along the disk major axis (PA = 15°), perpendicular to the axis of the radio jet: the slice along the line connecting RA(J2000) = $18^h35^m08\overset{s}{.}125$, Dec(J2000) = −07°35′04.″5 and RA(J2000) = $18^h35^m08\overset{s}{.}145$, Dec(J2000) = −07°35′03.″5). Using the peak position of the dust continuum as the YSO position (P_0), we fitted the maser positions (P_j), along the slice, and $V_{\rm LSR}$, (V_j) to a Keplerian rotation profile around a central mass ($M_{\rm core}$; 8.8 $M_\odot$ from Hirota et al. 2022) and line-of-sight inclination (i) using

$$V_j = V_{\rm sys} \pm \sqrt{\frac{G\,M_{\rm core}}{P_j - P_0}}\ \sin\, i, \qquad (1)$$

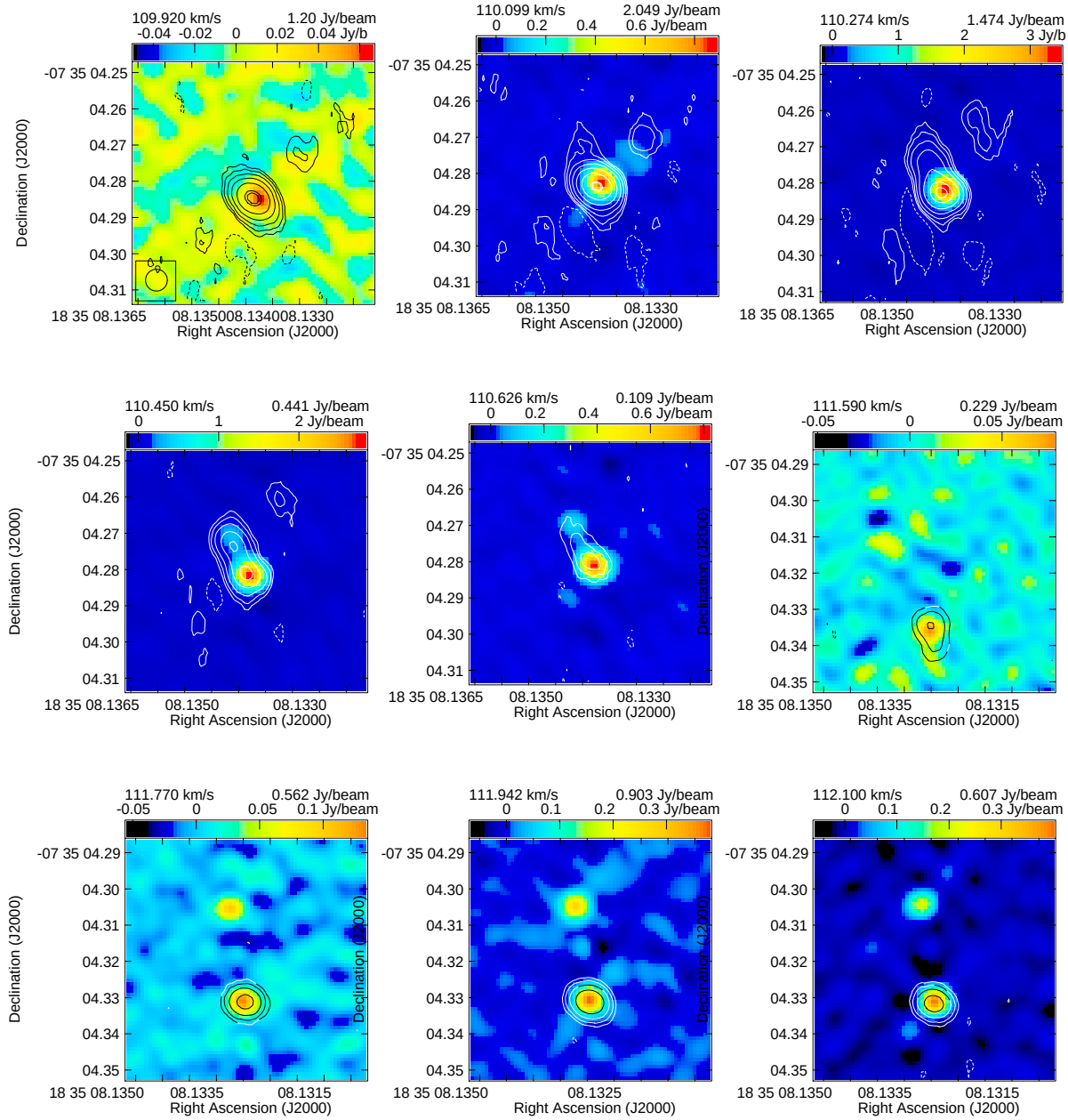

Fig. 12. Channel images showing co-propagation of 6.7 and 12.2 GHz methanol masers obtained at DOY:300. The first five images at velocities of 109.92 to 110.63 km s^{-1} represent 6.7 GHz Cloudlet 12 and 12.2 GHz Cloudlet 3, while the next four images show Cloudlets 10 (6.7 GHz) and 1 (12.2 GHz) for the velocity range of 111.59–112.10 km s^{-1} (Tables A.1 and A.2). Contours represent the 6.7 GHz methanol maser emission; the first contour corresponds to 30 mJy beam^{-1} ($\sim 3\sigma_{\rm rms}$). The next contours are at 2, 4, 8, 16, 32, 64, and 128 times $3\sigma_{\rm rms}$. The first negative contour is also shown, and the contour at the 90% of the peak emission. The numbers at the top of each panel correspond to the LSR velocities of each spectral channel and the peak intensity of the 6.7 GHz methanol maser emission. The color scale presents the 12.2 GHz methanol emission with ranges as indicated at the top of each map in Jy beam^{-1}.

where G is the gravitational constant, P_j–P_0 is the radius from the center of the disk (inner radius of 10 au and outer radius of 120 au), $V_{\rm sys}$ = 114.5 km s^{-1} is the systemic velocity of the core, and i varies from 0° to 90° in steps of 5°. The range of inclination is chosen to cover edge-on and face-on cases (Seifried et al. 2016). Figure A.8 shows the result of the Keplerian rotation fit, corresponding to the best fit inclination angle of 85° ± 3°. Our best fit at the inclination angle of 85° falls within the range of angles where a recognizable Keplerian disk rotation profile is observable for edge-on disks (Seifried et al. 2016). The outcome of our Keplerian disk rotation fit indicates that the 6.7 GHz methanol masers are tracing the inner part of the disk enclosing a significant fraction of the mass. However, we note that the result depends on the sensitivity of the interferometric observations used in making the maser map. Non-detection of outward red- or blueshifted maser features may have impacted our findings. Dodson et al. (2004) observed that masers can be several au to 10s of au in size. Very long baselines could resolve out slightly extended maser features. Therefore, more sensitive maser mapping observations, especially sensitive to extended maser emission, will be required to improve our fit results.

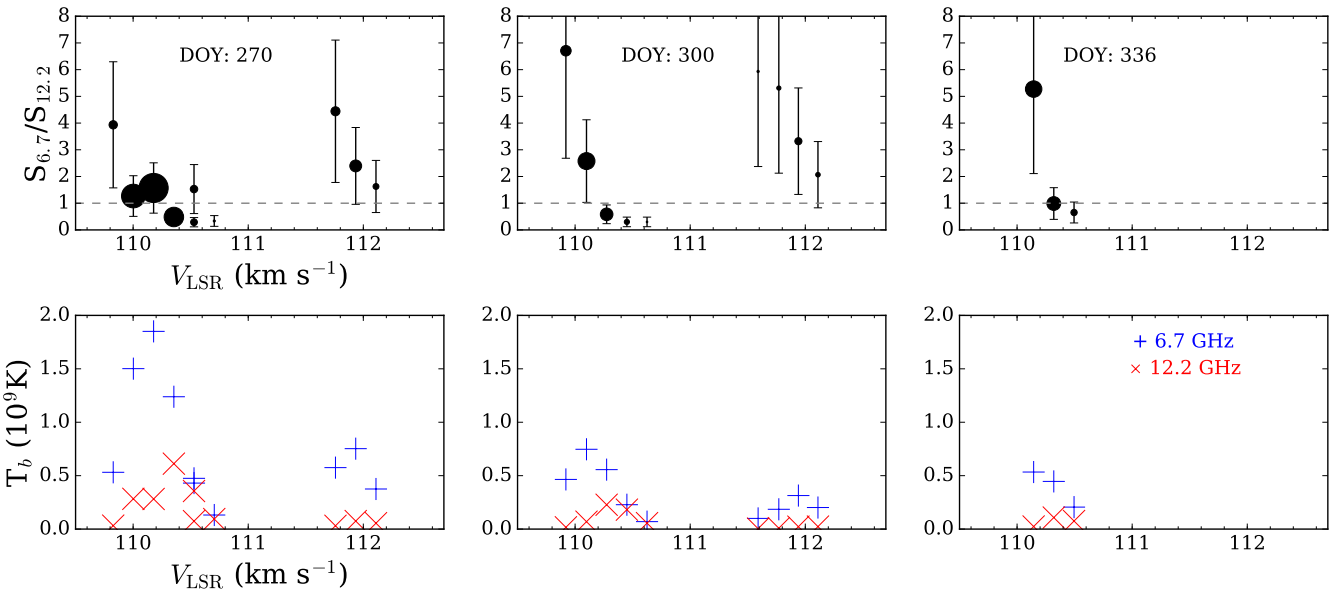

Fig. 13. Details of co-propagating 6.7 and 12.2 GHz methanol masers through the same gas volume. *Top:* ratios of flux densities. The size of the circles is proportional to the flux density of the 6.7 GHz emission. *Bottom:* brightness temperatures of co-propagating spots.

4.4. Maser internal structure with respect to source kinematics

Considering the pre-flare data obtained in 2009, we attempted to identify cloudlets that persisted over 10 yr. As we mention above, the 2009 data show three masing regions, to the NE, W, and SE. Assuming the same persistent LSR velocities, as we did not notice any velocity drifts, we note that the NE masers correspond to the 2019 epoch Cloudlet 3, the W masers have a position similar to that of Cloudlet 9, while the SE masers correspond to Cloudlets 10 and 12 (Fig. 2). For proper motion analysis, we determined the barycenters, weighted by the spot brightness, of individual cloudlets, as in Bartkiewicz et al. (2020). Relative motions with respect to the barycenters do not show any obvious and regular motions indicating expansion, infall, or rotation with an accuracy of 6 mas over 10 yr, corresponding to an upper limit of velocity of 19.1 km s^{-1}. The main difference between the 2009 and 2019 epochs is the appearance of new maser features, in particular to the S and W where the redshifted spots are located. We found Gaussian characteristics in eight velocity profiles of ten cloudlets seen in 2009 (Table A.4). The average and median FWHM values in 2009 were 0.14±0.01 km s^{-1} and 0.14 km s^{-1}, respectively, and they were smaller than in 2019 (0.18–0.24 km s^{-1} and 0.17–0.21 km s^{-1}). These values are two times smaller than the typical values of FWHMs in the sample presented in Bartkiewicz et al. (2016). In 2019 VLBA DOY: 270, the spectral feature at the LSR velocity of 115.3 km s^{-1} dominated the 6.7 GHz spectrum with the flux density of 20.9 Jy and it decreased by a factor of two after 66 days (Fig. 2). We note that it was the weakest feature in 2009 in the interferometric and single-dish observations.

A detailed analysis of the 6.7 GHz methanol maser cloudlets distribution shows a diverse behavior of these mas structures on a three-month timescale. Cloudlet 3 shows a remarkable arched and stable emission structure with the same velocity gradient in all five epochs. Cloudlets 1, 6, and 9 show a linear morphology of increasing length and preserved PAs over two months (see Cloudlet 6 in Fig. A.4 for example). It suggests that the flare causes an increase in the gas volume where the maser amplification takes place. In Cloudlet 12, the PA was stable,

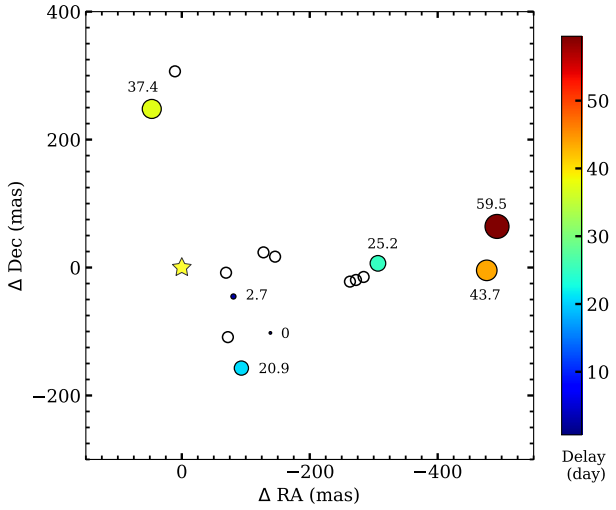

Fig. 14. Map of the 6.7 GHz methanol maser cloudlets detected with VLBA at DOY: 270. The time lags as fitted to the 32 m telescope measurements (Fig. 8) are marked by color and circle size, as indicated in the wedge. The size of symbols is proportional to the square root of delay. Cloudlets without meaningful measurements are marked as open circles. The yellow star is as in Fig. 1.

but the structure shrank, suggesting a reduction in the gas volume sustaining the maser amplification. There is a hint that some cloudlets may have changed their orientation during the observing period. For instance, monotonic changes in the PA of Cloudlet 4 might indicate the occurrence of ordered motion (Table A.1, Fig. A.4). Similar variations may have occurred in Cloudlets 2, 13, and 14, but the emission is too weak to draw a firm conclusion. These cloudlets are close to the central object, while those preserving PAs lie at farther distances (Fig. 1). We note a general trend that the PA of the W cloudlets is roughly −70°; the exception is Cloudlet 9, which persisted 10 yr and whose PA is close to the PA of the whole structure. The remaining cloudlets in W (Cloudlets 1, 4, 6, 7, and 8) appear during the flare, and their PAs are perpendicular to the PA of the whole

structure. The PAs of the SE cloudlets are typically ∼17°, which may indicate a large-scale order.

Figure 14 shows the distribution of 6.7 GHz cloudlets where the symbol size is proportional to the fitted time lags shown in Fig. 8. One of the cloudlets nearest to the central object is chosen as the reference. There is a clear trend of increase in the time lag with projected distance from the central star, implying, for the assumed distance of 7.2 kpc, propagation of excitation conditions at 0.3–0.5 the speed of light. For a simple disk–envelope model with a diameter comparable to the measured size of the 6.7 GHz maser structure of 3500 au (Fig. 1) the maximum time lag of 59.5 days indicates that thermal heat inducing the maser flare propagates on average at 0.33 the speed of light. Our VLBI maps prove that this process does not affect the morphological structure of the 6.7 GHz maser on a two-month timescale. It is in contrast to the extreme transformation of 6.7 GHz maser morphology on a 26-day timescale reported in accreting HMYSO G358-MM1 that has been interpreted as an effect of propagation of thermal infrared radiation at 0.04–0.08 the speed of light (Burns et al. 2020). We suggest that the flare in G24 is induced by an episode of enhanced production of infrared photons, but much less energetic than those observed in G358-MM1 and S255-NIRS3, likely triggered by accretion bursts (Burns et al. 2020; Moscadelli et al. 2017).

Considering the 12.2 GHz methanol maser emission, we note that only Cloudlet 3 was visible during all three epochs of VLBA observations. Its structure and velocity gradient persisted, but the flux density decreased (Fig. A.5). The remaining cloudlets at this transition gradually dimmed and disappeared at DOY: 336.

The 22.2 GHz water masers showed stable structure with velocity gradient over two months with emission between Cloudlets 1 and 2 at the intermediate LSR velocities (Fig. A.6). Therefore, we state that during the flare, the majority of 6.7 and 12.2 GHz masers are not destroyed, but they brighten or dim. Furthermore, the 6.7 GHz methanol masers showed the peak of the emission on DOY: 330, which is different from the 22.2 GHz water cloudlets that systematically increased in their intensities during the flare reaching the maximum at DOY: 336. We performed a proper motion analysis similar to that for the 6.7 GHz methanol maser emission, and we state that the two elongated structures remained at a distance from each other at the level of 0.08 mas during 66 days, corresponding to an upper limit in velocity of 0.26 km s^{-1}.

4.5. Time-dependent IR position shift

The temporal brightening of a YSO due to an accretion burst may lead to an echo seen in scattered light, for example, as in the case of S255IR-NIRS3 (Caratti o Garatti et al. 2017), or thermal emission. Because of the lower optical depth in the outflow cavities, photons will preferentially propagate along them. Only for an outflow in the plane of the sky does the centroid location remain unchanged during light propagation. In general, the projected distance of the light travel path is larger for light scattered from the lobe facing toward the observer. For the receding lobe, the light will travel backward first, and only then will it be scattered into the line of sight. Thus, the projected distance will be smaller. Moreover, since back scattering off dust grains is less efficient than forward scattering, the echo from the receding lobe will be fainter. Both effects lead to a displacement of the light centroid along the blueshifted cavity lobe. A temporal centroid shift caused by a light echo has been observed in the case of G107.298+5.639 (Stecklum et al. 2018).

For G24 the centroid shift of about 0.″5 amounts to 3600 au at the assumed distance of 7.2 kpc, which corresponds to a light travel time of approximately 20 days. So, if the shift during 10.5 yr was due to a light echo, it must be highly subluminal. Such a slowdown of the light propagation would require extremely high optical depths over this distance, which is unrealistic. Furthermore, the offset of the 4.6 μm position from that of the dust continuum measured with ALMA (Hirota et al. 2022) is smaller during the dim state between the flares and greater during the brightness peak. This is opposite to what has been observed for the light echo of G107.298+5.639 (Stecklum et al. 2018). Since the comparison of the G24 centroid positions to those of neighboring objects rules out an instrumental origin, the reason for the observed shift remains open.

5. Conclusions

We imaged the 6.7 and 12.2 GHz methanol masers and the 22.2 GHz water maser in HMYSO G24 during the 6.7 GHz maser flare in 2019 and monitored the target in the 6.7 GHz transition with the 32m telescope.

The 6.7 GHz masers are spread over an area of ∼3500 au, whereas the 12.2 GHz maser region is an order of magnitude smaller. The 12.2 GHz maser cloudlets coincide with those at the 6.7 GHz transition, supporting the standard models with a broad range of gas temperatures and densities of maser environments. The 22.2 GHz masers located in the central region do not co-propagate with the methanol masers and could trace the base of bipolar outflow or jet observed with ALMA. The 6.7 and 12.2 GHz methanol masers lie in the inner part of the rotating disk revealed by ALMA.

The maser cloudlets in G24 commonly show a clear velocity gradient and linear or elongated morphology that, for most of them, is preserved over approximately two months of VLBI observations during the 6.7 GHz flare. The brightness of the methanol cloudlets varies synchronously with the total 6.7 GHz maser flux density monitored with the single dish. In contrast, the water cloudlets gradually increase with moderate changes in size and orientation and a velocity drift of −0.17 km s^{-1} month^{-1} was observed for the strongest 22.2 GHz cloudlet. The sizes of specific 6.7 GHz cloudlets increase at the flare maximum, which can be caused by changes in gas volume that favor maser emission. The observed variations in brightness and size of the methanol cloudlets are fully consistent with the radiative scheme of excitation of the methanol maser transitions indicated by a high correlation of the 6.7 GHz and 4.6 μm flux densities found in G24.

The estimates of time lags of the flux density maxima of 6.7 GHz features, together with the map of counterpart cloudlets, reveal that a change in physical conditions causing the maser flare propagates at one-third the speed of light. It can be a thermal heat wave postulated to explain dramatic changes in the 6.7 GHz maser structure in accretion bursting HMYSOs (Burns et al. 2020). We state that the overall maser structure in G24 is stable on a 2-month timescale. Furthermore, comparison with the archival map taken in a quiescent state (i.e., before the discovery of the first flare), and proper motion analysis does not reveal any signs of expansion or infall within ∼6 mas on a 10 yr timescale.

The high similarity of the flare profile in 2011 and 2019 suggests that G24 may be a long-period (∼8.2 yr) maser source and can be a good objective for further testing of the causes of variability, and more generally the causes of the accretion bursts.

Acknowledgements. We acknowledge the useful discussions about astrometry with Dr. Anita Richards from the Jodrell Bank Centre for Astronomy, University of Manchester. The 32m radio telescope is operated by the Institute of Astronomy, Nicolaus Copernicus University and supported by the Polish Ministry of Science and Higher Education SpUB grant. A.B., A.K., M.S., M.D., P.W. acknowledge support from the National Science Centre, Poland through grant 2021/43/B/ST9/02008. TH is financially supported by the MEXT/JSPS KAKENHI Grant Numbers 17K05398, 18H05222, and 20H05845. M.O. thanks the Ministry of Education and Science of the Republic of Poland for support and granting funds for the Polish contribution to the International LOFAR Telescope (arrangement no. 2021/WK/02) and for maintenance of the LOFAR PL-612 Baldy (MSHE decision no. 28/530020/SPUB/SP/2022). O.B. acknowledges financial support from the Italian Ministry of University and Research – Project Proposal CIR01_00010. This work was supported by resources provided by the Pawsey Supercomputing Centre with funding from the Australian Government and the Government of Western Australia. This publication makes use of data products from the Near-Earth Object Wide-field Infrared Survey Explorer ((NEO)WISE), which is a joint project of the Jet Propulsion Laboratory/California Institute of Technology and the University of Arizona. (NEO)WISE is funded by the National Aeronautics and Space Administration.

References

Anglada, G., Rodríguez, L. F., & Carrasco-González, C. 2018, A&ARv, 26, 3
Baek, G., Lee, J.-E., Hirota, T., Kim, K.-T., & Kyoung Kim, M. 2022, ApJ, 939, 84
Bartkiewicz, A., Szymczak, M., & van Langevelde, H. J. 2012, A&A, 541, A72
Bartkiewicz, A., Szymczak, M., & van Langevelde, H. J. 2016, A&A, 587, A104
Bartkiewicz, A., Sanna, A., Szymczak, M., et al. 2020, A&A, 637, A15
Beltrán, M. T., & de Wit, W. J. 2016, A&ARv, 24, 6
Breen, S. L., Fuller, G. A., Caswell, J. L., et al. 2015, MNRAS, 450, 4109
Brogan, C. L., Hunter, T. R., Cyganowski, C. J., et al. 2018, ApJ, 866, 87
Burns, R. A., Handa, T., Nagayama, T., Sunada, K., & Omodaka, T. 2016, MNRAS, 460, 283
Burns, R. A., Sugiyama, K., Hirota, T., et al. 2020, Nat. Astron., 4, 506
Burns, R. A., Kobak, A., Caratti o Garatti, A., et al. 2022, in European VLBI Network Mini-Symposium and Users' Meeting 2021, 19
Caratti o Garatti, A., Stecklum, B., Garcia Lopez, R., et al. 2017, Nat. Phys., 13, 276
Caswell, J. L. 2003, MNRAS, 341, 551
Caswell, J. L., & Green, J. A. 2011, MNRAS, 411, 2059
Charlot, P., Jacobs, C. S., Gordon, D., et al. 2020, A&A, 644, A159
Chibueze, J. O., Imai, H., Tafoya, D., et al. 2012, ApJ, 748, 146
Chibueze, J. O., MacLeod, G. C., Vorster, J. M., et al. 2021, ApJ, 908, 175
Cragg, D. M., Sobolev, A. M., & Godfrey, P. D. 2002, MNRAS, 331, 521
Cragg, D. M., Sobolev, A. M., & Godfrey, P. D. 2005, MNRAS, 360, 533
Cyganowski, C. J., Whitney, B. A., Holden, E., et al. 2008, AJ, 136, 2391
Darwish, M. S., Edris, K. A., Richards, A. M. S., et al. 2020, MNRAS, 493, 4442
Deller, A. T., Brisken, W. F., Phillips, C. J., et al. 2011, PASP, 123, 275
Dodson, R., Ojha, R., & Ellingsen, S. P. 2004, MNRAS, 351, 779
Fujisawa, K., Yonekura, Y., Sugiyama, K., et al. 2015, The Astronomer's Telegram, 8286, 1
Gray, M. D., Etoka, S., Richards, A. M. S., & Pimpanuwat, B. 2022, MNRAS, 513, 1354
Green, J. A., & McClure-Griffiths, N. M. 2011, MNRAS, 417, 2500
Hirota, T., Wolak, P., Hunter, T. R., et al. 2022, PASJ, 74, 1234
Hu, B., Menten, K. M., Wu, Y., et al. 2016, ApJ, 833, 18
Hunter, T. R., Brogan, C. L., MacLeod, G. C., et al. 2018, ApJ, 854, 170
Inayoshi, K., Sugiyama, K., Hosokawa, T., Motogi, K., & Tanaka, K. E. I. 2013, ApJ, 769, L20
MacLeod, G. C., Smits, D. P., Goedhart, S., et al. 2018, MNRAS, 478, 1077
Mainzer, A., Bauer, J., Cutri, R. M., et al. 2014, ApJ, 792, 30
McCarthy, T. P., Orosz, G., Ellingsen, S. P., et al. 2022, MNRAS, 509, 1681
Menten, K. M. 1991, ApJ, 380, L75
Moscadelli, L., Sanna, A., & Goddi, C. 2011, A&A, 536, A38
Moscadelli, L., Sanna, A., Goddi, C., et al. 2017, A&A, 600, A8
Purser, S. J. D., Lumsden, S. L., Hoare, M. G., & Kurtz, S. 2021, MNRAS, 504, 338
Reid, M. J., Menten, K. M., Brunthaler, A., et al. 2019, ApJ, 885, 131
Richards, A. M. S., Moravec, E., Etoka, S., et al. 2022, arXiv e-prints, [arXiv:2207.05591]
Sanna, A., Moscadelli, L., Surcis, G., et al. 2017, A&A, 603, A94
Seifried, D., Sánchez-Monge, Á., Walch, S., & Banerjee, R. 2016, MNRAS, 459, 1892
Stecklum, B., Caratti o Garatti, A., Hodapp, K., et al. 2018, in Astrophysical Masers: Unlocking the Mysteries of the Universe, 336, eds. A. Tarchi, M. J. Reid, & P. Castangia, 37
Szymczak, M., Olech, M., Sarniak, R., Wolak, P., & Bartkiewicz, A. 2018a, MNRAS, 474, 219
Szymczak, M., Olech, M., Wolak, P., Gérard, E., & Bartkiewicz, A. 2018b, A&A, 617, A80
Virtanen, P., Gommers, R., Oliphant, T. E., et al. 2020, Nat. Methods, 17, 261
Wolak, P., Olech, M., Szymczak, M., Bartkiewicz, A., & Durjasz, M. 2019, The Astronomer's Telegram, 13080, 1
Wright, E. L., Eisenhardt, P. R. M., Mainzer, A. K., et al. 2010, AJ, 140, 1868
Wrobel, J. M., & Walker, R. C. 1999, in Synthesis Imaging in Radio Astronomy II, eds. G. B. Taylor, C. L. Carilli, & R. A. Perley, Astronomical Society of the Pacific Conference Series, 180, 171

Appendix A: Figures and tables

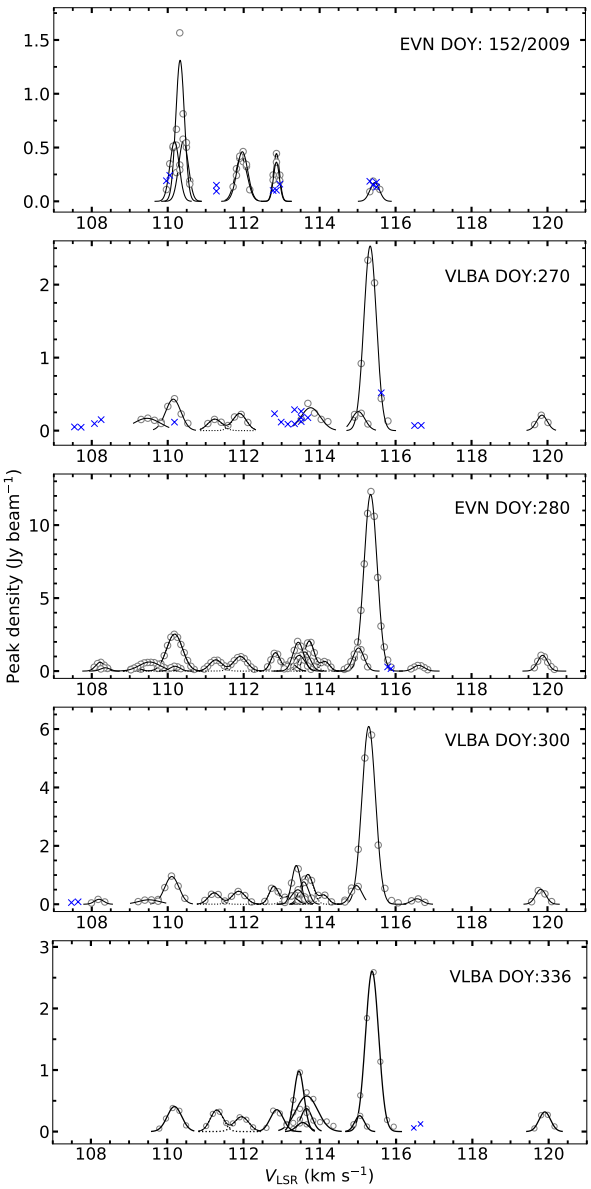

Fig. A.1: Cross-correlation spectra of 6.7 GHz methanol maser line with Gaussian fittings of individual cloudlets. The fits (solid lines) present the Gaussian profiles. Each circle traces the emission level of a single maser spot, as presented in Fig. 2. The blue crosses indicate spots in cloudlets with no Gaussian profile.

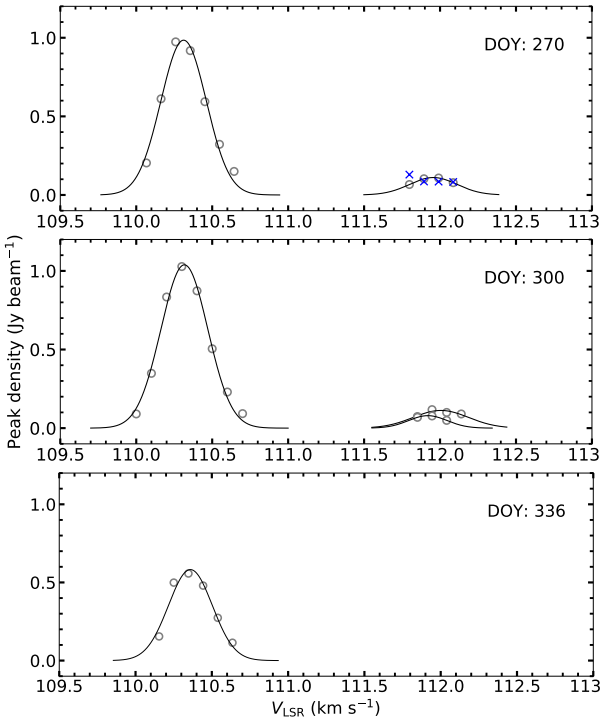

Fig. A.2: Same as Fig. A.1, but for 12.2 GHz methanol emission.

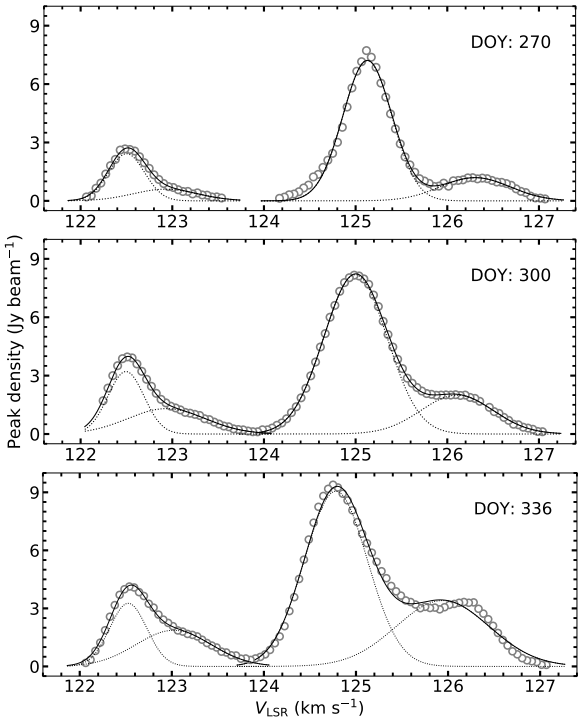

Fig. A.3: Same as Fig. A.1, but for 22.2 GHz water emission.

Table A.1: Parameters of the 6.7 GHz methanol maser cloudlets with Gaussian velocity profiles in five epochs in 2019.

No. of cloudlet Epoch	$V_{\rm p}$ (km s^{-1})	$V_{\rm fit}$ (km s^{-1})	FWHM (km s^{-1})	$S_{\rm fit}$ (Jy beam^{-1})	$r_{\rm s}$	$r_{\rm v}$	ΔRA×ΔDec (mas×mas)	$V_{\rm grad}$ (km s^{-1} mas^{-1})	PA (°)
Cloudlet 1									
DOY: 270 (VLBA)	119.84	119.85	0.17	0.2	1.00	1.00	2.2 × 0.8	0.15	−69
DOY: 271 (LBA)	119.86	119.89	0.12	1.0	-	-	2.9 × 1.6	-	-
DOY: 280 (EVN)	119.83	119.87	0.16	1.1	0.76	1.00	2.8 × 3.3	0.13	−53
DOY: 300 (VLBA)	119.76	119.82	0.16	0.5	0.77	1.00	2.7 × 2.1	0.15	−60
DOY: 336 (VLBA)	119.98	119.90	0.18	0.3	0.99	1.00	3.9 × 1.2	0.13	−66
Cloudlet 2									
DOY: 270	116.68	-	-	-	-	-	-	-	-
DOY: 271	116.61	116.64	0.14	0.3	0.83	0.89	2.1 × 2.0	0.07	+54
DOY: 280	116.58	116.61	0.17	0.4	0.86	0.95	3.2 × 1.7	0.12	−65
DOY: 300	116.60	116.56	0.17	0.2	-	-	1.9 × 0.5	-	-
DOY: 336	116.64	-	-	-	-	-	-	-	-
Cloudlet 3									
DOY: 270	115.27	115.33	0.17	2.5	-	-	1.2 × 3.3	-	-
DOY: 271	115.38	115.37	0.17	12.6	-	-	4.6 × 7.7	-	-
DOY: 280	115.35	115.34	0.20	12.1	-	-	4.0 × 6.7	-	-
DOY: 300	115.37	115.29	0.21	6.1	-	-	2.7 × 5.0	-	-
DOY: 336	115.41	115.37	0.20	2.6	-	-	2.0 × 5.7	-	-
Cloudlet 4									
DOY: 270	115.10	115.02	0.20	0.3	0.93	0.98	1.7 × 1.6	0.26	−53
DOY: 271	115.03	115.04	0.15	1.0	0.99	0.91	3.4 × 2.0	0.12	−67
DOY: 280	115.00	115.02	0.17	1.6	0.52	1.00	2.1 × 0.5	0.25	−69
DOY: 300	115.02	114.97	0.17	0.6	0.60	1.00	1.5 × 0.2	0.20	−85
DOY: 336	115.06	115.04	0.15	0.3	-	-	0.2 × 0.9	-	-
Cloudlet 5									
DOY: 270	113.51	-	-	-	-	-	-	-	-
DOY: 271	113.50	113.52	0.11	0.3	-	-	0.7 × 1.3	-	-
DOY: 280	113.51	113.46	0.20	1.1	-	-	1.8 × 4.7	-	-
DOY: 300	113.44	113.43	0.19	0.5	0.98	0.90	0.3 × 4.9	0.07	−3
DOY: 336	113.48	113.55	0.18	0.2	-	-	0.3 × 5.0	-	-
Cloudlet 6									
DOY: 270	113.69	113.76	0.30	0.3	1.00	0.98	3.7 × 2.0	0.17	−62
DOY: 271	113.76	114.17	0.12	0.5	0.93	0.97	5.7 × 2.0	0.14	−70
		113.76	0.15	1.7					
DOY: 280	113.77	114.14	0.14	0.7	0.99	0.98	3.6 × 2.2	0.17	−60
		113.73	0.16	2.1					
DOY: 300	113.61	114.11	0.15	0.3	0.92	0.97	4.1 × 2.9	0.18	−59
		113.69	0.16	1.0					
DOY: 336	113.66	113.66	0.33	0.6	0.94	0.98	7.8 × 5.0	0.13	−58
Cloudlet 7									
DOY: 270	113.69	-	-	-	-	-	-	-	-
DOY: 271	113.67	113.64	0.12	0.6	0.97	0.96	2.3 × 0.7	0.09	−72
DOY: 280	113.60	113.61	0.17	1.3	0.98	0.97	1.8 × 1.6	0.11	−48
DOY: 300	113.61	113.58	0.15	0.8	0.99	1.00	1.4 × 1.7	0.18	−41
DOY: 336	113.66	113.65	0.18	0.4	-	-	0.6 × 1.4	-	-
Cloudlet 8									
DOY: 270	113.34	-	-	-	-	-	-	-	-
DOY: 271	113.50	113.48	0.15	1.7	0.72	0.61	6.2 × 1.7	0.10	−77
DOY: 280	113.42	113.44	0.16	2.0	0.99	0.98	10.0 × 1.6	0.04	−81
DOY: 300	113.44	113.38	0.14	1.3	0.99	1.00	3.0 × 1.5	0.16	−64
DOY: 336	113.48	113.45	0.15	1.0	0.95	1.00	2.7 × 0.6	0.13	−78

Table A.1: continued

No. of cloudlet Epoch	V_p (km s^{-1})	V_{fit} (km s^{-1})	FWHM (km s^{-1})	S_{fit} (Jy beam^{-1})	r_s	r_v	ΔRA×ΔDec (mas×mas)	V_{grad} (km s^{-1} mas^{-1})	PA (°)
Cloudlet 9									
DOY: 270	112.81	-	-	-	0.71	0.90	2.3 × 1.8	0.12	+64
DOY: 271	112.88	113.21	0.14	0.2	0.84	0.84	4.1 × 3.3	0.11	+50
		112.87	0.12	1.1					
DOY: 280	112.81	113.25	0.16	0.5	0.93	0.94	4.0 × 3.4	0.15	+49
		112.84	0.14	1.3					
DOY: 300	112.73	113.23	0.20	0.3	0.89	0.93	3.8 × 3.0	0.18	+56
		112.79	0.14	0.6					
DOY: 336	112.78	112.87	0.20	0.4	0.94	0.95	3.8 × 4.1	0.11	+54
Cloudlet 10									
DOY: 270	111.93	111.89	0.21	0.3	0.99	0.99	0.2 × 1.6	0.89	+11
		111.24	0.21	0.2	0.55	1.00	0.5 × 0.4	0.58	−64
DOY: 271	111.87	111.93	0.19	0.9	-	-	1.8 × 3.3	-	-
		111.28	0.17	0.5	-	-	1.1 × 1.2	-	-
DOY: 280	111.93	111.91	0.21	1.0	0.68	0.95	0.2 × 1.6	0.33	−6
		111.26	0.19	0.8	0.73	0.95	1.4 × 4.3	0.33	−42
DOY: 300	111.85	111.87	0.22	0.4	0.76	0.99	0.5 × 1.5	0.51	+30
		111.22	0.18	0.4	1.00	0.95	0.9 × 1.8	0.25	−27
DOY: 336	111.37	111.95	0.22	0.3	-	-	0.4 × 1.5	-	-
		111.30	0.21	0.4	0.62	0.71	0.9 × 2.7	0.19	−26
Cloudlet 11									
DOY: 270	110.18	-	-	-	-	-	-	-	-
DOY: 271	110.20	110.21	0.05	0.3	0.71	0.94	1.0 × 0.8	0.07	−61
DOY: 280	110.17	110.19	0.15	0.3	-	-	0.2 × 0.4	-	-
DOY: 300	-	-	-	-	-	-	-	-	-
DOY: 336	-	-	-	-	-	-	-	-	-
Cloudlet 12									
DOY: 270	110.18	110.14	0.23	0.1	0.99	0.87	2.6 × 9.6	0.07	+16
DOY: 271	110.16	110.50	0.07	0.3	0.99	0.90	3.9 × 12.0	0.06	+17
		110.15	0.18	1.9					
DOY: 280	110.17	110.18	0.25	2.5	0.98	0.93	2.8 × 10.3	0.09	+15
		109.17	0.15	0.2	-	-	0.3 × 1.4	-	-
DOY: 300	110.10	110.11	0.22	0.9	0.99	0.78	1.5 × 7.0	0.10	+12
DOY: 336	110.14	110.19	0.23	0.4	0.98	0.96	2.2 × 7.3	0.07	+14
Cloudlet 13									
DOY: 270	109.48	109.45	0.42	0.2	0.69	0.91	0.2 × 2.5	0.20	+9
DOY: 271	109.63	109.56	0.30	0.5	-	-	2.7 × 2.9	-	-
		109.41	0.10	0.2					
DOY: 280	109.56	109.52	0.32	0.6	0.75	0.98	2.7 × 2.9	0.24	+50
DOY: 300	109.57	109.51	0.32	0.2	0.91	0.94	0.9 × 1.4	0.30	+36
DOY: 336	-	-	-	-	-	-	-	-	-
Cloudlet 14									
DOY: 270	108.25	-	-	-	-	-	-	-	-
DOY: 271	108.22	108.25	0.11	0.6	0.74	0.86	2.0 × 0.7	0.21	−65
DOY: 280	108.24	108.22	0.14	0.6	0.68	0.86	0.2 × 0.6	0.53	−27
DOY: 300	108.17	108.19	0.14	0.2	-	-	0.3 × 0.7	-	-
DOY: 336	-	-	-	-	-	-	-	-	-
Cloudlet 15									
DOY: 270	107.54	-	-	-	-	-	-	-	-
DOY: 271	107.61	107.61	0.15	0.2	-	-	1.3 × 0.7	-	-
DOY: 280	108.33	108.35	0.14	0.2	0.96	0.97	0.2 × 1.0	0.18	+14
DOY: 300	107.64	-	-	-	-	-	-	-	-
DOY: 336	-	-	-	-	-	-	-	-	-

Table A.2: Same as Table A.1 but for the 12.2 GHz methanol maser line.

No. of cloudlet Epoch	V_p (km s^{-1})	V_{fit} (km s^{-1})	FWHM (km s^{-1})	S_{fit} (Jy beam^{-1})	r_s	r_v	ΔRA×ΔDec (mas×mas)	V_{grad} (km s^{-1} mas^{-1})	PA (°)
Cloudlet 1									
DOY:270	111.80	-	-	-	-	-	1.4 × 2.7	-	-
DOY:300	111.95	112.01	0.21	0.1	-	-	0.8 × 1.3	-	-
DOY:336	-	-	-	-	-	-	-	-	-
Cloudlet 2									
DOY:270	111.99	111.96	0.18	0.1	-	-	0.5 × 1.4	-	-
DOY:300	111.95	111.92	0.15	0.08	-	-	0.1 × 0.7	-	-
DOY:336	-	-	-	-	-	-	-	-	-
Cloudlet 3									
DOY:270	110.26	110.31	0.18	1.0	0.93	0.99	0.3 × 1.0	0.51	+22
DOY:300	110.31	110.33	0.18	1.0	0.59	0.98	0.5 × 2.5	0.40	+13
DOY:336	110.35	110.36	0.17	0.6	0.60	0.94	0.4 × 0.8	0.63	−12

Table A.3: Same as Table A.1 but for the 22.2 GHz water vapour maser line.

No. of cloudlet Epoch	V_p (km s^{-1})	V_{fit} (km s^{-1})	FWHM (km s^{-1})	S_{fit} (Jy beam^{-1})	r_s	r_v	ΔRA×ΔDec (mas×mas)	V_{grad} (km s^{-1} mas^{-1})	PA (°)
Cloudlet 1									
DOY:270	125.12	126.30	0.45	1.2	0.90	0.91	1.4 × 1.4	1.42	−50
		125.13	0.31	7.2					
DOY:300	124.98	126.11	0.46	2.0	0.96	0.94	1.2 × 1.1	1.84	−47
		125.00	0.41	8.2					
DOY:336	124.75	125.94	0.60	3.4	0.97	0.94	1.3 × 1.4	1.65	−44
		124.78	0.40	9.1					
Cloudlet 2									
DOY:270	122.48	122.92	0.41	0.6	0.78	0.89	0.2 × 0.5	1.07	−19
		122.50	0.23	2.4	0.57	0.79	0.1 × 0.3	3.31	−57
DOY:300	122.51	122.94	0.50	1.3	0.69	0.78	0.5 × 0.8	1.45	+41
		122.49	0.23	3.2	0.88	0.92	0.2 × 0.1	3.63	−76
DOY:336	122.54	123.02	0.48	1.9	0.83	0.79	0.5 × 0.9	0.93	+42
		122.53	0.24	3.3	0.18*	0.90	0.3 × 0.2	3.63	−96*

∗ - value left to show decline in V_{grad}, PA can be unrealistic.

Table A.4: Same as Table A.1 but for the 6.7 GHz 2009 EVN observations*.

No. of cloudlet Epoch	V_p (km s^{-1})	V_{fit} (km s^{-1})	FWHM (km s^{-1})	S_{fit} (Jy beam^{-1})	r_s	r_v	ΔRA×ΔDec (mas×mas)	V_{grad} (km s^{-1} mas^{-1})	PA (°)
1	115.41	115.45	0.15	0.2	-	-	0.6 × 4.3	-	-
2	115.32	-	-	-	-	-	0.8 × 2.2	-	-
3	112.86	112.86	0.09	0.4	1.00	0.98	1.5 × 2.3	0.06	+33
4	112.86	112.86	0.09	0.4	-	-	0.6 × 1.4	-	-
5	112.95	-	-	-	-	-	0.7 × 1.5	-	-
6	111.99	111.93	0.18	0.4	-	-	1.9 × 1.7	-	-
7	111.99	111.96	0.17	0.5	0.83	0.90	1.4 × 1.6	0.10	+23
8	110.40	110.41	0.15	0.6	0.81	0.94	2.3 × 1.7	0.11	+54
9	110.40	110.33	0.13	1.3	0.94	0.93	2.0 × 3.0	0.11	+36
10	110.23	110.18	0.15	0.6	0.92	0.86	0.9 × 2.2	0.11	+27

∗ - data set from (Bartkiewicz et al. 2016).

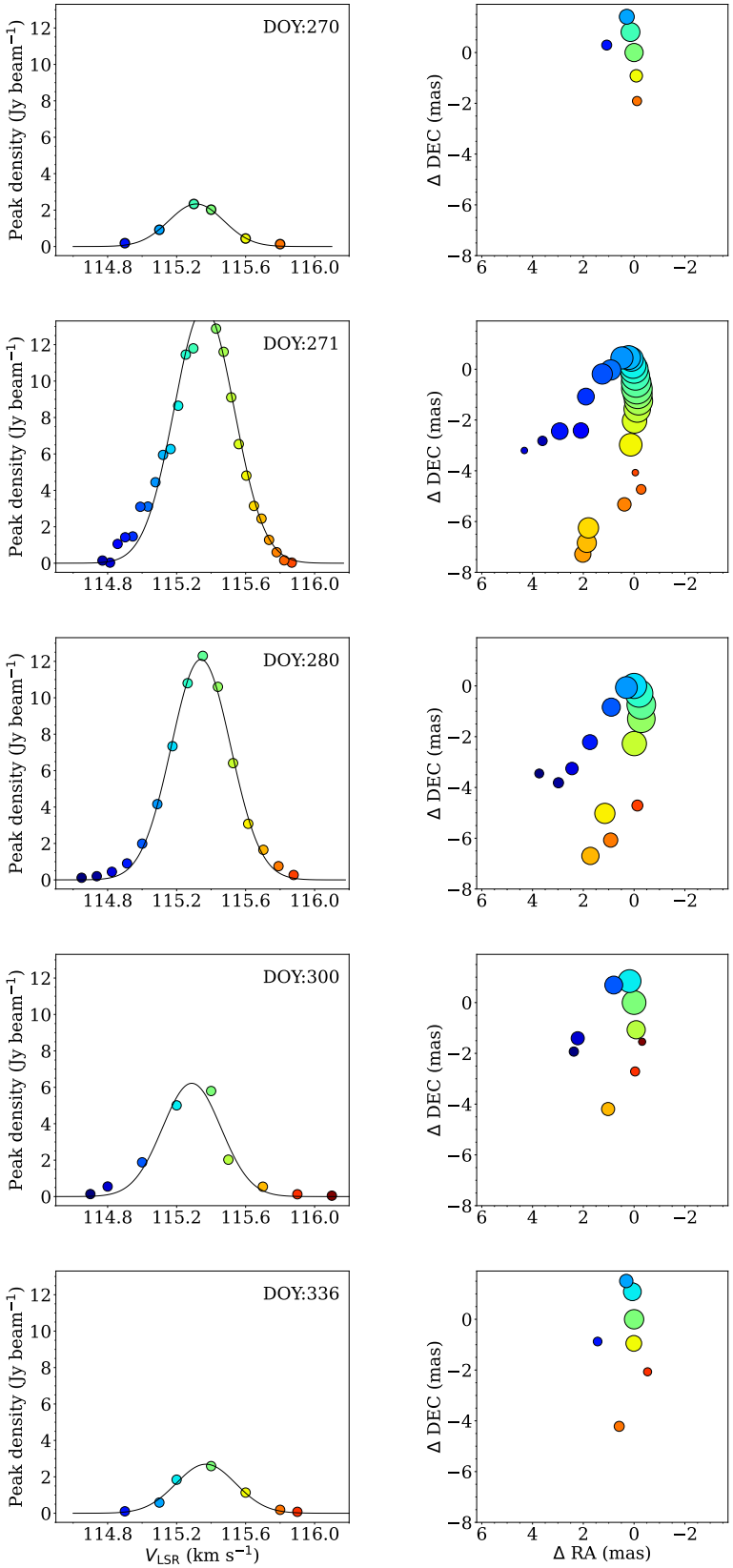

Fig. A.4: Examples of Gaussian characteristics of the individual spectra (left) and the spatial distributions of single spots (right) of the 6.7 GHz methanol maser cloudlets. Here **Cloudlet 3** is presented (Table A.1). The cloudlet shows the arched structure in all epochs of observations, and therefore no linear fits were done.

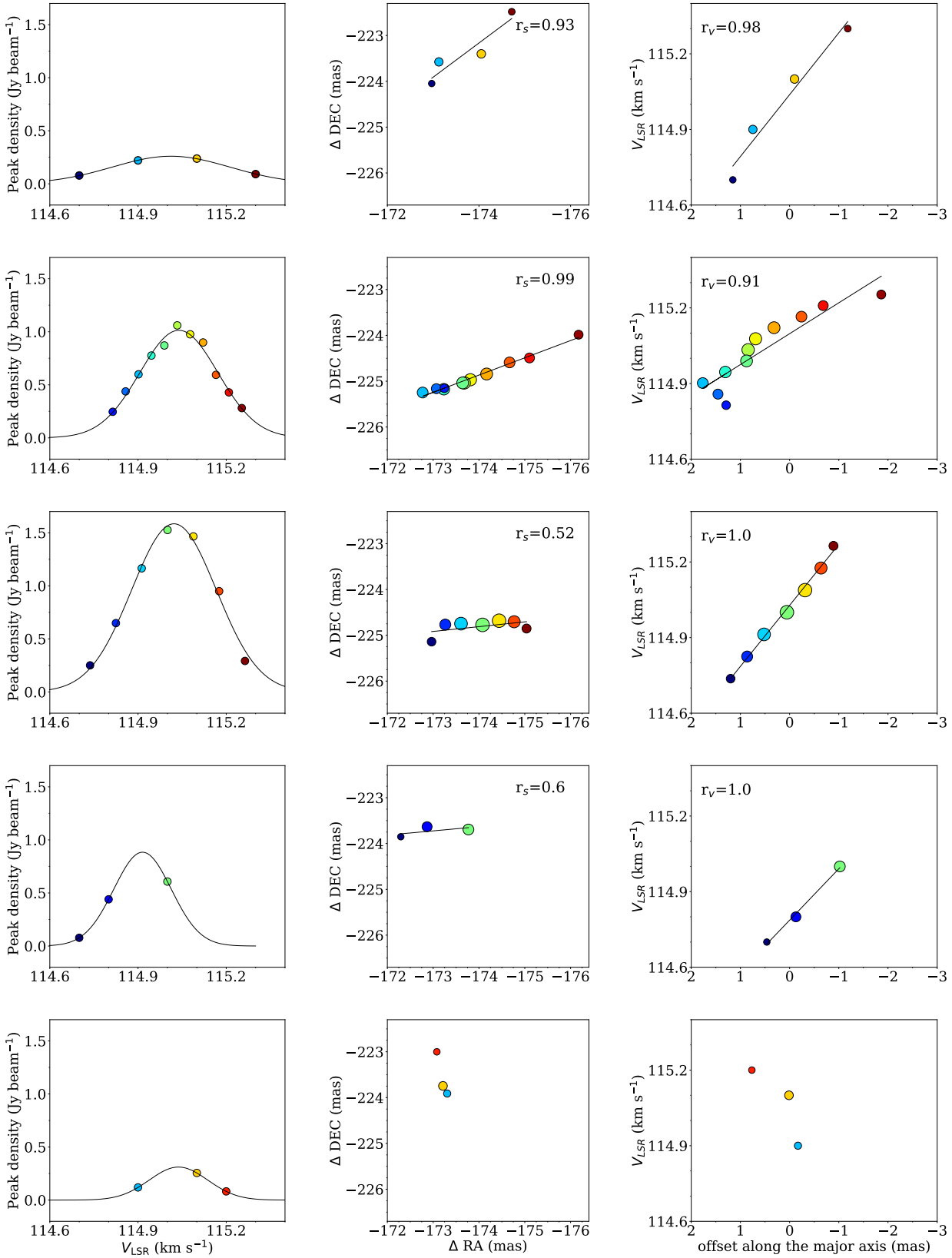

Fig. A.4: continued. **Cloudlet 4** as in Table A.1. The left and middle panels are the same as for Cloudlet 3. The right panel shows the spot V_{LSR}–position offset along the major axis of the spot distributions. There is no fit in DOY: 336 due to the weakness of the spots.

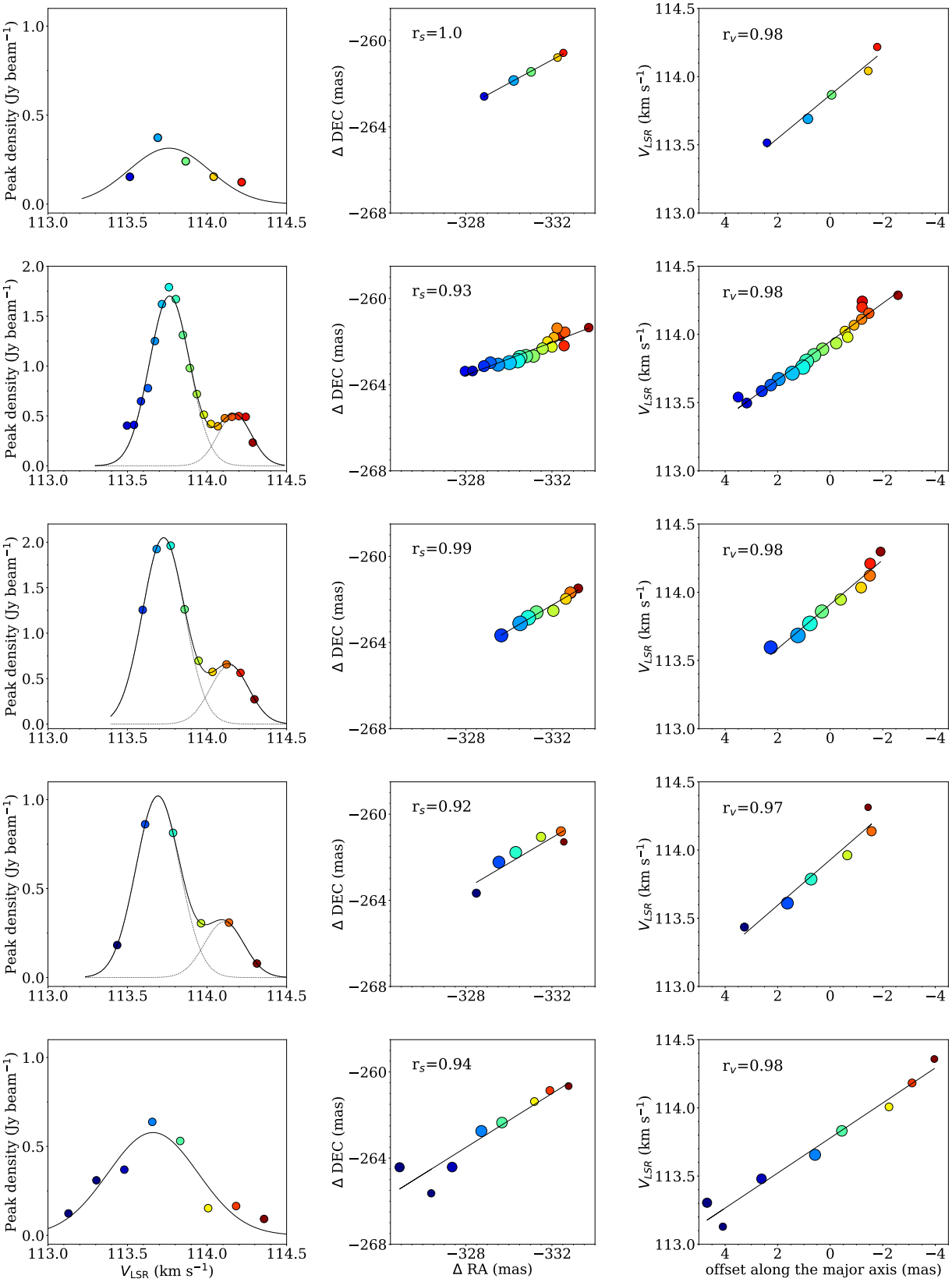

Fig. A.4: continued. **Cloudlet 6**.

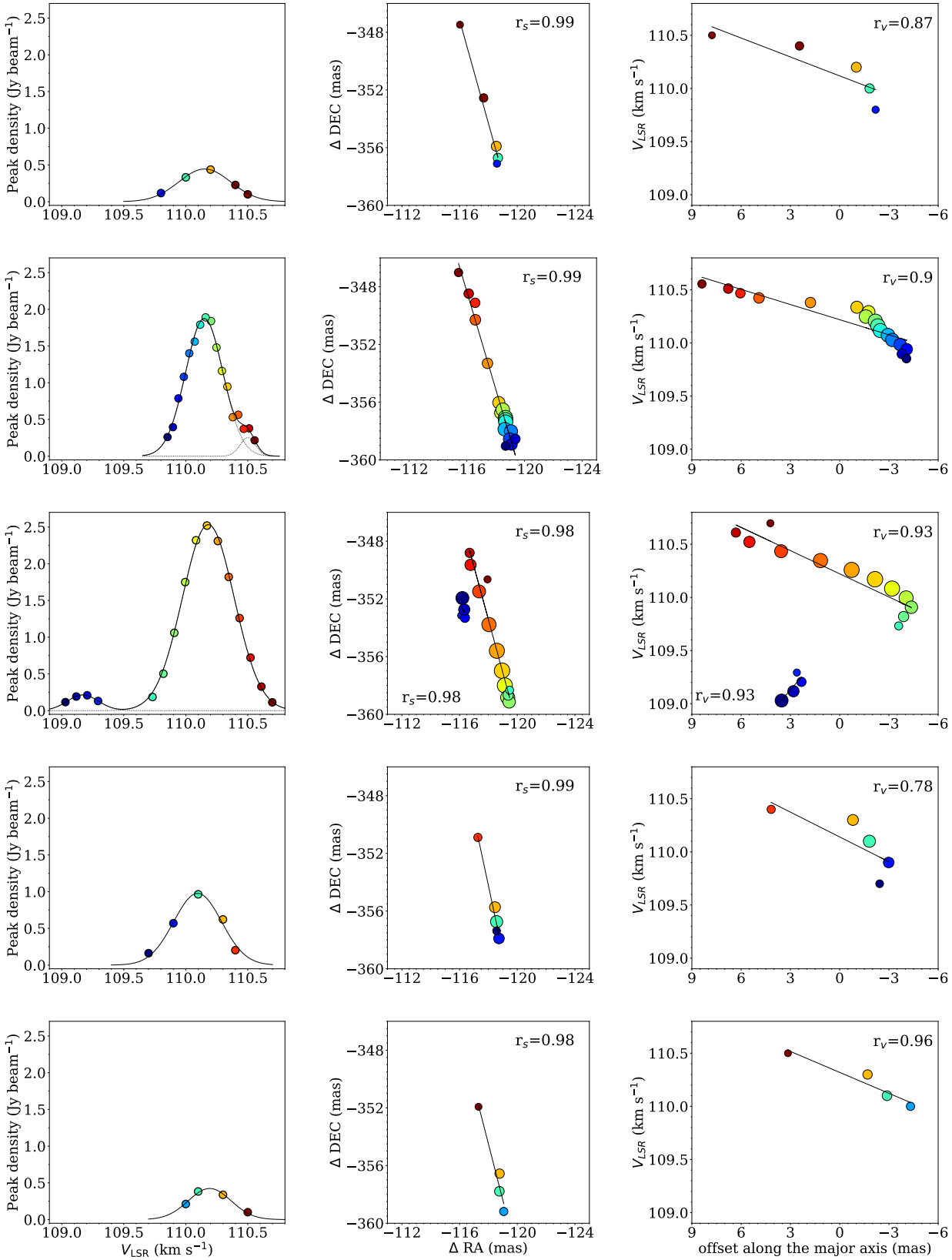

Fig. A.4: continued. **Cloudlet 12**.

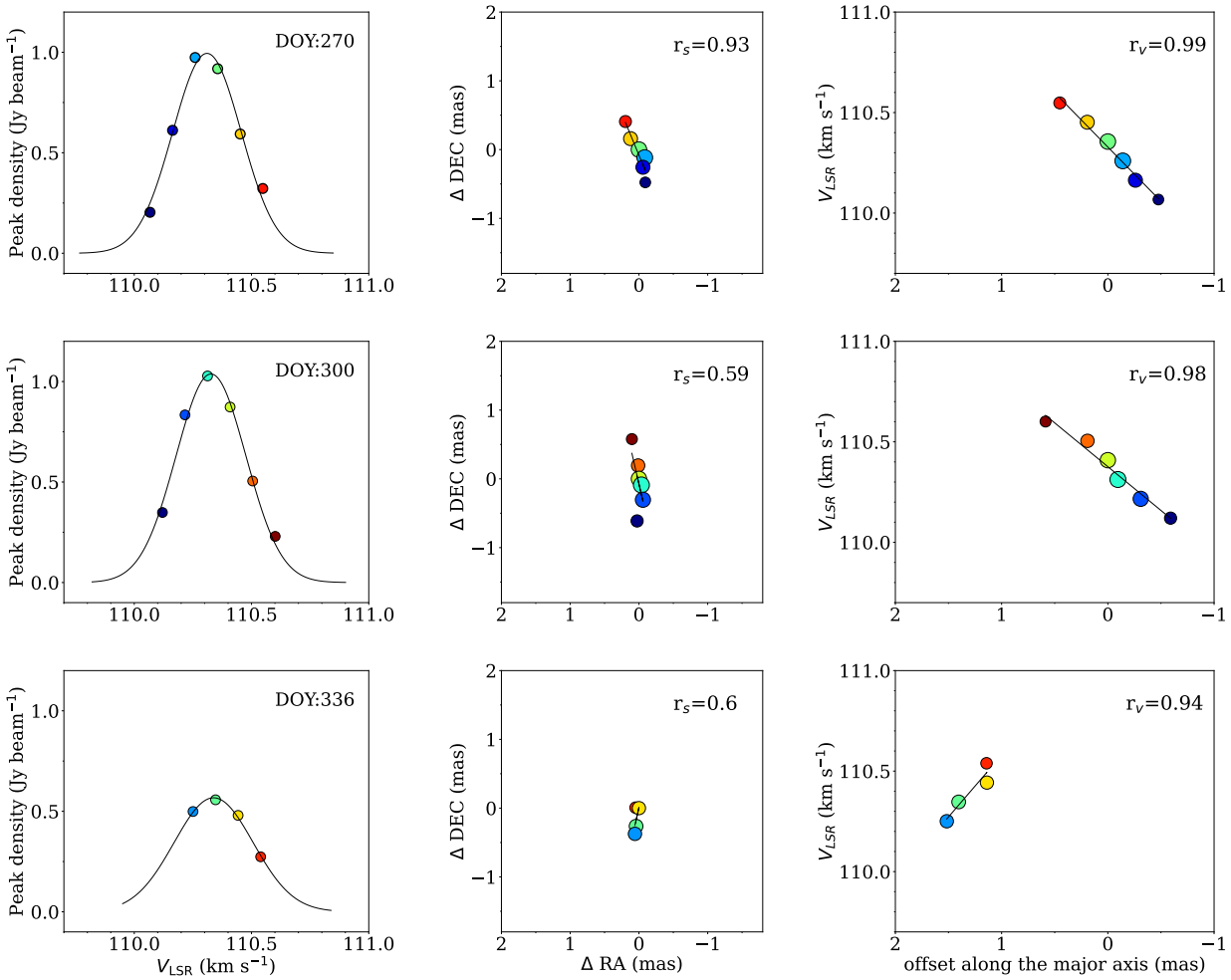

Fig. A.5: Gaussian characteristics of the 12.2 GHz methanol maser Cloudlet 3 (Table A.2). Shown are the individual spectra (left), the spatial distributions of single spots (middle), and the spot V_{LSR}–position offset along the major axis of the spot distributions (right).

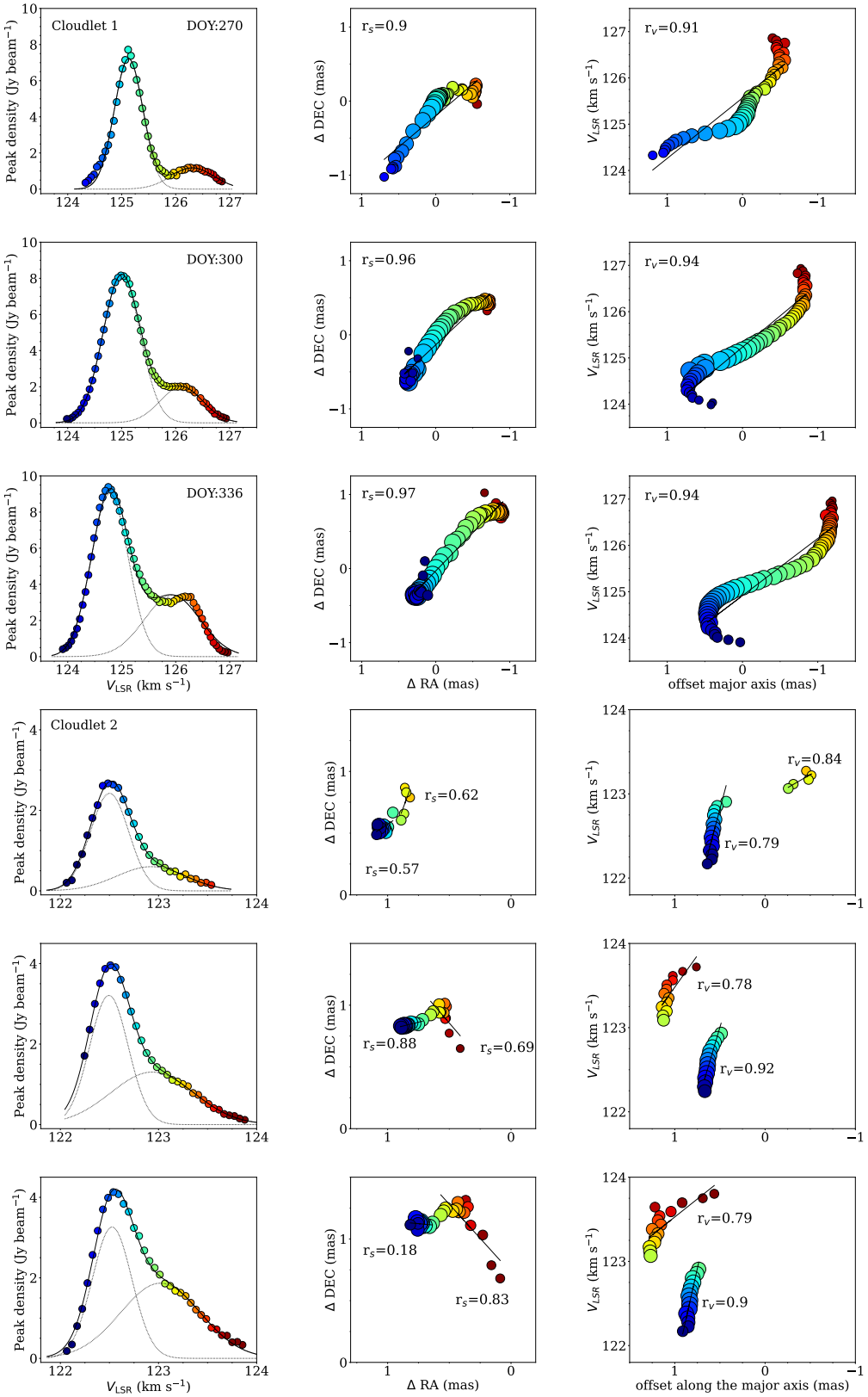

Fig. A.6: Gaussian characteristics of 22.2 GHz water maser Cloudlet 1 (top three panels) and Cloudlet 2 (bottom three panels; Table A.3). Shown are the individual spectra (left), the spatial distributions of single spots (middle), and the spot V_{LSR}–position offset along the major axis of the spot distributions (right).

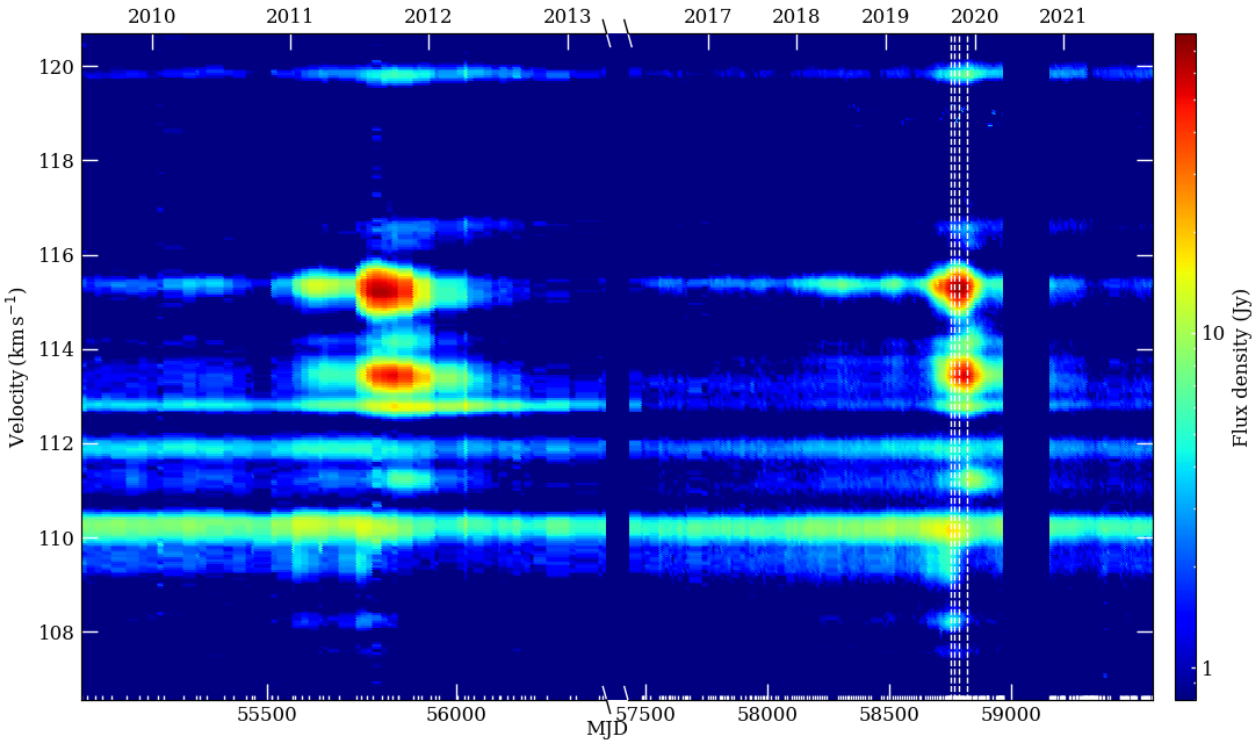

Fig. A.7: Dynamic spectrum of 6.7 GHz methanol maser emission of G24. The velocity is measured with respect to the local standard of rest. The vertical bars on the bottom ordinate correspond to the dates of the observed spectra. The white dashed vertical lines indicate the epochs of VLBI observations. There were no observations in the periods 56387<MJD<57482 and 58967<MJD<59153.

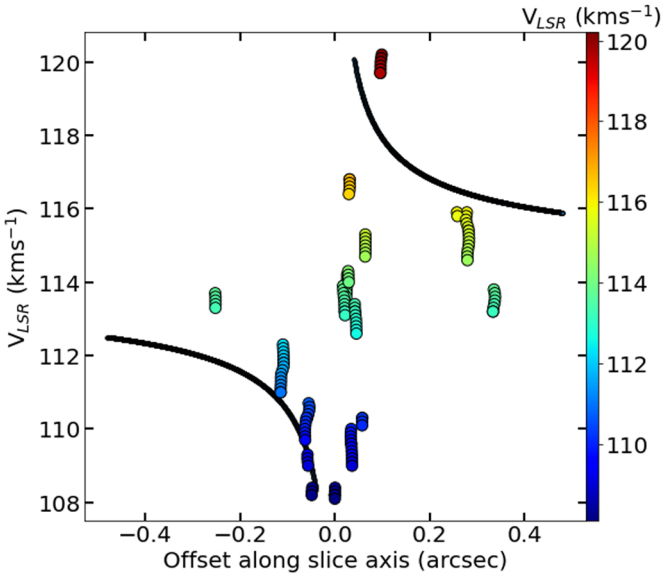

Fig. A.8: Best fit Keplerian disk rotation model (bold dashed black lines) derived using a central mass of 8.8 $M_\odot$ (Hirota et al. 2022), inner and outer disk radii of 10 AU and 120 AU, and disk inclination of 85°, overlaid on the position-velocity diagrams of the observed maser features.

A&A, 695, A149 (2025)
https://doi.org/10.1051/0004-6361/202452657

Astronomy & Astrophysics

Physical conditions around high-mass young star-forming objects via simultaneous observations of excited OH and methanol masers

A. Kobak[1,⋆], A. Bartkiewicz[1], K. L. J. Rygl[2], A. M. S. Richards[3], M. Szymczak[1], and P. Wolak[1]

[1] Institute of Astronomy, Faculty of Physics, Astronomy and Informatics, Nicolaus Copernicus University, Grudziadzka 5, 87–100 Torun, Poland
[2] INAF-Istituto di Radioastronomia, Via P. Gobetti 101, 40129 Bologna, Italy
[3] JBCA, Department of Physics and Astronomy, University of Manchester, Manchester, UK

Received 18 October 2024 / Accepted 27 January 2025

ABSTRACT

Context. Astrophysical masers are widely used in star formation studies. In particular, they are valuable in investigations of high-mass star-forming regions that are difficult to observe at optical frequencies.
Aims. We used multi-transition data to derive physical conditions in the immediate environment of forming high-mass stars.
Methods. Simultaneous observations of two maser transitions, excited OH at 6.035 GHz and methanol at 6.668 GHz, were made using e-Merlin. Both transitions are radiatively pumped but prefer diverse physical conditions.
Results. We imaged ten high-mass star-forming sites with milliarcsecond angular resolution, identifying regions where excited OH and methanol masers coexist and where they avoid each other. Moreover, we identified circularly polarized Zeeman splitting pairs of the OH transition, estimating magnetic field strengths in the range from 0.2 to 10.6 mG. The detection of linearly polarized components enabled us to compare the directions of magnetic field vectors with the outflows coming from the young star-forming objects.
Conclusions. We found that the two maser lines appeared to coexist in six high-mass star-forming regions, in cloudlets separated by up to 205 au. Where the lines show avoidance, this can be related to changes in dust and gas temperatures; we also found a few examples suggestive of a high gas density. In seven sources, Kolmogorov-Smirnov tests show the nonrandom relationship between the position angles of distribution of the two maser transitions. We did not obtain consistent results regarding the direction of the magnetic field and outflow.

Key words. masers – polarization – stars: formation – stars: massive – ISM: magnetic fields – ISM: molecules

1. Introduction

Astrophysical masers are used to study high-mass young star-forming objects (HMYSOs), in particular maser emission from hydroxyl (OH), water (H_2O), and methanol (CH_3OH) molecules. In this publication, we focus on two maser transitions: excited OH at 6.035 GHz (hereafter ex-OH) and methanol at 6.668 GHz (hereafter 6.7 GHz). Both are excited via thermal, infrared emission from warm dust that is heated by nearby protostars and may or may not occur in the same volume of gas, depending on the physical conditions, as was modeled in Cragg et al. (2002). The OH radical is a paramagnetic molecule; therefore, Zeeman splitting can be observed from the left- and right-hand circularly polarized (LHCP and RHCP) spectra, and the strength and direction of the magnetic fields can be derived from the separations of both features in the velocity domain (e.g., Avison et al. 2016; Szymczak et al. 2020; Ouyang et al. 2022). If a third, linearly polarized component is detected at the central, unshifted velocity, a Zeeman triplet is identified (e.g., Hutawarakorn et al. 2002; Green et al. 2015). As methanol is diamagnetic, the Zeeman splitting is much smaller and requires very high angular and velocity resolution for detection (e.g., Vlemmings et al. 2011; Surcis et al. 2012; Surcis et al. 2013; Surcis et al. 2015; Surcis et al. 2019; Surcis et al. 2022). Observations and modeling show that the 6.7 GHz transition is the brightest methanol maser under a wide range of physical conditions, such as a kinetic temperature of 30–150 K, appearing at dust temperatures above 100 K and diminishing when the gas temperature approaches or exceeds the dust temperature. The excitation of the 6.7 GHz methanol maser requires a hydrogen number density, n, in the range from 10^5 to $10^{8.3}$ cm^{-3}; the brightness temperature is independent of n up to 10^8 cm^{-3} and above this value falls abruptly (Cragg et al. 2002). The 6.035 GHz OH emission arises from a main-line excited-state transition and appears at lower gas temperatures. It is quenched at a kinetic temperature above 70 K, and is independent of dust temperature. The ex-OH line is also related to high-number-density conditions, extending up to $10^{8.5}$ cm^{-3} with a maximum brightness temperature in the range from 10^7 to 10^8 cm^{-3} (Cragg et al. 2002).

The morphology and kinematics, including proper motion studies, of the methanol maser at 6.7 GHz in HMYSOs have been relatively broadly examined (e.g., Bartkiewicz et al. 2009, 2014, 2016, 2020, 2024; Goddi et al. 2011; Moscadelli et al. 2011; Pandian et al. 2011; Sanna et al. 2010a,b; Sugiyama et al. 2008). Still, it is not clear where exactly 6.7 GHz methanol masers arise. In a few cases, the 6.7 GHz maser reveals a ring-like morphology (Bartkiewicz et al. 2009), which may indicate a disk seen face-on or an outflow oriented along the line of sight (Bartkiewicz et al. 2005). However, detailed studies have shown that complex scenarios are common, in which the masers kinematics can result

⋆ Corresponding author; akobak@astro.umk.pl

from a combination of rotation and expansion (Bartkiewicz et al. 2024). Sugiyama et al. (2011) measured the proper motions of 6.7 GHz maser spots around the well-known HMYSO ON1 and concluded that the internal motions either traced the expanding ultracompact HII region or were associated with a molecular outflow. In HMYSO G23.01−0.41, the velocity field of methanol masers was explained in terms of a combination of slow radial expansion with rotation about an axis approximately parallel to the maser jet (Sanna et al. 2010b).

In the case of ex-OH masers, far fewer regions have been imaged in this transition, and they tend to be more compact relative to the methanol masers, preventing a detailed discussion of the kinematic structures in general (e.g., Desmurs et al. 1998; Desmurs & Baudry 1998; Etoka et al. 2012). The first untargeted survey of ex-OH, covering the Galactic longitude ranges 186°<l<60°, including the Galactic center, reported the detection of 127 sources, which is around 10% of the number of sources with 6.7 GHz methanol masers found in this region (Avison et al. 2016). In general, ex-OH masers are weaker than methanol masers, with brightness temperatures as much as two orders of magnitude lower. This statistic was confirmed by Szymczak et al. (2020), when they surveyed a sample of 445 HMYSOs, identified by the 6.7 GHz methanol transition, and detected 37 ex-OH targets, using the Torun 32-m radio telescope. Due to the small number of imaged regions, it is still uncertain where the ex-OH masers arise. They can be related to a disk, an outflow as well as an intermediate regions. Ex-OH masers may occur in the same place as ground-state (1.665 and 1.667 GHz) OH masers. The latter can trace a dense molecular disk (Hutawarakorn et al. 2002). However, Caswell & Green (2011) present a case in which the ground-state OH emission arises in a fast-moving outflow.

Multi-transition studies of maser emission are valuable in constraining the physical conditions in the gas around HMYSOs. Fish & Sjouwerman (2007) used the European VLBI Network and presented the distributions of ex-OH in the HMYSO W3(OH) compared with ground-state OH masers. The ex-OH masers trace the inner edge of a counterclockwise rotating torus of dense molecular gas, while the ground-state OH occurs predominantly to the west of this edge. The 1.667 GHz transition is generally associated with the ex-OH transition, but the 6.0 GHz masers may also appear without the presence of the 1.667 GHz masers. In contrast, 1.665 MHz transition is ubiquitous and can appear separately as well as in association with the ex-OH transition. Identified Zeeman pairs provided estimates of the magnetic field strength of a few milligauss and revealed a reversal of the line-of-sight direction of the magnetic field, oriented away from the observer in the west and toward the observer in the east. Green et al. (2007) imaged the 6.7 GHz methanol and ex-OH lines toward the HMYSO ON1 using MERLIN. Toward the southern part of the ultracompact (UC) HII region, the two masers were observed to present a spatial distribution elongated perpendicular to the large-scale bipolar outflow. The Zeeman pairs identified in ex-OH implied the existence of a magnetic field oriented toward the observer with a strength of up to 5.8 mG. The first tentative detection of Zeeman splitting in the 6.7 GHz methanol line was roughly consistent with the above value being −18±6 mG (a negative value corresponds to the direction pointing toward the observer). Global VLBI observations toward the same target revealed that ex-OH masers have a distribution similar to that of the ground-state OH masers, in contrast to the situation in W3(OH), and this suggests the absence of the highest-density knots in ON1 (Fish & Sjouwerman 2010).

This project aims to derive the physical conditions in a sample of HMYSOs via combined observations of ex-OH and methanol masers. In fact, the spatial coincidence or avoidance of these two masers implies specific physical conditions following the maser excitation models of Cragg et al. (2002). Moreover, the ex-OH maser observations provide: 1) the identification of Zeeman splitting, and thus estimates of the magnetic field strength, and 2) the detection of linearly polarized emission and estimation of the orientation of the magnetic field. This allows us to map the magnetic field structure in the close surroundings of HMYSOs. The continuum emission and methanol polarization will be reported in a future article.

2. Observations, data reduction, and methods

The source sample has been chosen based on a large survey of ex-OH carried out since 2018 with the Torun 32 m telescope (Szymczak et al. 2020). Among the 37 detections, we selected 10 sources in which the ex-OH line has a relatively strong (above 1.7 Jy) and non-variable flux density, as was found during two epochs of the survey (November-December 2018 and March-April 2019). In addition, our single-dish studies showed that the spectral features of the 6.7 GHz methanol and ex-OH maser transitions appear at similar LSR velocities.

The observations were made using the enhanced Multi-Element Remotely Linked Interferometer Network (e-MERLIN)[1], an array of six radio telescopes with baselines between 10–217 km (Garrington & Beswick 2016), under the project CY10206 in July–October 2020 and August 2022. All observations were recorded in full polarization (RR, RL, LR, LL, where R and L represent right- and left-handed circular polarization), and averaged to 4-sec integrations. We observed the masers in two separate sets of spectral tunings, one set covering the ex-OH line (6035.092 MHz) and the other the methanol line (6668.519 MHz). In each tuning, the line was covered by a narrow spectral window 1 MHz wide, consisting of 512 channels with a separation of 0.1 km s^{-1}. Each observation was made at constant frequency. Four wide-band (~0.13 GHz each) spectral windows were also observed in the frequency ranges of 6.00–6.51 GHz and 6.30–6.81 GHz (for the ex-OH and methanol tunings, respectively). For each individual source, the ex-OH and methanol tunings were interleaved, changing frequencies every few hours to ensure as near-simultaneous observations as was practical. In some cases, different targets were also interleaved to optimize visibility plane coverage. The list of sources with their phase calibrators, total on-source time, and the central local standard of rest (LSR) velocities is given in Table 1. J1331+3030 (3C286) was observed as a flux and polarization angle standard. J0319+4130 (3C84) and J1407+2827 (OQ208) were observed as bandpass calibrators.

The data were processed using the e-MERLIN CASA 5.8 pipeline (Moldon 2021). The e-MERLIN pipeline includes time- and frequency-dependent calibration of the wide-band data, including estimating the flux scale in janskys and deriving corrections from the phase calibrator source. We calibrated the narrow-band data using CASA 5.8 (McMullin et al. 2007). The first step was flagging any remaining bad data. Then, we used the bandpass calibrator 3C84 to calculate corrections for the phase offset between the wide- and narrow-band data and applied these

[1] e-MERLIN is a National Facility operated by the University of Manchester at Jodrell Bank Observatory on behalf of STFC. https://www.e-merlin.ac.uk/

Table 1. Details of eMERLIN observations.

Source name (l b) (° °)	Phase calibrator	Number of scans exOH	meth	Total time on source exOH (h:m)	meth (h:m)	Center Vlsr exOH (km s^{-1})	meth (km s^{-1})
G20.237+0.065	J1818−1108	8	8	00:56	00:56	72.3	64.2
G24.148−0.009	J1825−0737	9	6	01:03	00:42	16.7	9.5
G25.648+1.049	J1827−0405	8	8	00:56	00:56	37.4	29.6
G34.267−0.210	J1858+0313	33	33	03:18	03:18	58.0	49.8
G43.149+0.013	J1922+0841	33	33	03:18	03:18	13.5	5.2
G48.990−0.299	J1922+1530	10	10	01:10	01:10	56.4	48.3
G49.490−0.388	J1924+1540	10	10	01:10	01:10	43.7	36.8
G69.540−0.976	J2010+3322	12	12	01:24	01:24	−8.7	−16.4
G81.871+0.781	J2018+3851	18	18	02:06	02:06	11.9	3.7
G108.766−0.986	J2301+5706	13	12	01:31	01:24	−66.0	−73.9

Table 2. Rms noises (1σ) in channels without emission for image cubes in each Stokes parameter.

Source name (l b)	$\sigma_{\mathrm{I\_meth}}$ (mJy beam^{-1})	$\sigma_{\mathrm{I\_exOH}}$ (mJy beam^{-1})	$\sigma_{\mathrm{Q\_exOH}}$ (mJy beam^{-1})	$\sigma_{\mathrm{U\_exOH}}$ (mJy beam^{-1})	$\sigma_{\mathrm{LHCP\_exOH}}$ (mJy beam^{-1})	$\sigma_{\mathrm{RHCP\_exOH}}$ (mJy beam^{-1})
G20.237+0.065	18.4	17.0	16.6	17.6	19.4	22.8
G24.148−0.009	28.7	12.7	12.3	12.6	16.9	15.9
G25.648+1.049	15.9	12.0	11.5	11.8	18.2	16.4
G34.267−0.210	16.3	8.0	8.1	8.9	11.4	10.1
G43.149+0.013	14.3	15.2	16.5	16.0	22.3	20.6
G48.990−0.299	55.6	15.9	16.4	15.9	23.0	20.7
G49.490−0.388	59.8	19.9	21.7	22.1	29.8	27.1
G69.540−0.976	18.3	17.8	18.2	17.5	20.6	21.1
G81.871+0.781	8.5	9.9	9.8	10.2	14.9	13.9
G108.766−0.986	13.9	27.2	22.5	21.9	33.5	31.7

to the narrow-band 3C84 data, along with the pipeline time-dependent wide-band delay, phase, and amplitude corrections. Next, we performed frequency-dependent calibration to derive a bandpass correction table for amplitude and phase. For ex-OH observations, we also derived corrections for polarization leakage (using 3C84, assumed to be unpolarized) and polarization angle by setting the Stokes parameter polarization flux densities for 3C286 for the known position angle (PA) of 33° (Perley & Butler 2013).

Next, we applied the narrow-band bandpass calibration, the offset correction, the phase calibrator solutions, and, when applicable, the polarization calibration to the narrow-band target data. We split out the corrected target data, adjusting to constant velocity (LSR, radio convention, relative to the rest frequency of the line) in the target frame. Lastly, we self-calibrated each target using a selected bright channel; for ex-OH, we took care to preserve the relative flux densities in RR and LL, and thus the accuracy of Stokes V (Green et al. (2007); Darwish et al. (2020), as implemented in CASA). We applied the solutions to all narrow channels and made spectral image cubes for each target (in full polarization, for ex-OH). Using uniform weighting to optimize resolution, the nominal 2-D Gaussian fits to the dirty beam varied from 121×26 mas at the lowest declination to 54×20 mas for the higher-declination targets (the long axis being close to N–S for the low-declination sources). Since the e-MERLIN beam is quite irregular, we used an intermediate weighting (robust 0.5) and a standard restoring beam of 65 mas×45 mas at a PA of −50°, which has a slightly larger area than the nominal beam fits. This minimizes sidelobe artifacts and makes it easier to compare the images. Since we use component fitting to make measurements, the exact beam shape does not affect the results.

We used the JMFIT procedure in AIPS (NRAO 2022; Greisen 2003) to fit 2D Gaussian components to Stokes I (total intensity) maser spots for both the methanol and ex-OH masers, and thus measured the positions and the peak flux densities. In addition, using the positions of the I Stokes ex-OH maser spots, we measured their Q and U Stokes parameters as well as the LHCP and RHCP. For further analysis, we took only those spots with a total intensity above 2σ that appear in at least two consecutive channels. Table 2 lists the root mean square (rms) for all cubes measured in channels without emission.

Tables 3 and 4 summarize the properties of the brightest maser spot in each source: the absolute coordinates (RA, Dec), the LSR velocity (V_{p}), and the peak flux density (S_{p}). The astrometric accuracies presented in both tables were calculated following the procedure described in Richards et al. (2022): (1) the uncertainty (δ_1) of the position of the phase calibrator, taken from VLBA Catalog[2], (2) the positional errors (δ_2) due to the image rms noise, calculated for the weakest spots to get their upper limits, (3) phase errors (δ_3) due to the phase-calibrator and target separation (including the time difference and the angular separation); values of δ_3 range from 12 to 81 mas, due to variations in atmospheric conditions, and 4) the antenna position errors (δ_4) – we assume a typical baseline error of 2 cm. The total astrometric accuracy is $\delta_{\mathrm{tot}} = (\delta_1^2 + \delta_2^2 + \delta_3^2 + \delta_4^2)^{0.5}$.

[2] https://obs.vlba.nrao.edu/cst/

Table 3. Parameters of the brightest methanol maser spot in each target.

Source name (l b)	$RA_{S_p^{6.7}} \pm \delta_{tot,RA}$ (h m s s)	$Dec_{S_p^{6.7}} \pm \delta_{tot,Dec}$ (° ′ ″ ″)	$V_p^{6.7}$ (km s^{-1})	$S_p^{6.7}$ (Jy beam^{-1})	T_B $\times 10^9$(K)	$\gamma_{6.7}$ (mas)
G20.237+0.065	18 27 44.5613±0.0029	−11 14 54.216±0.043	72.0	22.65	1.58	41.8
G24.148−0.009	18 35 20.9399±0.0014	−07 48 55.775±0.021	17.6	15.32	1.12	19.0
G25.648+1.049	18 34 20.9069±0.0032	−05 59 42.261±0.048	41.8	95.01	6.77	47.1
G34.267−0.210	18 54 37.2500±0.0029	01 05 33.615±0.043	54.5	5.90	0.41	42.2
G43.149+0.013	19 10 11.0464±0.0042	09 05 20.371±0.063	13.2	7.51	0.59	62.3
G48.990−0.299	19 22 26.1312±0.0014	14 06 39.696±0.021	71.5	2.78	0.19	20.5
G49.490−0.388	19 23 43.9461±0.0018	14 30 34.366±0.027	59.2	613.87	41.44	25.8
G69.540−0.976	20 10 09.0436±0.0025	31 31 34.989±0.038	14.6	65.14	4.39	36.7
G81.871+0.781	20 38 36.4097±0.0038	42 37 35.110±0.056	4.6	195.65	14.32	53.0
G108.766−0.986	22 58 51.1857±0.0018	58 45 14.380±0.026	−45.7	12.25	0.83	25.4

Notes. Note that the γ parameter is estimated for the weakest methanol spot.

Table 4. The parameters of the brightest ex-OH maser spots (Stokes I) in each target.

Source name (l b)	$RA_{S_p^{6.035}} \pm \delta_{tot,RA}$ (h m s s)	$Dec_{S_p^{6.035}} \pm \delta_{tot,Dec}$ (° ′ ″ ″)	$V_p^{6.035}$ (km s^{-1})	$S_p^{6.035}$ (Jy beam^{-1})	T_B $\times 10^7$(K)	$\gamma_{6.035}$ (mas)
G20.237−0.065	18 27 44.5623±0.0023	−11 14 54.065±0.034	71.4	1.29	9.89	32.6
G24.148−0.009	18 35 20.9398±0.0025	−07 48 55.773±0.037	17.2	1.14	8.68	35.8
G25.648+1.049	18 34 20.9313±0.0034	−05 59 42.655±0.051	39.5	1.55	12.72	49.7
G34.267−0.210	18 54 37.2497±0.0030	01 05 33.622±0.045	54.1	1.91	14.62	44.1
G43.149+0.013	19 10 11.0632±0.0037	09 05 20.250±0.056	11.1	1.44	10.24	54.4
G48.990−0.299	19 22 26.1350±0.0019	14 06 39.704±0.018	68.1	1.12	20.43	17.3
G49.490−0.388	19 23 43.9017±0.0015	14 30 33.548±0.023	54.8	5.32	40.14	22.1
G69.540−0.976	20 10 09.0859±0.0023	31 31 34.840±0.035	14.4	4.46	34.41	33.6
G81.871+0.781	20 38 36.4209±0.0054	42 37 34.741±0.081	6.7	2.72	20.67	79.1
G108.766−0.986	22 58 51.1786±0.0021	58 45 14.317±0.031	−45.9	0.83	6.27	30.2

Notes. Note that the γ parameter is estimated for the weakest ex-OH spot.

For the analysis of the coexistence of both maser transitions, we presumed that the lines coincide when: i) Their spectral features at least partially overlie each other in the LSR velocity range; we analyzed both polarizations of ex-OH to take into account the Zeeman splittings on this emission (see an example in Fig. 1). In the case of methanol emission, we neglected the splitting of the two polarizations due to the magnetic field, since its value is significantly smaller (less than one tenth) than the width of one spectral channel. ii) The angular separation between methanol and ex-OH spots is less than $0.5(\gamma_{6.7} + \gamma_{6.035})$, where γ is calculated as $(\delta_2^2 + \delta_3^2)^{0.5}$ for both transitions, respectively. Since we compare observations made with the same phase calibrator and antennas, we do not need to consider errors δ_1 and δ_4. The values of γ are listed in Tables 3 and 4, respectively.

3. Results

The distributions of the Stokes *I* maser spots and spectra of methanol and ex-OH are presented in the top panels on Figs. 2, 3, and B.1-B.8. When the coincidence of both transitions occurs, we mark them with non-filled symbols. The kinematic distances used to estimate linear sizes of sources were calculated using the parallax-based distance calculator[3] by Reid et al. (2019). In some cases, the ambiguity was resolved using the HI absorption by Green & McClure-Griffiths (2011). In the case of G48.990−0.299, G69.540−0.976, and G81.871+0.781, direct distance measurements were available via the trigonometric parallax method.

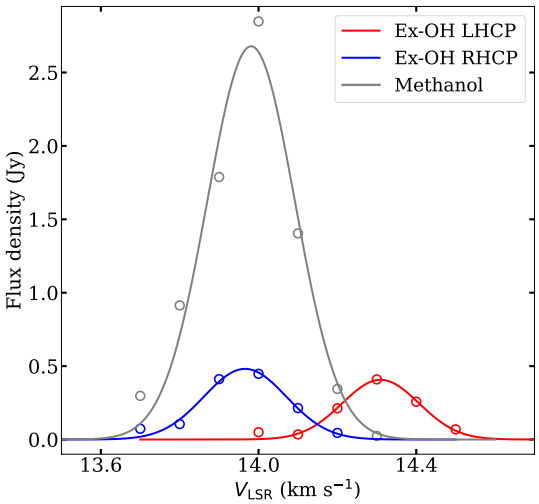

Fig. 1. Example of the overlap of both maser transitions when Zeeman splitting is identified in the ex-OH transition. Profiles are from a maser group in G43.149+0.013 named as Z_8 in ex-OH (Table C.1). The dots correspond to the flux density measured on single-channel maps, and the lines are Gaussian profiles fit to the spectral features.

[3] http://bessel.vlbi-astrometry.org/node/378

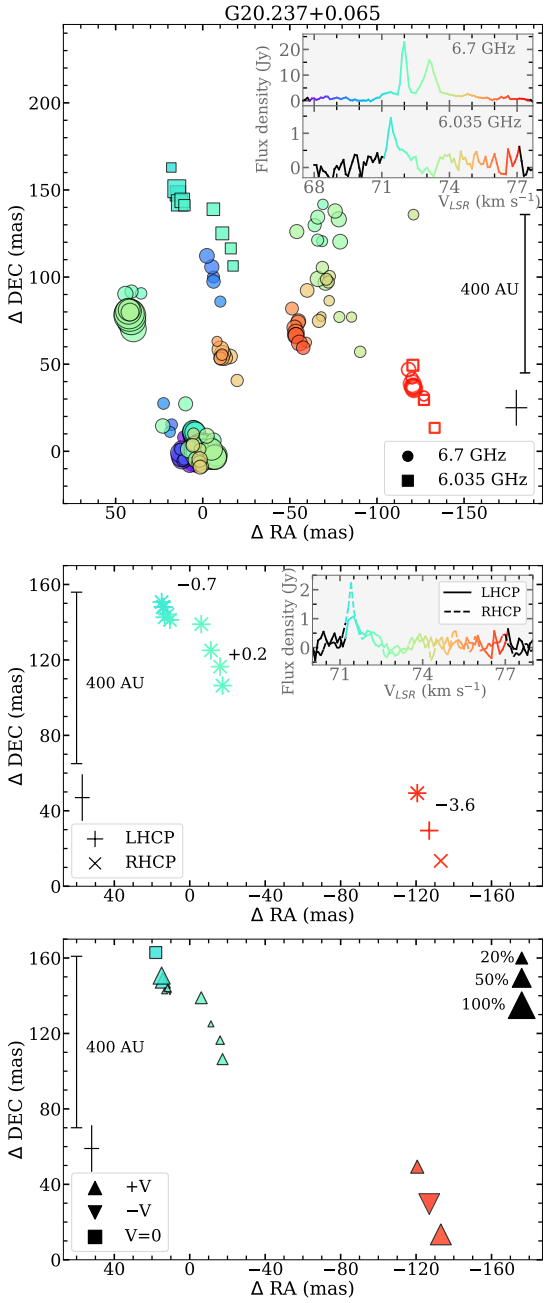

Fig. 2. Methanol and ex-OH maser emission in G20.237+0.065. *Top*: distribution of the 6.7 (circles) and 6.035 GHz (squares) Stokes *I* maser spots. Symbol size is proportional to the square root of intensity, and the color corresponds to the LSR velocity, as is given in the total intensity spectra inserted at the top. LSR velocity ranges with no detections are shown in black. Non-filled symbols correspond to cases in which the coincidence of both transitions occurs. *Middle*: distributions of LHCP and RHCP of ex-OH maser spots. Numbers are the values of the line-of-sight magnetic field strength (in milligauss). *Bottom*: distribution of *V* Stokes of ex-OH. Symbol size is proportional to the degree of circular polarization. The black cross indicates the maximum position error for the spot position.

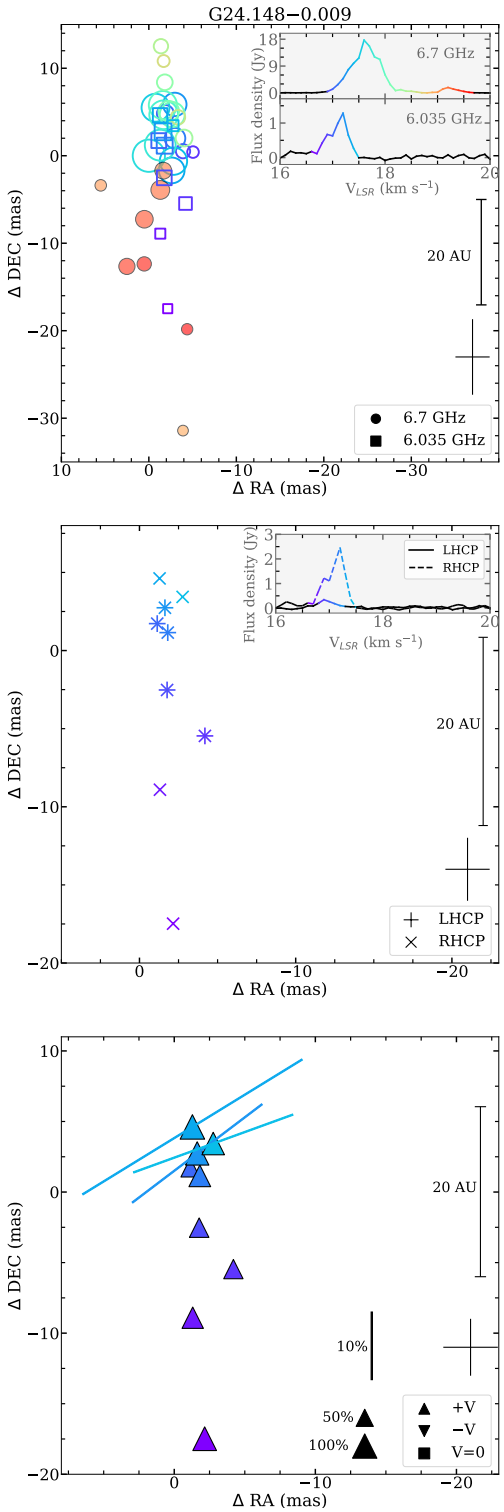

Fig. 3. Same as Fig. 2 but for G24.148−0.009. In the *bottom panel*, the bars represent the direction of the planes containing the electric field vector. Their lengths are proportional to the percentage of linear polarization and their colors correspond to the LSR velocity, as is indicated in the inserted spectra in the *top and middle panels*.

The LHCP and RHCP ex-OH emission is presented in the middle panels of Figs. 2, 3, and B.1-B.8, where we also give the magnetic field strength along the line of sight derived from the identified Zeeman pairs. The relationship between Stokes *I* and both circular polarizations is: 0.5×(RHCP+LHCP). As is noted in Sect. 2, we measured the properties of RHCP and LHCP spots in the same position as I spots in each channel to ensure that we sampled the same gas when identifying Zeeman pairs. Only position error δ_2 is applicable to comparisons within the same data cube. The worst accuracy for the faintest spots is ∼16 mas, which is less than the physical size of the emitting regions,

estimated from the angular extent of series of spots in consecutive channels, ensuring that detected associations between the polarizations are genuine.

Table C.1 lists the parameters of the identified Zeeman pairs: the flux density of the brightest maser spot in each polarization ($S_{\rm max}$) and the parameters of the fit Gaussian profile to the spectrum; the peak amplitude ($S_{\rm fit}$), the full width at half maximum of the profile ($FWHM_{\rm fit}$), and the peak velocity ($V_{\rm fit}$). We also list $\Delta V_{\rm Z} = V_{\rm fit}$(RHCP)$-V_{\rm fit}$(LHCP), with the errors based on the accuracy of the fit Gaussian profiles, and the de-magnetized velocity that is assumed to be the mean of velocities of both polarized peaks: $V_{\rm d} = 0.5\times(V_{\rm fit}$(RHCP)$+V_{\rm fit}$(LHCP)). Using the formula $\Delta V_{\rm Z}/B$ =0.056 from Baudry et al. (1997), we calculated the magnetic field along the line of sight ($B_{\rm los}$), which is included in Figs. 2, 3, and B.1–B.8. The field is directed away from us when $V_{\rm fit}$(RHCP) > $V_{\rm fit}$(LHCP) and is directed toward us when $V_{\rm fit}$(RHCP) < $V_{\rm fit}$(LHCP).

The bottom panels in Figs. 2, 3, and B.1-B.8 show the circular and linear degrees of polarization of ex-OH emission. They were calculated as follows: $m_{\rm c} = V/I$ and $m_{\rm l} = P_{\rm l}/I$, respectively. The V Stokes parameter, which is defined as 0.5×(RHCP−LHCP), and the linearly polarized flux density, $P_{\rm l}$, which is defined as $(Q^2 + U^2)^{0.5}$, are also presented. All spots with nonzero linearly polarized emission are summarized in Table C.2 with their values of I, Q, U, $P_{\rm l}$, and $m_{\rm l}$, the electric vector PA (defined as $\chi_{\rm l} = 0.5\times\arctan(U/Q)$, positive from north to east), $m_{\rm c}$, and the total polarization $m_{\rm f} = \sqrt{m_{\rm l}^2 + m_{\rm c}^2}$. The linear polarization vector is directed along the PA of the electric vector. The orientation of the magnetic field, $\Phi_{\rm B}$, is perpendicular to the linear polarization vector for σ components. When the fraction of linear polarization exceeds 71%, the amplification of π component gain is high and so $\Phi_{\rm B}$ can become parallel (e.g., Fish & Reid 2006).

We calculated the brightness temperature ($T_{\rm B}$) as in Wrobel & Walker (1999), for the brightest maser in each source and transition. Since the maser spots are unresolved and we used the synthesized beam size as the area of the emission, $T_{\rm B}$ is a lower limit. Below, we describe the individual sources in detail.

G20.237+0.065 (hereafter G20)

The maser distributions of G20.237+0.065 are presented in Fig. 2. The calculated near-kinematic distance is 4.41±0.39 kpc; the kinematic distance ambiguity was resolved by Green & McClure-Griffiths (2011) through HI self-absorption. The methanol maser emission is spread over 170 mas×150 mas, corresponding to 750 au×660 au. The morphology is complex, as was noted by Bartkiewicz et al. (2016) based on EVN images. The ex-OH emission lies within a region of similar extent, 150 mas×150 mas (660 au×660 au), but this line is significantly weaker and has a simpler structure – two groups of spots in the northeast and one in the southwest. The 6.7 GHz transition covers a $V_{\rm LSR}$ range from 67.7 to 77.5 km s^{-1}, and the 6.035 GHz transition covers from 71.1 to 77.0 km s^{-1}. We notice that in the most redshifted group, in the southwest, the two transitions coincide in velocity (within 0.5 km s^{-1}) and position (within 34 mas) and can be assumed to be coexisting in the same volume of gas, as was analyzed according to the procedure described in Sect. 2: 34 mas ≤ 0.5(42 mas+33 mas). The brightness temperature ($T_{\rm B}$) is at least 1.6×10^9 K for the methanol masers and 9.9×10^7 K for the ex-OH masers.

We identify three Zeeman pairs (Z_1-Z_3) in the ex-OH line, which indicate magnetic field strengths from +0.2 to −3.6 mG (Table C.1). The magnetic field is directed toward the observer, with a possible reversal toward the middle group. The degree of circular polarization is below 40% for Z_1 and Z_2; for the redshifted pair (Z_3), we detect 29–74% of circular polarization. We did not detect linear polarization from this source above a threshold of 34 mJy (3σ), implying that the magnetic field lines may be oriented closer to the line of sight.

There is another 6.7 GHz masing region 8.″6 toward the northeast, G20.239+0.065 (see Sect. 4.1). We recovered the methanol emission similarly as Bartkiewicz et al. (2016) but we have no detection of ex-OH maser above a threshold of 51 mJy beam^{-1} (3σ).

G24.148−0.009 (hereafter G24)

The maser emission from both transitions is presented in Fig. 3. The near kinematic distance is 1.66±0.25 kpc with a probability of 69%, corresponding to the central velocity[4] of 18.1 km s^{-1}. The masing region is compact and elongated in the north-south direction. The centroids of the 6.7 GHz spots occur within an area of 11 mas×44 mas (18 au×73 au) and those of the ex-OH spots within an area of 3 mas×22 mas (5 au×37 au). The emission covers the velocity ranges from 16.8 km s^{-1} to 19.6 km s^{-1} at 6.7 GHz and from 16.6 km s^{-1} to 17.4 km s^{-1} at the 6.035 GHz line. Coexistence of both lines occurs in the whole masing region except for the redshifted emission of the methanol line. The $T_{\rm B}$ is at least 1.1×10^9 K for methanol masers and 8.7×10^7 K for ex-OH masers.

We are not able to identify Zeeman splitting due to a different number of spectral features in each polarization and attenuation or suppression of the LHCP feature, therefore estimation of the strength of the magnetic field is impossible. The source is strongly polarized (bottom panel of Fig. 3); $m_{\rm c}$ is from 59% to 100%, and three out of nine spots show $m_{\rm l}$ within a range from 24% to 38%. The directions of linear polarization vectors are from −52° to −70° (Table C.2), indicating a magnetic field oriented nearly northeast-southwest at $\Phi_{\rm B}$ = +30±6°.

G25.648+1.049 (hereafter G25)

The maser distribution is presented in Fig. B.1. The near kinematic distance is 3.8±1 kpc with a probability of 70% for the central velocity of 41.4 km s^{-1}. Green & McClure-Griffiths (2011) obtains a far kinematic distance of 12.5±0.4 kpc, derived from HI self-absorption.

The regions of methanol and excited OH emission are clearly separated both in the spatial and in the velocity domain. Each transition forms three groups and ex-OH masers lie southward relative to the methanol masers. The 6.7 GHz maser covers an area of 450 mas×325 mas (1700 au×1225 au and 5600×4100 au for the near and far kinematic distances, respectively) and appears at a velocity range of 38.3–43.8 km s^{-1}, whereas the 6.035 GHz maser is spread over 300 mas×100 mas (1130 au×377 au and 3750×1250 au for the near and far kinematic distances, respectively) and covers a velocity range of 38.3–39.9 km s^{-1}. The smallest angular separation between these two transitions is ∼50 mas. The $T_{\rm B}$ is at least 6.8×10^9 K for the methanol masers and 1.3×10^8 K for the ex-OH masers.

Three Zeeman pairs are identified, showing a similar line-of-sight magnetic field strength from −6.2 to −7.0 mG and indicating that the magnetic field is directed toward the observer

[4] We use the central velocity of masers, in cases where we do not have measurements of systemic velocities.

(Table C.1). The emission shows strong circular polarization; 16 out of 31 spots are polarized above 80%, and seven spots have m_c below 50%. One spot has linear polarization with m_l=95% and a PA of +5° (Table C.2), indicating a magnetic field directed east-west with $\Theta_B = -85 \pm 2°$. We did not find strong evidence for the existence of a π component (see Sect. 4.3.3), so we assume that the linear polarization comes from σ components and that Θ_B is perpendicular to the linearly polarized vector.

G34.267−0.210 (hereafter G34)

The results are presented in Fig. B.2. The near and far kinematic distances are 2.94±0.18 kpc and 9.6±0.5 kpc, with similar probabilities (Reid et al. 2019). The methanol maser emission is significantly more complex compared with ex-OH. It is spread over an area of 125 mas×220 mas (370 au×650 au and 1200 au×2100 au for the near and far kinematic distances, respectively) and emission occurs in the LSR velocity range from 47.8 to 54.9 km s^{-1}. The redshifted part is located in the east and coincides with the ex-OH maser spots within 40 mas and 0.1 km s^{-1}. The T_B is at least 4.1×10^8 K for the methanol masers and 1.5×10^8 K for the ex-OH masers.

We are not able to identify any Zeeman pairs in the ex-OH transition. The LHCP emission is brighter but RHCP shows a more complicated spectrum. We notice a clear shift in velocity between these two polarizations, with RHCP being more positive; that indicates that the B_{los} is directed away from the observer and puts a lower limit on the magnetic field strength of 2.84 mG. Six out of eleven spots have m_c above 80%, and seven spots show m_l from 6% to 36%. The planes of electric vectors rotate from one masing group to another over 50 au without any systematic changes. Φ_B for the brightest four spots is −58±21°, while for three weaker it is +23±3°. Therefore, we cannot clearly state the direction of the magnetic field in this target.

G43.149+0.013 (hereafter G43)

The ex-OH and methanol maser emission is presented in Fig. B.3. This target is part of the high-mass star formation region W49N lying at a distance of $11.11^{+0.79}_{-0.69}$ kpc (Zhang et al. 2013). In this source, the ex-OH masers are more complex than the methanol masers. The ex-OH emission is spread over 280 mas×250 mas (3100 au×2800 au) and over a LSR velocity range of 9.5–14.5 km s^{-1}. It forms two groups elongated perpendicular to each other (the blueshifted emission is at a PA, from north to east, of +77°, while the redshifted emission is at −53°). The methanol masers appear at redshifted velocities from 13 km s^{-1} to 14.2 km s^{-1}, in three groups, similar to the appearance in VLBI images (Bartkiewicz et al. 2014), over a region of 150 mas×110 mas (1700 au×1200 au). We notice the coincidence of both maser transitions in these three groups. The brightest, blueshifted part of the ex-OH transition appears not to have methanol maser counterparts. The T_B is at least 5.9×10^8 K for the methanol masers and 1.0×10^8 K for the ex-OH masers.

We identify eight Zeeman pairs. The two most easterly ones imply values of the magnetic field strength above +3.0 mG directed away from the observer, while in the remaining clumps the field is directed toward the observer with values from −1.3 to −6.5 mG. That indicates the reversal of the magnetic field. Twenty out of fifty-four spots are circularly polarized above 80% and twenty-two spots below 50%. Eight spots (all belonging to three Zeeman pairs) show linear polarization, from 8% to 48%. The mean Φ_B of the eastern part is −66±24°, while the electric vector of the redshifted linearly polarized ex-OH spot is 15°, indicating that Φ_B=−75±9°. Such differences in the spot distributions and the orientation of the magnetic field may indicate that these two regions are related to diverse kinematic regions.

G48.990−0.299 (hereafter G48)

The results are presented in Fig. B.4. The distance is $5.62^{+0.59}_{-0.49}$ kpc, as was estimated by Nagayama et al. (2015). Again, in this target, the ex-OH emission is more complex than the methanol masers. The methanol maser emission shows a simple structure, two spots at LSR velocities of 71.5 km s^{-1} and 71.6 km s^{-1}. The ex-OH masers appear in a wider velocity range from 66.7 to 69.6 km s^{-1} and cover a region of 290 mas×135 mas, which corresponds to 1630 au×760 au. They are elongated along a line from southeast to northwest. The T_B is at least 1.9×10^8 K for the methanol masers and 2.0×10^8 K for the ex-OH masers. Nagayama et al. (2015) report water maser emission at 22 GHz at LSR velocities from 65 km s^{-1} to 68 km s^{-1} showing north-south elongation and proper motions implying expansion.

The ex-OH transition forms four Zeeman pairs. Two western groups have positive values of B_{los} (+2.7 and +2.3 mG), directed away from the observer, and two eastern groups, separated by ∼250 mas, have negative values (−0.7 and −4.8 mG) of B_{los}, indicating a magnetic field directed toward the observer. Circular polarization is below 50% for 18 out of 29 spots and above 80% for 5 out of 29 spots. Linear polarization is detected for six spots in the two brightest groups, with degrees 8–31%. The electric vectors are consistent over the whole region with PAs from −17 to −56°, indicating Φ_B= +54±7°. Again, we see a clear reversal of the line-of-sight magnetic field.

G49.490−0.388 (hereafter G49)

This target belongs to the well-known high-mass star formation region W51. The ex-OH and methanol maser emission is presented in Fig. B.5. The distance is $5.41^{+0.31}_{-0.28}$ kpc, based on the trigonometric parallax measurement using water masers by Sato et al. (2010); we note that the result of $5.1^{+2.9}_{-1.4}$ kpc using 12.2 GHz methanol masers, by Xu et al. (2009), is less accurate. The 6.7 GHz methanol maser emission covers an area of 0.″47×0.″55, corresponding to 2550 au×3000 au, and appears in two velocity ranges, from 51.2 to 52.3 km s^{-1} and from 57.5 to 60.2 km s^{-1}. The emission is very bright, with a maximum flux density of 684 Jy. The morphology agrees well with the distribution derived from EVN observations, but it is more extended. Fujisawa et al. (2014) reported a smaller masing region of 0.″37×0.″31. However, Etoka et al. (2012) imaged emission over 3″×2″. Ex-OH masers are weaker with a maximum flux density of 7 Jy and are located in the west over a region of 0.″27×0.″53 (1460 au×2870 au) at intermediate LSR velocities from 51.6 to 58.3 km s^{-1}. Like Etoka et al. (2012), we do not find any spatial overlap between the two transitions. The T_B is at least 5.9×10^8 K for the methanol masers and 1.0×10^8 K for the ex-OH masers.

We identified nine Zeeman pairs. Z_1-Z_3 are new ones compared with the results of Etoka et al. (2012) (their Table 3). For all groups, the field is directed away from the observer, and its values are from +3.3 mG to +8.1 mG, which is consistent with Etoka et al. (2012). The emission is strongly polarized; 41 of 85 spots have a degree of circular polarization above 80% and only 20 spots below 50%. Twenty spots in four Zeeman pairs show linear polarization in the range 5–22%. The mean PA of the electric vectors of 0±10°indicates the magnetic field oriented at −90°. However, we notice different values of χ_1 for each maser group, similar to in G34.

G69.540−0.976 (hereafter G69)

This target is associated with the high-mass star formation region Onsala 1 (ON1). The maser distributions are presented in Fig. B.6. The distance based on the trigonometric parallax is $2.57^{+0.34}_{-0.27}$ kpc (Rygl et al. 2010). The methanol masers cover an area of 0.″47×1.″09, or 1220 au×2800 au, over two ranges of LSR velocities, from −0.5 km s^{-1} to 2.6 km s^{-1} and from 14.1 km s^{-1} to 15.7 km s^{-1}. The observed spatial distribution of the 6.7 GHz masers is more complex compared to images obtained using EVN in 2006–2008 by Rygl et al. (2010), since these authors reported only two groups with an angular separation of 0.″94. However, our results agree well with the EVN images taken in 2015 by Surcis et al. (2022), in which three groups were reported similarly as by Sugiyama et al. (2011) using JVN in 2006–2008. The ex-OH masers are spread over 1.″05×1.″08, i.e. 2690 au×2775 au, and also come from two velocity ranges: from −1.6 km s^{-1} to 2.3 km s^{-1} and from 12.2 km s^{-1} to 15.2 km s^{-1}. We identify two regions where the overlap of both transitions is seen: in the north, the blueshifted masers coincide within 46 mas (33.8 mas in RA and 31.6 mas in Dec); and in the south, the redshifted masers coincide within 28 mas (23.6 mas in RA and 13.6 mas in Dec). The T_B is at least 4.4×10^9 K for the methanol masers and 3.4×10^8 K for the ex-OH masers.

We identify five Zeeman pairs in the ex-OH transition, at redshifted velocities, implying a negative magnetic field (directed toward us): B_{los} is from −1.2 mG to −6.2 mG. The same five pairs were reported by Green et al. (2007). We are not able to identify the Zeeman splitting for the blueshifted emission due to different LCHP and RCHP spectral features. The degree of circular polarization is below 50% for 59 of 96 spots and above 80% for 38 spots. In each Zeeman pair, there are spots (in total 26) that are linearly polarized with degrees from 8% to 48%. The means of Φ_B are: $-50 \pm 17°$ for the northern and blueshifted region and $+80 \pm 12°$ for the southern and redshifted region. Green et al. (2007) reported two ex-OH features with m_l of 18.5% and 10% and χ_l of $-87.7° \pm 2°$ and $-42.5° \pm 0.7°$, respectively. They correspond to the spots at the LSR velocity of 14.3–14.5 km s^{-1} listed in Table C.2. We note that Surcis et al. (2022) estimated a mean magnetic field direction of $-51 \pm 69°$ from linearly polarized methanol masers.

G81.871+0.781 (hereafter G81)

This target is in the well-known high-mass star formation region W75N. Its distance is 1.30±0.07 kpc (Rygl et al. 2012). The methanol and ex-OH maser distributions are presented in Fig. B.7. The methanol masers are spread over an area of 0.″49×1.″065, or 638 au×1384 au, and appear in the V_{LSR} range of 2.6–9.7 km s^{-1}. That is consistent with EVN results from Rygl et al. (2012). Ex-OH maser emission is less complex; it is located in the central part of the 6.7 GHz emission over an area of 59 mas×312 mas (77 au×406 au), over a V_{LSR} range of 6.2–9.2 km s^{-1}. It appears as three groups. We notice an overlap between the two masers in the southern group: two spots coincide within 21 mas (15.3 mas in RA and 14.7 mas in Dec). Similarly, in the northern group, six spots coincide within 65 mas (22 mas in RA and 61.6 mas in Dec), and in the centrally located group, nine spots coincide within 61 mas (33.7 mas in RA and 50.5 mas in Dec). The T_B is at least 14.3×10^9 K for the methanol masers and 2.1×10^8 K for the ex-OH masers.

We report three Zeeman pairs, for which the B_{los} is positive and directed away from the observer with values of +2.3 mG for the southern group and of +7.3 and +8.5 mG for the central pairs. In the northern group, we are not able to identify LHCP and RHCP features belonging to a likely Zeeman pair. The degree of circular polarization is above 80% for 16 of 39 spots and below 50% for 14 spots. Fourteen spots show linear polarization, the majority of which have a degree from 4% to 15%. Three redshifted spots at V_{LSR} 8.3–8.6 km s^{-1} are much more polarized; their degrees are 38–58%. The mean value of the PAs of the electric vector planes is 29±13°, indicating a magnetic field directed approximately along −61°. Again, the source shows diverse directions of the magnetic field, possibly reflecting changes in the gas kinematics.

G108.766−0.986 (hereafter G108)

The distributions of both methanol and ex-OH masers are compact (8 mas×11 mas and 7 mas×30 mas, respectively) and well separated in position (by around 80 mas). These are presented in Fig. B.8. The near kinematic distance is 2.81±0.23 kpc, with a probability of 72% for the central velocity of −45.6 km s^{-1}, implying a spatial separation between the two maser transitions of 225 au. Both lines appear at a similar LSR velocity range, from −46.4 km s^{-1} to −44.8 km s^{-1} for the methanol maser and from −46.1 km s^{-1} to −44.8 km s^{-1} for the ex-OH maser line. The smallest angular separation between the two masers is 67 mas, which exceeds twice the γ parameter, and we assume no overlap of both transitions. The T_B is at least 8.3×10^8 K for the methanol masers and 6.3×10^7 K for the ex-OH masers.

We identify two Zeeman pairs and we estimate the value of the magnetic field as −8.5 mG and −10.5 mG, indicating that the B_{los} is directed toward the observer. The ex-OH emission consists of 12 spots, of which three are more than 80% circularly polarized and two are less than 50% polarized. Only one spot shows linear polarization with a degree of 12%, indicating the value of $\Theta_B = +22 \pm 9°$.

4. Discussion

4.1. Counterparts

First, we discuss the counterparts of HMYSOs at other frequencies to derive information on the HMYSO environment on a larger scale. Centimeter radio emission identifies thermal jet or UCHII regions and, thus, a more evolved stage of the HMYSO. The earliest phases are seen in the ALMA dust continuum emission at 1 and 3 mm, which identifies star-forming cores, disks, and envelopes. To trace outflows, and in particular the outflow direction, which is interesting to compare to the magnetic field orientation, we used 22 GHz water masers and archival ALMA[5] spectral line data of SiO, SO, and the CO isotopologs in ALMA Band 6. The SiO, SO, and water masers are all shock tracers, while the CO isotopologs (^{12}CO, ^{13}CO) trace large-scale gas motions. We typically used ^{13}CO because it is more widespread and brighter than the (often) optically thin C^{18}O transition but not as optically thick (and complex) as the ^{12}CO line. For warm gas, CH_3CN and HC_3N can be used as disk tracers, and the CH_3CN K ladder to obtain rotational temperatures and H_2CO along with thermal methanol to trace young star-forming object (YSO)-heated gas. To constrain the clump properties, we used *Spitzer* 3.5, 4.5, 6, 8, and 24 μm, and *Herschel* 70 μm data that trace the warm dust heated by the central object(s). In

[5] The ALMA Science Archive is available at https://almascience.org/aq/?result_view=observations

Table C.3, we list the HMYSOs' positions from the Hi-GAL catalog (Molinari et al. 2016a,b; Elia et al. 2021). The Herschel astrometric accuracy is ∼2 arcsec (Molinari et al. 2016a). The target positional accuracy of *Spitzer* is about 1 arcsec, and the angular resolution is ∼2 arcsec[6]. The detailed descriptions of counterparts of all sources along with figures are in Appendix D.

4.2. Evolutionary stage

As a tracer of warm dust, the far IR 70 μm emission increases in strength as the protostar evolves. Table C.3 shows the strongest 70 μm emission for G49 and for G43, G25, and G48. That suggests that those objects are the most evolved in our sample. G20, G24, and G34 show weak 70 μm emission, indicating an earlier evolutionary phase, but the ratio $S_{70\ \mu m}/S_{24\ \mu m}$ suggests that only G34 is an early HMYSO. We do not have information about 70 μm emission for G69, G81, and G108. Another evolutionary indicator is $\frac{L_{bol}}{M}$ (Molinari et al. 2008). Higher values indicate a later evolutionary phase. This criterion also supported G43 as the most evolved source, followed by G25; these sources are also characterized by the highest average dust temperatures in our sample, of 39 and 40 K, respectively. Based on the $\frac{L_{bol}}{M}$ indicator, G20 and G34 are the youngest sources, and G24 and G48 are slightly more evolved. All those sources have T_D in the range between 21 and 25 K. We do not have information about $\frac{L_{bol}}{M}$ and T_D for G49, G69, G81, and G108. Both indicators, IR 70 μm emission as well as $\frac{L_{bol}}{M}$, concern the evolutionary states of clumps, but these can host more than one core or YSO. A better evolutionary indicator for a single YSO is the existence of thermal jets or a UCHII region. The sources with the strongest UCHII emission are G69, G43, and G48. In the case of G20 and G24, we did not find any confirmation as to whether observable radio continuum emission is related to a UCHII region or to a jet. However, the $S_{70\ \mu m}/S_{24\ \mu m}$ ratio indicates that both sources are in late evolutionary phases, so we can assume that the radio continuum emission is related to UCHII emission, rather than to a thermal jet. G81 is associated with the radio continuum VLA1, which was identified as a radio jet. Also, G25 shows evidence that the radio continuum is associated with the radio jet. G34 and G108 do not have observable radio continuum emission. G49 is close to the UCHII but the maser emission can be related to the eastern core, which is the dominant accretion source in that region (Shi et al. 2010) and where the radio continuum was not detected (Gaume et al. 1993). We further analyze the source evolutionary phase in Sect. 4.4.

4.3. Polarization properties and magnetic field

4.3.1. Zeeman pairs

In total, we have identified 37 Zeeman pairs in eight HMYSOs: G20, G25, G43, G48, G49, G69, G81, and G108. We list the observed and fit peak flux densities and other parameters for all Zeeman pairs in Table C.1. Toward G24, we are not able to identify any Zeeman splitting due to the weakness of LHCP emission, and similarly, toward G34, we do not report any Zeeman splitting since it is impossible to define clearly the RHCP feature related to the single LHCP feature appearing in the ex-OH emission. The calculated magnetic field along the line of sight is from 0.2 mG up to 10.6 mG, with mean and median values of 4.8 mG and 5.2 mG, respectively. These values are typical for high-mass star-forming regions (e.g., Bartkiewicz et al. 2005; Fish et al. 2005; Vlemmings 2008; Green et al. 2015). However, Surcis et al. (2022) report slightly higher $|B_{los}|$, in a range from 9 mG to 40 mG in their sample of 31 targets, based on methanol masers' 6.7 GHz transition.

[6] https://irsa.ipac.caltech.edu/

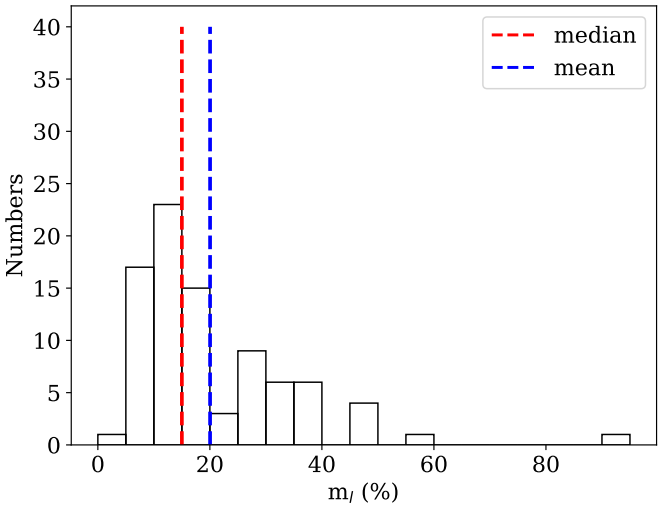

Fig. 4. Histogram of the percentage of linear polarization of all spots with detected linearly polarized emission. They are listed in Table C.2.

The direction of B_{los} is consistent for all measurements for five sources. The magnetic field is directed toward the observer in G25, G69, and G108 and away from the observer in G49 and G81. In the case of G43 and G48, we observe magnetic field reversals similar to the one reported for Cep A (Bartkiewicz et al. 2005). This may indicate a toroidal component of the magnetic field related to a disk. We do not notice any dependence between the size of the masing region and the magnetic field reversals. G43 and G48 are sampled by the Zeeman pairs over regions of 2000–3600 au, similar to G69, which shows the magnetic field directed to the observer over the whole region.

The relationship between the strength of the magnetic field and gas number density in molecular clouds in which the contraction is driven by ambipolar diffusion is defined as $|B| \sim n^{0.47}$ (Crutcher 1999). We estimated the gas density following Bayandina et al. (2014), considering B_{los} in the range of 0.2–10.6 mG, which leads to derived gas densities (n_{H_2}) in the range from 0.1 to 378×10^6 cm^{-3}.

4.3.2. Sky-plane B orientation

In nine HMYSOs, we found linearly polarized ex-OH masers: G24, G25, G34, G43, G48, G49, G69, G81, and G108. The linear polarization percentage is generally low, less than 40% for the majority of spots, and the mean and medium are 20% and 15%, respectively (Fig. 4). G49 and G69 show the most numerous linearly polarized spots (more than 20).In two sources, G25 and G108, we found only one maser spot with m_l of 95% and 12%, respectively. In G25, a linearly polarized ex-OH maser spot indicates that the plane of the magnetic field is −85 ± 2°if the emission is associated with a σ component or +5 ± 2°if the emission is associated with a π component. In both cases, the magnetic field is not parallel or perpendicular to the outflow.

In G20, we did not find any linearly polarized emission above a threshold of 2σ, implying that the magnetic field lines may be oriented closer to the line of sight. In G24 and G48, the electric vectors are well ordered, as are the vectors for the most blueshifted emission from G43. That indicates a consistent

Table 5. Comparisons of positions angles of the magnetic field, methanol maser distributions, ex-OH distributions, and the PAs of outflows.

Source	Φ_B (°)	$PA_{6.7}$ (°)	$PA_{6.035}$ (°)	PA_{out} (°)	$\lvert PA_{6.7}\text{-}PA_{6.035}\rvert$ (°)	$\lvert\Phi_B\text{-}PA_{out}\rvert$ (°)	$\lvert\Phi_B\text{-}PA_{6.7}\rvert$ (°)	$\lvert\Phi_B\text{-}PA_{6.035}\rvert$ (°)
G20.237	–	−70	+50	–	60	–	–	–
G24.148	+30±6	−1	+2	+90	3	60	21	28
G25.648	*−85±2*	−72	+84	−30	24	*55*	*13*	*11*
G34.267	+80±23	+8	+24	–	16	–	72	56
G43.149	−66±24/−75±9(*)	–/−54	+77/−53(*)	*+40*	–/1	*106/115*	-/21	37/22
G48.990	+54±7	*+44*	−69	+20 (1)	67	30	*10*	57
G49.490	−90±10	+41	+10	−46 (2)	31	44	49	80
G69.540	−50±17/+80±12(**)	+39/−68(**)	+47/−60(**)	−69 (3)	8/8	19/31	89/32	83/40
G81.871	−61±13	−4	−7	+43 (4)	3	76	57	54
G108.766	+22±9	−68	+4	–	72	–	90	18

Notes. Less reliable values are marked by italics: methanol maser emission in G48 consists of only two spots; therefore, the determined PA is not precise. (*)Ex-OH masers in G43 form two diverse regions: eastern (blueshifted) and northwestern (redshifted), respectively. (**)Ex-OH and methanol masers in G69 form two regions: northern blueshifted and southern redshifted emission. PA_{out} is estimated based on (1)Nagayama et al. (2015), (2)Goddi et al. (2020), (3)Kumar et al. (2004), (4)Torrelles et al. (1997).

large-scale magnetic field orientation in the sky plane. Similar well-ordered linear polarized vectors were noticed by Surcis et al. (2013, 2015, 2019, 2022) from observations of bright 6.7 GHz methanol masers.

In G34, G49, G69, and G81, and the more redshifted parts of G43, the directions of electric vectors are strongly variable, and changes do not correlate with spot velocities. Koch et al. (2018) used ALMA dust polarization observations to estimate the direction of the magnetic field at different angular scales in G49 (W51e2e): at a resolution of 2 arcsec, the magnetic field is directed almost east to west, while at the higher angular resolution it is radially distributed, suggesting that the field is being dragged by the mass inflow. Ex-OH masers, lying offset from the young star and indicating a mean magnetic field oriented from east to west, fit well into this picture by tracking the large-scale magnetic field. Etoka et al. (2012) inferred that the ex-OH was part of a flow in which the dynamics were magnetically dominated.

The magnetic field in G81, estimated from 18 cm OH masers by Hutawarakorn et al. (2002), reverses its direction on opposite sides of the disk, indicating a toroidal component of the magnetic field in the disk. Surcis et al. (2011) analysed the 22 GHz water masers associated with the VLA 1 and VLA 2 radio continuum sources. They reported a tightly ordered magnetic field around VLA 1 (aligned with the large-scale molecular outflow) and revealed an ordered magnetic field around VLA 2 (not parallel to the outflow). These strong magnetic fields, 0.7 G and 1.7 G, around VLA 1 and VLA 2, respectively, are related to shock compression of the gas. It is not easy to compare our results with the previous observations due to the time difference and proper motions of masers, which might be significant at this relatively close distance. We do not detect such a magnetic field reversal, since the ex-OH masers trace a more compact region than the 18 cm OH masers (2 arcsec). The magnetic field strength and orientation (away from the observer) derived from Zeeman splitting of ex-OH is consistent with measurements of the Zeeman splitting of 18 cm OH (see Fig. 11 of Hutawarakorn et al. 2002).

Table 5 lists the mean directions of the magnetic fields estimated using linearly polarized ex-OH masers (Φ_B), methanol and ex-OH elongation directions ($PA_{6.7}$ and $PA_{6.035}$), estimated from least-square fitting to the spot distributions. These are compared with the directions of outflows (PA_{out}) where available (see Sect. 4.1). Based on the Kolmogorov-Smirnov test, we cannot find any correlation for the linear distributions of both masers with the outflows and with the estimated magnetic field orientations in the sky plane as well as between outflows and magnetic field vectors themselves. Even for the targets with the most elongated maser structures, such as G24, G43, G48, or G81, we still cannot sketch a clear scenario relating to maser structures and the magnetic field. This is similar to the conclusions of Surcis et al. (2013). However, in Surcis et al. (2022), the summary for a whole sample of 31 targets reports a bimodal distribution, with: 1) half the magnetic field directions being perpendicular, and 2) the other half being parallel to the outflow. It is difficult to study dependencies between sub-arcsecond maser data and images with a larger angular scale searching for outflows and disks.

4.3.3. Zeeman triplets

Green et al. (2015) found 18 Zeeman triplet candidates among 112 Zeeman patterns in the ex-OH transition (detection rate of 16%) when using ATCA with a spectral resolution of 24 m s^{-1}. As we reported above, we detected 37 Zeeman pairs. The circularly polarized features (RHCP and LHCP) are the σ components of the Zeeman splittings; they are shifted in the velocities by the magnetic field. A third component, the π component, is the linearly polarized feature, unshifted in velocity. When comparing the Zeeman pairs and the linearly polarized spots that we identified (Tables C.1 and C.2), we find that in eight cases (21%), namely Z_3 and Z_4 of G48, Z_6 and Z_7 of G49, Z_1, Z_2, and Z_5 of G69, and Z_2 of G81, we can suspect the existence of a Zeeman triplet; we mark these candidates with "T" in Table C.2. However, better angular and spectral resolution is needed to confirm that.

In G25, the linearly polarized emission at the LSR velocity of 39.6 km s^{-1} differs by only one spectral channel (0.1 km s^{-1}) from the demagnetized velocity of 39.506 km s^{-1}. A similar ambiguity is in Z_1 of G81. We mark such cases with "v" (for verification needed) in Table C.2, and again, observations with better angular and spectral resolution and good sensitivity are needed to verify the existence of Zeeman triplets.

In G43, the linearly polarized spots coincide with the RHCP feature of Z_2, LHCP of Z_8, and interestingly with both circularly

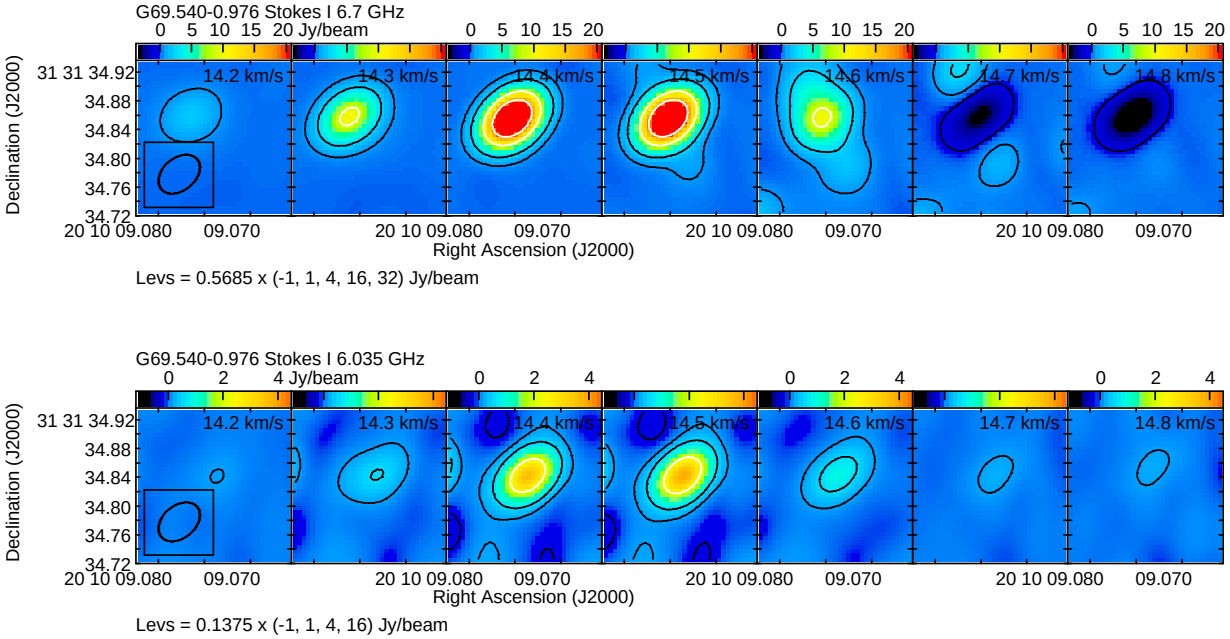

Fig. 5. Channel images showing evidence for the coexistence of 6.7 GHz methanol (*top*) and 6.035 GHz ex-OH (*bottom*) masers obtained for G69. The ex-OH emission corresponds to Zeeman pair Z_5 as in Table C.1. Contours represent the emission; the first contours correspond to $3\sigma_{\rm rms}$ of the image, and the next contours are at 4, 8, 16, $32\times3\sigma_{\rm rms}$. The first negative contour is also shown. The numbers in the top right corner of each panel correspond to the LSR velocities of each spectral channel.

polarized features of Z_3 with an avoidance of the central velocities. Similarly, the avoidance of unshifted velocities is seen in G49 and Z_4, Z_5. That can indicate that this emission is associated with the σ components, but also that the line-of-sight velocity can change due to effects such as turbulence.

Green et al. (2015) showed that the flux densities of the π components of the triplets are from 3% to 85% of the average circular component flux, with a median of 16%, indicating the detection of π components only toward the brightest Zeeman splittings. We do not confirm such a trend among our candidates for triplets. However, as we noted above, more sensitive and better angular and spectral resolution observations are needed to verify the existence of the potential Zeeman triplets. The lack of π components may be related to the magnetic field orientation; if the magnetic field is parallel to the line of sight, the π component is not seen.

4.4. Coincidence and avoidance of ex-OH and methanol masers

We note that the 6.7 GHz methanol maser emission is brighter than the ex-OH line in all targets, but the ratio $S_{\rm p}^{6.7}/S_{\rm p}^{6.035}$ is diverse, from 2.5 to 115 with a median of 15. In six of the targets, the 6.7 GHz methanol maser is spread over larger regions in the sky than the ex-OH maser, again with a broad range of size ratios, from 1.1 to 2700, with a median of 6. In G43, G48, and G69, the ex-OH line emission has more complex structures and covers larger regions than methanol masers and in G108 the size of both transitions is similar. It is possible that the behavior stems from a lower kinetic temperature. The estimates of $T_{\rm rot}$ from CH_3CN lines give much lower temperatures for G43 and G69 than for G20 and G25, where methanol masers are more complex (see Appendix A).

We carefully examined the data, searching for coexistence, according to our method described in the last paragraph of Sect. 2, of both maser lines. In six targets, namely G20, G24, G34, G43, G69, and G81, we find coincidences of both transitions, considering the astrometric positions and overlap of the LSR velocities (see Fig. 5 as the example). In total, in these six sources, we find 12 groups of masers that are coexisting via the same gas volume. In seven cases among these 12 groups, the ex-OH shows Zeeman splitting. In more detail, in G20, G69, and G81, we find cases in which a few ex-OH and methanol spots coincide, but other regions where they are separated. In these targets, the brightest methanol spots are not associated with ex-OH emission. In G24 and G34, all ex-OH spots coexist with methanol emission, and the ex-OH masers are located in compact areas. The strongest methanol masers coexist with ex-OH masers, with spot positions within 20 mas. The two maser transitions avoid each other in the four remaining targets; that is, G25, G48, G49, and G108.

We checked correlations with other properties between areas showing the coexistence of both transitions and ones without this phenomenon. For this purpose, in all sources, we coupled the closest 6.7- and 6.035 GHz cloudlets: 12 pairs with coexistence (as was noted above) and 8 couples with avoidance. Next, we checked the following parameters for all 20 pairs: the separations of the barycenters, the velocities of the peaks, and the ratios of brightness temperatures. We note that the coincidence of both maser transitions appears for the cloudlets with their barycenters separated by less than 205 au and separations of their peak velocities below $0.7\,{\rm km\,s^{-1}}$. We did not find any correlations with brightness temperature or the ratio of maximum brightness temperatures.

Based on the models by Cragg et al. (2002), the coincidence of both transitions happens when $n_{\rm H_2}$ is from 10^5 to $10^{8.3}\,{\rm cm^{-3}}$, $T_{\rm K}$ is below 70 K, and $T_{\rm D}$ is larger than 100 K. The number densities can be calculated from the $B_{\rm los}$ estimated from the 37 Zeeman pairs identified (see Sect. 4.3.1 and Table C.1). In the case of four pairs (two in G108, one in G49, and one in G81), $n_{\rm H_2}$ exceeds a value of $10^{8.3}\,{\rm cm^{-3}}$. In fact, in all these cases, no coexistence appears for the maser lines. For the other 33 Zeeman

pairs, avoidance and coincidence must be related to gas and/or dust temperatures.

In sources G20, G43, G69, and G81, there are regions of coincidence and also regions where ex-OH emission occurs without methanol transition. We have already noted that the redshifted feature (Z_3) in G81 does not have a methanol counterpart because of the high density of the gas. In the other three sources, we know the kinetic temperature has to be below 70 K from the model. Thus, the reason for the presence of ex-OH without 6.7 GHz masers could be a decrease in the dust temperature below 100 K on scales of hundreds of astronomical units (around 500 au for G20, 1000 au for G43, and 400 au for G69).

In sources G20, G24, G34, G69, and G81, there are regions of coincidence and regions where methanol emission occurs without ex-OH transition. We know T_D has to be above 100 K. Thus, a possible reason for the absence of the ex-OH maser could be an increase in the kinetic temperature above 70 K, whereby the condition $T_K < T_D$ has to be conserved. The scale of variability of T_K is around 170 au for G20 and G34, 1000 au for G69, and 450 au for G81.

As has been noted, in G25, G48, G49, and G108 we do not find any coexistence of the maser transitions. For G108, as for G81, we inferred a number of high densities in the volume of gas where ex-OH occurs. G25 and G49 have very bright methanol maser emission, which requires a strong IR source. From Table C.3, it can be seen that the G25 is the most massive YSO and has the highest bolometric luminosity. Hence, the main factor influencing the avoidance of both transitions in these two sources may be the distance from the YSO. In regions that are closer to the central object, and thus hotter, the 6.7 GHz maser occurs, and in distant and cooler regions, the 6.035 GHz maser transition appears. In G48, the brightness of both transitions is similar, but we observe a significant shift in the velocity domain at 1.9 km s^{-1} between methanol and ex-OH. This supports the hypothesis that these transitions appear in different volumes of gas. This target has the weakest bolometric luminosity and the smallest mass of YSO, which explains why a very weak methanol maser appeared, consisting of only two spots (Table C.3).

We find that the distributions of both masers are roughly parallel in seven targets (G24, G25, G34, G43, G49, G69, and G81), $|PA_{6.7}\text{-}PA_{6.035}| < 31°$ (Table 5). Kolmogorov-Smirnov tests for these two parameters confirm a nonrandom relationship between $PA_{6.7}$ and $PA_{6.035}$ values. This indicates that both masers could be associated with the same kinematic structures, although they do not necessarily trace the same parts. The blue- and redshifted maser velocities are consistent with the velocities of SO, CH_3CN, and HC_3N lines in G25, G43, and G69. That may imply that the masers arise from a disk but further data including proper motion studies are needed to verify this scenario. In Sect. 1, we pointed out that methanol masers in G69 were also considered to be associated with the outflow (Sugiyama et al. 2011). Among the other sources, we did not find signs of rotation, based on ALMA data presented in the Sect. 4.1. The masers in G24 have similar $PA_{6.7}$ and $PA_{6.035}$, perpendicular to the known outflow, which may indicate a disk seen edge-on. For G34, we see a ring-like maser morphology, but the lack of other data prevents us from determining the kinematic structure. The situation is similarly unresolved for G49 and G81. Considering the findings of the counterpart star formation tracers presented in Sect. 4.1, we notice that circular cores of millimeter dust continuum emission overlaps maser emission in G20, G24, G43, and G69. All these sources show the coincidence of both maser transitions. G43 and G69, which show more complex ex-OH emission, have much brighter 1.3 mm cores, of 159 mJy and 236 mJy, respectively, than G20 and G24, which have a brightness of 20 mJy and 3 mJy, respectively. In G49 and G81, maser emission is clearly separated from irregular millimeter cores. Those two sources are the brightest in our sample, but 6.7 and 6.035 GHz masers coexist only in G81. We cannot determine any association between kinematic structure and/or morphology and the coexistence of both maser transitions. In four sources (G24, G25, G43, and G69), masers seem to be associated with the disk, but in G25, we notice the avoidance of both maser transitions, and in the other three sources, we found partial coincidence.

Relating to our analysis of the evolutionary stages of our sample (Sect. 4.2), taking into account all three evolutionary indicators, the most evolved sources are sequentially G69, G43, and G48. All three characterize the most complex distributions of ex-OH compared to methanol masers. G69 has very bright 6.7 GHz emission, ~100 Jy, but G43 and G48 are relatively weak. G69 and G43 show the coexistence of the two maser transitions, and G48 shows avoidance. We found signs of rotating disks for three sources in our sample. Among them, two are the most evolved: G69 and G43. We can also notice that, in our sample, only these three, the most evolved sources, have more complex and extended ex-OH maser structures than methanol maser structures. The next sources in the evolutionary sequence are G20, G24, G25, and G81. Three of them show coexistence, and one, G25, shows avoidance. They also have various morphologies, and only for G25 do we find the sign of a rotating disk. The last three sources, G49, G34, and G108, are in an early evolutionary phase (our interpretation for G49 could be wrong because it is not clear with which core masers emissions are associated). These sources are extremely different. G49 is the brightest source in the 6.7 GHz line in our sample and does not show a coincidence with the ex-OH line, similarly to G108, which has one of the weakest methanol maser emissions. Both sources also show a similarly complex morphology for both transitions. On the other hand, G34 shows very compact ex-OH emission, which does coincide with methanol emission.

To summarize, we do not notice a relationship between the phase of the evolution of YSO and the presence of regions with coexistence or avoidance of methanol and ex-OH masers. Some of the most evolved sources, like G43 and G69, show coincidence, but the next most evolved one, G48, shows avoidance. Also, two sources in the very early evolutionary phase, G34 and G108, show coincidence and avoidance, respectively. The factors that impact the appearance of the two transitions seem to be due to local changes in gas and dust temperatures and gas density, on the scales of a few hundred astronomical units, correlated with the distance between the maser and star and the brightness of the YSO.

5. Conclusions

We examined ten HMYSOs in detail, considering two maser transitions: 6.7 GHz methanol and 6.035 GHz OH. The ex-OH maser line was imaged for the first time for eight of them. The 6.7 GHz methanol maser emission is brighter than the ex-OH line in all targets and is spread over larger regions in the sky than ex-OH masers in six of these. In three HMYSOs (G43, G48, and G69), the ex-OH masers have more complex structures and cover larger regions than methanol masers, and in one (G108) the size of both transitions is similar.

We identified regions where the two maser transitions coincided or showed avoidance. Comparing our result with archival

ALMA data, we deduced that avoidance happens due to local changes in temperatures and/or densities, which are directly correlated with the brightness and distance of the masers from the YSO and not with the evolutionary stage of the HMYSO. We also attempted to identify kinematic structures, but we did not notice a correlation with the coexistence of both masers.

We detected Zeeman splitting of the ex-OH transition in eight HMYSOs, leading to magnetic field estimates of a few milligauss. In two cases, we observed a reversal of magnetic field lines along the line of sight. We detected linearly polarized ex-OH emission in nine HMYSOs and were able to compare orientations of the magnetic fields with the directions of outflows on the sky-plane, but the results are not coherent enough. We detected eight possible Zeeman triplets with two circularly polarized features at velocities bracketing a linearly polarized feature; however, observations with better angular and spectral resolution are needed to verify this result.

Data availability

An extra appendices containing tables of polarization details, figures of masers distributions, and counterparts descriptions are available on Zenodo at: https://doi.org/10.5281/zenodo.14865259.

Acknowledgements. We acknowledge support from the National Science Centre, Poland through grant 2021/43/B/ST9/02008. We thank a referee for the very detailed and constructive revision of the manuscript. e-MERLIN is a National Facility operated by the University of Manchester at Jodrell Bank Observatory on behalf of STFC This paper makes use of the following ALMA data: ADS/JAO.ALMA2021.1.00311.S, ADS/JAO.ALMA2019.1.00059.S., and ADS/JAO.ALMA2015.1.01596.S. ALMA is a partnership of ESO (representing its member states), NSF (USA) and NINS (Japan), together with NRC (Canada), NSTC and ASIAA (Taiwan), and KASI (Republic of Korea), in cooperation with the Republic of Chile. The Joint ALMA Observatory is operated by ESO, AUI/NRAO and NAOJ. The National Radio Astronomy Observatory is a facility of the National Science Foundation operated under cooperative agreement by Associated Universities, Inc. This work is based on observations made with the *Spitzer* Space Telescope, which is operated by the Jet Propulsion Laboratory, California Institute of Technology under a contract with NASA. This research has made use of the NASA/IPAC Infrared Science Archive, which is funded by the National Aeronautics and Space Administration and operated by the California Institute of Technology. Herschel is an ESA space observatory with science instruments provided by European-led Principal Investigator consortia and with important participation from NASA.

References

Araya, E., Hofner, P., Kurtz, S., Bronfman, L., & DeDeo, S. 2005, ApJS, 157, 279
Avison, A., Quinn, L. J., Fuller, G. A., et al. 2016, MNRAS, 461, 136
Bartkiewicz, A., Szymczak, M., Cohen, R. J., & Richards, A. M. S. 2005, MNRAS, 361, 623
Bartkiewicz, A., Szymczak, M., van Langevelde, H. J., Richards, A. M. S., & Pihlström, Y. M. 2009, A&A, 502, 155
Bartkiewicz, A., Szymczak, M., & van Langevelde, H. J. 2014, A&A, 564, A110
Bartkiewicz, A., Szymczak, M., & van Langevelde, H. J. 2016, A&A, 587, A104
Bartkiewicz, A., Sanna, A., Szymczak, M., et al. 2020, A&A, 637, A15
Bartkiewicz, A., Sanna, A., Szymczak, M., et al. 2024, A&A, 686, A275
Baudry, A., Desmurs, J. F., Wilson, T. L., & Cohen, R. J. 1997, A&A, 325, 255
Bayandina, O. S., Alakoz, A. V., & Val'tts, I. E. 2014, Astron. Rep., 58, 462
Caswell, J. L., & Green, J. A. 2011, MNRAS, 411, 2059
Cragg, D. M., Sobolev, A. M., & Godfrey, P. D. 2002, MNRAS, 331, 521
Crutcher, R. M. 1999, ApJ, 520, 706
Darwish, M. S., Richards, A. M. S., Etoka, S., et al. 2020, MNRAS, 499, 1441
Desmurs, J. F., & Baudry, A. 1998, A&A, 340, 521
Desmurs, J. F., Baudry, A., Wilson, T. L., Cohen, R. J., & Tofani, G. 1998, A&A, 334, 1085
Elia, D., Merello, M., Molinari, S., et al. 2021, MNRAS, 504, 2742
Etoka, S., Gray, M. D., & Fuller, G. A. 2012, MNRAS, 423, 647
Fish, V. L., & Reid, M. J. 2006, ApJS, 164, 99
Fish, V. L., & Sjouwerman, L. O. 2007, ApJ, 668, 331
Fish, V. L., & Sjouwerman, L. O. 2010, ApJ, 716, 106
Fish, V. L., Reid, M. J., Argon, A. L., & Zheng, X.-W. 2005, ApJS, 160, 220
Fujisawa, K., Sugiyama, K., Motogi, K., et al. 2014, PASJ, 66, 31
Garrington, S., & Beswick, R. 2016, Astron. Geophys., 57, 3.28
Gaume, R. A., Johnston, K. J., & Wilson, T. L. 1993, ApJ, 417, 645
Goddi, C., Moscadelli, L., & Sanna, A. 2011, A&A, 535, L8
Goddi, C., Ginsburg, A., Maud, L. T., Zhang, Q., & Zapata, L. A. 2020, ApJ, 905, 25
Goldsmith, P. F., & Langer, W. D. 1999, ApJ, 517, 209
Green, J. A., & McClure-Griffiths, N. M. 2011, MNRAS, 417, 2500
Green, J. A., Richards, A. M. S., Vlemmings, W. H. T., Diamond, P., & Cohen, R. J. 2007, MNRAS, 382, 770
Green, J. A., Caswell, J. L., & McClure-Griffiths, N. M. 2015, MNRAS, 451, 74
Greisen, E. W. 2003, in Astrophysics and Space Science Library, 285, Information Handling in Astronomy – Historical Vistas, ed. A. Heck, 109
Hutawarakorn, B., Cohen, R. J., & Brebner, G. C. 2002, MNRAS, 330, 349
Jiménez-Donaire, M. J. 2017, PhD thesis, Ruprecht-Karls University of Heidelberg, Germany
Koch, P. M., Tang, Y.-W., Ho, P. T. P., et al. 2018, ApJ, 855, 39
Kumar, M. S. N., Tafalla, M., & Bachiller, R. 2004, A&A, 426, 195
McMullin, J. P., Waters, B., Schiebel, D., Young, W., & Golap, K. 2007, in Astronomical Society of the Pacific Conference Series, 376, Astronomical Data Analysis Software and Systems XVI, eds. R. A. Shaw, F. Hill, & D. J. Bell, 127
Moldon, J. 2021, eMCP: e-MERLIN CASA pipeline, Astrophysics Source Code Library [record ascl:2109.006]
Molinari, S., Pezzuto, S., Cesaroni, R., et al. 2008, A&A, 481, 345
Molinari, S., Schisano, E., Elia, D., et al. 2016a, A&A, 591, A149
Molinari, S., Schisano, E., Elia, D., et al. 2016b, VizieR Online Data Catalog: Hi-GAL. inner Milky Way: +68>=l>=70 (Molinari+, 2016), VizieR On-line Data Catalog: J/A+A/591/A149. Originally published in: 2016A&A...591A.149M
Moscadelli, L., Cesaroni, R., Rioja, M. J., Dodson, R., & Reid, M. J. 2011, A&A, 526, A66
Nagayama, T., Kobayashi, H., Omodaka, T., et al. 2015, PASJ, 67, 65
Ouyang, X.-J., Chen, X., Shen, Z.-Q., et al. 2022, ApJS, 260, 51
Pandian, J. D., Momjian, E., Xu, Y., Menten, K. M., & Goldsmith, P. F. 2011, ApJ, 730, 55
Pankonin, V., Churchwell, E., Watson, C., & Bieging, J. H. 2001, ApJ, 558, 194
Perley, R. A., & Butler, B. J. 2013, ApJS, 206, 16
Reid, M. J., Menten, K. M., Brunthaler, A., et al. 2019, ApJ, 885, 131
Richards, A. M. S., Moravec, E., Etoka, S., et al. 2022, arXiv e-prints [arXiv:2207.05591]
Rosero, V., Hofner, P., Kurtz, S., Bieging, J., & Araya, E. D. 2013, ApJS, 207, 12
Rygl, K. L. J., Brunthaler, A., Reid, M. J., et al. 2010, A&A, 511, A2
Rygl, K. L. J., Brunthaler, A., Sanna, A., et al. 2012, A&A, 539, A79
Sanna, A., Moscadelli, L., Cesaroni, R., et al. 2010a, A&A, 517, A71
Sanna, A., Moscadelli, L., Cesaroni, R., et al. 2010b, A&A, 517, A78
Sato, M., Reid, M. J., Brunthaler, A., & Menten, K. M. 2010, ApJ, 720, 1055
Shi, H., Zhao, J.-H., & Han, J. L. 2010, ApJ, 718, L181
Sugiyama, K., Fujisawa, K., Doi, A., et al. 2008, PASJ, 60, 23
Sugiyama, K., Fujisawa, K., Doi, A., et al. 2011, PASJ, 63, 53
Surcis, G., Vlemmings, W. H. T., Curiel, S., et al. 2011, A&A, 527, A48
Surcis, G., Vlemmings, W. H. T., van Langevelde, H. J., & Hutawarakorn Kramer, B. 2012, A&A, 541, A47
Surcis, G., Vlemmings, W. H. T., van Langevelde, H. J., Hutawarakorn Kramer, B., & Quiroga-Nuñez, L. H. 2013, A&A, 556, A73
Surcis, G., Vlemmings, W. H. T., van Langevelde, H. J., et al. 2015, A&A, 578, A102
Surcis, G., Vlemmings, W. H. T., van Langevelde, H. J., Hutawarakorn Kramer, B., & Bartkiewicz, A. 2019, A&A, 623, A130
Surcis, G., Vlemmings, W. H. T., van Langevelde, H. J., Hutawarakorn Kramer, B., & Bartkiewicz, A. 2022, A&A, 658, A78
Szymczak, M., Wolak, P., Bartkiewicz, A., Aramowicz, M., & Durjasz, M. 2020, A&A, 642, A145
Torrelles, J. M., Gómez, J. F., Rodríguez, L. F., et al. 1997, ApJ, 489, 744
Vlemmings, W. H. T. 2008, A&A, 484, 773
Vlemmings, W. H. T., Torres, R. M., & Dodson, R. 2011, A&A, 529, A95
Wilson, T. L., & Rood, R. 1994, ARA&A, 32, 191
Wrobel, J. M., & Walker, R. C. 1999, in Astronomical Society of the Pacific Conference Series, 180, Synthesis Imaging in Radio Astronomy II, eds. G. B. Taylor, C. L. Carilli, & R. A. Perley, 171
Xu, Y., Reid, M. J., Menten, K. M., et al. 2009, ApJ, 693, 413
Zhang, B., Reid, M. J., Menten, K. M., et al. 2013, ApJ, 775, 79

Appendix A: Methyl cyanide

Methyl cyanide (CH_3CN) $J = 12 - 11$ rotational transition could be analyzed for a number of sources using the data from the ALMA Science Archive. Under the assumption that the lines are optically thin, a rotational temperature can be derived from the line intensities of various K components. If the lines are optically thick, the various K intensities versus the upper energy level will deviate from a linear slope, and the slope may flatten, which leads to overestimated temperatures (Goldsmith & Langer 1999). When also the ^{13}C isotopolog, $CH_3^{13}CN$, is detected, the optical depth of $CH_3^{12}CN$ can be derived from the K line intensity ratio under the assumptions that $CH_3^{13}CN$ is optically thin and the $^{12}C/^{13}C$ line ratio of 50 (Wilson & Rood 1994). See Jiménez-Donaire (2017) for a detailed explanation.

Following the analysis outlined in Pankonin et al. (2001), Araya et al. (2005) and Rosero et al. (2013) we analyzed available ALMA archival data. We used eight Gaussians to fit contemporaneously the $K = 0$ to $K = 7$ components, constraining the line width of all lines to be the same as for the bright and unblended $K = 3$ component, and fixing positions of the lines to the rest frequencies, after taking into account the LSR velocity of the target. The results of the fits are given in Table A.1.

Strong deviations from linear were found for G20 and G25, less so for G43, and least for G69. Since also the $K = 2$ $CH_3^{13}CN$ could be detected, the optical depth of the main isotopolog ($\tau_{^{12}C}$) could be calculated. We find that $CH_3^{12}CN$ is indeed optically thick for all our sources, more so for those with a stronger deviation from linear. Therefore, all of our estimated temperatures are overestimated, and our column densities are underestimated. On the argument of beam dilution, which is often invoked in the past single-dish analysis of CH_3CN, we are less worried because we use ALMA interferometric data. We measured the spectra in ellipses chosen to include most of the CH_3CN emitting core which overlapped or was closest to the maser emitting region. The smallest minor axis was 0.4 arcsec and the largest major axis was 1.2 arcsec, these being (slightly) larger than the beam sizes. The emission of the CH_3CN $J = 12 - 11$ transition observed by ALMA is thus slightly extended, making it plausible to use a beam filling factor of unity.

Table A.1: Derived parameters of the CH_3CN $J = 12 - 11$ ALMA observations.

Source	vlsr	linewidth	$\int T\delta v$						Trot	N	^{13}C	ratio	$\tau_{^{12}C}$
			$K = 0$	$K = 1$	$K = 2$	$K = 3$	$K = 4$	$K = 5$	$K = 6$	$K = 7$	K	(e^{14} cm^{-2})			
	(km s^{-1})	(km s^{-1})	(K km s^{-1})												
G20	72.5	3.4	87.5	80.2	87.9	91.2	55.4	50.6	43.2	21.9	335(79)	25.1(3.8)	y	7.7	6.5
G25	42.0	4.2	456.9	491.1	514.6	566.4	407.0	345.9	362.6	150.4	446(143)	229(32)	y	7.6	6.5
G43	12.0	2.1	37.4	30.4	28.9	31.6	14.8	9.3	9.5	3.4	177(15)	4.4(0.5)	y	8.4	5.9
G69	14.0	1.7	167.3	155.2	145.1	162.2	95.1	64.7	56.8	14.5	180(18)	23.7(2.9)	y	14.8	3.4

Appendix B: Figures

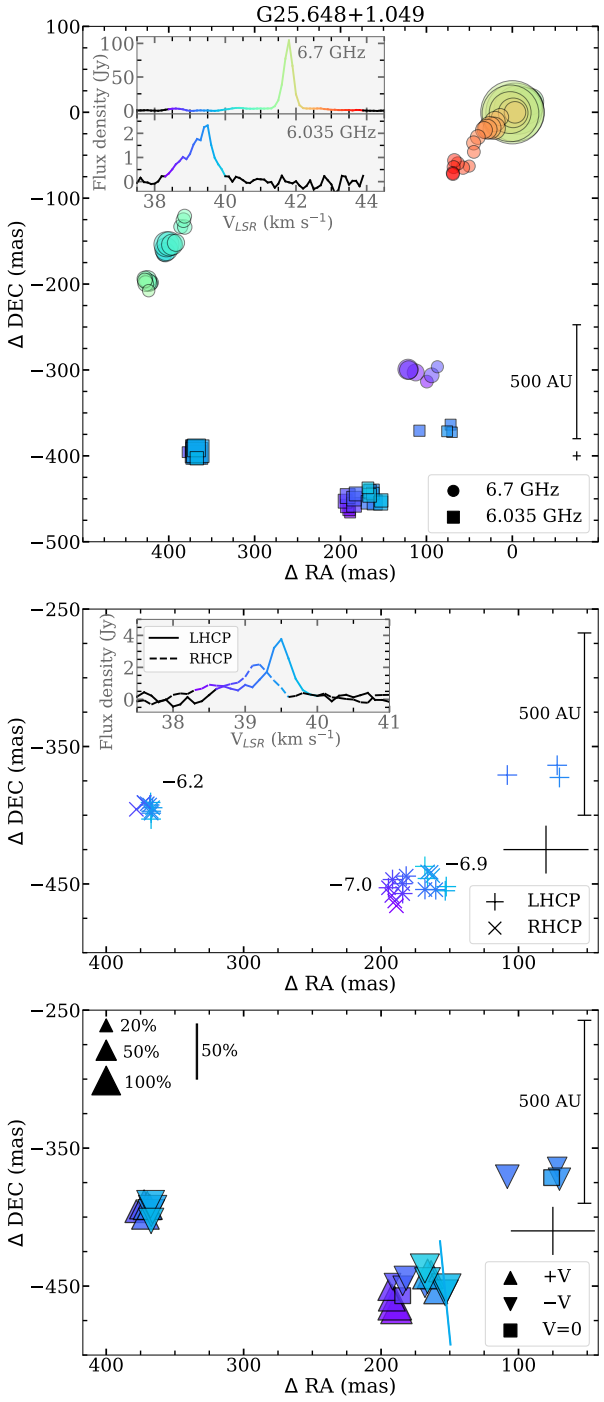

Fig. B.1: The same as Figs 2 and 3 but for G25.648+1.049.

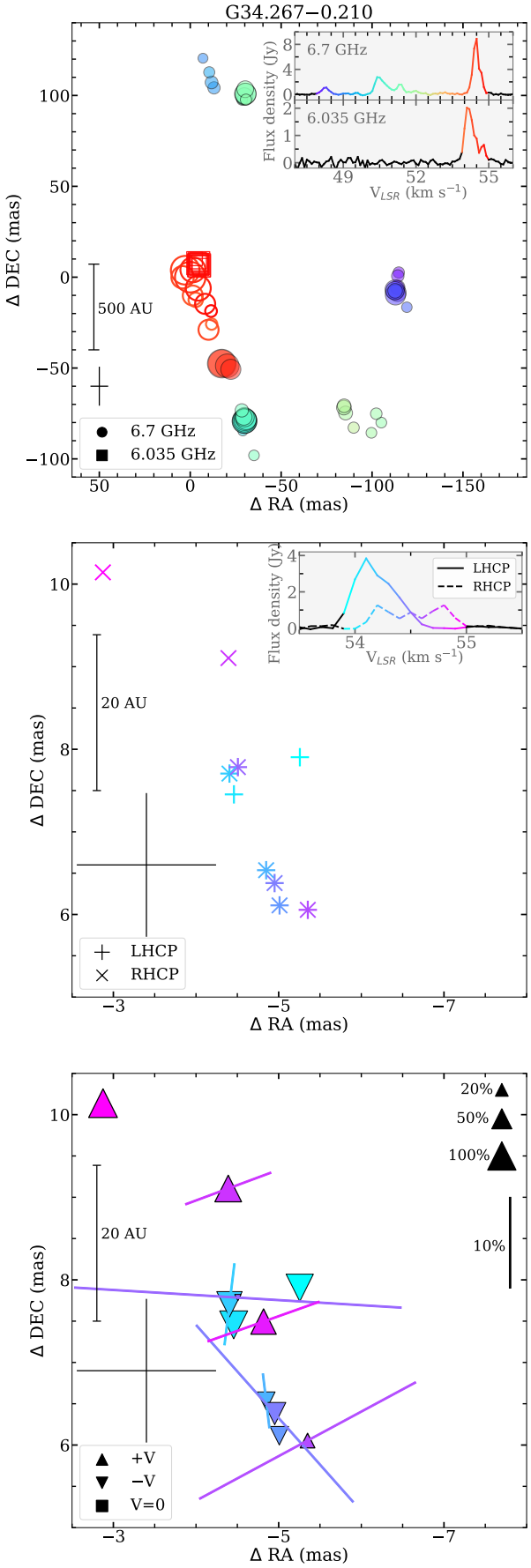

Fig. B.2: The same as Figs 2 and 3 but for G34.267−0.210.

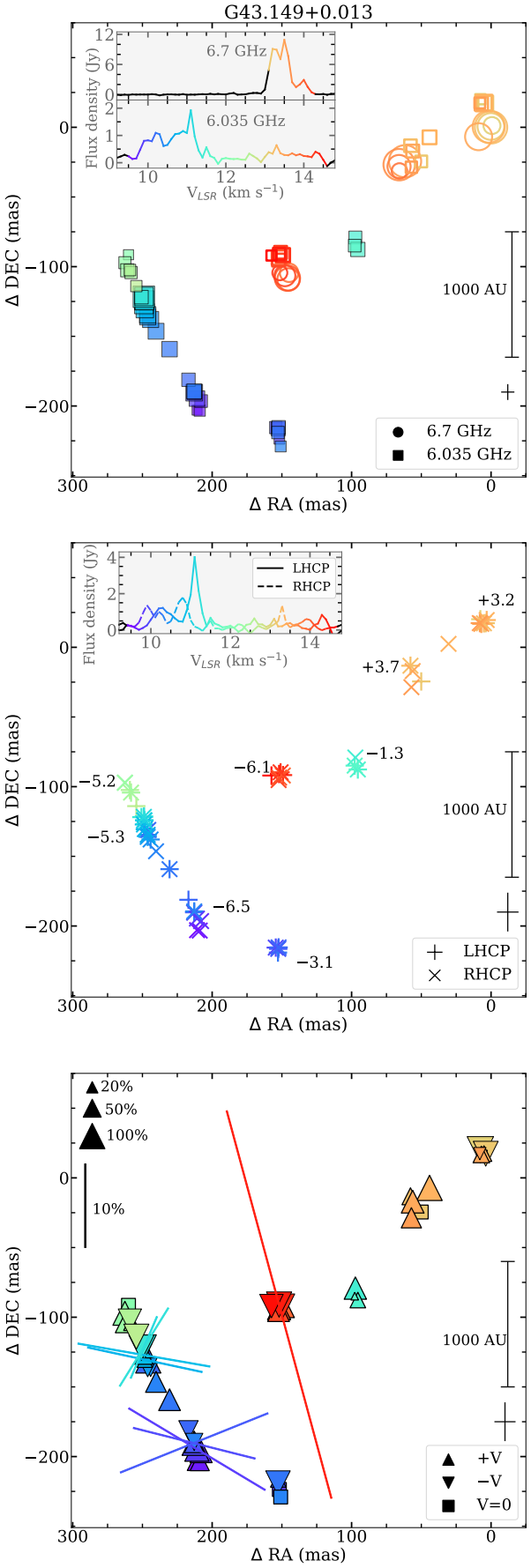

Fig. B.3: The same as Figs 2 and 3 but for G43.149+0.013.

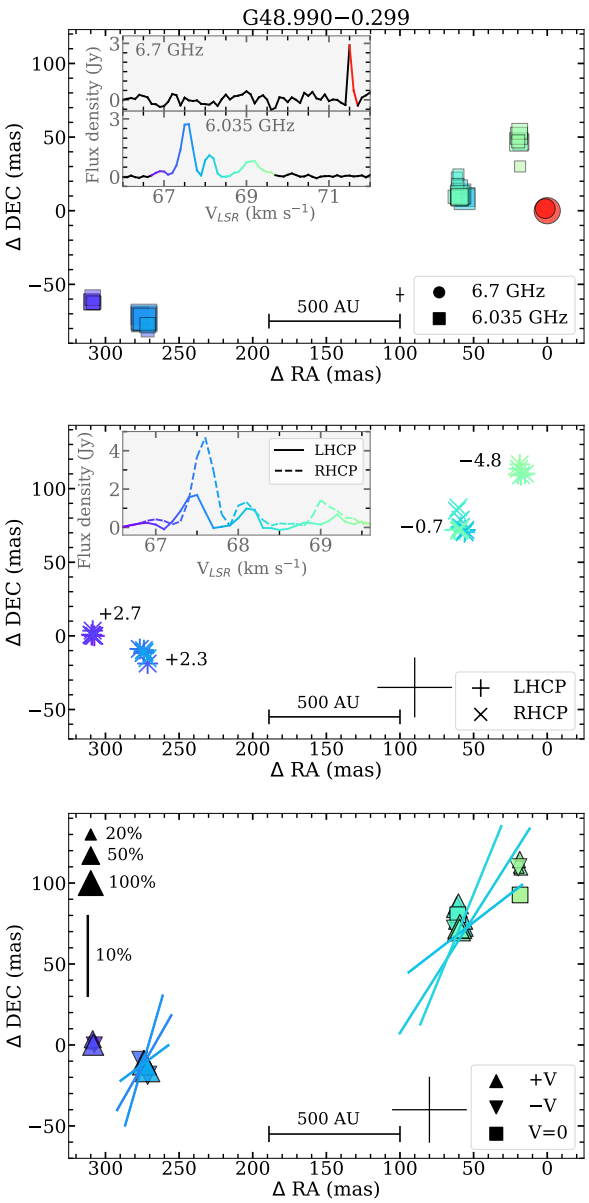

Fig. B.4: The same as Figs 2 and 3 but for G48.990−0.299.

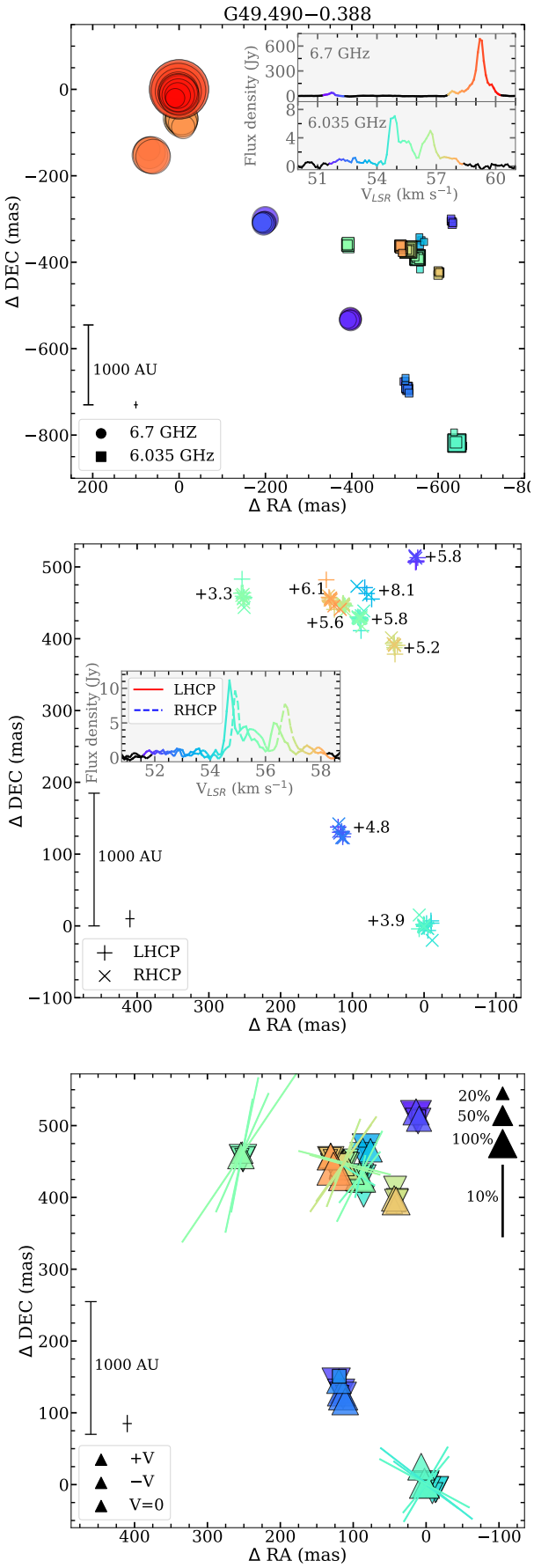

Fig. B.5: The same as Figs 2 and 3 but for G49.490−0.388

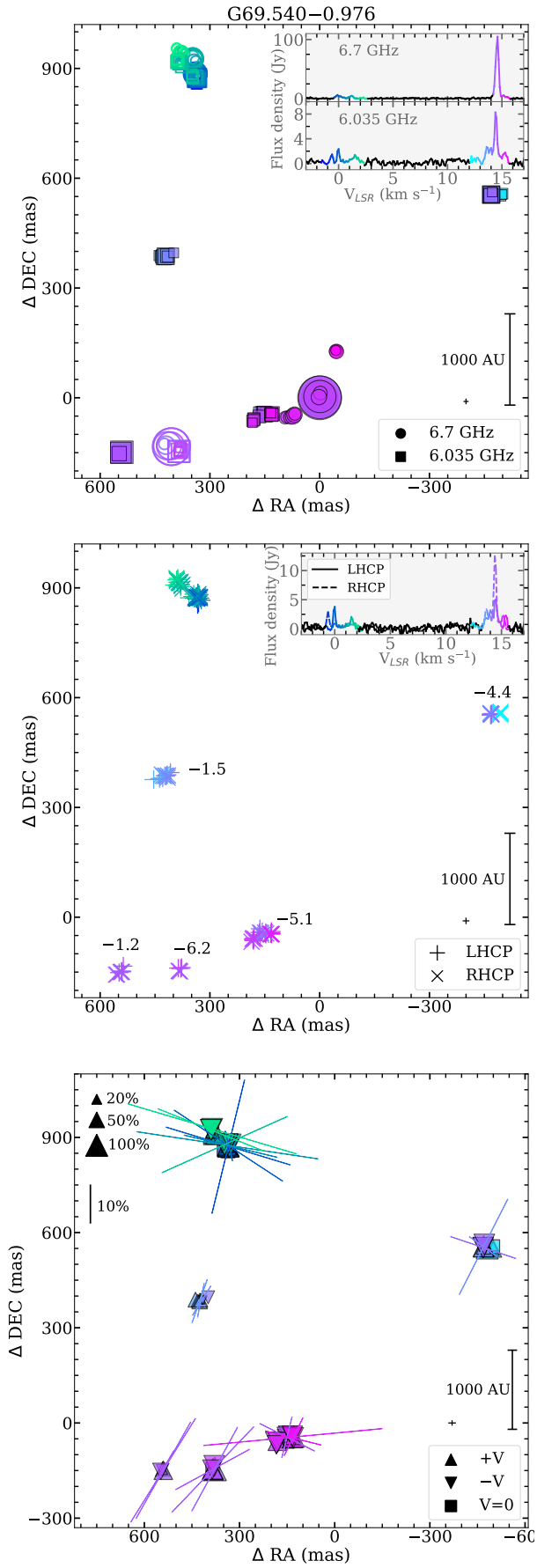

Fig. B.6: The same as Figs 2 and 3 but for G69.540−0.976

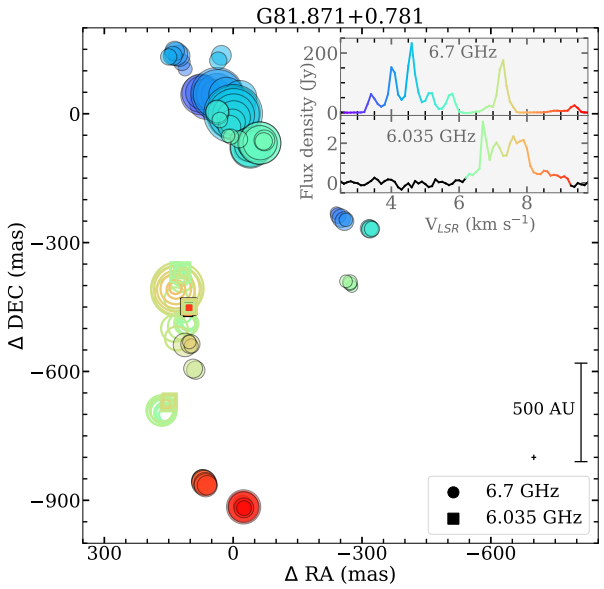

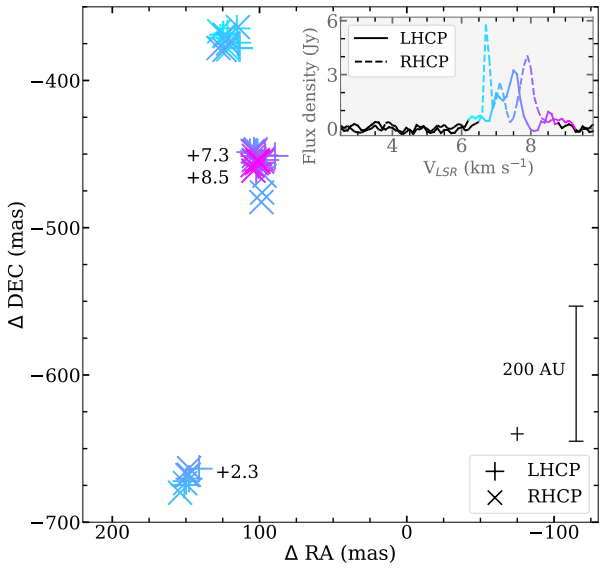

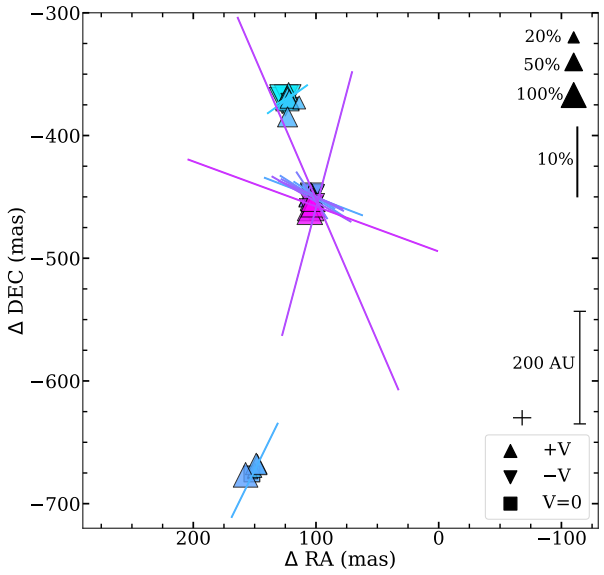

Fig. B.7: The same as Figs 2 and 3 but for G81.871+0.781

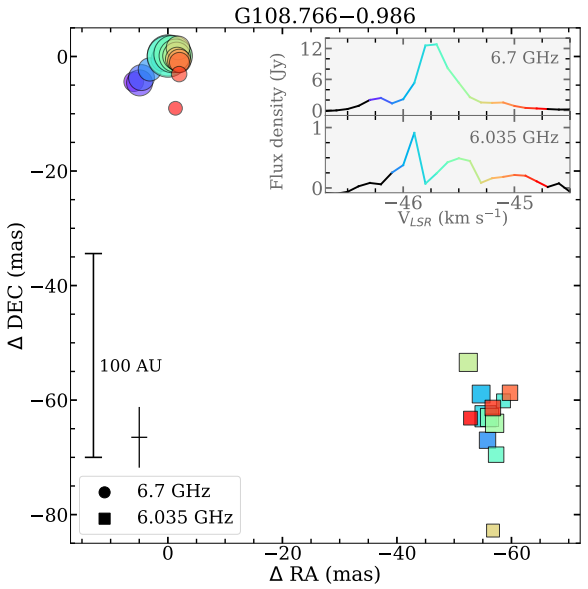

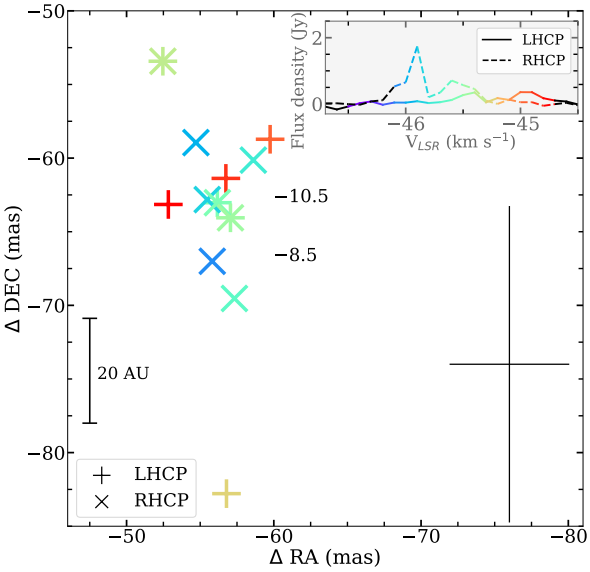

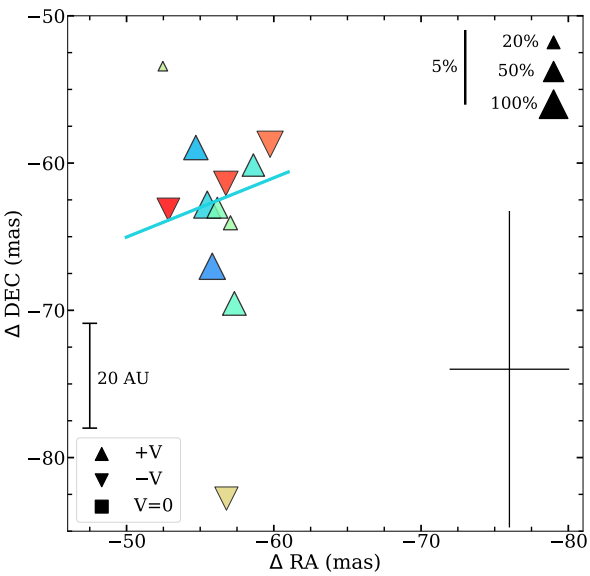

Fig. B.8: The same as Fig.2 and Fig.3 but for G108.766−0.986

Appendix C: Tables

Table C.1: Details of 6.035 GHz OH maser line Zeeman pairs detected using eMERLIN.

No.	Polzn.	$S_{\max}$ (Jy)	$S_{\rm fit}$ (Jy)	$FWHM_{\rm fit}$ (km s^{-1})	$V_{\rm fit}$ (km s^{-1})	$\Delta V_{\rm Z}$ (km s^{-1})	$V_{\rm d}$ (km s^{-1})	$B_{\rm los}$ (mG)	$n_{\rm H_2}$ $\times 10^6$ (cm^{-3})
G20.237+0.065									
Z_1	LHC	1.12	1.06	0.23	71.442	−0.039±0.018	71.423	−0.7	1.2
	RHC	2.34	2.09	0.16	71.403				
Z_2	LHC	0.44	0.44	0.18	72.070	+0.012±0.008	72.076	+0.2	0.1
	RHC	0.41	0.41	0.22	72.082				
Z_3	LHC	0.19	0.21	0.12	77.057	−0.204±0.006	76.955	−3.6	38.2
	RHC	0.23	0.25	0.11	76.853				
G25.648+1.049									
Z_1	LHC	0.68	0.67	0.27	38.955	−0.392±0.017	38.759	−7.0	157.2
	RHC	0.69	0.65	0.32	38.563				
Z_2	LHC	0.68	0.71	0.15	39.698	−0.384±0.011	39.506	−6.9	152.4
	RHC	0.81	0.77	0.17	39.314				
Z_3	LHC	3.46	3.54	0.14	39.466	−0.345±0.008	39.294	−6.2	121.4
	RHC	1.57	1.53	0.20	39.121				
G43.149+0.013									
Z_1	LHC	0.28	0.27	0.14	10.155	−0.173±0.010	10.069	−3.1	27.8
	RHC	0.29	0.30	0.10	9.982				
Z_2	LHC	0.55	0.58	0.13	10.242	−0.363±0.005	10.061	−6.5	134.2
	RHC	0.77	0.77	0.12	9.879				
Z_3	LHC	2.72	2.60	0.11	11.108	−0.299±0.028	10.959	−5.3	86.9
	RHC	1.23	1.27	0.17	10.809				
Z_4	LHC	0.18	0.20	0.12	11.552	−0.075±0.005	11.515	−1.3	4.4
	RHC	0.36	0.37	0.10	11.477				
Z_5	LHC	0.25	0.27	0.10	12.569	−0.293±0.003	12.423	−5.2	83.5
	RHC	0.32	0.33	0.11	12.276				
Z_6	LHC	0.12	0.12	0.09	13.120	+0.208±0.012	13.224	+3.7	40.5
	RHC	0.36	0.35	0.10	13.328				
Z_7	LHC	0.57	0.60	0.08	13.123	+0.177±0.009	13.212	+3.2	29.7
	RHC	0.84	0.84	0.08	13.300				
Z_8	LHC	0.41	0.41	0.11	14.310	− 0.344±0.008	14.138	−6.1	117.3
	RHC	0.45	0.48	0.12	13.966				
G48.990−0.299									
Z_1	LHC	0.31	0.31	0.15	66.810	+0.153±0.029	66.887	+2.7	43.3
	RHC	0.47	0.50	0.17	66.963				
Z_2	LHC	1.67	1.74	0.14	67.454	+0.130±0.005	67.519	+2.3	14.7
	RHC	4.74	4.83	0.14	67.584				
Z_3	LHC	0.95	1.08	0.10	68.138	−0.040±0.014	68.118	−0.7	1.1
	RHC	1.35	1.41	0.12	68.098				
Z_4	LHC	0.63	0.62	0.09	69.197	−0.106±0.045	69.144	−4.8	70.4
	RHC	1.50	0.89	0.24	69.091				
	LHC	-	0.26	0.11	69.447	−0.428±0.079	69.233		
	RHC	-	0.74	0.06	69.019				

Table C.1: continued

No.	Polzn.	$S_{\max}$ (Jy)	$S_{\rm fit}$ (Jy)	$FWHM_{\rm fit}$ (km s^{-1})	$V_{\rm fit}$ (km s^{-1})	$\Delta V_{\rm Z}$ (km s^{-1})	$V_{\rm d}$ (km s^{-1})	$B_{\rm los}$ (mG)	$n_{\rm H_2}$ $\times 10^6$ (cm^{-3})
G49.490−0.388									
Z_1	LHC	0.39	0.43	0.13	51.720	+0.325±0.009	51.883	+5.8	105.3
	RHC	0.27	0.30	0.10	52.045				
Z_2	LHC	1.00	1.01	0.15	52.200	+0.270±0.011	52.335	+4.8	70.4
	RHC	1.00	1.00	0.18	52.470				
Z_3	LHC	0.23	0.25	0.14	53.374	+0.451±0.014	53.600	+8.1	214.4
	RHC	0.22	0.23	0.10	53.825				
Z_4	LHC	10.14	9.98	0.12	54.702	+0.221±0.004	54.815	+3.9	45.3
	RHC	9.93	10.09	0.12	54.923				
Z_5	LHC	3.84	3.84	0.26	55.142	+0.328±0.006	55.306	+5.8	105.3
	RHC	3.94	3.89	0.26	55.470				
Z_6	LHC	1.59	1.66	0.17	55.666	+0.185±0.006	55.759	+3.3	31.7
	RHC	1.70	1.79	0.16	55.851				
Z_7	LHC	4.06	4.00	0.22	56.411	+0.316±0.006	56.569	+5.6	97.8
	RHC	7.30	7.16	0.22	56.727				
Z_8	LHC	0.43	0.29	0.19	57.108	+0.294±0.041	57.255	+5.2	83.5
	RHC	0.31	0.31	0.30	57.402				
Z_9	LHC	1.10	1.10	0.24	57.616	+0.339±0.011	57.786	+6.1	117.3
	RHC	1.35	1.38	0.22	57.955				
G69.540−0.976									
Z_1	LHC	1.02	0.97	0.18	13.675	−0.084±0.009	13.633	−1.5	5.9
	RHC	1.84	1.78	0.16	13.591				
Z_2	LHC	1.77	1.86	0.19	14.019	−0.246±0.015	13.896	−4.4	58.5
	RHC	2.22	2.21	0.18	13.773				
Z_3	LHC	4.13	4.80	0.09	14.461	−0.067±0.004	14.428	−1.2	3.7
	RHC	4.65	4.71	0.09	14.394				
Z_4	LHC	0.34	0.34	0.10	14.801	−0.348±0.001	14.627	−6.2	121.4
	RHC	6.57	7.77	0.10	14.453				
Z_5	LHC	0.36	0.40	0.11	14.266	−0.297±0.015	14.118	−5.1	80.1
	RHC	0.35	0.38	0.10	13.969				
	LHC	1.86	1.85	0.07	14.600	−0.336±0.004	14.432		
	RHC	1.07	1.27	0.07	14.264				
	LHC	0.63	0.64	0.11	15.000	−0.263±0.009	14.869		
	RHC	0.59	0.65	0.11	14.737				
	LHC	0.85	0.96	0.11	15.356	−0.243±0.006	15.235		
	RHC	1.26	1.28	0.11	15.113				
G81.871+0.781									
Z_1	LHC	1.07	1.07	0.11	7.003	+0.126±0.004	7.066	+2.3	14.7
	RHC	2.01	2.05	0.13	7.129				
Z_2	LHC	2.24	2.24	0.25	7.453	+0.409±0.008	7.658	+7.3	171.8
	RHC	3.14	3.08	0.23	7.862				
Z_3	LHC	0.57	0.59	0.18	8.523	+0.474±0.086	8.760	+8.5	237.5
	RHC	0.39	0.26	0.44	8.997				
G108.766−0.986									
Z_1	LHC	0.35	0.35	0.11	−45.447	−0.478±0.031	45.686	−8.5	237.5
	RHC	1.74	1.91	0.06	−45.925				
Z_2	LHC	0.36	0.37	0.15	−44.950	−0.594±0.056	45.247	−10.6	378.0
	RHC	0.71	0.68	0.17	−45.544				

Notes. Positive or negative $B_{\rm los}$ values correspond to the magnetic field directed away from us or towards us, respectively. In a case of blended features, where multiple Gaussian profiles are fitted, we calculated the mean value of the magnetic field i.e. Z_4 in G48 and Z_5 in G69.

Table C.2: The linearly polarized 6.035 GHz maser spots detected using eMERLIN.

V_{LSR} (km s^{-1})	I (Jy beam^{-1})	Q (Jy beam^{-1})	U (Jy beam^{-1})	P_l (Jy beam^{-1})	χ_l °	$\delta\chi_l$ °	m_l %	δm_l %	m_c %	δm_c %	m_f %	δm_f %	Notes
G24.148−0.009													
17.2	1.1375	−0.0754	−0.2687	0.2791	−52	2	24	2	92	3	95	3	
17.3	0.6246	−0.1094	−0.2160	0.2422	−58	2	38	4	100	5	100	12	
17.4	0.2081	−0.0406	−0.0339	0.0529	−70	10	25	11	86	9	89	12	
G25.648+1.049													
39.6	0.2317	0.2170	0.0446	0.2215	5	2	95	12	82	9	100	24	Z_2 v
G34.267−0.0210													
54.1	1.9094	0.1810	−0.0446	0.1864	−6	2	9	1	81	1	81	2	
54.2	1.9024	0.1258	0.0307	0.1295	6	3	6	1	40	1	40	1	
54.4	0.9766	0.0310	0.2575	0.2594	41	1	26	2	62	2	67	3	
54.5	0.8472	−0.3062	0.0377	0.3085	86	1	36	2	5	2	36	2	
54.6	0.3943	−0.0598	−0.0910	0.1089	−61	3	27	4	27	4	38	5	
54.7	0.4850	−0.0400	−0.0344	0.0528	−69	7	10	3	89	3	89	3	
54.8	0.5765	−0.0585	−0.0476	0.0754	−70	5	13	3	81	3	82	3	
G43.149+0.013													
9.8	0.3962	−0.0357	0.0668	0.0758	59	8	19	6	92	7	93	8	Z_2
9.9	0.5250	−0.0700	0.0377	0.0795	75	3	15	4	92	6	93	6	Z_2
10.0	0.2933	−0.0416	−0.0399	0.0577	−68	11	19	8	60	11	62	13	Z_2
10.7	0.6284	−0.0812	0.0366	0.0891	77	3	14	3	37	5	39	6	Z_3
10.8	0.8230	−0.1283	0.0460	0.1363	80	5	16	3	54	5	56	5	Z_3
11.1	1.4419	0.0865	−0.0900	0.1249	−23	3	8	2	93	3	93	3	Z_3
11.2	0.8031	0.0406	−0.0820	0.0915	−31	3	11	3	95	4	95	5	Z_3
14.4	0.1466	0.0619	0.0360	0.0716	15	9	48	20	100	19	100	26	Z_8
G48.990−0.299													
67.5	2.5830	0.1617	−0.3379	0.3746	−32	2	14	1	37	2	39	2	Z_2 T
67.6	2.5911	0.3611	−0.2555	0.4423	−17	2	17	1	68	2	70	2	Z_2 T
67.7	1.5059	−0.0485	−0.1200	0.1295	−56	5	8	2	93	2	93	2	Z_2 T
68.0	0.7635	−0.0508	−0.1402	0.1491	−54	4	19	4	39	4	43	5	Z_3 T
68.1	1.1175	0.1207	−0.3284	0.3499	−34	2	31	3	15	3	34	4	Z_3 T
68.2	0.9448	0.1737	−0.1956	0.2615	−24	3	27	3	1	1	27	3	Z_3 T
G49.490−0.388													
54.6	3.0553	−0.1171	0.4833	0.4973	51	2	16	2	82	2	83	2	Z_4
54.7	5.1865	−0.1716	0.5598	0.5855	53	2	11	1	81	2	81	2	Z_4
54.9	5.2083	0.3341	−0.5822	0.6713	−30	2	12	1	79	2	79	2	Z_4
55.0	3.9374	0.0900	−0.4044	0.4143	−38	2	10	1	88	2	88	2	Z_4
55.1	0.8489	−0.0666	0.1045	0.1239	61	7	14	4	100	20	100	22	Z_4
55.7	1.1392	0.1756	−0.0679	0.1882	−10	5	16	3	26	4	30	5	Z_6 T
55.8	1.2042	0.2511	−0.1098	0.2740	−11	4	22	3	30	4	37	5	Z_6 T
55.9	0.9844	0.1259	−0.1358	0.1852	−23	5	18	4	58	5	60	6	Z_6 T
56.0	0.4786	0.0538	−0.1295	0.1403	−33	6	29	8	89	8	93	10	Z_6 T
55.1	2.3317	0.1251	−0.0635	0.1403	−13	6	6	2	59	2	59	3	Z_5
55.2	2.5460	−0.0658	0.1367	0.1517	57	6	5	2	31	2	31	2	Z_5
55.5	2.1511	0.0468	−0.1984	0.2038	−38	4	9	2	63	3	63	3	Z_5
55.8	0.5459	0.0493	−0.0642	0.0809	−26	11	14	7	100	10	100	11	Z_5
56.2	1.0155	−0.1196	0.0672	0.1371	75	7	13	4	96	4	96	5	Z_7 T
56.3	1.7191	−0.1579	0.0987	0.1862	73	5	10	2	82	3	82	4	Z_7 T
56.6	3.9403	0.1581	−0.1886	0.2461	−25	4	6	1	41	2	41	2	Z_7 T
56.7	4.1011	0.1254	−0.2799	0.3067	−32	3	7	1	72	2	72	2	Z_7 T
56.8	3.4878	0.3522	−0.3107	0.4696	−20	2	13	1	82	2	83	2	Z_7 T
56.9	2.2160	0.1004	−0.2824	0.2997	−35	3	13	2	97	2	97	3	Z_7 T
57.0	1.2035	0.072	−0.1862	0.1997	−34	5	16	3	100	6	100	7	Z_7 T

Table C.2: continued.

V_{LSR} (km s^{-1})	I (Jy beam^{-1})	Q (Jy beam^{-1})	U (Jy beam^{-1})	P_l (Jy beam^{-1})	χ_l °	$\delta\chi_l$ °	m_l %	δm_l %	m_c %	δm_c %	m_f %	δm_f %	Notes
G69.540−0.976													
−0.4	0.3774	0.1233	−0.0641	0.1390	−13	5	36	9	91	7	97	10	
−0.1	1.7919	−0.5138	0.3445	0.6186	73	2	34	2	73	3	80	3	
0.0	2.1293	−0.2978	0.6808	0.7431	56	1	34	2	69	2	76	3	
0.1	0.8815	0.0674	0.0351	0.0759	13	8	8	3	50	4	50	4	
0.6	0.3132	−0.0726	0.0366	0.0813	76	7	25	8	61	9	65	12	
0.9	0.3268	−0.1524	0.0467	0.1594	81	6	48	22	85	7	97	17	
1.7	0.2375	−0.0580	−0.0650	0.0871	−65	7	36	12	88	11	95	14	
2.2	0.2427	−0.0532	0.0506	0.0735	68	9	30	11	95	11	99	13	
13.5	0.9403	0.0890	−0.0713	0.1140	−19	6	12	3	50	4	51	4	Z_1 T
13.6	1.3458	0.1192	−0.0479	0.1285	−10	5	9	2	39	3	40	3	Z_1 T
13.7	1.1541	0.0492	−0.1009	0.1122	−32	6	9	2	9	3	12	3	Z_1 T
13.7	1.1927	0.2008	−0.2744	0.3401	−26	2	28	3	88	4	92	4	Z_2 T
13.9	1.7185	−0.0541	0.1592	0.1681	54	4	9	2	8	2	12	2	Z_2 T
14.2	0.7002	−0.1036	0.0781	0.1297	71	5	18	4	89	5	90	5	Z_2 T
14.3	1.5880	0.2444	−0.4073	0.4750	−29	2	29	2	71	3	76	4	Z_3
14.4	4.4601	0.6337	−1.2972	1.4437	−31	1	32	1	16	1	35	2	Z_3
14.5	3.3037	0.2127	−0.3699	0.4267	−30	2	12	1	29	2	31	2	Z_3
14.3	0.5823	0.0818	−0.1271	0.1511	−28	5	25	6	100	21	100	24	Z_4
14.4	3.6289	0.0488	−1.1529	1.1539	−43	1	31	1	88	2	93	2	Z_4
14.5	3.8891	−0.4723	−0.7338	0.8726	−61	1	22	1	89	2	91	2	Z_4
14.3	0.7779	0.0796	−0.0425	0.0902	−14	7	11	4	45	5	46	6	Z_5 T
14.6	0.9527	−0.0953	0.1275	0.1592	63	4	16	3	87	5	88	6	Z_5 T
15.1	0.6818	0.0493	−0.0644	0.0811	−26	8	11	4	92	5	92	5	Z_5 T
15.2	0.4793	−0.2256	−0.0430	0.2297	−84	3	47	6	49	7	67	9	Z_5 T
15.4	0.4897	−0.0681	0.0368	0.0774	75	9	15	6	90	6	91	7	Z_5 T
G81.871−0.781													
6.7	2.7156	−0.0558	−0.1153	0.1281	−57	3	4	1	91	1	91	1	
6.8	1.8215	−0.046	−0.1319	0.1397	−54	1	7	1	88	2	88	2	
7.1	1.0569	0.0988	−0.128	0.1617	−26	3	15	2	54	2	56	2	Z_1 v
7.2	0.5418	−0.0629	0.0567	0.0847	69	5	15	3	87	4	88	5	Z_2 T
7.3	0.8037	−0.0248	0.0578	0.0629	56	2	7	2	94	3	94	3	Z_2 T
7.4	0.8246	−0.0403	0.0873	0.0962	57	2	11	2	88	3	88	3	Z_2 T
7.7	1.2051	0.0389	0.0912	0.0992	33	4	8	2	62	3	62	3	Z_2 T
7.8	1.1495	−0.0694	0.0957	0.1182	62	4	10	2	84	3	84	3	Z_2 T
7.9	1.0303	−0.0599	0.0631	0.087	66	5	8	2	93	4	93	4	Z_2 T
8.0	0.7447	−0.0537	0.058	0.079	66	6	10	3	100	4	100	4	Z_2 T
8.1	0.5281	−0.0348	0.0594	0.0688	60	6	13	3	82	5	83	5	Z_2 T
8.3	0.1977	0.068	−0.0389	0.0783	−14	5	39	9	42	9	57	13	Z_3
8.4	0.238	0.0958	0.1017	0.1397	23	3	58	9	11	7	59	10	Z_3
8.6	0.2265	−0.0662	0.0562	0.0868	69	5	38	8	90	7	97	10	Z_3
G108.766−0.986													
−45.9	0.8324	−0.0779	−0.0749	0.1081	−68	9	12	5	89	6	89	7	Z_1

Notes. In the last column, we mark the name of the Zeeman pairs from Table C.1 which the linearly polarized component belongs to. 'T' denotes the candidate for the Zeeman triplets, while 'v' is the possible candidate for the Zeeman triplets - verification is needed.

Table C.3: The YSOs' positions and brightness from the Hi-GAL catalog (Molinari et al. 2016a,b) and SED values from Elia et al. (2021) catalogue.

Source	$RA_{S_{70\mu m}}$ (h m s s)	$DEC_{S_{70\mu m}}$ (° ′ ″ ″)	$S_{70\mu m}$ (Jy)	Separation[7] (arcsec)	M $M_\odot$	T_D K	L_{bol} $L_\odot$	T_{bol} K	$\frac{L_{bol}}{M}$
G20.237	18 27 44.4072	−11 14 54.182	26.125	2.3	519.65	21.64	8694.85	46.22	16.7
G20.239	18 27 44.8008	−11 14 50.014	66.238	5.5	-	-	-	-	-
G24	18 35 20.9088	−07 48 54.785	66.761	1.1	95.22	24.07	2646.43	46.45	27.8
G25	18 34 21.0000	−05 59 42.342	994.174	1.4	4433.61	40.00	423777.75	53.40	95.6
G34	18 54 37.1976	+01 05 34.598	47.195	1.3	1208.23	22.43	19789.24	43.34	16.4
G43	19 10 10.9056	+09 05 18.132	1533.370	3.1	1785.3	39.0	570610.5	57.55	319.6
G48	19 22 26.2896	+14 06 42.458	569.424	3.6	89.58	23.83	2024.0	52.58	22.6
G49	19 23 43.9968	+14 30 32.288	3522.030	2.2	-	-	-	-	-

Appendix D: Counterparts - descriptions and figures

G20.237+00.065

The G20 is presented in Fig. D.1 showing the 1.3 mm dust continuum emission from ALMA archival data (project 2021.1.00311.S) overlaid with the methanol and ex-OH masers contours from G20.237+00.065. The source belongs to a cluster of three cores. The core associated with the masers has a flux density of 20.0 ± 4.6 mJy. The peak of the 8 μm *Spitzer* infrared emission is to the northwest of the maser emission and dust continuum emission. The region also hosts radio continuum emission (measured using VLA at two 1 GHz bands: 4.9840–6.0080 GHz and 6.6245–7.6485 GHz, with an angular resolution of ca. 3″), with an integrated flux density of 0.27 mJy (Hu et al. 2016). The $S_{70\mu m}/S_{24\mu m}$ ratio indicates the evolutionary stage, as shown by Purser et al. (2021). We estimated the ratio, using $S_{70\mu m}$ from Hi-GAL and $S_{24\mu m}$ from MIPSGAL (Carey et al. 2009; Gutermuth & Heyer 2015), to be 18.3. That supports the hypothesis that G20 contains an evolved MYSO (as it has multiple cores that may not be in the same evolutionary state).

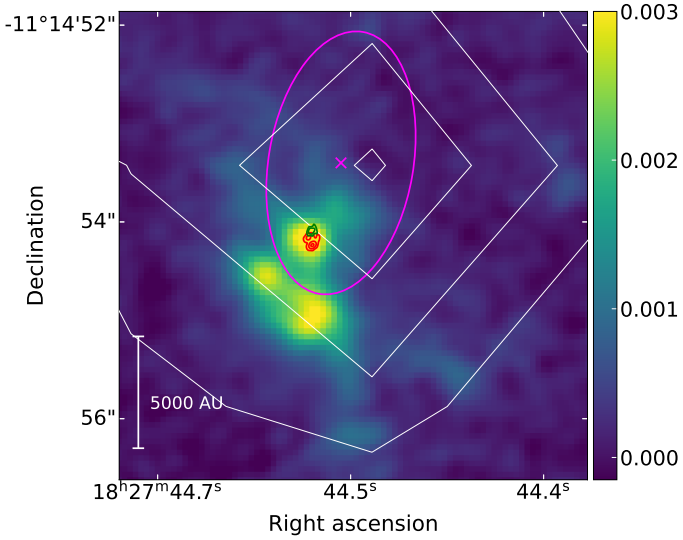

Fig. D.1: The 1.3 mm dust continuum emission from ALMA (color map) overlaid with the methanol and ex-OH masers contours of moment zero maps (marked by red and green colors, respectively) from G20.237+00.065. The wedge relates to the intensity in Jy beam−1. The white contours trace the *Spitzer* 8 μm emission at levels of 520, 620, 720, 820 MJy sr^{-1}. The magenta ellipse represents the resolved size of radio continuum emission from Hu et al. (2016), with the peak marked by a magenta cross.

We searched for spectral line data using the ALMA Science Archive and found no notable SiO emission toward either region, therefore, we can not identify any outflow. Compact thermal methanol 10(2)-9(3) at 231.281 GHz, ^{13}CO(2-1) and SO emission were found to be related to the masing region, but we are not able to detect any sign of rotation. ^{13}CO(2-1) does not show a clear velocity gradient. The shock-tracer SO shows only a small velocity gradient covering only 2 km s^{-1} (Fig. D.2).

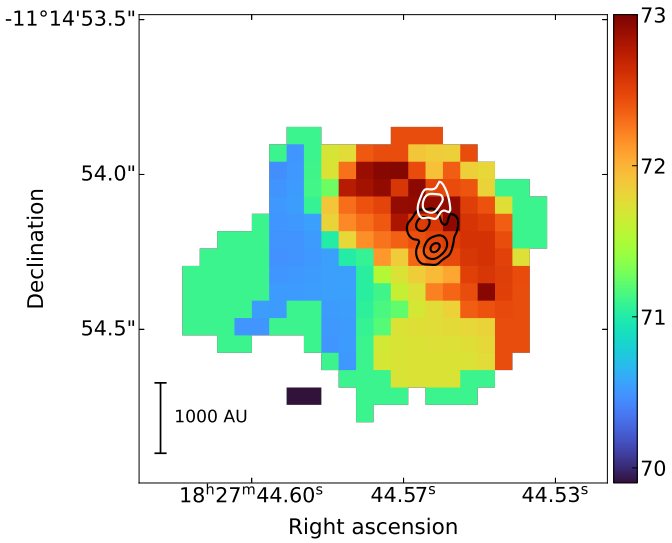

Fig. D.2: First moment image of SO with methanol and ex-OH masers contours of moment zero maps marked by the black and white colors, respectively from G20.237+00.065. The wedge relates to the velocities km s^{-1}.

G24.148−0.009

The G24 site is presented in Fig. D.3 with the ALMA archival data 3.1 mm dust continuum (2022.1.01204.S) and *Spitzer* 8 μm emission. The 3.1 mm continuum shows a compact continuum core with a peak flux of 3 mJy beam^{-1}. Both masers coincide with the 3.1 mm peak. The source has radio continuum emission with an integrated flux density of 1.23 mJy at 6 GHz (Hu et al. 2016), elongated in the N–S direction similar to the IR emission and maser emission.

We see extended ^{13}CO emission on the eastern side of the maser. We note that SO emission, which may be a tracer of accretion shocks at the disk-envelope interface in a UV-radiation field (van Gelder et al. 2021) but which can be found in outflows as well (Wells et al. 2024), is also located on the eastern side and is blue-shifted relative to the maser emission. We assume that there is an outflow in roughly the EW direction. The **position angle (PA$_{out}$) of this outflow is** listed in the Table 5. The ratio $S_{70\mu m}/S_{24\mu m}$ is 27.2, indicating, as in the case of G20, the late evolutionary phase of the HMYSO (Purser et al. 2021).

G25.649+1.049

The radio continuum at 6 GHz, 12 GHz, 22 GHz, and 44 GHz shows an elongated structure in the N-S direction (Bayandina et al. 2019), and the methanol and ex-OH masers are related to the continuum source VLA 2 according to the nomenclature of Bayandina et al. (2019). The IRAM 30m 3 mm data of SiO and HCO$^+$ indicate the existence of large-scale bipolar outflows at a PA of ca. −30° (Sánchez-Monge et al. 2013). Water masers also support such an outflow at the scale of a few arcseconds with PA slightly closer to the N–S direction, agreeing with the elongation of the radio continuum emission with a peak flux density of 3.83 mJy (Hu et al. 2016) as well as with the elongation of source VLA 2 (Bayandina et al. 2019). The ^{13}CO shows (Fig. D.5) collimated blue-shifted emission and a red-shifted lobe extended at a PA similar to the SiO and HCO$^+$ emission. Emission from CH_3CN and HC_3N (Figs. D.6 and D.7), which trace dense and warm gas, shows a blue-shifted arc on the east of the maser emis-

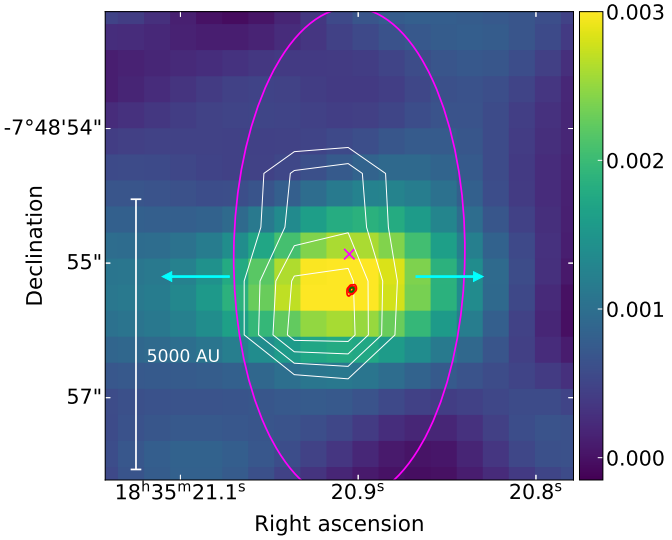

Fig. D.3: The 3.1 mm dust continuum emission from ALMA (color map) overlaid with the methanol and ex-OH maser contours of moment zero maps (marked by red and green colors, respectively) from G24.148−0.009. The wedge relates to the intensity in Jy beam^{-1}. The white contours trace the *Spitzer* 8 μm emission at the levels of 360, 460, 560, 660 MJy sr^{-1}. The magenta ellipse represents the resolved size of radio continuum emission from Hu et al. (2016), with the peak marked by a magenta cross. The blue arrows show the direction of the outflow from Table 5.

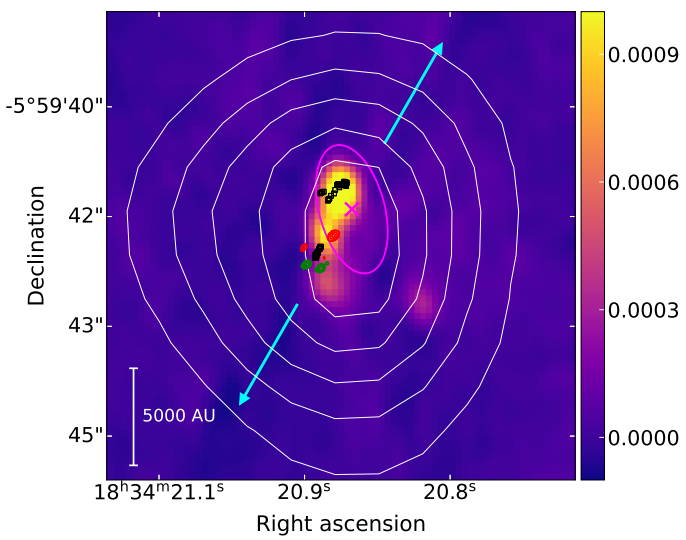

Fig. D.4: The 22 GHz continuum emission from the VLA (color map from Bayandina et al. (2019)) overlaid with the methanol and ex-OH maser contours of moment zero maps (marked by red and green colors, respectively) from G25.649+1.049. The wedge relates to the intensity in Jy beam^{-1}. The white contours trace the *Spitzer* 3.5 μm emission at the levels of 400, 800, 1200, 1600, 1900 MJy sr^{-1}. The black squares represent water maser emission from Bayandina et al. (2019). The magenta ellipse represents the resolved size of radio continuum emission from Hu et al. (2016), with the peak marked by a magenta cross. The blue arrows show the direction of the outflow from Table 5.

sion. That can suggest an almost face-on disc and imply that the outflow may have a small inclination angle or these molecules can trace shock fronts.

G34.267+0.210

The methanol and ex-OH maser emission lies westward from the peak of weak 4.5 μm IR emission.No radio continuum emission was detected by Hu et al. (2016), indicating the likely young evolutionary phase of the HMYSO. The ratio $S_{70\mu m}/S_{24\mu m}$ is 140, which confirms an early evolutionary phase infra-red dark cloud (IRDC, Purser et al. 2021). No other data were found to estimate the orientation of an outflow from this HMYSO.

G43.149+0.013

Region G43 is presented in Fig. D.8. Using ALMA archival data (2021.1.00311.S), we detect compact 1.3 mm emission with $S_{1.3mm}$=0.159±0.004 Jy. The methanol and ex-OH masers coincide with this mm core. A second and brighter 1.3 mm source (0.176±0.005 Jy) is located to the SW, but we do not find any masers above a 3 σ threshold of 0.045 Jy beam^1. According to Hu et al. (2016), the masers are located at an edge of the extended HII region with an integrated flux of almost 2 Jy, while Kalcheva et al. (2018) using the VLA CORNISH survey, at 5 GHz and 1.5″angular resolution, report two UCHII regions of 695 mJy and 44 mJy; the masers are related to the weaker emission. The UCHII region is unresolved and hence, the size marked in Fig. D.8 is an upper limit. The ALMA band 6 data shows NE–SW outflows at PAs of about 40°in ^{13}CO and C^{18}O lines (Figure D.9) and we list this value in Table 5. The H_2CO and CH_3CN show N–S velocity gradients of about 3 and 6 km s^{-1}, respectively, at a position angle of about 0°for both lines (Figure D.10).

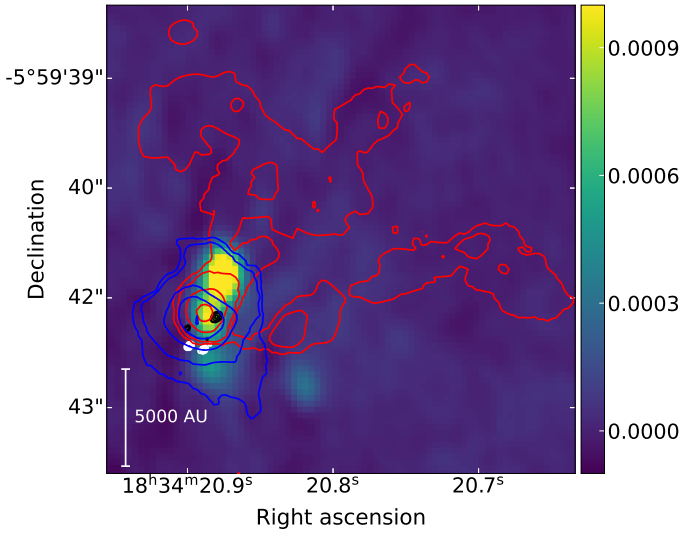

Fig. D.5: The 22 GHz continuum emission from VLA overlaid (colour map) with methanol and ex-OH masers contours of moment zero maps marked by the black and white color, respectively, from G25.649+1.049, and with ^{13}CO moment zero maps marked by contours: blue for 22-42 km s^{-1} emission and red for 42-62 km s^{-1} emission. The wedge relates to the intensity in Jy beam^{-1}.

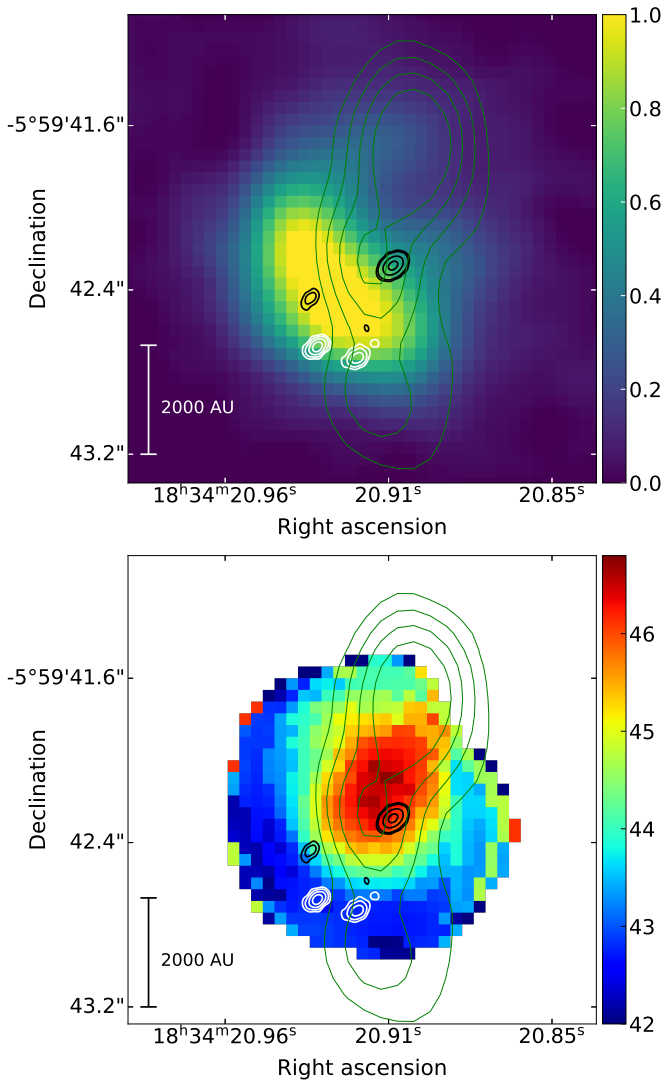

Fig. D.6: Zero (*top*) and first (*bottom*) moment image of CH_3CN with 22 GHz continuum contours of moment zero maps marked by the green color, and methanol and ex-OH masers contours of moment zero maps marked by the black and white colors, respectively from G25.649+1.049. The wedge relates to the intensity in Jy beam^{-1} on *top* and in km s^{-1} on *bottom*.

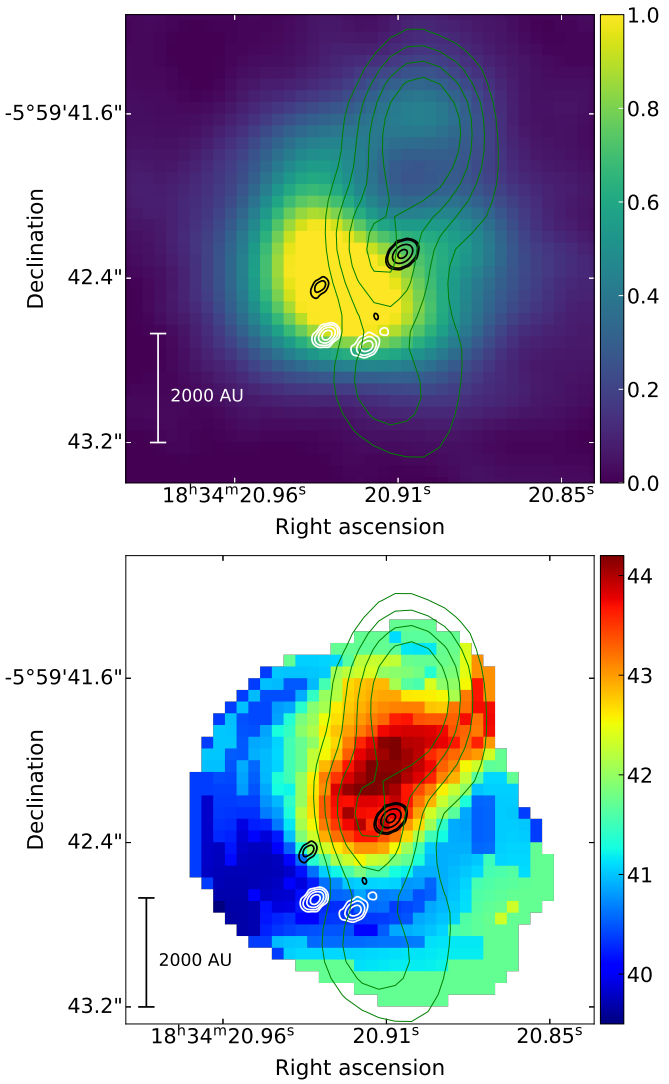

Fig. D.7: Zero (*top*) and first (*bottom*) moment image of HC_3N with 22 GHz continuum contours of moment zero maps marked by the green color, and methanol and ex-OH masers contours of moment zero maps marked by the black and white colors, respectively from G25.649+1.049. The wedge relates to the intensity in Jy beam^{-1} on *top* and in km s^{-1} on *bottom*.

G48.990−0.299

Region G48 is presented in Fig. D.11. The maser emission lies on the eastern edge of a compact 8 μm IR emission and coincides with a UCHII region with a flux density of 7.53 mJy (Kalcheva et al. 2018). The UCHII region is unresolved and hence, the size marked in Fig. D.11 is an upper limit. Water maser emission was detected to the south (at a separation of ∼0.″45 from the methanol and ex-OH masers) by Nagayama et al. (2015) and their elongated structure in the NS direction in a small area less than 20 mas (at a PA of +20°) together with proper motion studies indicated an outflow. This PA in reported in Table 5 since the separation between the various maser species is only ca. 2500 AU.

G49.490−0.388

The region G49 is presented in Fig. D.12 with the ALMA archival data 1.3 mm dust continuum emission (2015.1.01596.S) overlaid with maser contours. The dust emission from W51e2e, the eastern source, shows a central, circular core (with a radius of ca. 500 au) and four filamentary structures extending ca. 2700 au. The luminosity of the core corresponds to a B1V main-sequence star with a mass of 11 $M_\odot$ as reported by Goddi et al. (2020). They also found a bipolar outflow traced by ^{12}CO at a position angle of −37° and SiO at a position angle of −56°. Therefore, we list the mean of these values in Table 5. The western core of 1.3 mm dust continuum emission, W51e2w, corresponds to a UCHII region (Gaume et al. 1993). Shi et al. (2010b) suggested that W51e2w consists of a hyper-compact HII core, <0.06″(<310 au), with an ionized outflow.

The methanol and ex-OH maser emission arises at the SW of W51e2e and at the south of W51e2w, respectively. Shi et al. (2010a) reported that W51e2e core is associated with bipolar

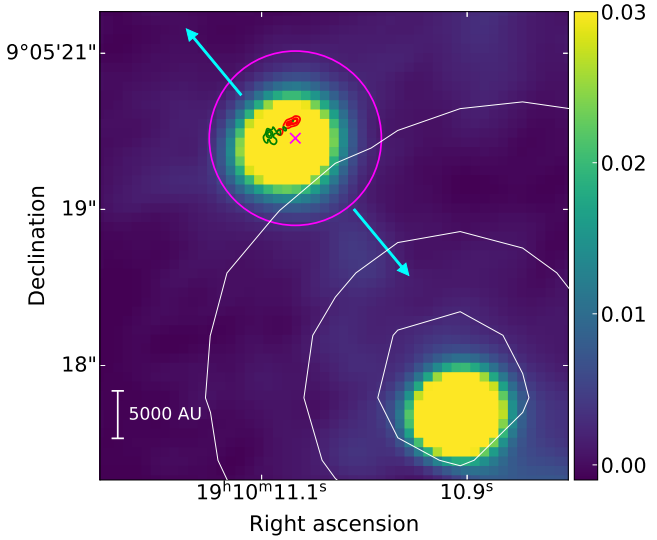

Fig. D.8: The 1.3 mm dust continuum emission from ALMA (color map) overlaid with the methanol and ex-OH maser contours of moment zero maps (marked by red and green colors, respectively) from G43.149+0.013. The white contours trace the *Spitzer* 6 μm emission at the levels of 4000, 9000, 14000 MJy sr^{-1}. The wedge relates to the intensity in Jy beam^{-1}. The magenta ellipse represents the UCHII region from Kalcheva et al. (2018), with the peak marked by a magenta cross. The blue arrows show the direction of the outflow from Table 5.

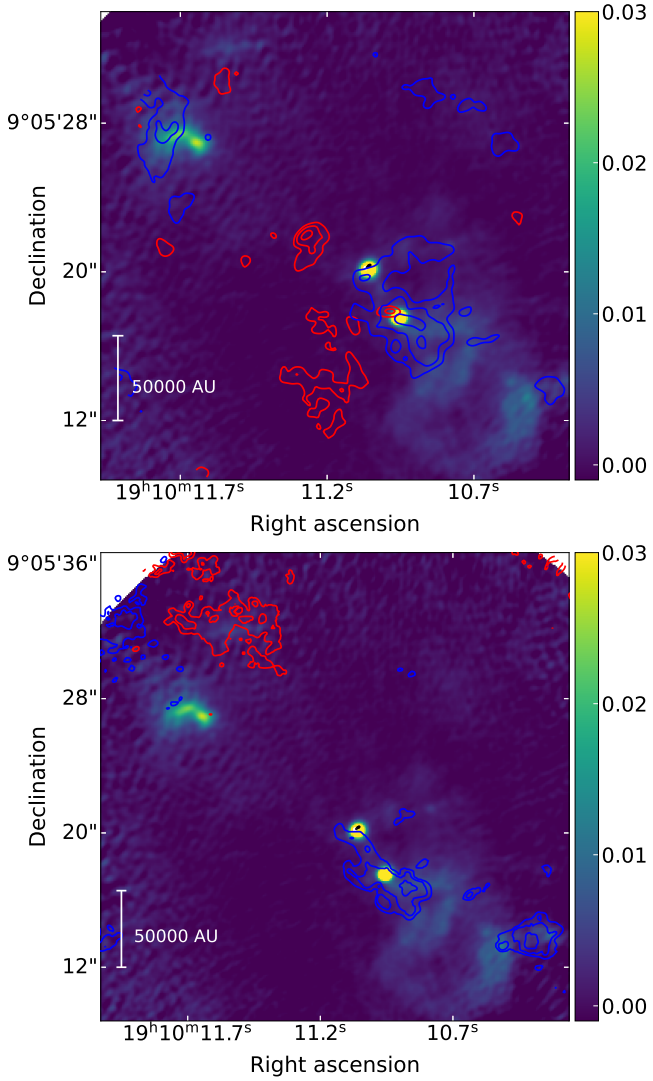

Fig. D.9: The 1.3 mm dust continuum emission from ALMA (color map) overlaid with methanol and ex-OH masers contours of moment zero maps marked by the black and white color, respectively, from G43.149−0.013, and with ^{13}CO (*top*) and C^{18}O (*bottom*) moment zero maps marked by contours: blue for 2-10 km s^{-1} emission and red for 12-20 km s^{-1} emission. The wedge relates to the intensity in Jy beam^{-1}.

molecular CO(3-2) outflow in the NW–SE direction at position angle −40 at an inclination angle ∼45°, which agrees with the CO outflow properties reported by Goddi et al. (2020). The closest peak of IR 6 μm emission appears to the south, ∼3″from the maser emission, and coincides with the peak of 70 μm emission from HIGALPB049.4894−0.3881 (Table C.3).

G69.540−0.976

The masers in the G69 region are presented in Fig. D.13 overlaid on the ALMA archival data 1.3 mm dust continuum emission (2021.1.00311.S). The source consists of three cores. The methanol and ex-OH masers are detected toward the western core, which has a 1.3 mm flux density of 236±64 mJy. These cores are in the central part of a WISE 8 μm emission source. The peak of radio continuum emission, with an integrated flux of 103.6 mJy (Hu et al. 2016), corresponds well with the methanol and ex-OH emission. That continuum emission was confirmed as a UCHII region (Zheng et al. 1985; Argon et al. 2000). Nagayama et al. (2008) postulated the existence of a binary system comprising the YSO in WMC 1 related to the NE 1.3 mm core and the B0 star exciting the UCHII region, related to the western 1.3 mm core. There is also a third YSO WMC 2 related to the southern 1.3 mm core (see their figure 4). Kumar et al. (2004) reported two molecular outflows (see their figure 3): one traced by H^{13}CO$^+$ and SiO at a PA of +44° and the second by CO at a PA of −69°. Surcis et al. (2022) suggested that the 6.7 GHz maser is more likely to be associated with the CO outflow, and following that, we adopt this value in Table 5. ALMA 1 mm H_2CO transitions ($3_{22} - 2_{21}$) and ($3_{03} - 2_{02}$), presented in Fig. D.15, show that there is a velocity gradient of about 6 km s^{-1} across the continuum core with the maser emission presenting blue-shifted velocities (from ca. 8 km s^{-1}) in the NE to red-shifted velocities (ca. 14 km s^{-1}) in the SW with a PA of ca. 40°. This may indicate an edge-on viewing angle of a rotating disk/envelope. This is consistent with the outflow at PA of −69°.

G81.871+0.781

The masers in region G81 are presented in Fig. D.16 overlaid on the ALMA archival data 3 mm dust continuum emission (project 2019.1.00059.S). Sensitive, high-angular resolution (0.1″) observations revealed three peaks of 1.3 cm continuum emission named VLA 1, VLA 2, and VLA 3 (Torrelles et al. 1997). The central region, VLA 2, shows a quasi-circular morphology interpreted as a UCHII region. VLA 1 and VLA 3 show elongated radio continuum structures interpreted as thermal jets. The methanol and ex-OH masers are related to the northern region VLA 1, which is elongated at a PA of +43°. Surcis et al. (2014) reported polarimetric observations of water masers towards both VLA 1 and VLA 2, confirming the elliptical expansion of the

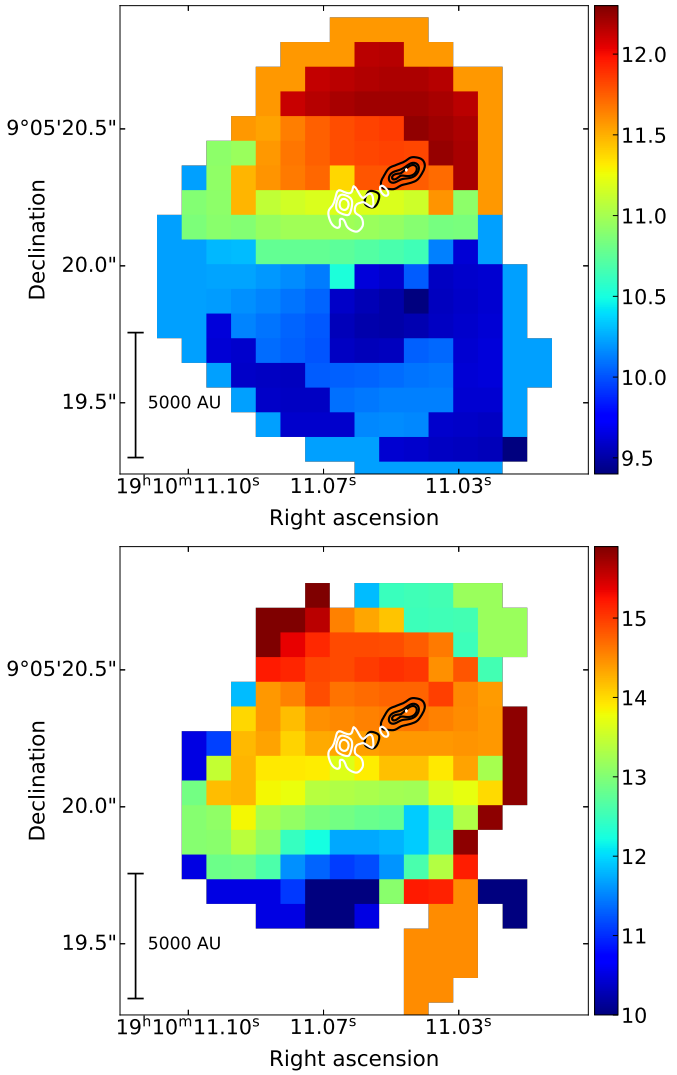

Fig. D.10: First moment image of H_2CO (*top*) and first moment of image CH_3CN (*bottom*) with methanol and ex-OH masers contours of moment zero maps marked by the black and white colors, respectively from G43.149−0.013. The wedge relates to the velocities km s^{-1}.

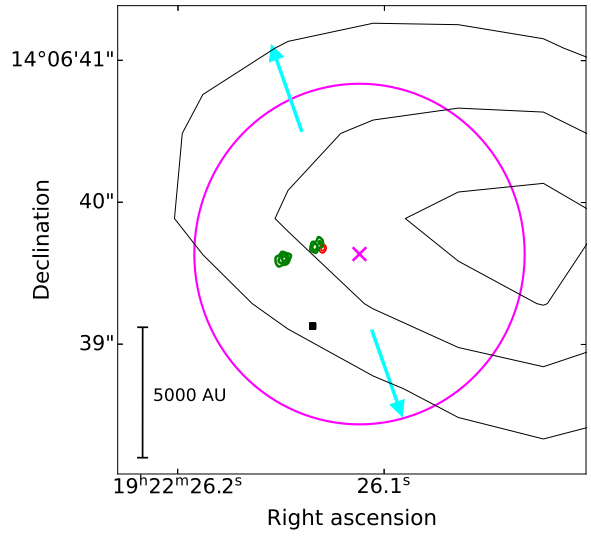

Fig. D.11: The methanol and ex-OH maser contours of moment zero maps (marked by red and green colors, respectively) from G48.990−0.299. The black squares represents water maser emission from Nagayama et al. (2015). The black contours trace the *Spitzer* 8 μm emission at the levels of 650, 750, 850 MJy sr^{-1}. The magenta ellipse represents the UCHII region from Kalcheva et al. (2018), with the peak marked by a magenta cross. The blue arrows show the direction of the outflow from Table 5.

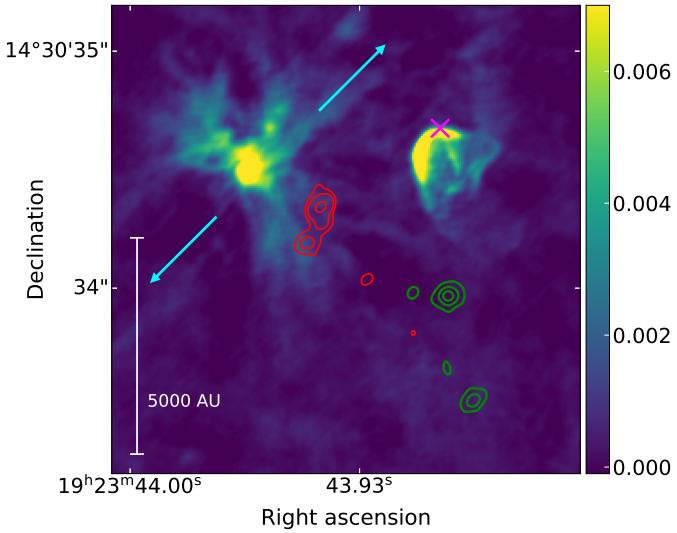

Fig. D.12: The 1.3 mm dust continuum emission from ALMA (Goddi et al. 2020) (color map) overlaid with the methanol and ex-OH maser contours of moment zero maps (marked by red and green colors, respectively) from G49.490−0.388. The wedge relates to the intensity in Jy beam^{-1}. The magenta cross represents the peak of UCHII region (Gaume et al. 1993).
The blue arrows show the direction of the outflow from Table 5.

shell-like structure around VLA 2 and the stability of the water maser distribution and the magnetic field around VLA 1 over 7 yr.

Hutawarakorn et al. (2002) showed that the 18-cm OH masers are distributed over a large region of 5″ across, elongated in the NW–SE direction. The distribution was interpreted in terms of a rotating disc orthogonal to the bipolar outflow which is seen in CO and H_2. ALMA observations of ^{12}CO confirmed the NE–SW direction of the outflow (Figure D.17), although the ^{12}CO emission shows significant self-absorption in the velocity range 4 to 10 km s^{-1}.

G108.766−0.986

In the region G108 Hu et al. (2016) did not detect any radio continuum emission, therefore, we can assume that this HMYSO is in an early stage of evolution, similar to G34. The masers in both transitions lie to the south of a very weak 4.5 μm IR source. We do not find any more data in the ALMA Archive, so cannot investigate the existence and direction of any outflow.

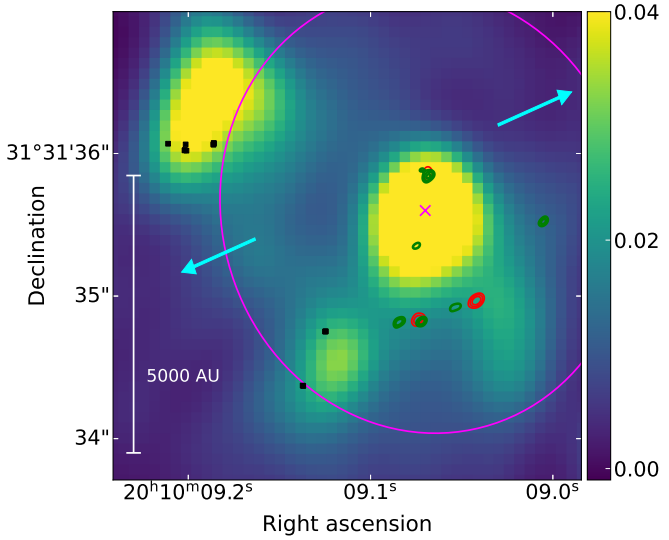

Fig. D.13: The 1.3 mm dust continuum emission from ALMA (color map) overlaid with the methanol and ex-OH maser contours of moment zero maps (marked by red and green colors, respectively) from G69.540−0.976. The black squares represent water maser emission from Nagayama et al. (2008). The wedge relates to the intensity in Jy beam^{-1}. The magenta ellipse represents the resolved size of the UCHII region from Hu et al. (2016), with the peaked mark by a magenta cross. The blue arrows show the direction of the outflow from Table 5.

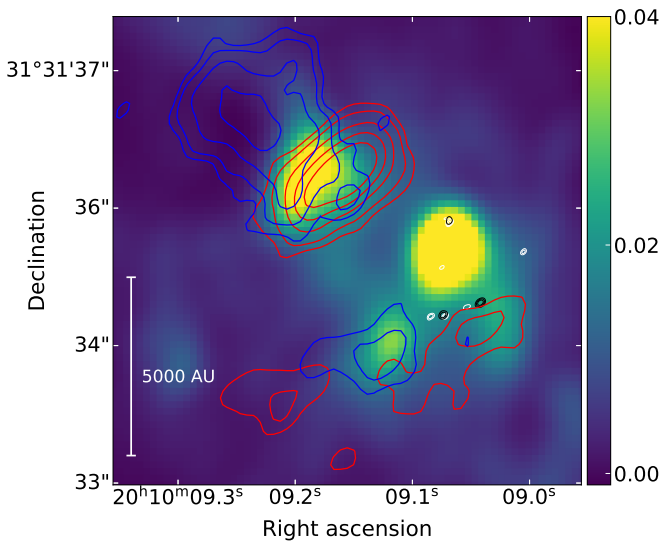

Fig. D.14: The 1.3 mm dust continuum emission from ALMA (color map) overlaid with methanol and ex-OH masers contours of moment zero maps marked by the black and white colors, respectively, from G69.540−0.976, and with SiO moment zero maps marked by contours: blue for −60-10 km s^{-1} emission and red for 14-60 km s^{-1} emission The wedge relates to the intensity in Jy beam^{-1}.

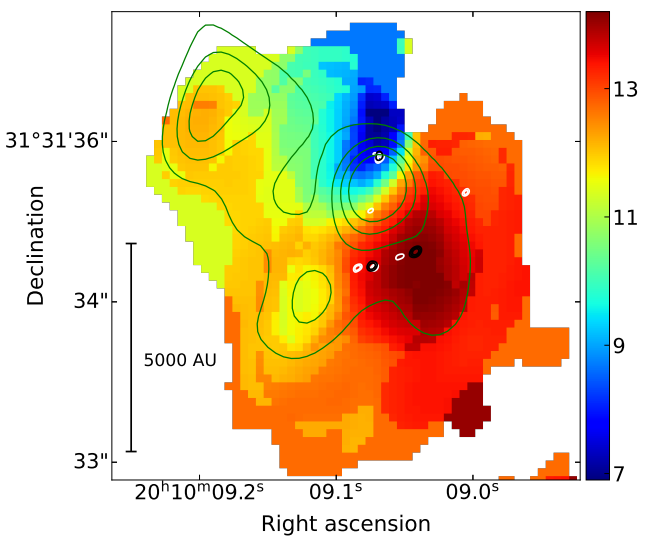

Fig. D.15: First moment image of H_2CO with methanol and ex-OH masers contours of moment zero maps marked by the black and white color, respectively, from G69.540−0.976, and with 1.3 mm dust continuum emission marked by green contours. The wedge relates to the intensity in km s^{-1}.

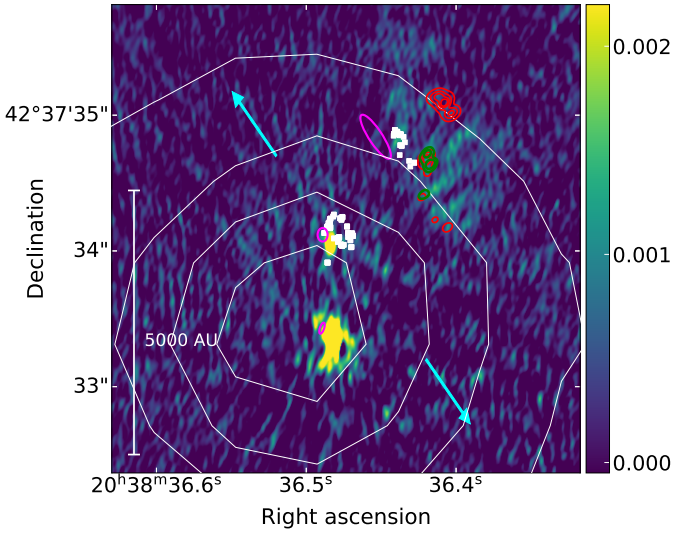

Fig. D.16: The 3 mm dust continuum emission from ALMA (color map) overlaid with the methanol and ex-OH maser contours (marked by red and green colors, respectively) from G81.871+0.781. The white squares represent water maser emission. The white contours trace the *Spitzer* 8 μm emission at the levels of 2000, 5000, 8000, 11000 MJy sr^{-1}. The wedge relates to the intensity in Jy beam^{-1}. The white squares represent water maser emission from Surcis et al. (2014). The magenta ellipses represent the resolved size of the radio continuum emission from Torrelles et al. (1997), from the north, VLA 1, VLA 2, and VLA 3. The blue arrows show the direction of the outflow from Table 5.

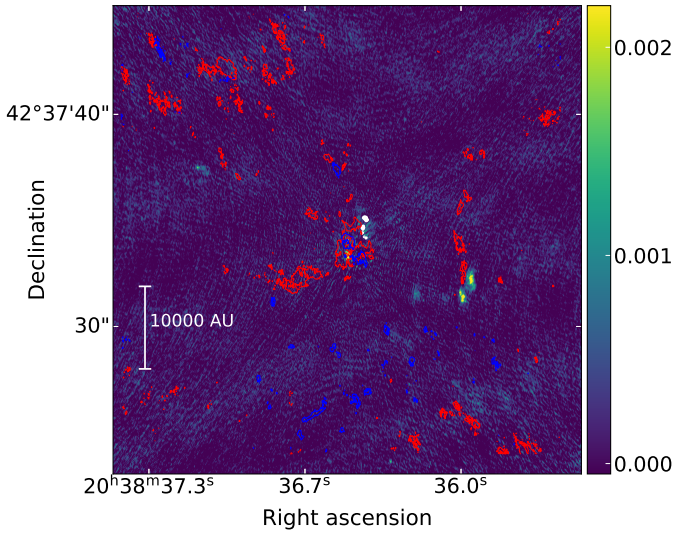

Fig. D.17: The 3 mm dust continuum emission from ALMA (color map) overlaid with methanol and ex-OH masers contours of moment zero maps marked by the white color, from G81.871−0.781, and with ^{12}CO moment zero maps marked by contours: blue for −30-4 km s^{-1} emission and red for 10-40 km s^{-1} emission The wedge relates to the intensity in Jy beam^{-1}.

A&A, 701, A101 (2025)
https://doi.org/10.1051/0004-6361/202555576

Astronomy & Astrophysics

A search for the favored hyperfine transition of a 6.7 GHz methanol maser line

A. Kobak[1,⋆], G. Surcis[2], A. Bartkiewicz[1], W. H. T. Vlemmings[3], and M. Szymczak[1]

[1] Institute of Astronomy, Faculty of Physics, Astronomy and Informatics, Nicolaus Copernicus University, Grudziadzka 5, 87–100 Torun, Poland
[2] INAF – Osservatorio Astronomico di Cagliari, Via della Scienza 5, 09047 Selargius, Italy
[3] Department of Space, Earth and Environment, Chalmers University of Technology, 412 96 Gothenburg, Sweden

Received 19 May 2025 / Accepted 1 July 2025

ABSTRACT

Context. The polarized emission of astrophysical masers, especially OH and CH_3OH lines, is an effective tool to study the magnetic field in high-mass star-forming regions. The magnetic field strength measurement via the Zeeman effect of OH maser emission is well established, but that of the CH_3OH maser emission is still under debate because of its complex hyperfine structure.
Aims. We aim to identify the dominating hyperfine transition of the Class II 6.7 GHz CH_3OH maser emission by comparing the magnetic field strength measured with the 6.0 GHz excited OH maser emission and the Zeeman splitting of the CH_3OH maser emission.
Methods. We used quasi-simultaneous European VLBI Network observations of the two maser emissions at 6.035 GHz (excited OH maser) and 6.668 GHz (CH_3OH maser) toward two well-known high-mass young stellar objects: G69.540-0.976 (ON 1) and G81.871+0.781 (W75N). The observations were performed in full polarimetric mode and in phase-referencing mode to couple the maser features of the two maser emissions in each source.
Results. We detected linearly and circularly polarized emission in both maser transitions and high-mass young stellar objects. Specifically, we measured the magnetic field strength in twelve and five excited OH maser features toward ON 1 and W75N, respectively, and the Zeeman splitting of the CH_3OH maser spectra in one and three maser features toward ON 1 and W75N, respectively. We determined that the two maser emissions likely probe the same magnetic field but at different densities. Indeed, a direct comparison of the magnetic field strength and the Zeeman splitting as measured with the excited OH and CH_3OH maser spots, respectively, provided values of the Zeeman splitting coefficient (α_Z) for the 6.7 GHz CH_3OH maser that do not match with any of the table values present in the literature.
Conclusions. We are not able to uniquely identify the dominating hyperfine transition; however, through density considerations we can narrow the choice down to three hyperfine transitions: 3→4, 6→7A, and 7→8. Furthermore, we support the previously proposed idea that the favored hyperfine transition is not always the same, but that in different high-mass young stellar objects, the dominating one can be any of these three hyperfine transitions.

Key words. masers – polarization – stars: formation – stars: massive – ISM: magnetic fields – ISM: molecules

1. Introduction

The magnetic field plays a crucial role in the high-mass star formation process, primarily because it can suppress the fragmentation process and transport angular momentum, keeping the matter close to the central object, where it can be accreted (e.g., Price & Bate 2007; Beuther et al. 2018; Krumholz & Federrath 2019). Observations at high angular resolution of maser emission lines from hydroxyl (OH), water (H_2O), or methanol (CH_3OH) molecules are the best way to study the kinematics of gas in high-mass young stellar objects (HMYSOs; e.g., Moscadelli et al. 2011; Etoka et al. 2012; Bartkiewicz et al. 2016), whereas studying their polarized emission allows us to estimate the morphology and strength of magnetic fields (e.g., Bartkiewicz et al. 2005; Vlemmings et al. 2010; Surcis et al. 2011a). The pumping mechanism of the maser levels responsible for the CH_3OH maser emission at 6.7 GHz and of the excited OH (hereafter ex-OH) maser emission at 6.035 GHz is due to the infrared emission from warm dust heated by nearby HMYSOs. In addition, these maser emissions also share similar physical conditions such as temperature and density, making them possibly arise in the same volume of gas (Cragg et al. 2002). Therefore, if they arise in the same volume of gas, they must probe the same magnetic field; i.e., the same morphology and strength.

Hydroxyl (OH) is a paramagnetic molecule; i.e., it strongly interacts with an external magnetic field. This implies that the Zeeman splitting of its maser lines, for typical field strengths in massive star-forming regions, is larger than their linewidths. In other words, the frequency difference between the left- and right-handed circular polarized emissions (LHCP and RHCP), which correspond to the shifted σ components produced by the Zeeman effect, is easily measurable. Furthermore, the Landé g-factor and, consequently, the Zeeman splitting coefficient (α_Z) are known for many of the OH maser transitions (Davies 1974; Baudry et al. 1997), making the estimation of the magnetic field strength straightforward. Unlike OH, the CH_3OH molecule is non-paramagnetic; consequently, the Zeeman splitting of its maser lines is smaller than that of the maser linewidths, making the estimation of the magnetic field strength challenging but feasible (e.g., Vlemmings et al. 2010, 2011). It is important to note that in this case, the Zeeman splitting is not directly measured, but it must be estimated either by modeling the circularly polarized emission of the masers or by using a cross-correlation

⋆ Corresponding author.

method (e.g., Modjaz et al. 2005; Vlemmings 2008; Vlemmings et al. 2010). In addition, all the CH_3OH masers show a very complex hyperfine structure (Lankhaar et al. 2016). For instance, eight hyperfine transitions can contribute to the maser emission at 6.7 GHz, and each one has its own Zeeman splitting coefficient (Lankhaar et al. 2018). At the moment, the dominant hyperfine transition for all of the CH_3OH masers is unknown, which prevents the estimation of the magnetic field strength from their Zeeman splitting estimates. Nevertheless, in the case of the 6.7 GHz CH_3OH maser emission the hyperfine transition F = 3→4 has been assumed to be the preferred one (e.g., Lankhaar et al. 2018; Surcis et al. 2022), although Dall'Olio et al. (2020) suggested that the dominant hyperfine transition might also be either F = 6→7A or F = 7→8. However, the uncertainty on which is the dominating hyperfine transition renders the Zeeman splitting estimates made so far toward a large sample of HMYSOs almost worthless (e.g., Surcis et al. 2022). Therefore, it is crucial to find an observational strategy that allows us to identify the dominating hyperfine transition of the 6.7 GHz CH_3OH maser emission. A potential good strategy is that of observing the 6.7 GHz CH_3OH and the 6.035 GHz ex-OH maser emissions simultaneously toward the same HMYSOs. Indeed, the two maser emissions are thought to arise in the same volume of gas (Cragg et al. 2002), and consequently they might probe the same magnetic field.

In this paper, we present the comparison between the magnetic field strength and the Zeeman splitting as measured and estimated from the circularly polarized emission of the well-known 6.035 GHz ex-OH and of the 6.7 GHz CH_3OH maser emissions, respectively, with the aim of identifying the dominating hyperfine transition of the latter. The polarized maser emissions have been observed with the European VLBI Network (EVN) near two well-known HMYSOs: G69.540−0.976 (ON 1) and G81.871+0.781 (W75N). We selected these two sources according to recent single-dish (Szymczak et al. 2018, 2020) and interferometric results of a larger sample (Kobak et al. 2025). Kobak et al. (2025) observed the two HMYSOs with the e-MERLIN and showed that in both HMYSOs the CH_3OH and ex-OH maser features are very bright and strongly polarized; they shared the same local-standard-of-rest velocity (V_{LSR}) range, and their projected positions on the plane of the sky coincided. Unfortunately, e-MERLIN results cannot be used for our scientific purposes because the spatial resolution does not ensure the absence of maser line blending, which can severely affect the Zeeman splitting estimates of the CH_3OH maser. Furthermore, single-dish monitoring observations indicate that both maser emissions are variable on a timescale of one week to a few years (e.g., Szymczak et al. 2018, 2020). Below, we report a brief introduction of the two HMYSOs.

G69.540−0.976[1] (also known as Onsala 1, hereafter ON 1) is a high-mass star-forming region (HMSFR) at a parallactic distance of $2.57^{+0.34}_{-0.27}$ kpc (Rygl et al. 2010). The archival ALMA data (2021.1.00311.S) show that the source hosts three cores of 1.3 mm dust continuum emission, the westernmost of which is an ultra-compact (UC) HII region that harbors an exciting type B0 star (Zheng et al. 1985; MacLeod et al. 1998; Argon et al. 2000; Nagayama et al. 2008; Hu et al. 2016) and is associated with 6.7 GHz CH_3OH and 6.035 GHz ex-OH masers (Nammahachak et al. 2006; Sugiyama et al. 2011; Surcis et al. 2022; Kobak et al. 2025). The other two cores, named WMC1 and WMC2, are associated with 22 GHz H_2O masers (Nagayama et al. 2008). Two molecular outflows were observed. The first one is traced by $H^{13}CO^+$ and SiO and it is oriented on the plane of the sky with a position angle (PA) of +44°, and the second one is traced by CO (PA=−69°; Kumar et al. 2004). It is still unclear which cores the two outflows are related to. The 6.7 GHz CH_3OH masers show a similar distribution to the 1.665 GHz OH masers, and both maser emissions are tracing an outward motion of the gas, likely suggesting the expansion of the UCHII region (Fish & Reid 2007; Sugiyama et al. 2011). Ground-state OH masers (1.665 GHz and 1.667 GHz) indicated magnetic field strength along the line of sight ($B_\parallel$) ranging from −0.9 mG to −5.1 mG (Fish et al. 2005), where a negative $B_\parallel$ indicates that the magnetic field is pointing toward the observer. Nammahachak et al. (2006) also measured a magnetic field of −0.4 mG and of −1 mG from two Zeeman pairs of 1.720 GHz OH masers. Recently, Kobak et al. (2025) measured magnetic fields in the −1.2 mG to −6.2 mG range from the 6.035 GHz ex-OH maser, which is consistent with those measured previously with the same ex-OH maser emission ($-1.1\,\mathrm{mG} \leq B_\parallel^{2007} \leq -5.8\,\mathrm{mG}$ and $-1.2\,\mathrm{mG} \leq B_\parallel^{2010} \leq -12.1\,\mathrm{mG}$; Green et al. 2007; Fish & Sjouwerman 2010). Green et al. (2007) also reported a magnetic field of −3.9 mG from the only Zeeman pair identified toward the OH maser emission at 6.031 GHz. In addition, they also estimated, using the cross-correlation method, the very first Zeeman splitting (ΔV_Z) of a 6.7 GHz CH_3OH maser –i.e., $\Delta V_Z = 0.9 \pm 0.3\,\mathrm{m\,s^{-1}}$– using the MERLIN. More recently, Surcis et al. (2022) observed the 6.7 GHz CH_3OH maser emission with the EVN, and using the full radiative transfer method (FRTM) code they estimated two Zeeman splitting values of $14.5\pm4.4\,\mathrm{m\,s^{-1}}$ and $1.2\pm0.2\,\mathrm{m\,s^{-1}}$.

G81.871+0.781, known as W75N, is an HMSFR at a parallactic distance of 1.30±0.07 kpc (Rygl et al. 2012). Several radio sources have been identified, among which the most interesting are VLA1 and VLA2 (e.g., Torrelles et al. 1997; Carrasco-González et al. 2010; Rodríguez-Kamenetzky et al. 2020). VLA1 is in an early stage of the photoionization, and it is driving a thermal radio jet (PA=+42°) whose morphology did not change over a period of 18 years (Rodríguez-Kamenetzky et al. 2020). VLA2 is a thermal, collimated, ionized wind surrounded by a dusty disk or envelope, and it varied its morphology between 1996 and 2014 from a compact, roundish source to an elongated source (PA=+65°; Carrasco-González et al. 2015). A large-scale CO outflow with PA of +66° was observed by Hunter et al. (1994). Different maser species are associated with VLA1 and VLA2: 6.7 GHz CH_3OH masers (e.g., Minier et al. 2001; Surcis et al. 2009), 1.665 GHz OH masers (e.g., Hutawarakorn et al. 2002; Fish et al. 2005, 2011), 6.035 GHz ex-OH masers (e.g., Kobak et al. 2025), and 22 GHz H_2O masers (e.g., Surcis et al. 2023). The CH_3OH and ex-OH masers are only detected toward VLA1; all the other maser species are detected toward both radio sources. A magnetic field strength between +3.7 and +8.1 mG, indicating that the magnetic field points away from the observer, was measured from the Zeeman effect of a 1.665 GHz OH maser line around VLA1 (Hutawarakorn et al. 2002; Fish et al. 2005), which is consistent with the values obtained from the Zeeman pair of 6.035 GHz ex-OH masers ($+2.3\,\mathrm{mG} \leq B_\parallel \leq +8.5\,\mathrm{mG}$; Kobak et al. 2025). Surcis et al. (2009) reported Zeeman splitting estimates, determined via the cross-correlation method, toward three 6.7 GHz CH_3OH maser features, these are +0.53, +0.75, and $+0.8\,\mathrm{m\,s^{-1}}$. In addition, the magnetic field was measured along VLA1 from the 22 GHz H_2O maser emission at different epochs, indicating typical values in the range $-764\,\mathrm{mG} \leq B_\parallel \leq -676\,\mathrm{mG}$ (Surcis et al. 2023). The high values measured from the H_2O masers are the consequence of the high densities where these masers arise.

[1] The name follows the Galactic coordinates of the target.

Table 1. Beam size and the rms noise (1σ) for each imaged data cube.

Source	Restoring beam (mas×mas)	Position angle (°)	σ_I (mJy beam^{-1})	σ_Q (mJy beam^{-1})	σ_U (mJy beam^{-1})	σ_V (mJy beam^{-1})	σ_{LL} (mJy beam^{-1})	σ_{RR} (mJy beam^{-1})	σ_{POLI} (mJy beam^{-1})
ON 1 (CH_3OH)	5.3×4.6	−40	4.3	5.1	5.1	4.3	7.1	4.9	3.3
ON 1 (ex-OH)	9.3×5.7	−17	1.7	9.9	9.9	–	6.1	3.3	6.5
W75N (CH_3OH)	5.9×4.3	−47	3.7	4.1	4.4	3.8	5.5	5.2	4.5
W75N (ex-OH)	7.3×5.8	−31	6.2	6.1	6.0	–	8.5	8.3	4.1

2. Observations and analysis

We observed ON 1 and W75N with nine antennas of the EVN (Jb, Wb, Ef, Mc, Nt, On, Tr, Ys, Ib) at 6035.092 MHz and 6668.519 MHz to detect the ex-OH and CH_3OH maser emissions (project code: EK052). To ensure quasi-simultaneous observations of the two maser species, we observed each source on two consecutive days: W75N on 29–30 May, 2023 and ON1 on 31 May-01 June, 2023. The observations were carried out with eight subbands of 4 MHz (~100 km s^{-1}) each, both in phase-referencing (with cycles phase-calibrator – target of 2–3 min) and full-polarization mode, for a total observing time of 48 hours. The phase-referencing calibrators were J2003+3034 (at separation 1.7°) and J2048+4310 (1.9°) for ON 1 and W75N, respectively. The data were correlated with the EVN software correlator (SFXC; Keimpema et al. 2015) in two correlation passes: a continuum pass for all eight subbands with 128 spectral channels; and a line pass for only the subband and the maser emission with 4096 spectral channels. The line pass allowed us to obtain a spectral resolution of ~1 kHz (velocity resolution at both frequencies of ~0.05 km s^{-1}) that is necessary to estimate the Zeeman splitting of the CH_3OH maser emission. All four polarization combinations (RR, LL, RL, and LR) were generated for all correlation passes.

The data were calibrated and imaged by using the Astronomical Image Processing Software package (AIPS, NRAO 2023) following the standard spectral polarimetric and phase-referencing procedures (e.g., Surcis et al. 2012, 2023). For all the datasets, we used the calibrator J2202+4216 (BL Lac) to calibrate the bandpass, the delay, the phase, the rates, and the D-terms. The calibration of the polarization angles was instead performed on the calibrator 3C286 ($I \approx 0.2$ Jy beam^{-1}; linear polarization percentage $P_l \approx 12\%$) for all but one dataset. We could not use 3C286 to calibrate the polarization angles of the CH_3OH masers in W75N due to a problem with the 3C286 data. Therefore, we decided to compare the calibrated polarization angle of J2202+4216 from the ON 1 dataset (PA= $-13°.2 \pm 2°.1$), which was calibrated using 3C286, with that observed in the W75N dataset, and then applied the rotation to the linear polarization vectors of the CH_3OH masers in W75N. The uncertainty of this calibration is equal to 7°. We self-calibrated the brightest maser spot of each dataset and applied the solutions to the corresponding dataset. To determine the absolute positions of the maser spots, we performed the phase-referencing calibration between the calibrator and the channel of the brightest maser spot for each dataset. The uncertainties of the absolute positions of the reference brightest maser spot were estimated following Kobak et al. (2025). Afterward, we imaged the four I, Q, U, and V Stokes cubes (the latter only for the CH_3OH masers) and the RR and LL cubes. The Q and U cubes were combined to produce cubes of linearly polarized intensity ($POLI = \sqrt{Q^2 + U^2}$) and polarization angle ($POLA = 0.5 \times \mathrm{atan}(U/Q)$). The root mean square (rms) noise and the beam size for each imaged cube is reported in Table 1.

The identification of CH_3OH and ex-OH maser features was done as described in Surcis et al. (2011a). In particular, the CH_3OH maser features were searched in the I Stokes cube and the ex-OH maser features in the I, RR, and LL cubes. A maser feature is identified when at least three maser spots in consecutive spectral channels are spatially coincident within the beam; therefore, the uncertainty in the identification process is equal to half of the beam. We measured the mean linear polarization percentage (P_l) and the mean linear polarization angle (χ) for each identified CH_3OH maser feature, considering only the consecutive channels (at least two) across the total intensity spectrum for which the polarized intensity is greater than or equal to $4\sigma_{POLI}$.

The linearly polarized CH_3OH maser features were then analyzed by using the full radiative transfer method (FRTM) code described in Surcis et al. (2019). With this code, we modeled the total intensity (I) and the $POLI$ spectra. The outputs of the FRTM code are the emerging brightness temperature ($T_b\Delta\Omega$, where Ω is the maser beaming solid angle), the intrinsic maser linewidth (ΔV_i), and the angle between the magnetic field and the maser propagation direction (θ). If θ is greater than the Van Vleck angle ($\theta_{crit} \approx 55°$), the magnetic field is perpendicular to the linear polarization angle; otherwise, it is parallel (Goldreich et al. 1973). We note that the FRTM code only works properly for unsaturated masers (e.g., Vlemmings et al. 2010; Surcis et al. 2011b). This implies that if the code is performed on a saturated maser, the ΔV_i and $T_b\Delta\Omega$ outputs are overestimated and underestimated, respectively (e.g., Surcis et al. 2011b). Furthermore, the saturation of the masers introduces a more complex dependence of the magnetic field with θ (Nedoluha & Watson 1992), and consequently the FRTM code provides an overestimate of θ for these masers, which could also reach values of 90°. A 6.7 GHz CH_3OH maser feature can be considered partially saturated if $T_b\Delta\Omega > 2.6 \times 10^9$ K sr. However, the orientation of the magnetic field with respect to the linear polarization vectors is not affected by the saturation of the masers (Surcis et al. 2011b). Finally, the best estimates of $T_b\Delta\Omega$ and ΔV_i were used to produce I and V models with the FRTM code that were used to fit the circularly polarized CH_3OH maser feature. A CH_3OH maser feature is considered circularly polarized if the measured V peak intensity is both $>3\sigma_V$ and $>3\sigma_{s.-n.}$, where $\sigma_{s.-n.}$ is the self-noise produced by the maser feature in its channels and becomes important when the power contributed by the astronomical maser is a significant portion of the total received power (Sault 2012). From the best I and V models, we were able to estimate the circular polarization percentage (P_V) and ΔV_Z of the CH_3OH maser features. We note that the FRTM code is able to estimate ΔV_Z even if these maser features are partially saturated. These estimates were also made by using the cross-correlation method between the RR and LL spectra.

For each ex-OH maser feature identified in I cubes, we determined its LL and RR counterparts ($>3\sigma_{LL}$ and $>3\sigma_{RR}$) based on their positions on the plane of the sky, to pair them in a so-called Zeeman pair (shifted σ components), similarly to what was done in Kobak et al. (2025). The LL and RR

features were fit with a Gaussian profile that provided the peak intensity and velocity of the maser features. From the velocity difference between the *LL* and *RR* peaks of a Zeeman pair, we measured ΔV_Z, and from their and corresponding *I* intensity peaks we measured P_V. Knowing that the Zeeman coefficient for the ex-OH at 6.035 GHz is $\alpha_Z^{ex-OH} = 0.056\,ms^{-1}G^{-1}$ (Davies 1974; Baudry et al. 1997), $B = \Delta V_Z/\alpha_Z^{ex-OH}$, which is equal to $B_\parallel$ if the unshifted π component due to the Zeeman effect is negligible. We measured P_l and χ for each identified ex-OH maser feature, similarly to what we did for the CH_3OH maser features, but in this case we considered the channels with polarized intensity greater than or equal to $3\sigma_{POLI}$. For OH masers, and consequently for ex-OH maser emission, the orientation of the magnetic field on the plane of the sky, Φ_B, is perpendicular to the linear polarization vector for σ components and parallel to it for the π component. As observations have shown in the past, the emission of σ components usually dominates over the π component, implying that the magnetic field is perpendicular to the linear polarization vector (e.g., Gray et al. 2003; Green et al. 2015). In particular, in about 16% of the observed cases the π component of ex-OH masers is detected, and only in ∼1% is no intrinsic π emission present, suggesting that in all the other cases some unidentified suppression mechanism of the linearly polarized emission (π component) must be at play (e.g., Green et al. 2015). Moreover, the magnetic field is only parallel to the linear polarization vector when $P_l \geq 71\%$. Indeed, only in this case does the unshifted π component contribute the most to P_l (Fish & Reid 2006). According to our findings (see Sect. 3), we can assume that the π component ($<3\sigma$) is negligible and, therefore, that the magnetic field is always perpendicular to the linear polarization vectors and we can assume $B \approx B_\parallel$ from our Zeeman splitting measurements.

3. Results

We detected the 6.7 GHz CH_3OH and 6.035 GHz ex-OH maser emissions toward both ON 1 and W75N. The distributions of the identified maser features are shown in Figure 1, and their parameters are reported in Tables A.1–A.4. Their total spectra are shown in Figures B.1 and B.2. Below, we briefly summarize our results.

3.1. G69.540−0.976 (ON 1)

We detected 11 CH_3OH (named G69.M01–G69.M11) and 24 ex-OH (named G69.E01–G69.E24) maser features toward ON 1. Both maser species are spatially distributed in two main groups: one blue-shifted and located in the north of the UCHII region and one red-shifted and located in the south (see Figure 1). Their distribution and V_{LSR} are very similar to those reported previously in Kobak et al. (2025).

Only the brightest CH_3OH maser feature (G69.M04, I=11 Jy beam^{-1} and V_{LSR}=14.68 km s^{-1}) shows polarized emission; in particular, we measured a linear polarization percentage of P_l=0.4% and a circular polarization percentage of P_V=0.6%, which is identical to what was measured in 2015 (Surcis et al. 2022). Although P_l is one third lower than previously measured, the linear polarization angle, χ=−58°±6°, is similar (χ^{2015}=−34°±9°; Surcis et al. 2022). We were able to properly fit G69.M04 with the FRTM code. The hyperfine transition F=3→4 was assumed as the preferred one, which provided a value of θ=+75°$^{+13}_{-37}$, indicating that the orientation of the magnetic field on the plane of the sky is more likely (with a probability of 66% that $\theta > 55°$) perpendicular to the linear polarization vector (see Sect. 2). We note that the FRTM code would provide similar output values, within the errors, for $T_b\Delta\Omega$, ΔV_i, and θ if we assume any other hyperfine transition, this is basically due to the size of our uncertainties. By modeling its *V* spectrum (see Figure 2) and by cross-correlating the *RR* and *LL* spectra, we estimated a Zeeman splitting of 3.2 m s^{-1}.

We measured linearly polarized emission toward five ex-OH maser features ($3.7\% \leq P_l \leq 16\%$), with a mean value equal to 7.8%±4.95% and a median value equal to 6.2%. The linear polarization vectors have position angles ranging from −93° to −42°, with mean and median values of −68°±24° and −75°, respectively. We measured circularly polarized emission toward all but one (G69.E13) of the ex-OH maser features, but only for 12 of them were we able to identify Zeeman pairs (for them $P_V \geq 77\%$). This implies that the shifted σ components dominate over the unshifted π component, and consequently the magnetic field is perpendicular to the linear polarization vectors (see Sect. 2). Therefore, Φ_B is oriented northeast-southwest (Φ_B^{ex-OH}=+22°±24°). Furthermore, we measured the magnetic field along the line of sight for four blue-shifted (−12.67 mG ≤ $B_\parallel$ ≤ −5.98 mG) and eight red-shifted (−6.37 mG ≤ $B_\parallel$ ≤ −1.35 mG) ex-OH maser features.

3.2. G81.871+0.781 (W75N)

We identified almost five times the number of 6.7 GHz CH_3OH maser features toward W75N than was previously done by Surcis et al. (2009); i.e., 47 (named here W75.M01-W75N.M47) versus 10. That is due to the high sensitivity of our EVN observations compared to those performed in 2008; indeed, Surcis et al. (2009) reported maser features with peak intensities of 2 Jy beam^{-1} ≤ I ≤ 95.4 Jy beam^{-1}, while we have maser features with 0.03 Jy beam^{-1} ≤ I ≤ 25.9 Jy beam^{-1} (see Table A.3). The maser distribution and the V_{LSR} range of the CH_3OH maser features are identical to those of 2008; i.e., +3.37 km s^{-1} ≤ V_{LSR} ≤ +9.51 km s^{-1} (see Fig. 1). We also identified five 6.035 GHz ex-OH maser features (named W75N.E01-W75N.E05) with +6.87 km s^{-1} ≤ V_{LSR} ≤ +8.13 km s^{-1} that spatially overlap on the plane of the sky with the CH_3OH maser features that have a similar velocity range (see Fig. 1 for a direct comparison). All maser features are associated with the radio continuum source VLA 1.

We detected linearly polarized emission from 16 CH_3OH maser features that show extremely high P_l, for all but one ($P_l^{W75N.M34}$=3.3%), ranging from 6.8 to 13.4%. For comparison, this was $0.9\% \leq P_l^{2008} \leq 4.5\%$ in 2008 (Surcis et al. 2009). The linear polarization vectors have position angles between −41° and +5°, with a mean value of −14°±7° (χ^{2008} = −17°±10°, Surcis et al. 2009). The high percentage of linear polarization suggests either that all the maser features might be saturated and/or that one hyperfine transition is preferred (Dall'Olio et al. 2020). However, we report the outputs (ΔV_i, $T_b\Delta\Omega$, and θ) of the FRTM code, where we assumed the hyperfine transition F=3→4 as the preferred one, in Table A.3. The estimated θ values are all greater than 55° (see Section 2); therefore, the magnetic field is perpendicular to the linear polarization vectors of the CH_3OH maser features. Actually, all the θ values are equal to 90°, suggesting that all the maser features might be partially saturated, and therefore the θ values might be overestimated but still greater than $\theta_{crit} \approx 55°$ (see Sect. 2). We detected circular polarization toward three CH_3OH maser features ($P_V^{W75N.M21}$ = 0.9%, $P_V^{W75N.M29}$ = 1.4%,

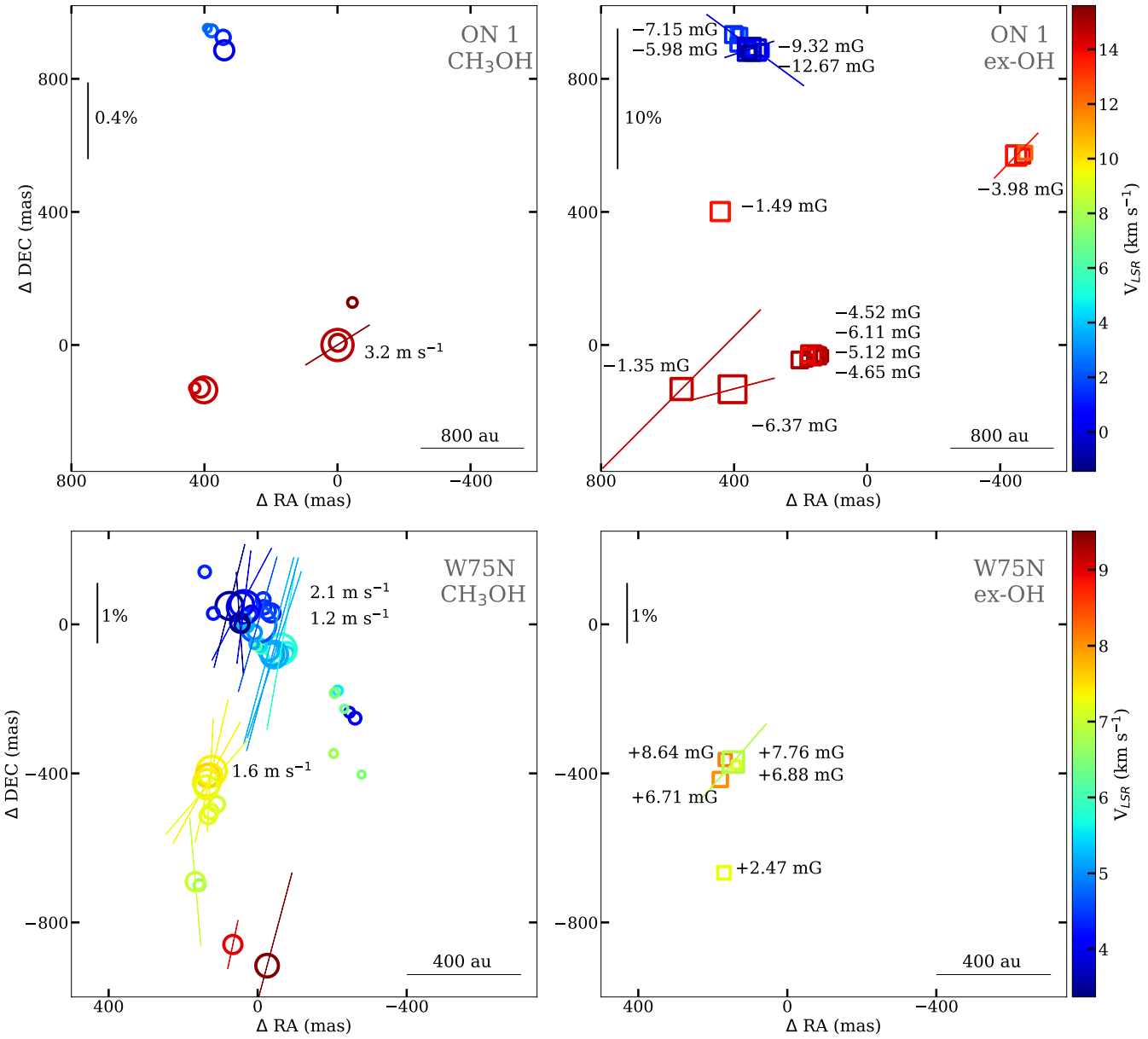

Fig. 1. Distribution of 6.7 GHz CH_3OH (left panels, circle symbols) and 6.035 GHz ex-OH (right panel, square symbols) maser features detected around ON 1 (top panels; $V^{\rm ON\,1}_{\rm LSR,sys}$ = +11.6 kms^{-1}; Bronfman et al. 1996) and W75N (bottom panels; $V^{\rm W75N}_{\rm LSR,sys}$ = +10.0 kms^{-1}; Shepherd et al. 2003). The size of the symbols is scaled logarithmically according to their peak intensity (see Tables A.1–A.4), while their colors indicate the $V_{\rm LSR}$ (see Tables A.1–A.4). The reference positions are RA(J2000)=20$^{\rm h}$10$^{\rm m}$09$^{\rm s}$.04272±0$^{\rm s}$.00007 and Dec(J2000)=+31°31′34″.9736±0″.0009 for ON 1; and RA(J2000)=20$^{\rm h}$38$^{\rm m}$36$^{\rm s}$.41744±0$^{\rm s}$.00008 and Dec(J2000)=+42°37′35″.1153±0″.0011 for W75N. The measured linear polarization vectors with their scales, the estimated $\Delta V_{\rm Z}^{CH_3OH}$, and the measured $B_{\parallel}^{ex-OH}$ are also reported.

and $P_{\rm V}^{\rm W75N.M43}$ 1.0%=). Actually, the detection of $P_{\rm V}^{\rm W75N.M43}$ must be considered as tentative since the V Stokes emission is about $2\sigma_{s.-n.}$ (see Fig. 2). From these features, we were able to estimate Zeeman splitting of $\Delta V_{\rm Z}^{\rm W75N.M21}$ = +1.2 m s^{-1}, $\Delta V_{\rm Z}^{\rm W75N.M29}$ = +2.1 m s^{-1}, and $\Delta V_{\rm Z}^{\rm W75N.M43}$ = +1.6 m s^{-1} by modeling the V spectra. The cross-correlation method provided consistent values for W75N.M21 and W75N.M29, but no value was determined for W75N.M43. In 2008, three CH_3OH maser features showed $P_{\rm V} \approx$ 0.5% and +0.5 m s^{-1} $\leq \Delta V_{\rm Z} \leq$ +0.8 m s^{-1}(Surcis et al. 2009).

We only measured linearly polarized emission toward the ex-OH maser feature W75N.E02, for which $P_{\rm l}$ = 1.7% ± 0.6% and χ = −36° ±11°, and circularly polarized emission for all the features ($P_{\rm V} \geq$ 82%). The sky component of the magnetic field is then oriented on the plane of the sky with an angle of $\Phi_{\rm B}^{ex-OH}$ = +54° ±11°. Furthermore, we identified five Zeeman pairs from which we measured magnetic field strength along the line of sight between +2.47 mG and +8.64 mG. These values are consistent with those obtained with the e-MERLIN observations –i.e., +2.3 mG $\leq B_{\parallel}^{\rm ex-OH,2025} \leq$ +8.5 mG– and reported in Kobak et al. (2025).

4. Discussion

The strategy to identify the most favored hyperfine transition of the 6.7 GHz CH_3OH maser emission is based on the successful calculations of the Zeeman splitting of CH_3OH and ex-OH

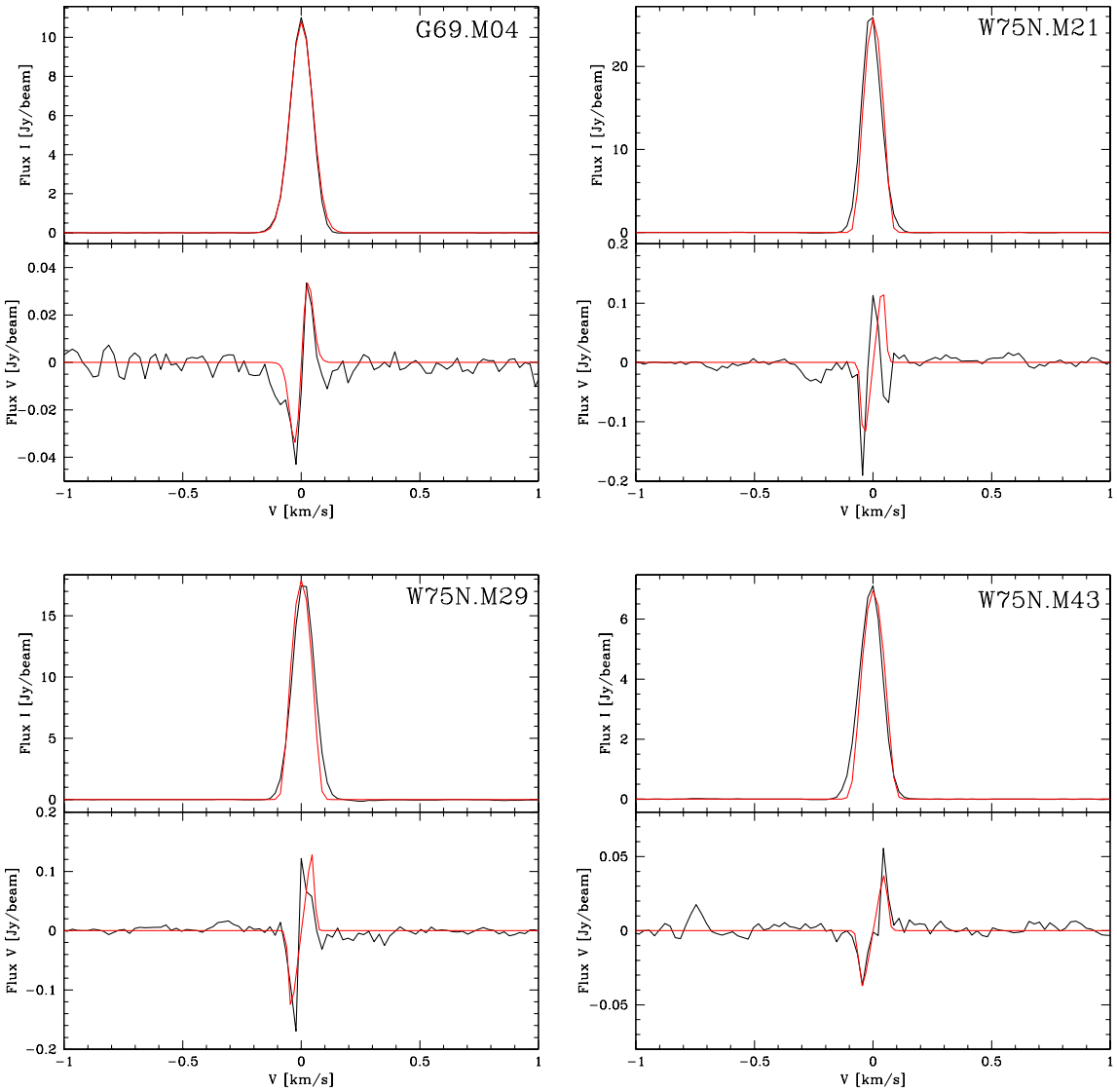

Fig. 2. Total intensity (I, upper panel) and circularly polarized intensity (V, lower panel) spectra for the 6.7 GHz CH_3OH maser features named G69.M04, W75N.M21, W75N.M29, and W75N.M43 (see Tables A.1, and A.3). The thick red lines are the best-fit models of I and V emissions obtained using the adapted FRTM code (see Sect. 2). The maser features were centered on zero velocity.

maser lines toward the same volume of gas. This can be done if we assume that the magnetic field probed by the two maser species is exactly the same and that its strength is constant within the volume of gas where the masers arise. Therefore, the first step is to determine if the two maser species are probing the same magnetic field (see Sect. 4.1) and then comparing the Zeeman splitting estimates (see Sect. 4.2). In Sect. 4.3, we compare the magnetic fields we measured with those obtained in the past.

4.1. Magnetic field orientation in ON 1 and W75N

If the CH_3OH and ex-OH masers are probing the same magnetic field, we expect that the orientation on the plane of the sky of the magnetic field, as estimated from the linearly polarized emission of the two maser species, is consistent within the same source. We note that, although we assumed the unshifted π component of the polarized ex-OH maser features negligible according to our measurements (see Tables A.2 and A.4), the magnetic field must not be considered purely parallel to the line of sight. However, only the π component can be suppressed by some still-unknown mechanism (e.g., Green et al. 2015). Indeed, from the linear polarization of the σ components, we were able to estimate the orientation of the magnetic field on the plane of the sky, which would have been impossible in the case of a magnetic field purely oriented along the line of sight. Therefore, comparing the projected orientation of the magnetic field as estimated from the two maser emissions is still a good approximation.

We measured the magnetic field orientations of $\Phi_B^{CH_3OH} = +32^\circ \pm 6^\circ$ and $\langle \Phi_B^{ex-OH} \rangle = +22^\circ \pm 24^\circ$ in ON 1. These measurements agree within the uncertainties (see Fig. 1). The magnetic field in ON 1 is almost oriented along one of the outflows observed toward the region, particularly the one traced by $H^{13}CO^+$ and SiO (PA=+44°). Also in the case of W75N the orientation of the magnetic field on the plane of the sky is consistent (see Fig. 1) between the one estimated from the polarized CH_3OH maser emission ($\langle \Phi_B^{CH_3OH} \rangle = +76^\circ \pm 7^\circ$) and that from the ex-OH maser-polarized emission ($\Phi_B^{ex-OH} = +54^\circ \pm 11^\circ$). According to our findings, we can assume that the two maser species are likely probing the same magnetic field in each source.

4.2. Attempts to identify the favored hyperfine transition for the 6.7 GHz CH_3OH maser emission

Because the 6.7 GHz CH_3OH and 6.035 GHz ex-OH masers trace a very similar orientation of the magnetic field on the plane of the sky in both sources, we can measure the Zeeman splitting coefficient of the CH_3OH maser ($\alpha_Z^{CH_3OH}$) using the following relation:

$$\alpha_Z^{CH_3OH} = \frac{\Delta V_Z^{CH_3OH}}{B_\parallel^{ex-OH}}, \quad (1)$$

where $\Delta V_Z^{CH_3OH}$ is the estimated Zeeman splitting of the CH_3OH maser and $B_\parallel^{ex-OH}$ is the magnetic field strength along the line of sight as measured from the ex-OH maser emission. We note that being able to use $B_\parallel^{ex-OH}$ rather than B^{ex-OH} reduces the sources of uncertainty. Indeed, from the estimation of $\Delta V_Z^{CH_3OH}$ it is only possible to measure $B_\parallel^{CH_3OH}$ (e.g., Vlemmings 2008) and not $B^{CH_3OH} = B_\parallel^{CH_3OH}/\cos\theta$, for which we would have introduced the large uncertainties in the estimation of θ. Our criteria to couple the ex-OH maser features with the CH_3OH maser features are, in order of importance, (1) the measurement of $B_\parallel^{ex-OH}$ and estimate of $\Delta V_Z^{CH_3OH}$; (2) the separation on the plane of the sky, the smaller the better; and (3) a similar V_{LSR}, the closer the better.

We estimated only one Zeeman splitting toward the 6.7 GHz CH_3OH maser features in ON 1, i.e., G69.M04 ($V_{LSR}^{G69.M04}$=+14.68 km s^{-1}). We can couple it with G69.E06, which is the closest ex-OH maser feature (with a separation of d=184 mas, i.e. 470 au) with similar velocity ($V_{LSR}^{G69.E06}$=+15.19 km s^{-1}), from which we measured magnetic field strength along the line of sight; i.e., $B_\parallel^{G69.E06}$=−4.52 mG.

In the case of W75N, we estimated the Zeeman splitting toward three CH_3OH maser features: W75N.M21, W75N.M29, and W75N.M43 (tentative, see Sect. 3.2). Unfortunately, only W75N.M43 ($V_{LSR}^{W75N.M43}$=+7.40 km s^{-1}) is almost coincident with ex-OH maser features (W75N.E01 at d=48 mas and W75N.E02 at d=182 mas, i.e., 63 au and 240 au, respectively) with similar velocities ($V_{LSR}^{W75N.E01}$=+7.20 km s^{-1} and $V_{LSR}^{W75N.E02}$=+6.87 km s^{-1}), for which we measured $B_\parallel^{ex-OH}$. The other two –i.e., W75N.M21 ($V_{LSR}^{W75N.M21}$=+4.64 km s^{-1}) and W75N.M29 ($V_{LSR}^{W75N.M29}$=+4.11 km s^{-1})– are much further from the closest ex-OH maser feature W75N.E02: 367 mas (480 au) and 417 mas (540 au), respectively.

We list the calculated $\alpha_Z^{CH_3OH}$ values (see Eq. (1)) in Table 2 (Col. 5) for all the pairs of maser features (Col. 1) mentioned above. The other parameters reported in Table 2 are the maser features' separation (Col. 2); the estimated Zeeman splitting of CH_3OH's maser emission (Col. 3); the magnetic field along the line of sight measured from the ex-OH maser features (Col. 4). The $\alpha_Z^{CH_3OH}$ obtained from Eq. (1) do not coincide with any of the Zeeman coefficients of the eight hyperfine transitions of the 6.7 GHz CH_3OH maser emission reported in the supplementary Table 3 of Lankhaar et al. (2018). This implies that the two maser emissions might not arise in the same volume of gas, or, in other words, that the gas density where they arise is slightly different. Indeed, this condition can still provide the same morphology of the magnetic field, but with a different strength.

To compare the number densities of the gas where the CH_3OH ($n_{H_2}^{CH_3OH}$) and ex-OH ($n_{H_2}^{ex-OH}$) maser emissions arise, we needed to determine the magnetic field strength ($B_\parallel^{CH_3OH}$) from the Zeeman splitting estimates of the 6.7 GHz CH_3OH maser emission. Indeed, following Crutcher & Kemball (2019) we know that

$$\eta \equiv \frac{n_{H_2}^{ex-OH}}{n_{H_2}^{CH_3OH}} = \left(\frac{|B_\parallel^{ex-OH}|}{|B_\parallel^{CH_3OH}|}\right)^2. \quad (2)$$

To estimate $B_\parallel^{CH_3OH}$, we can assume that one of the eight hyperfine transitions is more favored than the others. As suggested by Lankhaar et al. (2018), this might be F=3→4 ($\alpha_{Z,3\to4}^{CH_3OH}$=−50.955 m s^{-1} G^{-1}), because it shows the largest Einstein coefficient. Furthermore, it provides the lowest value of $B_\parallel^{CH_3OH}$ (Lankhaar et al. 2018). As expected (see Table 3), the $B_\parallel^{CH_3OH}$ values obtained assuming F=3→4 are larger than those obtained from the associated ex-OH maser features both in ON 1 and W75N. However, ON 1 $B_\parallel^{CH_3OH}$ and $B_\parallel^{ex-OH}$ have the same sign, while they are opposite in W75N for all the maser features. Moreover, while in ON 1 η is about 0.005, in W75N it is at least one order of magnitude larger. Therefore, we can suppose that F=3→4 might be the favored hyperfine transition in ON 1, but this is not the case in W75N. For W75N, we can thus assume that either F=6→7A ($\alpha_{Z,6\to7A}^{CH_3OH}$=+10.067 m s^{-1} G^{-1}) or F=7→8 ($\alpha_{Z,7\to8}^{CH_3OH}$=+21.176 m s^{-1} G^{-1}) is the favored one. Indeed, Dall'Olio et al. (2020) suggested these as alternative dominant hyperfine transitions. The results are listed in Table 3. The sign of $B_\parallel^{CH_3OH}$ matches that of $B_\parallel^{ex-OH}$ for both hyperfine transitions, and also the η values are comparable to what we measure in ON 1. Nevertheless, it is not possible to identify which of them is the most favorable. Speculatively, we can state that the two maser emissions arise close to each other, with the 6.7 GHz CH_3OH maser features being closer to the HMYSO, where the gas density is about two orders of magnitude larger than that where the ex-OH maser features arise. This statement can be considered in agreement with the theoretical number-density ranges for the two maser emissions: 10^5 cm^{-3} < $n_{H_2}^{CH_3OH}$ < 10^9 cm^{-3} and 3×10^6 cm^{-3} < $n_{H_2}^{ex-OH}$ < 3×10^8 cm^{-3} (Cragg et al. 2002, 2005).

Table 2. Estimated values of the Zeeman splitting coefficient for the 6.7 GHz CH_3OH maser emission as calculated from Eq. (1).

Maser features	d (mas)	$\Delta V_Z^{CH_3OH}$ (m s^{-1})	$B_\parallel^{ex-OH}$ (mG)	$\alpha_Z^{CH_3OH}$ (m s^{-1} G^{-1})
G69 (M04, E06)	184	3.2	−4.52	−707.96
W75N (M21, E02)	367	2.1	+7.76	+270.62
W75N (M29, E02)	417	1.2	+7.76	+154.64
W75N (M43, E02)	182	1.6	+7.76	+206.19
W75N (M43, E01)	48	1.6	+6.88	+232.56

4.3. Comparison of magnetic fields over a long period of time

Both ON 1 and W75N were previously searched for polarized maser emissions at 6.035 GHz (ex-OH) and 6.7 GHz (CH_3OH) to probe their magnetic field morphology and strength. Below, we describe their changes over the years.

4.3.1. G69.540-0.976 (ON 1)

ON 1 shows very stable magnetic field morphology over about 20 years. Indeed, Green et al. (2007) measured linear

Table 3. Comparison of the magnetic field along the line of sight as measured from the Zeeman splitting of the 6.7 GHz CH_3OH, considering three different hyperfine transitions, and 6.035 GHz ex-OH maser features in ON 1 and W75N.

(1) Maser features	(2) $\Delta V_Z^{CH_3OH}$ ($m\,s^{-1}$)	(3) $F_{up} \rightarrow F_{down}$	(4) $\alpha_Z^{CH_3OH}$ ($m\,s^{-1}\,G^{-1}$)	(5) $B_\parallel^{CH_3OH}$ (mG)	(6) $B_\parallel^{ex-OH}$ (mG)	(7) η (10^{-3})
G69 (M04, E06)	3.2	$3 \rightarrow 4$	−50.955	−62.8	−4.52	5.18
W75N (M21, E02)	2.1	$3 \rightarrow 4$	−50.955	−41.2	+7.76	35.48
		$6 \rightarrow 7A$	+10.067	+208.6		1.38
		$7 \rightarrow 8$	+21.176	+99.2		6.12
W75N (M29, E02)	1.2	$3 \rightarrow 4$	−50.955	−23.6	+7.76	108.12
		$6 \rightarrow 7A$	+10.067	+119.2		4.24
		$7 \rightarrow 8$	+21.176	+56.7		18.73
W75N (M43, E02)	1.6	$3 \rightarrow 4$	−50.955	−31.4	+7.76	61.08
		$6 \rightarrow 7A$	+10.067	+158.9		2.38
		$7 \rightarrow 8$	+21.176	+75.6		10.54
W75N (M43, E01)	1.6	$3 \rightarrow 4$	−50.955	−31.4	+6.88	48.01
		$6 \rightarrow 7A$	+10.067	+158.9		1.87
		$7 \rightarrow 8$	+21.176	+75.6		8.29

polarization vectors for two red-shifted 6.035 GHz ex-OH maser features ($\chi^{2007} = -87.7° \pm 2.0°$ and $-42.5° \pm 0.7°$), corresponding to our features G69.E22 and G69.E24, and for one red-shifted 6.031 GHz ex-OH maser feature ($\chi^{2007} = -43.1° \pm 1.9°$), corresponding to our G69.E03, which show the orientation on the plane of the sky to be identical, within the errors, to our measurements. However, we must note that Fish & Sjouwerman (2010) also reported three measurements of linear polarization vectors toward the 6.035 GHz ex-OH maser features. Two of them –their features K and Z ($\chi^{K,2010} = +52°$ and $\chi^{Z,2010} = -32°$)– can be associated with our features G69.E22 and G69.E03, respectively. Although a direct comparison is difficult because no errors are reported by Fish & Sjouwerman (2010), taking into account our uncertainties, we have differences of $-25°$ and $-11°$, respectively. It is important to emphasize that the linear polarization vectors measured by us toward the ex-OH maser features are all but one (G69.E03, with a difference of $-12°$) in perfect agreement with those measured with the e-MERLIN by Kobak et al. (2025). Therefore, for about 20 years the magnetic field, which is always perpendicular to the linear polarization vectors, has been constantly oriented southwest-northeast in the region where the red-shifted maser features arise. Besides the morphology of the magnetic field, we also find that $B_\parallel$ did not substantially vary over the same period of time. Green et al. (2007), Fish & Sjouwerman (2010), and Kobak et al. (2025) measured $B_\parallel$ toward five, eleven, and five maser features, respectively, with values in the ranges of $-5.8\,mG \leq B_\parallel^{2007} \leq -1.1\,mG$, $-12.1\,mG \leq B_\parallel^{2010} \leq -1.3\,mG$, and $-6.2\,mG \leq B_\parallel^{2025} \leq -1.2\,mG$. By comparing these values with our measurements, we note differences of less than 25%, which might be due to a high-performance modern instrument, a real magnetic field variation, or both. It is interesting to note that the magnetic field strength measured from the Zeeman effect of ground-state OH maser emissions (1.665 and 1.667 GHz) covers a similar range of values: $-3.6\,mG \leq B_\parallel^{OH} \leq -0.8\,mG$ (Fish et al. 2005; Nammahachak et al. 2006).

We can compare the magnetic field morphology as probed by the 6.7 GHz CH_3OH masers over eight years. In 2015, Surcis et al. (2022) measured linear polarization vectors for two maser features: one blue-shifted located in the north and one red-shifted in the south. The red-shifted one can be associated with our only maser feature that shows linearly polarized emission, i.e., G69.M04. For both maser features the magnetic field is perpendicular to the linear polarization vectors, indicating that the magnetic field is oriented southwest-northeast ($\Phi_B^{2022} = +56° \pm 9°$ and $\Phi_B^{G69.M04} = +32° \pm 6°$), which also agrees with the magnetic field orientation probed by the ex-OH maser features in the same red-shifted region. Also, Green et al. (2007) estimated linear polarization vectors toward two 6.7 GHz CH_3OH maser features ($\chi^{C,2007} = +20.6° \pm 2.0°$ and $\chi^{D,2007} = -76.7° \pm 2.0°$), but we cannot perform a direct comparison of the magnetic field morphology because no values of the θ angles were provided by them. Regardless of the favored hyperfine transition, we can compare our Zeeman splitting estimates with those made in the past. In 2005, Green et al. (2007) made one of the first attempts to recover the Zeeman splitting of a 6.7 GHz CH_3OH maser right next to ON 1. Using the cross-correlation method, they reported a value of $\Delta V_Z^{2007} = (+0.9 \pm 0.3)\ ms^{-1}$. Ten years later, Surcis et al. (2022) reported, for a feature about 400 mas westward, a value of $\Delta V_Z^{2022} = (+1.2 \pm 0.2)\ ms^{-1}$, which was estimated through the FRTM code. This last maser feature can be associated with our maser feature G69.M04, which shows $\Delta V_Z^{G69.M04} = (+3.2 \pm 0.6)\ ms^{-1}$. From these three estimates made over 18 years and assuming that the hyperfine transition responsible of the observed maser emission was always the same, we can conclude that the magnetic field where the CH_3OH maser emission arises might have increased over time. In particular, it might have increased by about 30% between 2005 and 2015 – if we assume that the magnetic field is uniform in the region– and 2.6 times between 2015 and 2023, in this case at the exact same location. This behavior is not observed in the magnetic field strength measured from the ex-OH maser emission.

4.3.2. G81.871+0.781 (W75N)

Differently from ON 1, in the case of W75N only the polarized emission of a 6.7 GHz CH_3OH maser was observed in the distant past. Indeed, the previous full polarimetric VLBI observations of the 6.7 GHz CH_3OH and 6.035 GHz ex-OH maser emissions

were performed in 2008 (Surcis et al. 2009) and 2020 (Kobak et al. 2025), respectively. As reported in Sect. 3.2, the magnetic field morphology and strength as measured from the ex-OH maser features can be considered consistent with what was measured by Kobak et al. (2025), with only a small difference of +6° for Φ_B^{ex-OH}.

The magnetic field, as measured from the linearly polarized CH_3OH maser emission, is constantly oriented northeast-southwest. Indeed, Surcis et al. (2009) estimated an average magnetic field angle of $\langle\Phi_B^{CH_3OH,2008}\rangle = +73°\pm10°$, and we estimated $\langle\Phi_B^{CH_3OH}\rangle = +76°\pm7°$. We can even associate each of the eight linearly polarized CH_3OH maser features detected by Surcis et al. (2009) (A1, A2, A3, A4, A5, B1, C3, and C4) with a maser feature detected by us (W75N.M35, .M29, .M21, .M10, .M12, .M43, .M34, and .M16). Although their peak intensity and P_l enormously decreased and increased, respectively, in the last 15 years, the local orientation of the magnetic field did not vary. We only notice a negligible difference <5° in three cases: A2, A3, and C3 (Surcis et al. 2009). We can only compare the estimated Zeeman splitting for the brightest maser feature detected by Surcis et al. (2009), for which $\Delta V_Z^{B1,2009} = (+0.53 \pm 0.04)\,m\,s^{-1}$. Our associated feature –i.e., W75N.M43– has a value of $\Delta V_Z^{W75N.M43} = (+1.6 \pm 0.3)\,m\,s^{-1}$, which is three times larger. This suggests an increment of the magnetic field strength in 15 years.

5. Conclusions

We observed the polarized emission of 6.7 GHz CH_3OH and 6.035 GHz ex-OH maser emissions with the EVN toward two HMYSOs: ON 1 and W75N. The observations at the two frequencies near the same source were performed quasi-simultaneously (only one day apart) to allow the comparison of the magnetic field measured from the ex-OH maser features with the estimated Zeeman splitting of CH_3OH maser features; we also attempted to determine a Zeeman splitting coefficient ($\alpha_Z^{CH_3OH}$) for the CH_3OH maser emission to identify the favored hyperfine transition responsible for the 6.7 GHz CH_3OH maser emission. We determined that the two maser emissions likely probe the same magnetic field, as we would expect, but at slightly different densities. Indeed, the measured values of $\alpha_Z^{CH_3OH}$ do not match with any of the table values in Lankhaar et al. (2018), implying that we are not able to uniquely identify the dominating hyperfine transition. However, through density considerations, we find that three hyperfine transitions might be responsible for the CH_3OH maser emission that we observed toward ON 1 and W75N. These are 3→4, 6→7A, and 7→8. This might also indicate, as previously suggested (e.g., Dall'Olio et al. 2020), that the preferred hyperfine transition is not always the same, but that in different HMYSOs this can be any of the three hyperfine transitions we report above.

Moreover, comparing our magnetic field measurements with those taken decades ago, we found that the magnetic fields toward ON 1 and W75N did not change their morphology over time. The magnetic field strengths in both sources as probed by the ex-OH maser emission, did not vary over time either. However, we observed a possible increment of the strengths as probed by the CH_3OH maser emission, if we assume that the dominating hyperfine transition did not change over time. These differences may be explained by a real variation of the magnetic field closer to the protostar, where the CH_3OH masers arise, or by a possible change of the dominating hyperfine transition over time.

In conclusion, we show that the quasi-simultaneous observations of maser emissions from different molecules can be very useful for understanding the physics of the emitting-maser process and of the environment where the masers arise. In our particular case, performing this kind of observation near a large sample of sources might help to statistically identify the most likely hyperfine transition responsible for the 6.7 GHz CH_3OH maser emission. This kind of study will benefit from the future upgrade of existing interferometric networks, such as the ngVLA. In particular, similar studies at higher frequencies could be performed with the EVN thanks to the planned installation of multi-frequency receivers at several stations.

Acknowledgements. We wish to thank an anonymous referee for making useful suggestions that have improved the paper. The European VLBI Network (www.evlbi.org) is a joint facility of independent European, African, Asian, and North American radio astronomy institutes. Scientific results from data presented in this publication are derived from the following EVN project code EK052. We acknowledge support from the National Science Centre, Poland, through grant 2021/43/B/ST9/02008.

References

Argon, A. L., Reid, M. J., & Menten, K. M. 2000, ApJS, 129, 159
Bartkiewicz, A., Szymczak, M., Cohen, R. J., & Richards, A. M. S. 2005, MNRAS, 361, 623
Bartkiewicz, A., Szymczak, M., & van Langevelde, H. J. 2016, A&A, 587, A104
Baudry, A., Desmurs, J. F., Wilson, T. L., & Cohen, R. J. 1997, A&A, 325, 255
Beuther, H., Soler, J. D., Vlemmings, W., et al. 2018, A&A, 614, A64
Bronfman, L., Nyman, L. A., & May, J. 1996, A&AS, 115, 81
Carrasco-González, C., Rodríguez, L. F., Torrelles, J. M., Anglada, G., & González-Martín, O. 2010, AJ, 139, 2433
Carrasco-González, C., Torrelles, J. M., Cantó, J., et al. 2015, Science, 348, 114
Cragg, D. M., Sobolev, A. M., & Godfrey, P. D. 2002, MNRAS, 331, 521
Cragg, D. M., Sobolev, A. M., & Godfrey, P. D. 2005, MNRAS, 360, 533
Crutcher, R. M., & Kemball, A. J. 2019, Front. Astron. Space Sci., 6, 66
Dall'Olio, D., Vlemmings, W. H. T., Lankhaar, B., & Surcis, G. 2020, A&A, 644, A122
Davies, R. D. 1974, IAU Symp., 60, 275
Etoka, S., Gray, M. D., & Fuller, G. A. 2012, MNRAS, 423, 647
Fish, V. L., & Reid, M. J. 2006, ApJS, 164, 99
Fish, V. L., & Reid, M. J. 2007, ApJ, 670, 1159
Fish, V. L., Reid, M. J., Argon, A. L., & Zheng, X.-W. 2005, ApJS, 160, 220
Fish, V. L., & Sjouwerman, L. O. 2010, ApJ, 716, 106
Fish, V. L., Gray, M., Goss, W. M., & Richards, A. M. S. 2011, MNRAS, 417, 555
Goldreich, P., Keeley, D. A., & Kwan, J. Y. 1973, ApJ, 179, 111
Gray, M. D., Hutawarakorn, B., & Cohen, R. J. 2003, MNRAS, 343, 1067
Green, J. A., Richards, A. M. S., Vlemmings, W. H. T., Diamond, P., & Cohen, R. J. 2007, MNRAS, 382, 770
Green, J. A., Caswell, J. L., & McClure-Griffiths, N. M. 2015, MNRAS, 451, 74
Hu, B., Menten, K. M., Wu, Y., et al. 2016, ApJ, 833, 18
Hunter, T. R., Taylor, G. B., Felli, M., & Tofani, G. 1994, A&A, 284, 215
Hutawarakorn, B., Cohen, R. J., & Brebner, G. C. 2002, MNRAS, 330, 349
Keimpema, A., Kettenis, M. M., Pogrebenko, S. V., et al. 2015, Exp. Astron., 39, 259
Kobak, A., Bartkiewicz, A., Rygl, K. L. J., et al. 2025, A&A, 695, A149
Krumholz, M. R., & Federrath, C. 2019, Front. Astron. Space Sci., 6, 7
Kumar, M. S. N., Tafalla, M., & Bachiller, R. 2004, A&A, 426, 195
Lankhaar, B., Groenenboom, G. C., & van der Avoird, A. 2016, J. Chem. Phys., 145, 244301
Lankhaar, B., Vlemmings, W., Surcis, G., et al. 2018, Nat. Astron., 2, 145
MacLeod, G. C., Scalise, Jr., E., Saedt, S., Galt, J. A., & Gaylard, M. J. 1998, AJ, 116, 1897
Minier, V., Conway, J. E., & Booth, R. S. 2001, A&A, 369, 278
Modjaz, M., Moran, J. M., Kondratko, P. T., & Greenhill, L. J. 2005, ApJ, 626, 104
Moscadelli, L., Sanna, A., & Goddi, C. 2011, A&A, 536, A38
Nagayama, T., Nakagawa, A., Imai, H., Omodaka, T., & Sofue, Y. 2008, PASJ, 60, 183
Nammahachak, S., Asanok, K., Hutawarakorn Kramer, B., et al. 2006, MNRAS, 371, 619
Nedoluha, G. E., & Watson, W. D. 1992, ApJ, 384, 185

Price, D. J., & Bate, M. R. 2007, MNRAS, 377, 77
Rodríguez-Kamenetzky, A., Carrasco-González, C., Torrelles, J. M., et al. 2020, MNRAS, 496, 3128
Rygl, K. L. J., Brunthaler, A., Reid, M. J., et al. 2010, A&A, 511, A2
Rygl, K. L. J., Brunthaler, A., Sanna, A., et al. 2012, A&A, 539, A79
Sault, R. 2012, EVLA Memo, 159
Shepherd, D. S., Testi, L., & Stark, D. P. 2003, ApJ, 584, 882
Sugiyama, K., Fujisawa, K., Doi, A., et al. 2011, PASJ, 63, 53
Surcis, G., Vlemmings, W. H. T., Dodson, R., & van Langevelde, H. J. 2009, A&A, 506, 757
Surcis, G., Vlemmings, W. H. T., Curiel, S., et al. 2011a, A&A, 527, A48
Surcis, G., Vlemmings, W. H. T., Torres, R. M., van Langevelde, H. J., & Hutawarakorn Kramer, B. 2011b, A&A, 533, A47
Surcis, G., Vlemmings, W. H. T., van Langevelde, H. J., & Hutawarakorn Kramer, B. 2012, A&A, 541, A47
Surcis, G., Vlemmings, W. H. T., van Langevelde, H. J., Hutawarakorn Kramer, B., & Bartkiewicz, A. 2019, A&A, 623, A130
Surcis, G., Vlemmings, W. H. T., van Langevelde, H. J., Hutawarakorn Kramer, B., & Bartkiewicz, A. 2022, A&A, 658, A78
Surcis, G., Vlemmings, W. H. T., Goddi, C., et al. 2023, A&A, 673, A10
Szymczak, M., Olech, M., Sarniak, R., Wolak, P., & Bartkiewicz, A. 2018, MNRAS, 474, 219
Szymczak, M., Wolak, P., Bartkiewicz, A., Aramowicz, M., & Durjasz, M. 2020, A&A, 642, A145
Torrelles, J. M., Gómez, J. F., Rodríguez, L. F., et al. 1997, ApJ, 489, 744
Vlemmings, W. H. T. 2008, A&A, 484, 773
Vlemmings, W. H. T., Surcis, G., Torstensson, K. J. E., & van Langevelde, H. J. 2010, MNRAS, 404, 134
Vlemmings, W. H. T., Torres, R. M., & Dodson, R. 2011, A&A, 529, A95
Zheng, X. W., Ho, P. T. P., Reid, M. J., & Schneps, M. H. 1985, ApJ, 293, 522

Appendix A: Tables

Table A.1. Parameters of the 6.7 GHz CH_3OH maser features detected in G69.540−0.976 (ON 1).

(1) Maser	(2) RA[a] offset (mas)	(3) Dec[a] offset (mas)	(4) Peak Intensity (I) (Jy beam^{-1})	(5) V_{LSR} (km s^{-1})	(6) Δv_L (km s^{-1})	(7) P_l^b (%)	(8) χ^b (°)	(9) ΔV_i^c (km s^{-1})	(10) $T_b\Delta\Omega^c$ (log K sr)	(11) P_V (%)	(12) ΔV_Z (m s^{-1})	(13) θ^d (°)
G69.M01	-44.763	127.548	0.100 ± 0.005	15.65	0.19	–	–	–	–	–	–	–
G69.M02	-9.487	-4.536	0.355 ± 0.047	14.51	0.19	–	–	–	–	–	–	–
G69.M03	-1.024	6.649	1.746 ± 0.008	14.81	0.19	–	–	–	–	–	–	–
G69.M04	0.000	0.000	11.022 ± 0.049	14.68	0.21	0.4 ± 0.1	−58 ± 6	$0.85^{+0.2}_{-0.3}$	$8.4^{+1.0}_{-0.5}$	0.6	3.2 ± 0.6	75^{+13}_{-37}
G69.M05	340.544	885.803	1.361 ± 0.010	0.06	0.54	–	–	–	–	–	–	–
G69.M06	343.715	924.751	0.438 ± 0.006	1.25	0.26	–	–	–	–	–	–	–
G69.M07	378.442	944.389	0.218 ± 0.005	2.30	0.25	–	–	–	–	–	–	–
G69.M08	390.989	952.068	0.049 ± 0.004	2.61	0.16	–	–	–	–	–	–	–
G69.M09	401.805	-135.044	4.730 ± 0.047	14.51	0.18	–	–	–	–	–	–	–
G69.M10	411.694	-129.734	0.943 ± 0.053	14.60	0.20	–	–	–	–	–	–	–
G69.M11	428.595	-129.059	0.133 ± 0.013	14.38	0.16	–	–	–	–	–	–	–

Notes. [a] The reference position is RA(J2000)=$20^h10^m09\overset{s}{.}04272\pm0\overset{s}{.}00007$ and Dec(J2000)=$+31°31'34\overset{''}{.}9736\pm0\overset{''}{.}0009$. [b] P_l and χ are the mean values of the linear polarization percentage and the linear polarization angle measured across the spectrum, respectively. [c] The best-fitting results obtained by using a model based on the radiative transfer theory of CH_3OH masers for $\Gamma + \Gamma_\nu = 1$ s^{-1} (Vlemmings et al. 2010; Surcis et al. 2011a). The errors were determined by analyzing the full probability distribution function. [d] The angle between the magnetic field and the maser propagation direction is determined by using the observed P_l and the fitted emerging brightness temperature. The errors were determined by analyzing the full probability distribution function.

Table A.2. Parameters of the 6.035 GHz ex-OH maser features detected in G69.540−0.976 (ON 1).

(1) Maser	(2) RA[a] offset (mas)	(3) Dec[a] offset (mas)	(4) Peak Intensity (I) (Jy beam^{-1})	(5) V_{LSR} (km s^{-1})	(6) P_V^b (%)	(7) ΔV_Z (km s^{-1})	(8) $B_\parallel$ (mG)	(9) P_l (%)	(10) χ (°)
G69.E01	−475.283	577.944	0.410 ± 0.0158	12.43	97	−0.22	−3.98	–	–
G69.E02	−467.692	568.098	0.587 ± 0.0221	13.98	*23*	–	–	–	–
G69.E03	−448.081	569.435	2.040 ± 0.0299	13.78	*100*	–	–	4.5 ± 0.8	−45 ± 2
G69.E04	135.659	−32.789	0.223 ± 0.0169	15.43	*100*	–	–	–	–
G69.E05	148.362	−32.934	0.912 ± 0.0293	14.71	*100*	–	–	–	–
G69.E06	154.601	−30.643	0.913 ± 0.021	15.19	90	−0.25	−4.52	–	–
G69.E07	168.114	−31.119	1.948 ± 0.0462	14.37	95	−0.34	−6.11	–	–
G69.E08	177.794	−30.877	0.340 ± 0.0199	14.03	100	−0.29	−5.12	–	–
G69.E09	182.286	−46.535	0.223 ± 0.0175	15.09	*100*	–	–	–	–
G69.E10	202.310	−44.848	0.875 ± 0.0197	14.85	97	−0.26	−4.65	–	–
G69.E11	316.602	884.971	0.371 ± 0.0152	0.74	*27*	–	–	–	–
G69.E12	336.457	886.498	2.490 ± 0.0139	0.06	*35*	–	–	8.6 ± 4.1	+87 ± 47
G69.E13	339.055	887.444	0.254 ± 0.0167	1.08	–	–	–	–	–
G69.E14	346.758	881.284	0.202 ± 0.0177	1.66	*98*	–	–	–	–
G69.E15	354.176	888.587	3.462 ± 0.0438	−0.43	97	−0.52	−9.31	3.7 ± 0.9	−75 ± 26
G69.E16	354.379	877.810	0.465 ± 0.0172	−1.45	100	−0.71	−12.67	–	–
G69.E17	359.054	889.443	0.739 ± 0.0171	0.49	*84*	–	–	–	–
G69.E18	382.130	931.563	0.471 ± 0.0176	1.61	*13*	–	–	–	–
G69.E19	389.840	902.838	0.419 ± 0.017	1.46	100	−0.40	−7.15	–	–
G69.E20	390.640	935.887	0.279 ± 0.0149	2.24	*79*	–	–	–	–
G69.E21	401.609	933.040	0.933 ± 0.0178	1.32	77	−0.33	−5.98	–	–
G69.E22	404.653	−132.930	7.548 ± 0.105	14.56	98	−0.36	−6.37	6.2 ± 1.4	−85 ± 18
G69.E23	441.565	401.135	1.593 ± 0.0304	13.67	82	−0.08	−1.49	–	–
G69.E24	557.808	−132.329	2.908 ± 0.0848	14.46	80	−0.08	−1.35	16.0 ± 5.1	−42 ± 3

Notes. [a] The reference position is RA(J2000)=$20^h10^m09\overset{s}{.}04272\pm0\overset{s}{.}00007$ and Dec(J2000)=$+31°31'34\overset{''}{.}9736\pm0\overset{''}{.}0009$. [b] The values reported in italics indicate that only one σ component has been detected and therefore no ΔV_Z can be measured.

Table A.3. Parameters of the 6.7 GHz CH_3OH maser features detected in G81.871+0.781 (W75N).

(1) Maser	(2) RA[a] offset (mas)	(3) Dec[a] offset (mas)	(4) Peak Intensity (I) (Jy beam^{-1})	(5) V_{LSR} (km s^{-1})	(6) Δv_L (km s^{-1})	(7) P_l^b (%)	(8) χ^b (°)	(9) ΔV_i^c (km s^{-1})	(10) $T_b\Delta\Omega^c$ (log K sr)	(11) P_V (%)	(12) ΔV_Z (m s^{-1})	(13) θ^d (°)
W75N.M01	-278.842	-402.912	0.040 ± 0.004	6.48	0.60	–	–	–	–	–	–	–
W75N.M02	-246.549	-236.130	0.132 ± 0.009	3.85	0.38	–	–	–	–	–	–	–
W75N.M03	-232.319	-226.574	0.039 ± 0.004	6.31	0.45	–	–	–	–	–	–	–
W75N.M04	-261.454	-251.808	0.273 ± 0.015	3.98	0.22	–	–	–	–	–	–	–
W75N.M05	-215.057	-177.788	0.099 ± 0.009	5.60	0.26	–	–	–	–	–	–	–
W75N.M06	-206.384	-184.334	0.083 ± 0.004	6.48	0.24	–	–	–	–	–	–	–
W75N.M07	-203.816	-346.684	0.057 ± 0.004	6.70	0.27	–	–	–	–	–	–	–
W75N.M08	-79.362	-77.820	0.397 ± 0.007	5.47	0.22	–	–	–	–	–	–	–
W75N.M09	-77.678	-71.812	1.299 ± 0.015	5.69	0.20	–	–	–	–	–	–	–
W75N.M10	-62.985	-66.975	12.001 ± 0.031	5.82	0.23	10.9 ± 1.5	−10 ± 1	$0.4^{+0.1}_{-0.2}$	$10.1^{+0.1}_{-1.0}$	–	–	90^{+7}_{-7}
W75N.M11	-44.670	-81.238	7.285 ± 0.028	5.21	0.24	11.7 ± 0.5	−18 ± 2	$0.4^{+0.1}_{-0.1}$	$10.3^{+0.1}_{-0.2}$	–	–	90^{+4}_{-4}
W75N.M12	-39.871	-80.288	3.693 ± 0.017	5.12	0.25	13.4 ± 2.1	−15 ± 3	$0.5^{+0.2}_{-0.3}$	$10.2^{+0.2}_{-1.1}$	–	–	90^{+7}_{-7}
W75N.M13	-35.997	30.689	1.530 ± 0.014	4.33	0.21	–	–	–	–	–	–	–
W75N.M14	-29.808	-71.411	2.092 ± 0.027	5.21	0.37	13.0 ± 1.2	−15 ± 8	$0.5^{+0.3}_{-0.1}$	$10.8^{+0.1}_{-0.2}$	–	–	90^{+8}_{-8}
W75N.M15	-25.977	36.072	0.960 ± 0.012	4.46	0.19	–	–	–	–	–	–	–
W75N.M16	-25.388	-916.046	3.827 ± 0.011	9.51	0.22	12.9 ± 0.6	−15 ± 1	$0.4^{+0.1}_{-0.1}$	$10.1^{+0.1}_{-0.2}$	–	–	90^{+4}_{-4}
W75N.M17	-16.841	45.914	0.493 ± 0.012	4.42	0.21	–	–	–	–	–	–	–
W75N.M18	-14.904	66.551	0.512 ± 0.013	4.42	0.19	–	–	–	–	–	–	–
W75N.M19	-10.189	-63.904	0.166 ± 0.009	6.00	0.23	–	–	–	–	–	–	–
W75N.M20	-7.157	-56.038	0.322 ± 0.008	5.47	0.30	–	–	–	–	–	–	–
W75N.M21	0.000	0.000	25.899 ± 0.051	4.64	0.19	9.4 ± 0.5	−16 ± 1	$0.4^{+0.1}_{-0.1}$	$10.0^{+0.1}_{-0.1}$	0.9	1.2 ± 0.2	90^{+5}_{-5}
W75N.M22	0.632	-58.525	0.047 ± 0.004	6.18	0.87	–	–	–	–	–	–	–
W75N.M23	8.294	-21.351	0.497 ± 0.014	4.99	1.95	–	–	–	–	–	–	–
W75N.M24	9.431	-53.616	0.074 ± 0.004	5.17	1.98	–	–	–	–	–	–	–
W75N.M25	17.388	30.617	0.499 ± 0.015	3.94	0.89	–	–	–	–	–	–	–
W75N.M26	17.472	27.020	0.166 ± 0.013	4.38	0.23	–	–	–	–	–	–	–
W75N.M27	31.703	-1.568	0.760 ± 0.028	5.21	0.23	–	–	–	–	–	–	–
W75N.M28	36.797	6.535	0.334 ± 0.015	5.30	0.21	–	–	–	–	–	–	–
W75N.M29	37.008	46.204	17.471 ± 0.047	4.11	0.21	7.6 ± 0.4	−7 ± 4	$0.4^{+0.1}_{-0.1}$	$10.1^{+0.1}_{-0.2}$	1.4	2.1 ± 0.3	90^{+6}_{-6}
W75N.M30	39.534	13.592	0.570 ± 0.016	5.34	0.22	–	–	–	–	–	–	–
W75N.M31	42.481	-2.518	0.568 ± 0.021	3.45	0.22	–	–	–	–	–	–	–
W75N.M32	42.818	53.776	4.600 ± 0.041	4.07	0.22	8.5 ± 1.2	−28 ± 13	$0.4^{+0.4}_{-0.1}$	$10.1^{+0.1}_{-0.6}$	–	–	90^{+9}_{-9}
W75N.M33	47.954	3.777	1.696 ± 0.011	3.37	0.19	6.8 ± 0.5	+4 ± 6	$0.4^{+0.2}_{-0.1}$	$9.9^{+0.1}_{-0.3}$	–	–	90^{+7}_{-7}
W75N.M34	66.563	-859.219	1.586 ± 0.006	8.94	0.19	3.3 ± 1.5	−12 ± 6	$0.4^{+0.2}_{-0.1}$	$9.7^{+0.2}_{-0.9}$	–	–	90^{+4}_{-4}
W75N.M35	75.699	49.385	7.693 ± 0.024	3.50	0.20	8.5 ± 1.5	−14 ± 6	$0.4^{+0.1}_{-0.2}$	$9.9^{+0.1}_{-1.1}$	–	–	90^{+8}_{-8}
W75N.M36	109.339	-482.712	0.771 ± 0.010	7.05	0.19	–	–	–	–	–	–	–
W75N.M37	118.938	29.186	0.272 ± 0.018	4.24	0.25	–	–	–	–	–	–	–
W75N.M38	123.569	-393.288	10.817 ± 0.047	7.36	0.20	9.8 ± 0.9	−13 ± 6	$0.4^{+0.3}_{-0.1}$	$10.0^{+0.1}_{-0.4}$	–	–	90^{+6}_{-6}
W75N.M39	126.222	-501.926	0.736 ± 0.045	7.23	0.19	–	–	–	–	–	–	–
W75N.M40	127.148	-404.903	4.089 ± 0.048	7.36	0.25	7.5 ± 1.4	−3 ± 9	$0.5^{+0.2}_{-0.3}$	$10.1^{+0.1}_{-1.0}$	–	–	90^{+11}_{-11}
W75N.M41	132.748	-513.611	1.014 ± 0.025	7.23	0.21	–	–	–	–	–	–	–
W75N.M42	134.811	-406.067	3.894 ± 0.016	7.58	0.22	–	–	–	–	–	–	–
W75N.M43	136.874	-425.190	7.114 ± 0.047	7.40	0.22	9.3 ± 1.1	−29 ± 5	$0.4^{+0.3}_{-0.1}$	$10.0^{+0.2}_{-0.7}$	1.0	1.6 ± 0.3	90^{+7}_{-7}
W75N.M44	137.379	-437.584	4.103 ± 0.025	7.23	0.20	8.3 ± 3.0	−41 ± 11	$0.5^{+0.2}_{-0.2}$	$9.8^{+0.1}_{-1.4}$	–	–	90^{+47}_{-47}
W75N.M45	142.094	140.930	0.258 ± 0.014	4.33	0.22	–	–	–	–	–	–	–
W75N.M46	156.030	-699.806	0.202 ± 0.004	6.61	2.71	–	–	–	–	–	–	–
W75N.M47	167.313	-690.742	1.641 ± 0.009	7.01	0.22	8.6 ± 1.2	+5 ± 11	$0.4^{+0.3}_{-0.1}$	$10.1^{+0.1}_{-0.7}$	–	–	90^{+8}_{-8}

Notes. [a] The reference position is RA(J2000)=20^{h}38^{m}36^s.41744±0^s.00008 and Dec(J2000)=+42°37′35″.1153±0″.0011. [b] P_l and χ are the mean values of the linear polarization percentage and the linear polarization angle measured across the spectrum, respectively. [c] The best-fitting results obtained by using a model based on the radiative transfer theory of CH_3OH masers for $\Gamma + \Gamma_\nu = 1$ s^{-1} (Vlemmings et al. 2010; Surcis et al. 2011a). The errors were determined by analyzing the full probability distribution function. [d] The angle between the magnetic field and the maser propagation direction is determined by using the observed P_l and the fitted emerging brightness temperature. The errors were determined by analyzing the full probability distribution function.

Table A.4. Parameters of the 6.035 GHz ex-OH maser features detected in G81.871+0.781 (W75N).

(1) Maser	(2) RA[a] offset (mas)	(3) Dec[a] offset (mas)	(4) Peak Intensity (I) (Jy beam^{-1})	(5) V_{LSR} (km s^{-1})	(6) P_V (%)	(7) ΔV_Z (km s^{-1})	(8) $B_\parallel$ (mG)	(9) P_l (%)	(10) χ (°)
W75N.E01	137.254	−377.349	0.063±0.007	7.20	100	+0.39	+6.88	–	–
W75N.E02	144.942	−369.462	2.596±0.012	6.87	84	+0.43	+7.76	1.7 ± 0.6	−36 ± 11
W75N.E03	166.882	−362.985	0.313±0.007	8.13	98	+0.48	+8.64	–	–
W75N.E04	169.924	−666.634	0.377±0.007	7.30	82	+0.14	+2.47	–	–
W75N.E05	179.807	−416.217	0.601±0.008	8.03	98	+0.38	+6.71	–	–

Notes. [a] The reference position is RA(J2000)=20^{h}38^{m}36^s.41744±0^s.00009 and Dec(J2000)=+42°37′35″.1153±0″.0013.

Appendix B: Spectra

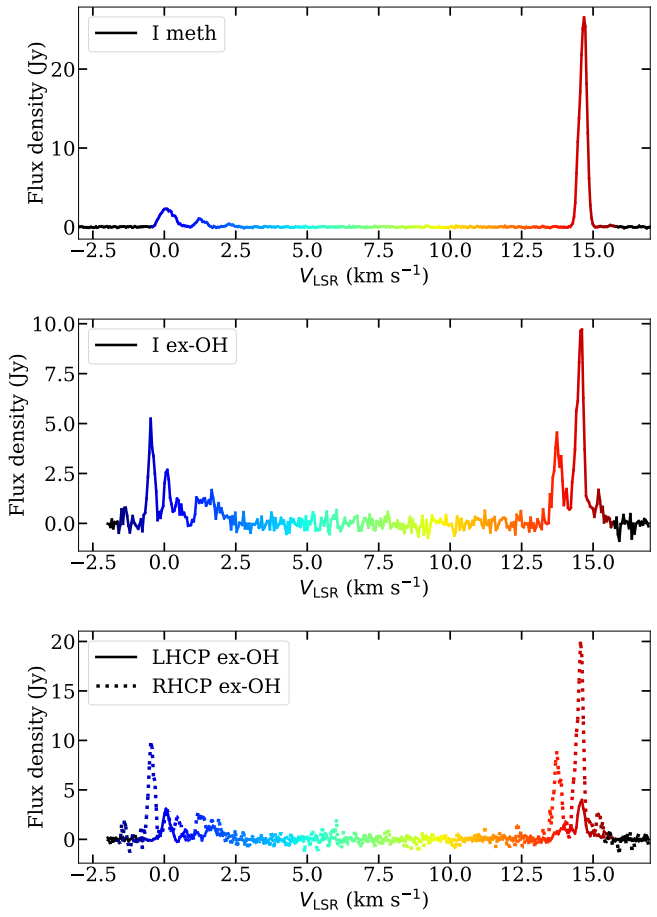

Fig. B.1. The total intensity (I) spectra of the 6.7 GHz CH_3OH (upper panel) and 6.035 GHz ex-OH (middle panel) maser emissions, and the left- and right-hand circular polarization (LHCP, RHCP) spectra (bottom panel) of the ex-OH maser emission detected toward G69.540-0.976 (ON 1). The systemic velocity of the region is $V^{\rm ON\,1}_{\rm LSR,sys}$ = +11.6 kms^{-1} (Bronfman et al. 1996).

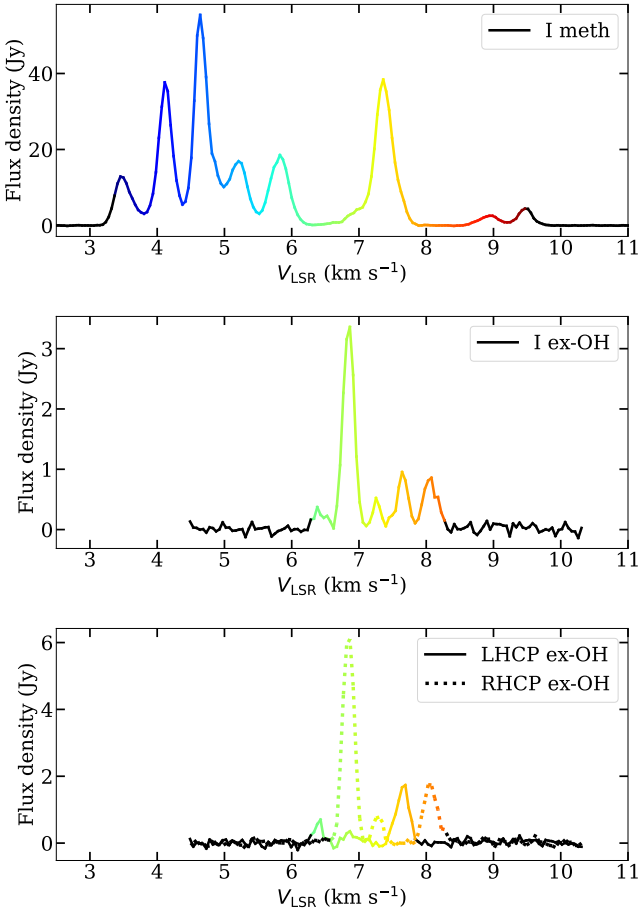

Fig. B.2. Similar to Fig. B.1 but for G81.871+0.781 (W75N). The systemic velocity of the region is $V^{\rm W75N}_{\rm LSR,sys}$ = +10.0 kms^{-1} (Shepherd et al. 2003).